5TH INTERNATIONAL MECHANICAL ENGINEERING CONGRESS

9TH & 10TH MAY 2015
KARACHI - PAKISTAN

5th IMEC Conference Proceedings

Jointly Organised by

The Institution of Engineers Pakistan
Karachi Centre

&

NED University of Engineering & Technology

in collaboration with

Federation of Engineering Institutions of Islamic Countries (FEIIC)

FEISCA

Federation of Engineering Institutions of South & Central Asia (FEISCA)

Designed & Printed by Classic Printers Ph: 32770826

Organizing and Scientific Advisory Committee

Organizing Committee

Engr.Farhat Adil, Chairman –IEP Karachi Centre

Engr.Syed Ali Hasnain Naqvi, Vice President-(Mech)-IEP

Engr.Sohail Bashir, Chairman International Affairs-IEP

Engr.Ayaz Mirza, Secretary-IEP Karachi Centre

Engr.Prof.Dr.Muhammad Tufail, Convener

Engr.Prof.Dr.Mubashir Ali Siddiqui, Co-Convener

Engr.Amanullah Hanif, Co-Convener

Engr.Dr.Maaz Akhtar, Secretary

Engr.Prof.Dr.Syed Amir Iqbal, Member

Engr.Prof.Dr.Nasir Uddin Shaikh, Member

Engr.Dr.Muhammad Shakaib, Member

Engr.Dr.Zahoor ul Hussain Awan, Member

Engr.Naveed Ur Rehman, Member

Engr.Syed Ahmed Raza, Member

Engr.Muhammad Muzammil, Member

Scientific Advisor and Review Committee

Dr.Muhammad Asif, Glasgow Calendonia University, UK

Eur.Ing.Dr.Ayrneric Girard, University of Adolfo Ibanez, Chile

Dr.Haroon Junaidi, University of Abertay, Dundee, UK

Dr.Saad Bin Mansoor, KFUPM, Saudi Arabia

Dr.Iqbal Ahmed, University of Malaysia, Pahang

Dr.Tariq Muneer, Edinburgh Napier University, UK

Dr.Fakhir Hasani, Al-Imam Mohammad Ibn Saud Islamic University

Dr.Muhammad Sohail Ahmed, Eastern Michigan University, USA

Dr.Tariq Shamim, Masdar Institute,UAE.

Dr.Sayyad Zahid Qamar, Sultan Qaboos University,Oman

TABLE OF CONTENTS

CHEMICAL LOOPING COMBUSTION (CLC): A NOVEL TECHNOLOGY FOR ENERGY PRODUCTION FROM THE COAL WITH INHERENT CO2 CAPTURE 1-5

M. Younas1 I. K. Swati1 and S. Gul1, Chemical Engineering Department, University of Engineering & Technology, Peshawar, Pakistan .

OFF-GRID ELECTRICITY PRODUCTION FOR SCHOOLS WITH HYBRID SYSTEM IN THE COASTAL REGION OF SINDH-PAKISTAN 6-10

A. Khalid1 , A.A. Ahmed , and S.A. Raza1Mechanical Engineering Department, NED University of Engineering & Technology, Karachi, Pakistan

LOW COST WATER PUMPING FOR SUSTAINABLE IRRIGATION USING RENEWABLE ENERGY BASED RAM PUMP 11-16

M. Adil1, A. Khan, M. A. Arshad, M. S. Aslam, R. Zafar and Samiullah1Department of Civil Engineering, University of Engineering & Technology, Peshawar, Pakistan National Institute of Urban Infrastructure Planning, University of Engineering & Technology, Peshawar, Pakistan

PRODUCTION OF BIODIESEL BY REACTIVE DISTILLATION SIMULATION STUDIES USING ASPEN PLUS 17-22

Awan Zahoor M.Saleem Chohan, Saud Hashmi1,Engr. Fahim Uddin, Department of Chemical Engineering, NED University Of Engineering and Technology Karachi, Pakistan. Department of Chemical Engineering, Universiti Teknologi, Malaysia

TEMPERATURE PREDICTION OF A SOLID BODY BY TWO-COLOR METHOD USING IMAGE-PROCESSING TECHNIQUE 23-28

Sohaib Z Khan, Muhammad A Khan, Hamza Ahmed1, Ali ZainUl Abedeen1, Tayyab Gulfaraz1, Hassaan Ul Haq Department of Engineering Sciences, PN Engineering College, National University of Sciences and Technology, Karachi, Pakistan.

UNSTEADY MOTION OF FRACTIONALIZED SECOND GRADE FLUID WITH SLIP EFFECTS 29-38

Muhammad Jamil1, Sanaullah Dehraj Department of Mathematics, NED University of Engineering & Technology, Karachi, Pakistan. Department of Mathematics and Statistics, Quaid-e-Awam University of Engineering, Science and Technology, Nawabshah, Pakistan.

EFFECT OF TEMPERING TEMPERATURE ON SUSCEPTIBILITY OF INTERGRANULAR CORROSION OF AUSTENITIC STAINLESS STEEL (AISI 304) 39-42

M.Rizwan1, Iftikhar A, M.Ali, Muzammily, Metallurgical Engineering Department, NED University of Engineering & Technology, Karachi, Pakistan Byco Petroleum Pakistan Limited.

SILVER NANOPARTICLES - SYNTHESIS, CHARACTERISATION AND THEIR APPLICATION AS POLYMER REINFORCEMENT. 43-47

Humair Ahmed, S.M Mohsin and M. Faizan, Materials Engineering Department, NED University of Engineering & Technology, Karachi, Pakistan.

SYNTHESIS OF ALUMINA - ALUMINUM TITANATE NANO COMPOSITE BY REACTION SINTERING AND ITS CHARACTERISATION 48-53

S. M. Mohsin Jafri1, M. Faizan and Humair A. Siddiqui, Materials Engineering Department, NED University of Engineering & Technology, Karachi, Pakistan.

DETERMINATION OF PITTING POTENTIALS OF PASSIVATING MATERIAL IN CHLORIDE ION CONTAINING ENVIRONMENT. 54-58

Muhammad Faizan1*,Humair Ahmed2, S. M Mohsin Jafri3, Department of Materials Engineering, NED University of Engineering & Technology, Karachi Pakistan.

DETERMINATION OF ACCURATE MACHINE-SETTINGS FOR THE FACE- MILLING OF HYPOID GEAR 59-67

M. Wasif,*, M. Rababah, S.M. Hasan1 and S.A. Iqbal, Department of Industrial & Manufacturing Engineering, NED University of Engineering & Technology, Karachi, Pakistan. Mechanical Engineering Department, Hashemite University, Zarqa, Jordan.

IMPLEMENTATION OF WASTE ASSESSMENT MATRIX AND LINE BALANCING FOR PRODUCTIVITY IMPROVEMENT IN A HIGH VARIETY/HIGH VOLUME MANUFACTURING PLANT 68-75

Basit Ali1, Sarah Jaweed and Dr. Muhammad Fahad, MEM Students, Industrial & Manufacturing Department, NED University of Engineering & Technology, Karachi, Pakistan.

COMPARISON IN PROFILE AND LEAD VARIATION OF SPUR GEAR DEVELOPED BY CNC WIRE-EDM AND HOBBING 76-81

Abdul Rahim, Aqueel Shah, Salman Nisar, Department of Industrial Manufacturing Engineering and Management, PN Engineering College National University of Sciences and Technology, PNS Jauhar,Pakistan.

AN EFFICIENT METHOD OF COLLISION DETECTION FOR 5-AXIS CNC MILLING 82-86

Aqeel Ahmed1, Liming Wang and Amir Iqbal, 1Industrial and Manufacturing Engineering Department, NED University of Engineering & Technology, Karachi, Pakistan. Research Centre for Sustainable Manufacturing Shandong University Jinan, China

EVALUATION OF MAINTENANCE MANAGEMENT PRACTICES IN AUTOMOTIVE INDISTRIES OF PAKISTAN 87-92
Javeria Younus1,DrMuhammad Fahad1, and Dr.Maqqasood A.Khan1, Department of Industrial and Manufacturing Engineering, NED University of Engineering & Technology, Karachi, Pakistan

AN APPLICATION OF SUB-STRUCTURING TECHNIQUE FOR A LARGE BODY DYNAMIC ANALYSIS 93-101
Nadeem Shafi Khan and Huda Zahid, National University of Sciences and Technology, Islamabad, Pakistan

ERGONOMIC ANALYSIS OF A HUMAN BODY IN A RESTRICTED SPACE ENVIRONMENT 102-110
Nadeem Shafi Khan and Faria Mazhar, CAE, National University of Sciences and Technology, Islamabad, Pakistan

NUMERICAL STUDY OF TENSILE TESTING OF THIN POLYDIMETHYLSILOXANE (PDMS) SAMPLE 111-114
Syed Murtuza Mehdi, Maaz Akhtar Soo Wan Kim and Muhammad Muzamil, Department of Mechanical Engineering, NED University of Engineering and Technology, Karachi, Pakistan.
Department of Mechatronics Engineering, Jeju National University, Jeju, South Korea.

NUMERICAL INVESTIGATION OF THERMAL PERFORMANCE OF SOLAR AIR HEATER WITH RIB-ROUGHENED CHANNELS 115-119
M. Shakaib, IslahUddin, I. Ahmed,Mechanical Engineering Department, NED University of Engineering & Technology, Karachi, Pakistan. Faculty of Engineering Technology, University Malaysia Pahang, Kuantan, Malaysia

HORIZONTAL AXIS WIND TURBINE BLADE MANUFACTURING THROUGH VARTM (VACUUM ASSISTED RESIN TRANSFER MOLDING) 120-125
Muhammad Muzamil, Daniyal Rizwan, Hassan Mehboob, Umair Mohiuddin and Sadiqeen Noor Mechanical Engineering Department, NED University of Engineering & Technology, Karachi, Pakistan

MHD VISCOUS FLUID FLOWS WHEN VORTICITY DISTRIBUTION PERTURBED BY UNIFORM AND EXPONENTIAL STREAMS 126-131
MUHAMMAD JAMIL, AFAQUE AHMED, Department of mathematics, NED University of Engineering & Technology Karachi, Pakistan

EFFECT OF HEAT TREATMENT ON THE CORROSION RATE OF AISI 1045 STEEL, WHEN SUBJECTED TO VARIOUS ENVIRONMENTS 132-135
M.Rizwan, M.Ali, M.Samiuddin, Metallurgical Engineering Department, NED University of Engineering & Technology, Karachi, Pakistan

COAL GASIFICATION AS A SOURCE OF SUSTAINABLE ENERGY – GEOMETRIC ANALYSIS USING ASPEN PLUS® MODEL 136-140
S. A. Taqvi1, F. Uddin, Dr. I. Memon and S. Nadeem, Chemical Engineering Department, University Technology Petronas Malaysia, Chemical Engineering Department, NED University of Engineering & Technology, Karachi Pakistan.

CHEMICAL LOOPING COMBUSTION (CLC): A NOVEL TECHNOLOGY FOR ENERGY PRODUCTION FROM THE COAL WITH INHERENT CO_2 CAPTURE

M. Younas[1,*], I. K. Swati[1] and S. Gul[1]
[1]Chemical Engineering Department, University of Engineering & Technology, Peshawar, Pakistan

[*]Corresponding author. Tel.: +92 333 3811139. Fax: +92 91 9216663
E-mail address: m.younas@uetpeshawar.edu.pk

Abstract

The current work investigates the theoretical behaviour of a CLC operated packed bed reactor for the combustion of syngas from coal gasification plant with Fe_2O_3 (Hematite) as oxygen carrier material. The simulation was performed for the I-D transient model of the packed bed reactor for oxidation and reduction cycle. The system is composed of two cycles, oxidation and reduction, whereas the flue gas from the reduction cycle contains CO_2 and H_2O and the flue gas from the oxidation cycle contains only N_2 and some un-reacted O_2. Thus, CO_2 and H_2O are inherently separated from the rest of the flue gases, and no major energy is required for this separation. Three different options were considered for the study as the base cases depending upon the weight fraction of Fe_2O_3, temperature of the feed gas and bed and flow direction of the feed gas for the succeeding cycle. One reactor is used with switching the feed gas over air or syngas for the oxidation and reduction cycles, respectively. The results showed that reverse flow CLC process achieves the maximum efficiency producing high temperature exit gas stream during the oxidation and the reduction cycles with no fuel slip.

Keywords: Chemical looping combustion (CLC); packed bed reactor; modelling and simulation; syngas; hematite.

1 INTRODUCTION

CO_2 is the most prevalent greenhouse gas which is the main contributor to global warming. Power generation via fossil fuel combustion with effective CO_2 capture appears to become a key contributor to the energy supply in the foreseeable future. Most of CO_2 capture technologies have high energy penalty for the separation of CO_2 from the rest of the flue gas components, which will result in a lower overall efficiency and in an increase in the price of the energy because of the cost for CO_2 capture [1, 2]. Chemical-looping combustion (CLC) is an emerging and promising technology for fossil fuel combustion, with inherent capture of CO_2. The produced gases, CO_2 and H_2O, leave the system as a separate stream from the exit of the fuel reactor. The H_2O can easily be removed by condensation and pure CO_2 is obtained. As a result, the requirement of CO_2 separation from flue gases, a major cost for CO_2 capture, is circumvented [3, 4].

To develop this promising technology for CO_2 capture at larger scale, further theoretical research work is needed. Both the development of adequate oxygen-carrier and an increased theoretical understanding of the behavior of this phenomenon in a continuous reactor system are necessary for the scale up of the process.

CLC process, conventionally, is operated in fluidized bed reactor but large pressure drop, problems associated in solid gas separation make the packed bed reactor a better alternative, in particular, for extremely high pressure (20-25 bar) and temperature (1100-1200^{0}C) processes [5].

2 MATERIALS AND METHODS

The CLC operated process in packed bed reactor (PBR) system is composed of two cycles, oxidation and reduction Fig-1, where the flue gas from reduction cycle contains CO_2 and H_2O and the flue gas from the oxidation cycle contains only N_2 and some unreacted O_2. Thus, CO_2 and H_2O are inherently separated from the rest of the flue gases, and no major energy is burned up for this separation. Thus only one reactor is used where the solid particles are stationary with the alternate switching of the feed gas e.g. air over to syngas and vice versa. PBR is packed with catalyst as an active metal oxide and an inert support/binder. Hematite (Fe_2O_3) and TiO_2 are the oxygen carrier material (catalyst) and the inert material, respectively [6, 7].

Theoretical model approach of the packed bed reactor (PBR) is based on the transient analysis of temperature of the reacting gas and concentration changes of the solid catalyst material and reacting gases along the length of the reactor. Theoretical model has been described in detail in previous

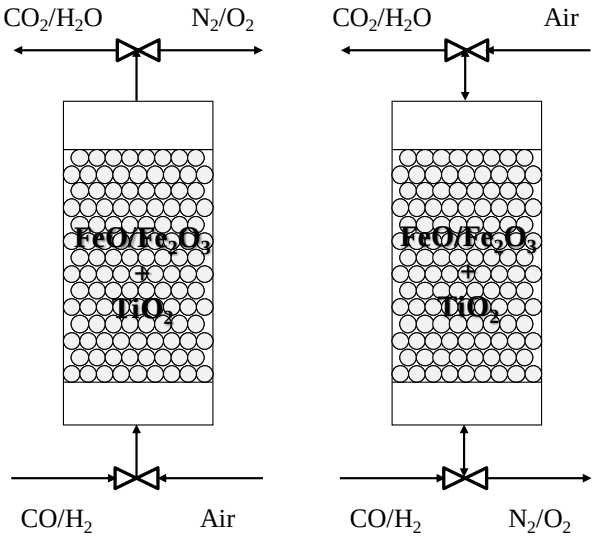

Figure 1: Schematic diagram of CLC operated packed bed reactor, (a) same direction flow, (b) reverse flow.

studies [8, 9]. Model was run in Borland Delphi. Typical syngas composition is described in Table 1. Table 2 enlists the target variables simulation parameters for 1-D transient model simulation.

3 RESULTS AND DISCUSSION

3.1 Oxidation cycle

1-D transient model of CLC packed bed reactor is capable to simulate and predict the instantaneous temperature profile along the axis of the reactor which is useful in determining the maximum temperature change within the reactor and cycle time of the respective cycle. For example, consider the Figure 2 where simulation was run in oxidation mode. Bed temperature in options 1, 2 and 3 was kept constant at 132 ^{0}C, 450 ^{0}C and 750 ^{0}C, respectively. It can be observed that the maximum temperature reaches at the exit of the reactor at a certain time depending upon the weight fraction of active content of Fe_2O_3. Total cycle time during an oxidation cycle is distributed into three different time duration zones;

Δt_1 = time during which exit (reactor) air stream reaches the maximum temperature.

Δt_2 = time during which exit air stream remains at maximum temperature.

Δt_3 = time during which exit air stream temperature drops from maximum temperature to a stead state bed temperature.

These time zones are of great importance while analyzing the different options in the contest of cycle efficiency. As high temperature exit stream will be used for power generation, the oxidation cycle with longer Δt_2 is favored for the CLC process. Therefore, high temperature of the bed and the feed gas guarantees the shorter Δt_1 and longer

Table 1: Syngas Composition

Species	Volume %
CO	60.5
H_2	21.9
CO_2	2.7
H_2O	0.3
N_2	14.6

Table 2: Base cases for 1-D transient reactor

Base case simulation	Feed temperature, T_{feed} (^{0}C)		Bed temperature, T_{feed} (^{0}C)		Flow direction of feed gas during consecutive cycle
Option number	Oxidation cycle	Reduction cycle	Oxidation cycle	Reduction cycle	
Op 1.1	450	132	132	Previous cycle profile	Reverse flow
Op 2.1	450	132	450	Previous cycle profile	Parallel flow
Op 2.2	450	132	450	Previous cycle profile	Reverse flow
Op 2.3	450	450	450	Previous cycle profile	Parallel flow
Op 2.4	450	450	450	Previous cycle profile	Reverse flow
Op 2.5	450	750	450	Previous cycle profile	Parallel flow

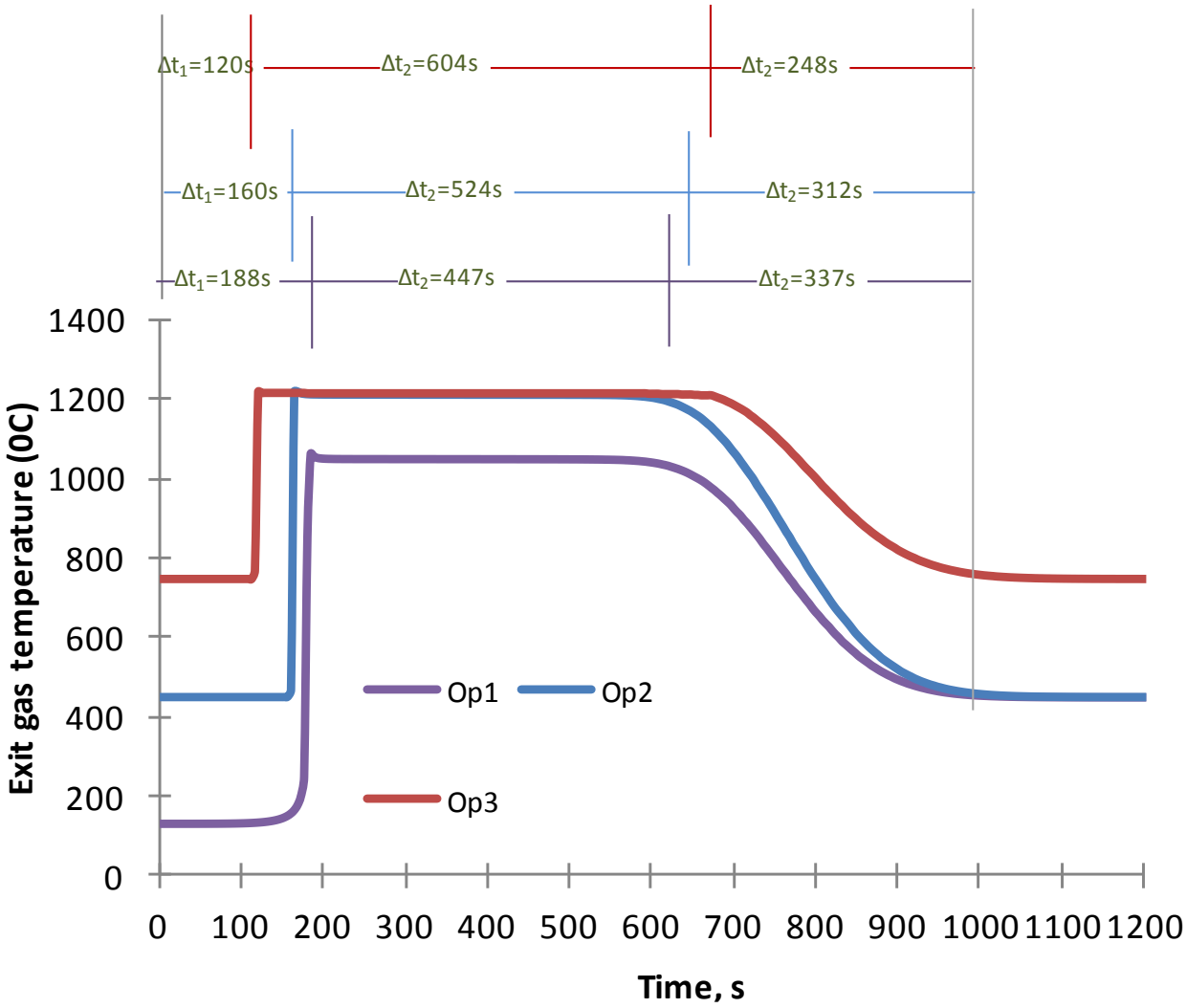

Figure 2: Transient temperature profile; Oxidation first cycle, T_{bed} = 132^{0}C for Op1, 450^{0}C for Op2, 750^{0}C for Op3.

Δt_2. On the other hand Δt_3 is also of great significance as the gas stream during this time at that temperature can be flushed back into the reactor to keep the bed at relatively high temperature for the succeeding reduction cycle or the bed profile at this position of time and length of the reactor can be used for the succeeding cycle either the feed gas is introduced in the same direction or in opposite direction to that of the preceding cycle. The current study is based on the later phenomenon. It is, therefore, inferred from the Figure 2 that high temperature stream at the exit of the air reactor is achieved in less time and remains at that temperature for longer time. Furthermore, less quantity of Fe_2O_3 is needed if bed is heated initially to high temperature. The only disadvantage is the heat penalty by keeping the bed and feed gas at high temperature.

3.2 Reduction cycle

The study of theoretical behavior of the reduction cycle is equally important to investigate the temperature change, cycle time, fuel slip and the pressure drop for the design of reactor. It is found from the thermodynamic investigation that reduction reaction of syngas with hematite is exothermic as a dynamic change in temperature can be observed. Furthermore, temperature change is improved with the increase of hematite, initial feed (syngas) temperature and feed flow rate.

Simulation is run for the fuel reactor under various operating and design parameters. The graphical representation of how temperature of the exit gas changes dynamically for the first reduction cycle is shown in Figures 3. It is noted that for each option, the bed profile of the preceding cycle of oxidation is utilized for the reduction cycle. It is observed that for those reduction options, exit gas stream remains at high temperature for certain time duration if reduction cycle is operated counter currently. In fact, by reverse flow, the feed gas takes in the heat of bed throughout the length of the reactor before the bed cools back to feed gas inlet temperature. Like the oxidation cycle, this high temperature gas

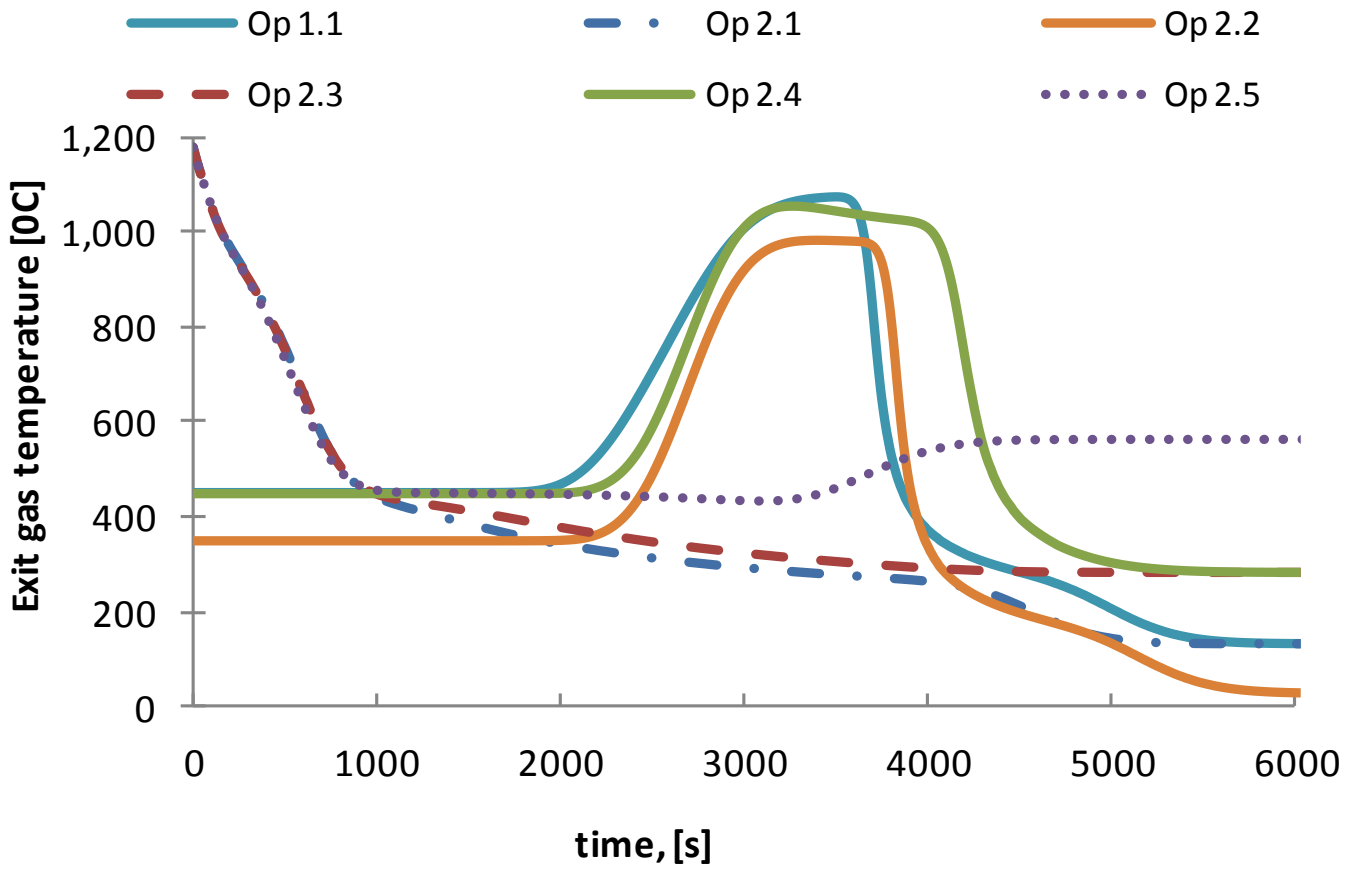

Figure 3: Transient temperature profile; Reduction cycle, Option 1 and 2; Solid line: feasible option; dashed lines: unfeasible option

stream can also be used for to run the steam turbine for power generation.

The dashed lines in Figure 3 denote the unfeasible options which provide insufficient heat for the syngas to be reduced with hematite.

4 CONCLUSIONS AND OUTLOOK

A numerical 1-D transient model of dynamically operated packed bed reactor was analyzed for the reactor performance at high operating and design parameters. The temperature profile for the different options was investigated to meet the target objectives. It was found that the amount of Fe_2O_3 (hematite) distributed in the bed is used to control the temperature of exit gas stream, in particularly from air reactor. Thus a correct amount of hematite should be selected for the first cycle at the start of the process. Cycle time is important since shorter cycle time might give less bed breading and less critical reduction of the material but also much better conversion of the syngas to steam and CO_2. For the same direction flow the feed air during all the oxidation cycle should be heated to 750 ^{0}C thus the bed remains at 750 ^{0}C at the end of oxidation cycle and start of the next reduction cycle.

5 REFERENCES

[1] D. Aoron; C. Tsouris. Separation of CO_2 from flue gas: A review. *Sep. Sci. Technol.* 2005, 40. 321.

[2] B. Metz, O.R. Davidson, P.R. Bosch, R. Dave, L.A. meyer. IPCC, 2007: Climate change 2007: Mitigation. *Contribution of working group III to the fourth assessment report of the intergovernmental panel on climate change*, Cambridge University Press, Cambridge, United Kingdom and New York, NY, USA.

[3] M. Ishida, H. Jin. A novel chemical-looping combustor without NOx formation. *Industrial and Engineering Chemistry Research*, 1996, 35(7): 2469-2472.

[4] F. Mattisson, F. Garcia-Labiano, F. B. Kronberger, A. Lyngfelt, J. Adenez, H. Hofbauer. Chemical-looping combustion using syngas as fuel. *International Journal of Greenhouse Gas Control*, 2007, 1(2): 158-169.

[5] M.M. Hossain, H.I. de Lasa. Chemical-looping combustion (CLC) for inherent CO_2 separations: A review. *Chemical Engineering Science*. 2008, 63, 4433-4451.

[5] A. Lyngfelt, B. Leckner, T.A. Mattisson. Fluidized-bed combustion process with inherent

CO_2 separation; application of chemical-looping combustion. *Chem. Eng. Sci.* 2001, 56:3101-3110.

[6] A. Abad, J. Adanez, A. Cuadrat, F. Garcia-Labiano, P. Gayan, L.F. de Diego. Kinetics of redox reactions of ilmenite for chemical-looping combustion. *Chem. Eng. Sci.* 2011, 66:689-702.

[7] J. Adánez, A. Cuadrat, A. Abad, P. Gayán, L.F. de Diego, F. García-Labiano. Ilmenite activation during consectutive redox cycles in Chemical-Looping Combustion. *Energy & Fuel*, 2010, 24: 1402–1413.

[8] M. Younas, I. K. Swati, I. Ali, N. Ullah, M.I. Ahmad, Performance study of a lab scale packed bed Chemical Looping Combustion reactor: Part b) Oxidation cycle. J. of the Pakistan Institute of Chemical Engineers, Lahore. 40 (1) 2012: 109-114.

[9] M. Younas, I. K. Swati, I. Ali, N. Ullah, M.I. Ahmad, Performance study of a lab scale packed bed Chemical Looping Combustion reactor: Part a) Reduction cycle. *J. of the Pakistan Institute of Chemical Engineers*, Lahore 40 (1) 2012: 114-119.

OFF-GRID ELECTRICITY PRODUCTION FOR SCHOOLS WITH HYBRID SYSTEM IN THE COASTAL REGION OF SINDH-PAKISTAN

A. Khalid[1,*], A.A. Ahmed[1], and S.A. Raza[1]
[1]Mechanical Engineering Department, NED University of Engineering & Technology, Karachi, Pakistan

[*]Corresponding author. *E-mail address*: akhalid@neduet.edu.pk (A. Khalid)

Abstract

Renewable energy technologies have become competitive with traditional power generation techniques. Solar and wind resources of Sindh are suitable for meeting the power needs of schools located in the coastal areas if PV and wind hybrid systems are employed. This study analyzes an off-grid or stand-alone PV-wind hybrid system for meeting electric load of a representative school. HOMER renewable energy optimization software was utilized to size the most cost effective system. The result of this analysis demonstrated that cost of electricity from proposed system is USD 0.27/kWh while cost of diesel-generated electricity is USD 0.31/kWh. Other benefits of the PV-wind hybrid system are independence from utility price fluctuation and positive environmental impact.

Keywords: PV-Wind Hybrid system; renewable energy; schools

1 INTRODUCTION

The current energy crisis in Pakistan is upsetting economic, political and social aspects of the society. Educational institutions in the rural areas are particularly affected by electric power crisis. A significant number of schools in Sindh are without electricity and those that have electricity suffer from frequent power outages. Renewable energy technologies such as wind and photovoltaic can meet major part of the electricity needs of schools. Electricity generated from renewable technologies is becoming cheaper due to dropping prices of photovoltaic and wind systems. On the other hand, the price of electricity generated from diesel or furnace oil is high.

This situation offers an opportunity to explore alternatives such as renewable energy technology for the generation of electric power. Condition is now encouraging in Sindh province, which has best wind and solar resources in Pakistan to adopt renewable energy technology to meet its electricity needs. PV electric generation is the most preferred renewable distributed generation system in Pakistan for small-scale users and wind energy is suitable in the coastal areas of Pakistan where several large wind farms have already been installed.

Once renewable energy technology becomes successful in schools the way will be clear for its large-scale adoption in other sectors of the society. A substantial penetration of renewable energy sources in the national power system would reduce CO_2 emissions significantly, contributing to the reduction of global warming [1]. It will also reduce our dependence on expensive imported oil and gas, which is used to generate electric power in thermal power plants.

An alternative option to renewable energy for school power generation is using small diesel generating sets. Although the price of diesel has dropped considerably in recent months, nonetheless, the cost of generation of electricity with diesel generating sets is still about USD 0.31/kWh. Transportation of diesel for power generation also costs money and theft of diesel is another problem. These issues are absent in the case of proposed hybrid power systems that do not require any fuel.

Low initial cost makes a grid connected PV system very suitable for consumers who are connected to utility. A grid connected PV system uses grid for exporting and importing of electricity when surplus power is available or when shortage occurs. On the other hand, for users who are not connected to local electric grid, the stand-alone or off-grid systems are more suitable. Off-grid system requires batteries to

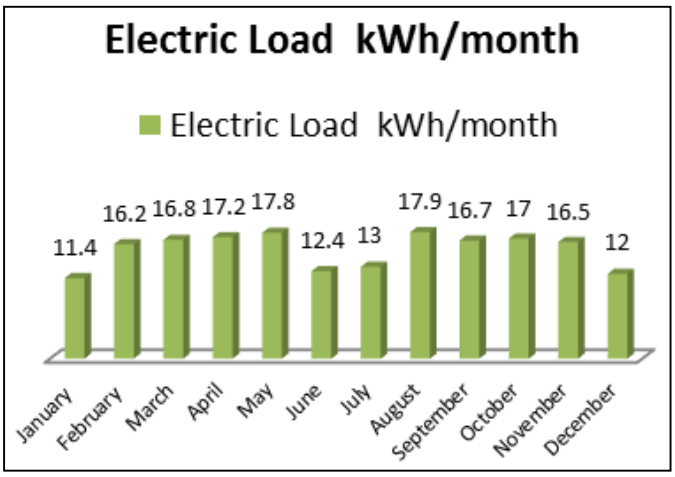

Figure 1. Monthly electric load of a typical school

supply electricity during the time when solar PV and wind energy are not available. For development of renewable energy sources, PV and wind power play a major role in hybrid systems that produce electricity intermittently [2].

A recent survey by Government of Sindh showed that quality and quantity of electric power is not ideal. Many schools in the coastal areas are connected to grid however, a significant number of schools have no electric connections. The stand-alone PV-wind hybrid system equipped with batteries for storage has the potential to meet electric power needs of such schools. The electrical load of a typical school is shown in Figure 1. The graph clearly shows low electricity consumption in summer vacations during June and July. Low electricity consumption in winter is attributable to no use of classrooms and office fans.

The very good solar radiation intensity in this province will help produce more electricity. The fortuitiuos condition of load and supply being in phase ensures that electricity is available for use in schools when it is needed. Schools and other users can employ wind turbine for power generation in the Wind-Energy-Corridor to augment PV system. Fortunately, the afternoon strong sea breeze blowing from the sea to land will start producing power as the sun sets in the west and the PV power drops.

This study was undertaken to show the feasibility of a hybrid PV-wind energy system for the schools of Sindh. This optimization analysis was carried out for local weather conditions to get an accurate quantitative estimate of stand-alone energy systems that can meet the power needs of schools during teaching hours. It is demonstrated through this study that renewable energy generated from PV-wind hybrid system costs less than the electricity produced from diesel power generators.

2 METHODOLOGY

Several design and optimization software are available to meet various needs of investigators in the area of renewable energy. Because of its ease of use, HOMER was employed in the present study to determine the optimum system configuration and to determine the technical and economic viability of hybrid PV-wind power systems for schools in coastal areas of Sindh. HOMER was developed by National Renewable Energy Laboratory (NREL) of USA. It is user-friendly software that is suitable for microgrid optimization for all sectors, from village power and island utilities to grid-connected campuses and military bases [3]. Homer is widely employed by designers, planners and researchers

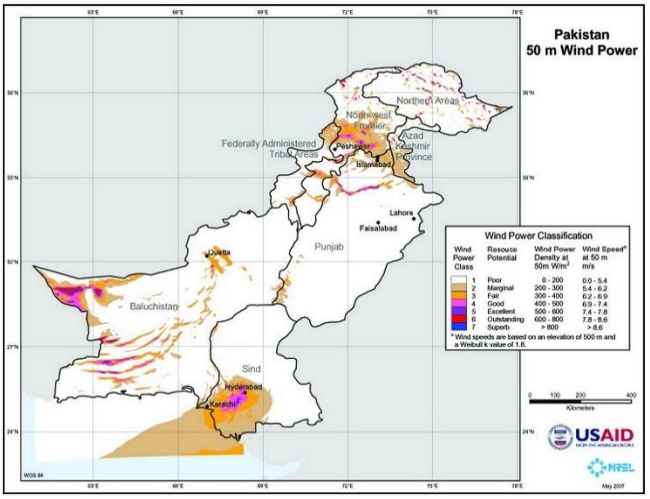

Figure 2. Wind energy potential of Pakistan [6]

for the optimization of renewable energy projects [4, 5].

Precise knowledge of climatic data of the locality where PV-wind system is to be installed is essential for HOMER to estimate the electric power generation capacity of a solar PV plant. Solar data for this project was acquired from NASA website and wind data was obtained from Alternate Energy Development Board (AEDB) of Pakistan [6]. Gharo city (24 N, 67E), which is one of the many towns located in the Wind-Energy-Corridor of Sindh province, was chosen for this study, Gharo receives decent solar radiation throughout the year its wind energy resource is also amongst the best in the country. The wind energy potential of Pakistan is shown in Figure 2.

A PV-wind hybrid system consists of PV array, wind turbine, inverter, battery bank, cables, different kind of switches and safety devices. A brief description of important components of the PV-wind hybrid system is given here.

PV modules are very suitable for electricity generation in Sindh due to high solar radiation intensity. Good quality imported mono-crystalline and poly-crystalline PV modules are available in local market at about PKR 60 per peak-watt. This price is very attractive for large-scale use. The modules can be safely installed on the roof of schools where shading of solar radiation is anticipated to be minimal. Electricity production with wind turbines is feasible in Sindh coastal areas. Small-scale wind turbines of about 1 kW are sufficient to meet the demands of schools. Wind turbines cost more than PV modules on per watt bases. For this study Whisper 1kW wind turbine was chosen for the simulation.

Batteries are required for several reasons such as reducing fluctuations in load and electricity

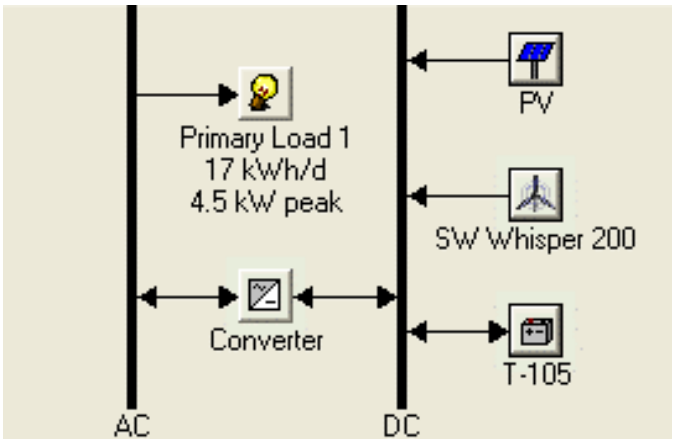

Figure 3. Stand-alone hybrid PV-wind system

generation, improving the hybrid system efficiency of operation and providing security for the energy supply. However, battery is an expensive component [6]. For this study Trojan T-105 battery was selected from HOMER components library.

Inverter is an important component of the renewable energy system that converts direct current (DC) power coming from PV array, wind turbine and batteries into alternating current (AC) power for use in the schools. A generic inverter was selected from HOMER library of components for this simulation. These renewable energy system variables were provided to HOMER along with solar radiation and wind speed data of the region as system inputs.

3 RESULTS AND DISCUSSIONS

HOMER simulation project arrangement is given below in Figure 3. The hybrid system consists of PV array, 1 kW SW Whisper wind turbine, Trojan T-105 battery bank, generic inverter and 17 kWh/day electric loads.

Optimization by HOMER yielded a hybrid PV-wind system of following specifications: PV array of 3.4 kW rated power, wind turbine SW Whisper 200 of 1.0 kW rated power, eight Trojan T-105 batteries and inverter of 3.4 kW rated power. The hybrid system's levelized cost of electricity came out to be USD 0.27/kWh. HOMER output for the important system parameters is given in Table 1. The hybrid system will produce about 10,189 kWh of electricity every year and some excess electricity will also be available.

Table 1. Hybrid PV-wind system HOMER output

Quantity	Amount	Units
Electricity generated	10,189	kWh/year
Excess electricity	3,359	kWh/year
Unmet electric load	266	kWh/year
Renewable fraction	1.00	
PV Capacity factor	19.3	%
PV hours of operation	4,400	hr/year
Turbine Capacity factor	50.6	%
Turbine hours of operation	7,895	hr/year
Levelized cost of electricity	0.27	$/kWh

The monthly production of electricity from PV and wind system is given in Figures 4 and 5, respectively. The dip in PV generation in July and August is due to cloud cover during these two monsoon months. However, it is balanced by increased production of electricity from wind turbine during this period. Although the wind turbine output is distributed throughout the day, most of it is produced during daytime.

Monthly electricity production and its breakup are given in Figure 6. This graph also reflects the reduction in PV output during the monsoon months of July and August. However, the total energy generated is balanced by the increase of wind turbine output. The reduction in power during the winter months coincides with the drop in electric demand because of winter vacation and non-usage of fans. The winter weather is generally pleasant enough that heaters are not needed in Sindh during daytime and hence, energy consumption is lower. Therefore, the drop in power in winter months is not an issue.

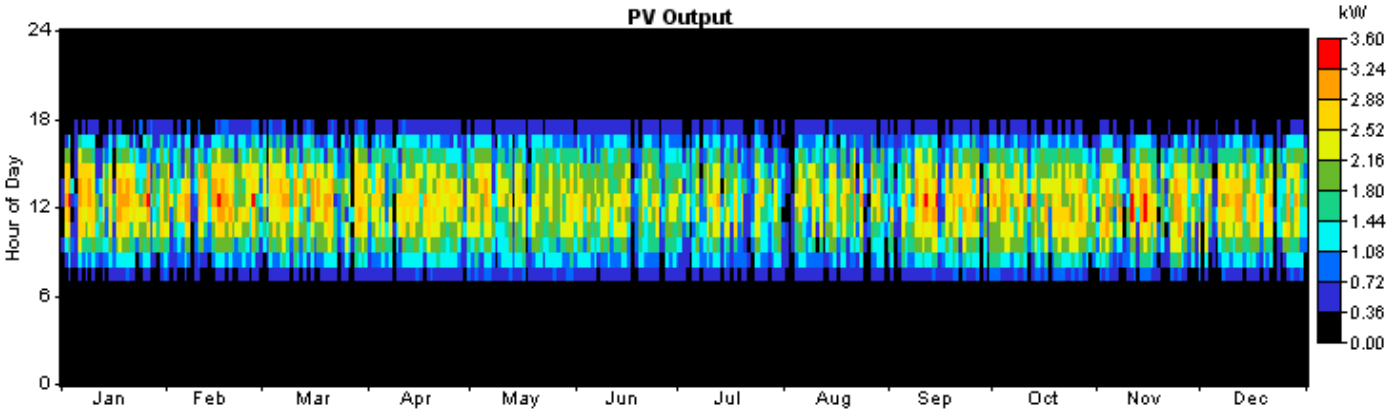

Figure 4. Annual electric power output of PV array

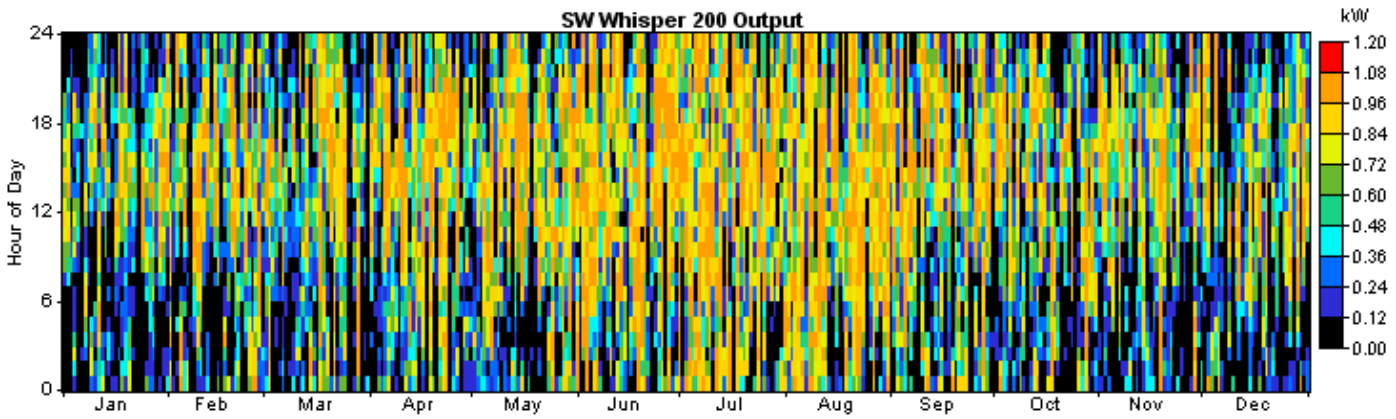

Figure 5. Annual electric power output of wind turbine

Cash flow diagram in Figure 7 shows that the most expensive item in electrical system is the battery bank. Inclusion of batteries in the system increases its availability during low wind condition and during non-sun light conditions such as night, early morning and evening. To a certain extent, need for a larger PV array diminishes as the size of the battery bank increases.

The important battery and inverter performance indicators are listed in Table 2 and 3, respectively. The expected life of the battery is about four and a half years and this causes a significant addition in the cost of the hybrid system during its life cycle. The battery and inverter will incur losses of about 888 kWh/year. The frequency of the state of charge of the battery during its lifetime is shown in the bar graph of Figure 8.

The analysis of the off grid PV system for schools of Sindh showed that solar supplied electricity could be cheaper than electricity supplied by diesel generators. The issues associated with diesel generators such as constant repair and maintenance needs, appointment of an attendant to look after starts and stops of the generator, theft of diesel, etc.

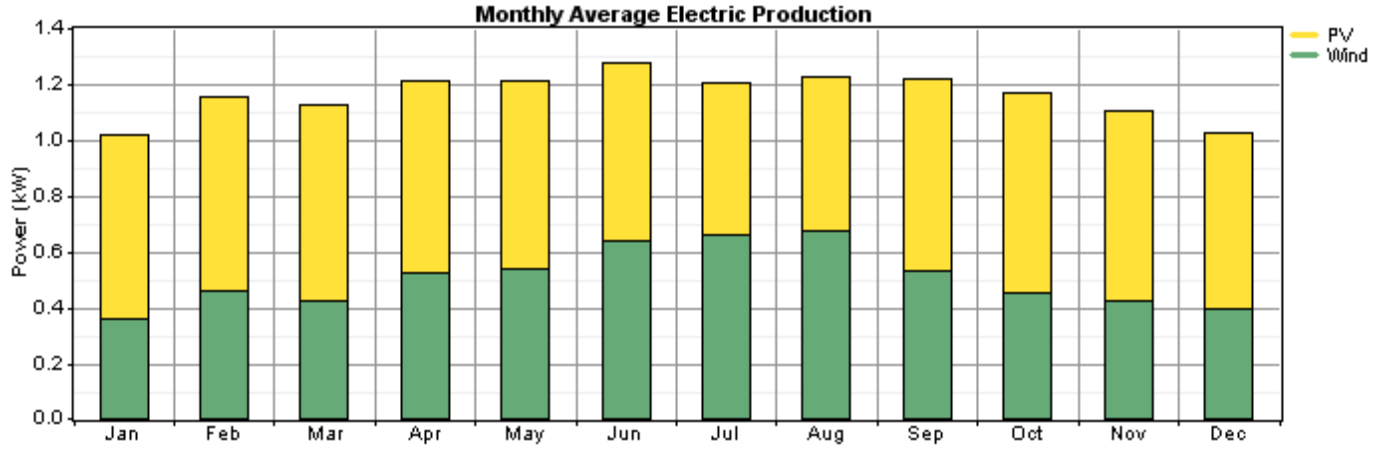

Figure 6. Monthly average electricity production of PV array and wind turbine

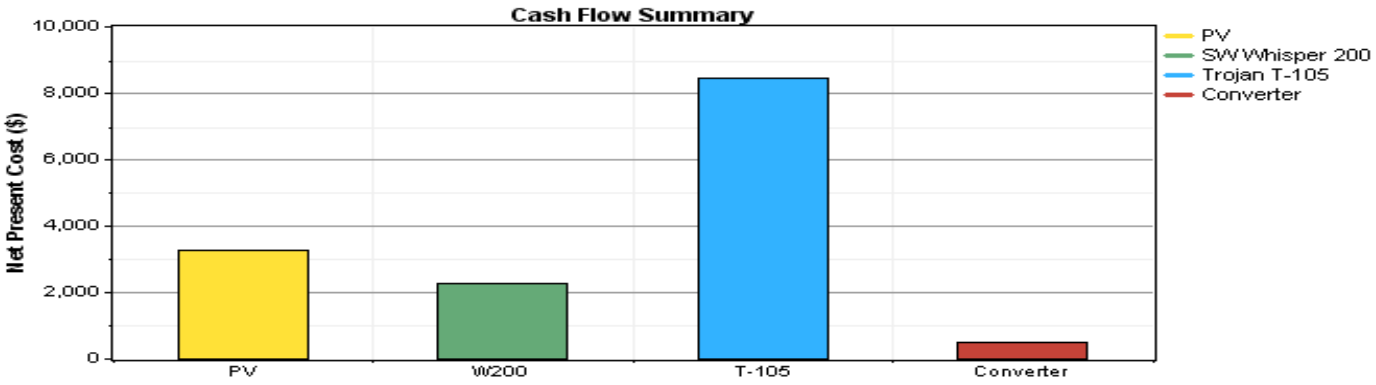

Figure 7. Cash flow diagram shows the cost contribution of different system components

Table 2. Battery performance indicators

Quantity	Amount	Unit
Energy in	1,560	kWh/year
Energy out	1,329	kWh/year
Storage depletion	3	kWh/ year
Losses	228	kWh/ year
Annual throughput	1,441	kWh/ year
Expected life	4.69	years

Table 3. Inverter performance indicators

Quantity	Amount	Unit
Capacity	4.0	kW
Hours of operation	4,379	hrs/ year
Energy in	6,599	kWh/ year
Energy out	5,939	kWh/ year
Losses	660	kWh/ year

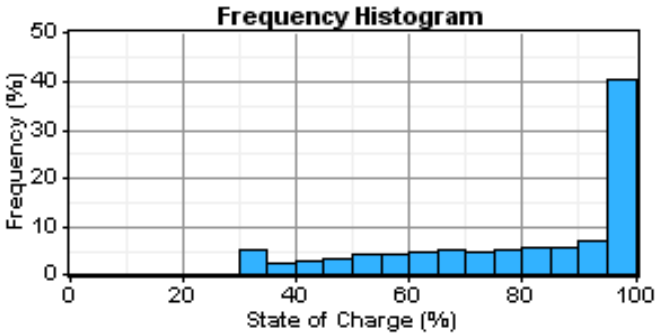

Figure 8. Frequency of state of charge of battery during its lifetime

are not present in the hybrid PV-wind based electric power supply system.

4 CONCLUSIONS

Electricity supplied by hybrid power plants can play a very important part in improving the quality of education in the coastal areas of Sindh where a significant number of schools are without any power. The Sindh government's decision to electrify schools in remote areas can be successful if the cost of electricity is low and the system that is installed is sufficiently robust. The optimization exercise undertaken using HOMER software showed that wind-PV hybrid electric system will meet the power requirement of the schools more than 95% of the time in a year. More than 10 MWh/year of electricity can be generated using the proposed system, with approximately 3.3 MWh/year of excess electricity. The levelized cost of electricity generation at USD 0.27/kWh is lower than diesel generated electricity at USD 0.31/kWh, which makes this option more attractive for use in schools.

REFERENCES

[1] H. Kim, S. Baek, E. Park, H. J. Chang, Optimal green energy management in Jeju, South Korea – On-grid and off-grid electrification, *Renewable Energy*, Volume 69, September 2014, Pages 123-133.

[2] M.H. Ashourian, S.M. Cherati, A.A. Mohd Zin, N. Niknam, A.S. Mokhtar and M. Anwari, Optimal green energy management for island resorts in Malaysia, *Renewable Energy*, Volume 51, March 2013, Pages 36-45.

[3] HOMER Energy optimization software, http://www.homerenergy.com/HOMER_pro.html.

[4] M. Mudasser, E. K. Yiridoe, K. Corscadden, Cost-benefit analysis of grid-connected wind–biogas hybrid energy production, by turbine capacity and site, *Renewable Energy*, Volume 80, August 2015, Pages 573-582.

[5] M.A.M. Ramli, A. Hiendro, K. Sedraoui, S. Twaha, Optimal sizing of grid-connected photovoltaic energy system in Saudi Arabia, *Renewable Energy*, Volume 75, March 2015, Pages 489-495.

[6] Alternative Energy Development Board website, Ministry of Water and Power, Government of Pakistan, http://www.aedb.org.

LOW COST WATER PUMPING FOR SUSTAINABLE IRRIGATION USING RENEWABLE ENERGY BASED RAM PUMP

M. Adil[1*], A. Khan[1], M. A. Arshad[1], M. S. Aslam[2], R. Zafar[1] and Samiullah[1]
[1]Department of Civil Engineering, University of Engineering & Technology, Peshawar, Pakistan
[2]National Institute of Urban Infrastructure Planning, University of Engineering & Technology, Peshawar, Pakistan

[*]Corresponding author. Tel.: +92 3139543411; fax: +92 91 9218223
E-mail address: adil@uetpeshawar.edu.pk (M. Adil)

Abstract

This paper presents the proof of concept of using a water powered ram pump for irrigation purpose. As a water powered ram pump is a self-powered renewable system, the running cost is tremendously reduced to almost zero. Other advantages of using a water powered ram pump include 1000% water lifting, no use of external power/fuel required etc. This paper fills the gap between the use of technology and agriculture industry, which is highly affected by the energy crisis in Pakistan. Agricultural sector is the backbone of Pakistan's economy. Power crisis in Pakistan has negatively affected crop production and relevant exports, which has huge impact on the GDP at national level and unemployment (45% of labour in Pakistan are related to the agriculture industry) and revenue generation for farmers and landlords. Also agriculture industry contributes 24% to GDP and provides employment to 45% of total labour force of the country. Almost 67.5% of the population resides in rural areas and earn its livelihood directly or indirectly, from agricultural sector. Pakistan's agricultural land is 23 million hectares (30% of total) in which 19 million hectares (83% of agricultural land) is irrigated; this is the severity of the demand of very low cost irrigation systems.

The presented irrigation system has a very low initial and operating cost, so it will find its place at all levels of the irrigation sector. It will also help in increasing crop production by improving the economy of farmers. It has been found that this technique can easily replace the existing counterpart fossil fuel based pumping systems for an average farmer in Pakistan.

Keywords: Ram Pump, sustainable irrigation, renewable energy

1 BACKGROUND

The Power crisis in Pakistan has negatively affected crop production and relevant exports, which has huge impact on the GDP at national level (Agriculture industry contributes on 24% of the national GDP) and unemployment as 45% of labour in Pakistan are related to agriculture industry [1]. Almost 67.5% of the population resides in rural areas and earn its livelihood directly or indirectly, from agricultural sector. Pakistan's agricultural land is 23 million hectares (30% of total) in which 19 million hectares (83% of agricultural land) is irrigated. About 35% of the public irrigation schemes of Khyber Pakhtunkhwa are lift schemes which require pumping. There are several private local farmers involved in installing pumps for irrigation for which they have to bear heavy operational and maintenance costs.

There is a need to develop an irrigation system having a very low initial and especially operating cost to implement it at all levels of the irrigation sector. Farmer's survey conducted at Swabi, KP, Pakistan revealed the dropping cultivation trend for specific crops where pumping demands are beyond their capability. Also they said that low cost pumping will save them money to which can then be used for buying seeds and fulfilling other requirements of cultivation. It was also claimed by one farmer that with lower cost of pumping they may be able to produce multiple crops per year compared to only one in current scenario in this region. It has been found from literature that ram pump irrigation may easily replace the existing counterpart fossil fuel based pumping systems for an average farmer in Pakistan.

2 SUSTAINABLE IRRIGATION

The concept of a sustainable system can be simply defined as a system which is technically sound, environmental friendly, socially acceptable, financially feasible, and institutionally viable for present and future generations. . There are variety of debates and discussions about the concept [2]. However, environmental component or pillar of sustainability is the key component for any sustainable system. This implies that no system can be termed as a sustainable system if its environmental aspect is ignored or compromised, and irrigation systems are not any exception to that. Factors contributing towards environmental

sustainability may vary depending on the nature of a system; however, dependency on non-renewable energy is commonly considered as a factor which impairs the environment in one or another shape. Wastage and depletion of non-renewable resources not only directly affects the environment and quality of life for present generations, but it also results in compromising the ability of future generations to fulfil their needs. In summary, minimal or no use of renewable energy is vital towards achieving sustainable irrigation systems.

Pakistan, like many other developing countries, is an energy deficient country. This energy deficient country is basically an agricultural economy based on its irrigation systems including pumping. Lack of available power through affordable non-renewable ways is coupled with low-voltage issues in many places, resulting in use of diesel engines. This situation further aggravates the problem leading towards an emerging demand for renewable energy resources for pumping for sustainable irrigation systems.

On other hand, quality of pumps under use is another major issue. Most of the pumps used for irrigation systems "are not energy-efficient, mainly due to low capital investment [3]. Majority of such pumps are used for groundwater pumping; however, limitations on capital investments are common for surface water pumping as they are in case of groundwater pumping. This poses a serious threat to sustainability of irrigation systems, especially, the environmental component of sustainability. The "Ram Pump" is investigated in this case study to move one step forward towards sustainable irrigation system in developing countries like Pakistan.

3 RAM PUMP

The first ram pump was installed at Oulton, Cheshire, in 1772 and raised water to a height of 16ft [4] since then ram pump designs have been improved over a number of years. Drive Tank Unit (DTU) [5] first developed plastic body ram pump with relatively shorter life of some components to two years, which was extensively tested in Zimbabwe till 1993 for irrigation of vegetable gardens from nearby streams. DTU pump design could irrigate 0.2 to 0.6 hectares of land in 24 hours. Being of lower discharge ram pumps have already been used for furrow, hose irrigation and filling overhead tanks for future irrigation. As low pressures are produced in ram pumps, they cannot be used for pressure dependent irrigation including sprinklers and water cannons etc. It was also found that use of stiffer material, like steel, increases the ability of the pump to lift water much further compared with plastic.

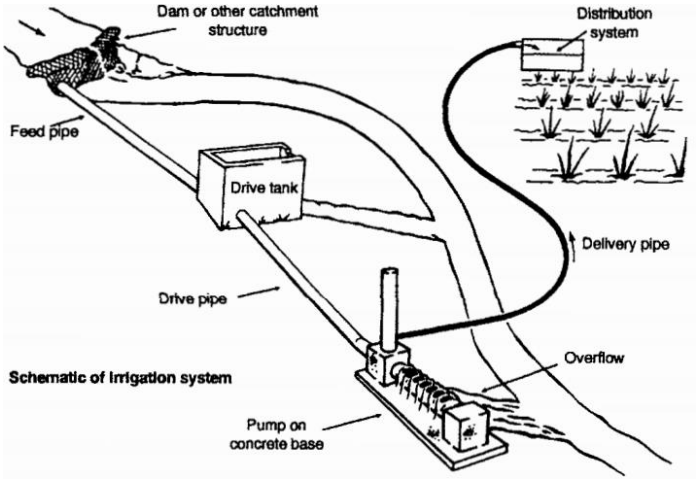

Figure 1 Schematic of irrigation system [5]

A typical ram pump irrigation system is shown in schematic form in Figure 1. Water is wasted at the dam, drive tank as well as pump site but it is fed back to the river, hence no waste. The feed pipe keep the drive tank filled so that a constant head is available to the pump through that drive pipe. The water hammer produced due to sudden opening and closing of overflow valves pushes the water in the delivery pipe through one way valve, thus provides water at higher levels for irrigation.

4 SWABI CASE STUDY

Swabi is a district of Khyber Pakhtunkhwa province of Pakistan, having four Sub-Divisions (called as Tehsils), namely Swabi, Lahor, Topi and Razzar. It has a total area of 1,543 km. sq. with a population of 1,654,000 [11]. Most of the cultivated area is rain-fed [12] (barani) which gives very good production of wheat, maize, tobacco, sugarcane etc. The Tarbela Dam, which is Pakistan's largest dam, is located in its neighboring Haripur district on Indus River, afterwards irrigating the Swabi region. Since the entire area is fertile a major part of the population is committed to irrigation, making it the primary source of living for the inhabitants of this district [14] (Figures 2 & 3).

Irrigating the entire region for cultivation is an important aspect [7]. The Beka area of Swabi region was selected for testing the water powered ram pump and checking the irrigating potential of a water powered ram pump. It is located on the Indus river side

Specifications of that ram pump that was installed and tested at Swabi had 2 inches diameter drive pipe that supplies water from the source to pump, and 1 inch diameter delivery pipe to the location where water is to be conveyed.

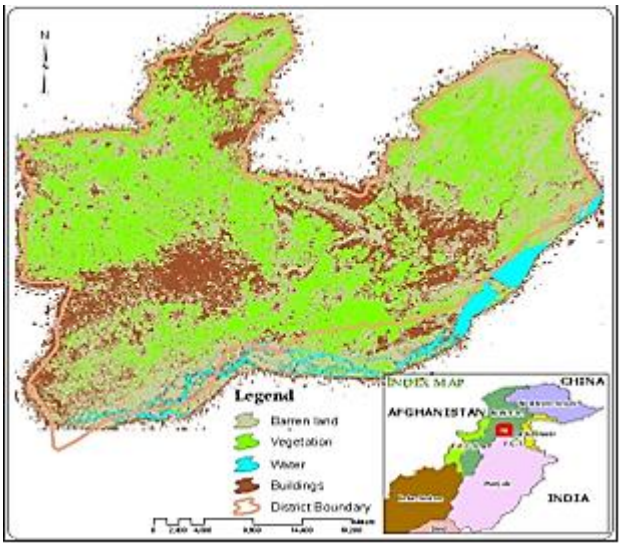

Figure 2. GIS Map of Swabi. [6]

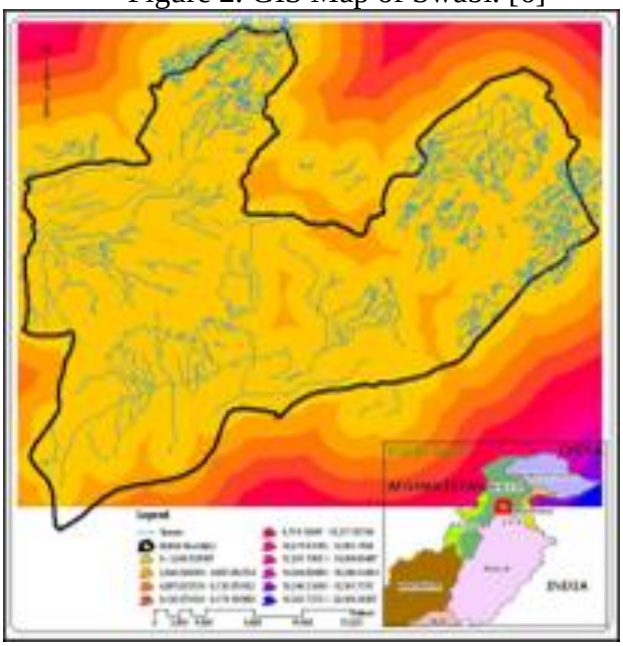

Figure 3. GIS Map of Swabi canal system. [6]

Figure 4. Successful test of Ram Pump at Swabi, KP, Pakistan

The ram pump fittings were of PVC, the drive pipe in our case was of rigid PVC pipe whereas flexible resin pipes were used for providing the supply water. The drive pipe had a total length of around 300 feet on the upstream side in order to get an inlet head of 3 feet that was used to operate the ram pump. This inlet head was converted to a total lift of 17 feet that could further be raised to 30 feet. Figure 4 shows the Swabi site and the installed ram pump with a successful test. The experimental and theoretical results of ram pump design for 4ft available and 12 ft drive head are shown in Table 1. All calculations are based on the heads measured at inlets and outlets of both drive and delivery pipes. Table 2 provides comparative ram pump performance parameters at maximum inflow and Figure-5 gives performance curve.

5 COST AND SOCIO-ECONOMIC ANALYSIS

The performance parameters at maximum inflow on ram pump are shown in comparison to other types of traditional pumps in Table 2. Although the principal cost of ram pump is nearly equal to diesel pump, its operational cost is nil. Therefore, ram pump returns its investment cost much quicker than ordinary diesel pumps.

Typical average ram pump performance is based on 60% pump efficiency [13], whereas standard performance of diesel and gasoline pump is based on 75% pump efficiency and 5% drive loss. In order to compare the efficiency of ram pump, two ram pumps with drive pipe diameter 8in, delivery pipe of diameter 4in and a maximum inflow of 800 gpm are required to generate power of 1whp-hr. Operational cost has been based on the current fuel prices in the studied region. However, the operational cost may differ subjected to fuel prices in the International Market [8]. The ram pump performance can be improved to 1hp-hr by adding extra pressure chambers.

The socio-economic analysis of pumping water for irrigation of wheat crop for one season has been conducted and summarised in Table 3. This analysis has been based on the methods provided by Arnold [9]. It has been observed that usage of ram pump for irrigation saves around 61 to 74% of the total cost required for pumping with gasoline, diesel or electric pumps [10]. Also it has been observed that ram pump based irrigation projects return the investment in around quarter time as required by other projects. And the feasibility of using ram pump for irrigation purpose is proven by the about 4 times more profit and 5 to 30 times more benefit to cost ratio, compared with other traditional pumping methods.

6 CONCLUSIONS

- The ram pump is more than two centuries old invention and has been used throughout the world for multiple applications including irrigation, its use in Pakistan is merely not found due to lack of awareness.
- It has been proven by the applications like this research and DTU that ram pumps can provide enough discharge to support irrigation of large areas.

- The locally produced ram pump was tested successfully in Swabi and large sized prototype will be produced for detailed life cycle analysis for irrigation purposes.
- Plastic ram pumps are cheap, and affordable but slightly inefficient compared to galvanised ram pumps of stiffer material. But the marginal cost difference and the slight reduction in performance is convincing enough to use plastic to develop this technology for irrigation.
- The principal cost of a water powered ram pump is nearly equal to diesel pump, its operational cost is nil. Therefore, ram pump returns its investment cost much quicker than ordinary diesel pumps.
- Ram pump irrigation saves around 61 to 74% of the total cost required for pumping in comparison with gasoline, diesel or electric pumps.
- Return on investment (ROI) for ram pump irrigation is around 4 times more in quarter time as compared with other types of pumping projects.
- The benefit to cost ratio compared with other traditional pumping methods (in Table 3) is 5 to 30 times more, for ram pump.

ACKNOWLDEGMENT

The authors would like to acknowledge the support and guidance from the local farmers of Swabi, for contributing in the survey conducted in this research work. We also thank Engr. Steve Godfrey for his guidance in this research.

Table 1. Ram Pump performance for 4 ft available head and 12 ft drive head.

Drive Pipe Diameter (in)	Delivery Pipe Diameter (in)	Drive Flow (gpm)	Available head (ft)	Drive head (ft)	Efficiency Factor	Expected Output (gpm)	Pumping Power (whp-hr)
0.75	0.5	2	4	12	60.00%	0.4	0.0013
1	0.5	6	4	12	60.00%	1.2	0.004
1.25	0.5	10	4	12	60.00%	2	0.007
1.5	0.75	15	4	12	60.00%	3	0.01
2*	1	33	4	12	60.00%	6.6	0.02
2.5	1.25	45	4	12	60.00%	9	0.03
3	1.5	75	4	12	60.00%	15	0.05
4	2	150	4	12	60.00%	30	0.10
6	3	400	4	12	60.00%	80	0.27
8	4	800	4	12	60.00%	160	0.54

*Tested at Swabi site

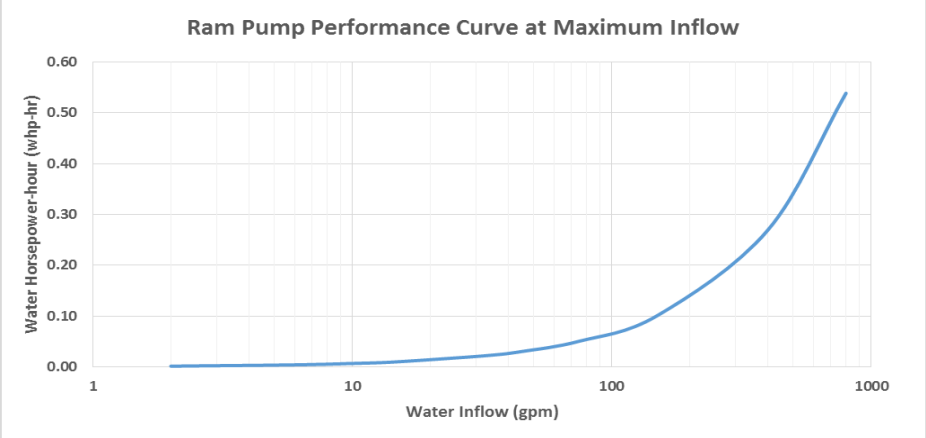

Figure 5. Theoretical performance curve of locally produced ram pump tested at Swabi.

Table 2. Comparative Ram Pump performance parameters at maximum inflow.

Pump Type	Pump Performance	Principal Cost in Pakistani rupees per whp-hr	Operational Cost
Ram Pump	0.54 whp-hr /800 gpm of water inflow	2units x 18,000 = Rs.36,000	Rs. 0/hr
Diesel Pump	12.5 whp-hr/gal	Rs.35,000	Rs. 25.76/hr
Gasoline Pump	8.55 whp-hr/gal	Rs.20,000	Rs. 32.75/hr
Electric Pump	0.885 whp-hr/kwh	Rs.18,000	Rs. 21.02/hr

Table 3. Socio-economic comparison of ram pump with other traditional pumps for irrigation of wheat crop.

Parameter	8in Hydraulic Ram Pump X 2 Units	1whp-hr Diesel Pump	1whp-hr Gasoline Pump	1whp-hr Electric Pump
Wheat Crop Water Requirement (gallons/ha)	1611450	1611450	1611450	1611450
Discharge Rate (gpm)	320	320	320	320
Principal Cost (PC) (Pak Rs)	36000	35000	20000	18000
Fixed Cost (FC) (Pak Rs)	5000	5000	5000	5000
Installation Cost (IC) (Pak Rs)	2000	1000	1000	1000
Opperational Cost (OC) (Pak Rs)	0	108192	137550	88284
Total Cost (PC+FC+IC+OC) (Pak Rs)	43000	149192	163550	112284
Cost of Pumping Water (PKR./gallon)	134.375	466.225	511.09375	350.8875
Savings on Cost of Diesel, Gasoline and Electricity respectively (%)	-	71.18	73.71	61.70
Capital Recovery (Pak Rs)	185000	185000	185000	185000
Payback Period (Yr)	0.23	0.81	0.88	0.61
Return on Investment (ROI) %	430.23	124.00	113.12	164.76
Benefit/Cost Ratio	3.30	0.24	0.13	0.65

REFERENCES

[1] World Development Indicators. The World Bank, 18 Dec. 2013. Web. 5 Apr. 2015. <http://databank.worldbank.org/data/databases.aspx>

[2] Aslam, M.S., (2013). "Sustainability of Community-Based Drinking Water Systems in Developing Countries." Department of Civil Engineering and Applied Mechanics, McGill University, Montreal, Canada.

[3] Qureshi, A. S; Shah, T.; Akhtar, M. 2003. The groundwater economy of Pakistan. Working Paper 64. Lahore, Pakistan: International Water Management Institute.

[4] Hydraulic Ram Pump, 21 Oct 2010. Web. 3 Apr. 2015 <https://catmontree.wordpress.com/2010/10/21/home-made-hydraulic-ram-pump/>

[5] DTU P90, Technical manual, University of Warick <http://www2.warwick.ac.uk/fac/sci/eng/research/civil/dtu/pubs/tr/lift/rptr12/tr12.pdf>

[6] Muhammad Shakir, Zahir Ali and Naveed Alam "Developing a Model for Locating Suitable Schools Sites using Multi-criteria Decision Analysis and Geographic Information System Techniques (A case study in the Swabi District of Khyber Pakhtunkhwa Province).", National Centre for Remote Sensing and Geo-Informatics (NCRG), SUPARCO HQs, Karachi-75270, Pakistan

[7] Community development organisation,2015, "Action against land grab" , Web: 5 April, 2015 <http://www.cdoswabi.org/index.php?option=page&item=show&item_id=7>

[8] Natural Resources Management and Environment Department. Web. 13 Apr. 2015. "Irrigation Water Management: Irrigation water needs..."

<http://www.fao.org/docrep/s2022e/s2022e02.htm>

[9] Arnold F. Dumaoal Sr, Franster A. Urbano, Benjay P. Pareja, 2000, "Design and performance evaluation of a local downdraft hydraulic ram pump".

[10] William Kranz, 2010, Updating the Nebraska Pumping Plant Performance Criteria University of Nebraska Proceedings of the 22nd Annual Central Plains Irrigation Conference, Kearney, NE., February 23-24, 2010

[11] Government of Pakistan, 1986, Agricultural Statistics of Pakistan.

[12] Statistical Bureau of Pakistan, 2015, Agriculture Statistics <http://www.pbs.gov.pk/content/agriculture-statistics>

[13] Energy Yearbook,1988,Directorate General of New and Renewable Energy Resources, Ministry of Petroleum and Natural Resources, Islamabad, Pakistan.

[14] Govt. of Khyber paktunkhwa, finance and planning department, 2015, Web: 5 Apr, 2015, <http://www.swabi.financekpp.gov.pk/index.php?option=com_content&view=article&id=53&Itemid=63>

PRODUCTION OF BIODIESEL BY REACTIVE DISTILLATION SIMULATION STUDIES USING ASPEN PLUS

Awan Zahoor[1]* M.Saleem Chohan[1], Saud Hashmi[1],Engr. Fahim Uddin[2],
[1]Department of Chemical Engineering, NED University Of Engineering and Technology Karachi-75270, Pakistan.
[2]Department of Chemical Engineering, Universiti Teknologi PETRONAS, 32610 Bandra Seri Iskandar, Perak Darul Ridzuan, Malaysia

*Corresponding author. Tel.: +92-99261261-8
E-mail address: zahoor@neduet.edu.pk

ABSTRACT

Biodiesel is one of the most substantial fuel to replace the dwindling reserve of conventional energy resources and their associated environmental problems. The major constraint in the commercialization of conventional biodiesel process is its high cost and downstream separating units .In this study, reactive distillation processes has been simulated effectively to eradicate these issues. Since Pakistan is facing a severe deficit of edible oils, the choice of non-edible Jatropha seed oil for biodiesel is worth significant which can easily be planted in barren areas of Pakistan. In this research, Process simulation was performed using Aspen plus ® and 99.99 % conversion of oil into biodiesel was achieved. The biodiesel produced has density 876.29 kg/m3 at 150C meeting the fuel standard ASTM D6751.The sensitivity analysis was also carried out for the best utilization of energy , reactants feed stage and feed ratio.

Keywords: Biodiesel production, Jatropha oil, Aspen Plus, reactive distillation, transesterification, sensitivity analysis

1 INTRODUCTION

Since the world's energy demand is growing rapidly as petroleum based fuels are being depleted, a substantial fuel is required to replace the dwindling reserve of conventional energy resources and their associated environmental problems .In this scenario, renewable energy has become an attractive clean fuel option derived from biomass or biological sources .Biodiesel has the potential to replace the petroleum diesel.Biodiesel is better than petro-diesel in terms of aromatic content, higher flash point 150 ^{0}C, biodegradibilty, sulfur content and lesser air-pollutant . [1, 2, 3].

Oil or fats are trigyceride molecules (glycerin bonded with three fatty acids. When triglycerides are reacted with acohol in the presence of a catalyst, fatty acids alkyl ester (FAAE) is formed commonly known as 'Biodiesel' and the reaction is called transesterification given in Figure-1 [4].

An extensive research is being carried out worldwide to produce this fuel in the most economical way [6-13]. Different feed-stocks and catalysts combinations [5,7,9] have been investigated but the conventional method of biodiesel production leads to separation problems and energy consumption making biodiesel cost ineffective. In this research , an attempt is made to explore the most potential and attractive process for biodiesel synthesis.

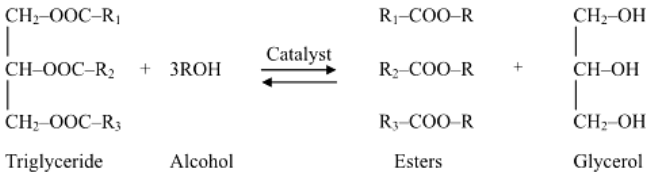

Figure 1. General transesterification reaction

Distillation continues being the most widely used separation technique in chemical industry, but requires high energy. Since process intensification takes into account reduction in energy consumption, integration of several operations into one unit, safe operation and others, may be the reactive distillation is the most representative operation in process intensification because the reaction and separation are carried in the same unit leading to energy saving due to internal integration and higher conversions in equilibrium reactions [13,14,15]. The primary objective of this work is concentrated on the analysis of a reactive distillation for biodiesel production.

Reactive distillation (RD) integrates a reactor and a distillation column in a single unit which shifts the chemical equilibrium to increase product yield by continuous separation of product from reaction

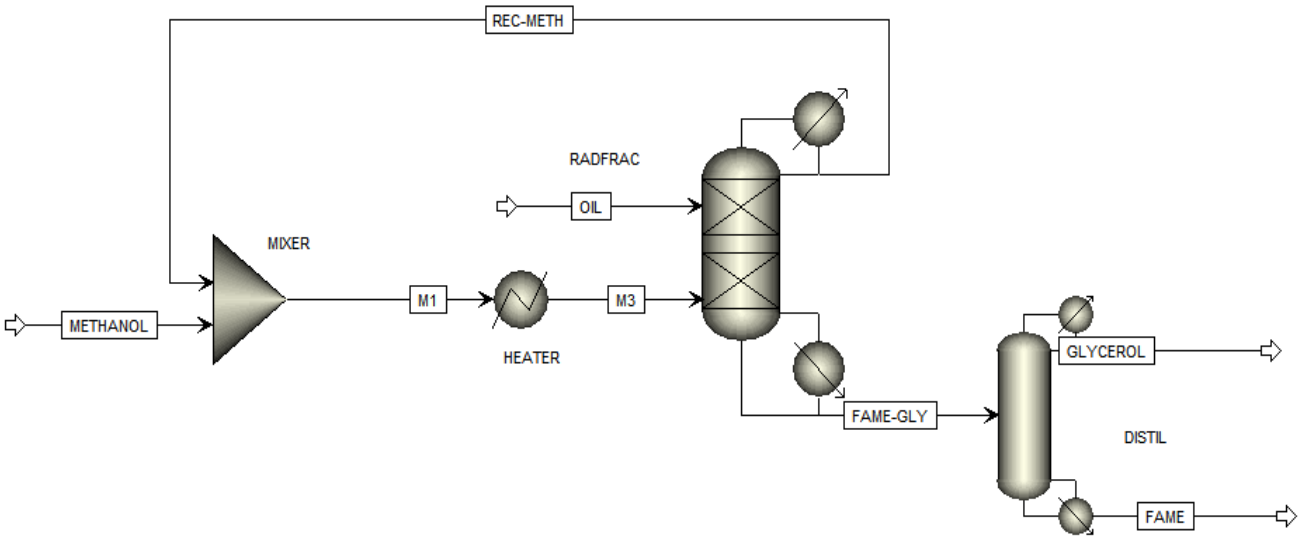

Figure 2. Reactive distillation model for biodiesel production

zone. It suppresses the side reactions and catalyst envelopes are packed inside the column to accelerate the reaction .Another distinct advantage is that RD utilizes the heat of reaction for mass transfer in case of exothermic reaction which avoids catalyst hot spots[16]. Since transesterification reaction is a reversible exothermic reaction and requires catalyst, it meets the design criteria of RD. Moreover the volatility difference of glycerol and FAME makes the RD more favorable. RD column has been operated at high pressure for biodiesel production in recent researches but in this study ,reactive distillation is carried out at atmospheric pressure.

In this study, Jatropha oil (non-edible) is chosen as the feedstock for biodiesel because Jatropha plant can easily be cultivated with little water in the less fertile regions of Punjab and Balochistan as well as in the deforested land of Pakistan. Jatropha oil found in Pakistan contains mainly the fatty acid contents:oleic C18:1(40%), linoleic C18:2 (37%) from which high quality biodiesel can be produced [17].

Since Jatropha oil contains relatively high free fatty acid (FFA) content, it requires the use of heterogeneous solid catalyst that avoids soap formation and does not require aqueous treatment steps. In this study, Calcium oxide (CaO) is selected as solid catalyst to meet the condition since it possesses relatively high basic strength and less environmental impacts due to its low solubility in methanol and its easier handling as compared to other catalysts like KOH/NaOH [18].

2 PROCESS MODEL

Fig. 2 describes the reactive distillation model developed in this study. There are two stages of the process. The first stage involves reactive distillation for transesterification along with methanol recovery. The second is product purification that is glycerol and biodiesel separation

In the first stage, feed streams containing Jatropha oil and preheated methanol are fed into the reactive distillation column from top and bottom respectively.The entire column is considered as reaction zone for transesterification.The design of the column is similar to multi-tray column with sieve trays for ample residence time and catalyst envelopes are packed inside the column to accelerate the reaction . One of product stream from top is excess methanol which is recycled back to the column after mixing with fresh methanol . The other product stream from the bottom contains biodiesel and glycerol. Since these two compounds are slightly soluble to each other , a mixture is formed with a thick layer of glycerol at bottom and biodiesel at top. It is therefore another separation unit is required in the second stage. The separation of these two compounds can be achieved by simple distillation technique since there is significant volatility difference .

3 PROCESS SIMULATION

Aspen Plus simulator version 8.0 was used for the process simulation since it is more powerful tool for simulating non-ideal properties, electrolytes, solids, azeotropes, and chemical reactions.

Triolein ($C_{57}H_{104}O_6$) was used to represent the triglycerides form of oleic acid which is readily available in the simulator, so the input components are triolein and methanol as the reactants whereas glycerol and fatty acid methyl ester (FAME) i.e biodiesel as the products. According to the literature cited[19], Non-Random Two-Liquid (NRTL) thermodynamic models is recommended to predict the activity coefficeints for highly polar components, methanol and glycerol in the process

Fig-3a shows the transesterification reaction of Jatropha curcas seed oil and methanol using solid calcium oxide catalyst that was modeled in the simulation.

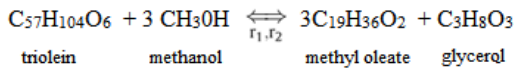

Fig-3a Transesterification reaction of Jatropha oil

There is usually a high molar ratio of methanol to oil, therefore the reverse reaction can be ignored, and methanol concentration can be assumed to be constant throughout the reaction. Thus, the reaction will be a pseudo-first-order reaction in which the rate of the reaction is a function only of the triglyceride.The residence time for the reaction is 1.64 hour[20]. The kinetic parameters for Arrhenius equation are in (1).

$$k = A \times \exp\left(\frac{-E}{RT}\right) \qquad (1)$$

$$k = 1.88 \times \exp\left(\frac{-4.57 \times 10^4}{8.314 \times 10^3 \times 333}\right) = 1.275 s^{-1}$$

The reactive distillation column was modeled by an Aspen inbuilt equilibrium rigorous two phase fractionation model RADFRAC . The column pressure was 1 atm with total no of 5 stages (incl. reboiler & total condenser), reflux ratio 0.6 and reactive zone was set between 2nd and 4th stage with residence time 1.64 hr. Oil and methanol were fed from top and bottom of the column at 4.536 kmol/hr and 16.732 kmol/hr respectively. Both reactants were fed at 1atm pressure and 60^0C temperature.

The biodiesel (FAME) and glycerol were separated in a distillation column operating with total no of stages (incl. reboiler & partial condenser), reflux ratio 10 and feed was fed at 2nd stage.

4 RESULTS & DISCUSSIONS

4.1 Base Case Simulation

The steady state simulation of reactive distillation for biodiesel was carried out in Aspen plus.The product conversion in the reactive distillation was 99.5% and the product purity was 99.99%. Fig-3b shows the liquid composition profile along the reactive distillation column and it is observed that the reactants oil and methanol mostly consume at the second stage.

Table.1 Liquid composition along the column

Stage	Methanol	FAME	Trilolein	Glycerol
1	0.9735	0.0097	1.4660E-29	0.0167
2	0.0226	0.7274	0.0001480	0.2497
3	0.0256	0.7316	8.0813E-08	0.2426
4	0.0769	0.6820	1.0713E-11	0.2410
5	0.0050	0.7462	4.0313E-14	0.2487

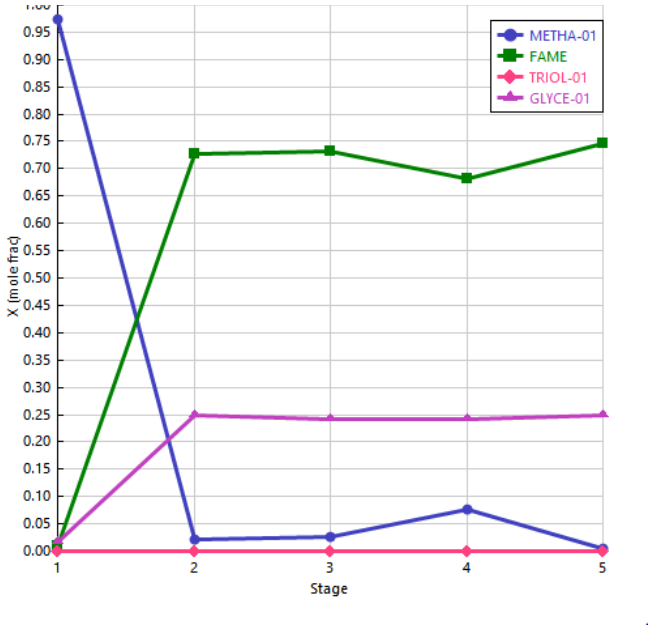

Figure-3b Liquid composition profile

The temperature profile along the reactive distillation column can be observed in fig.4 .The temperature is increasing from top to bottom and it is found that the reaction is exothermic in nature.

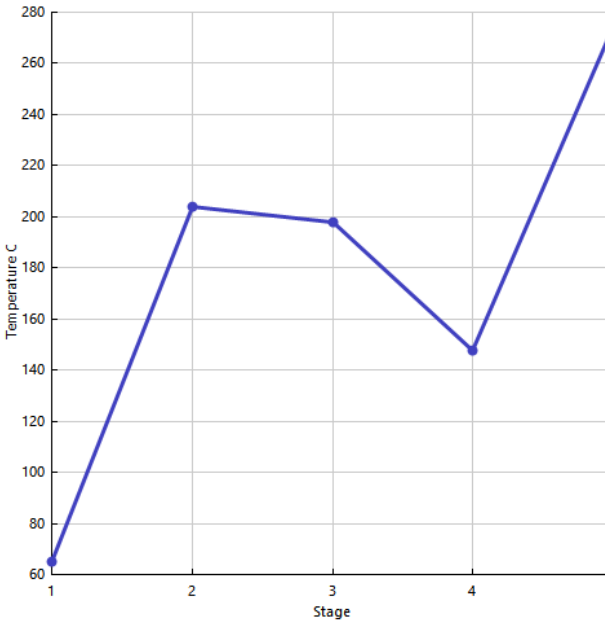

Figure 4. Temperature profile of reactive distillation column

The biodiesel (FAME) produced by reactive distillation has the density 876.2957 kg/m3 at 15°C with FAME 99.99 % by mass meeting the Fuel Standards (USA and Global) ASTM D6751.

4.2 Sensitivity Analysis

Some of the important design parameters such as no. of stages in reaction zone methanol & oil feed stage , column inside pressure, reflux ratio and reboiler duty have a direct impact on the reactant conversion ,composition, yield and purity of biodiesel. It is ,therefore , necessary to evaluate these effects by sensitivity analysis to get optimum parameters for experimental design.

1) *Effect Of No Of Stages Of Reaction Zone :* Keeping the parameters same in the base case, only the no. of stages for the reaction were varied from 2 to 4 to evaluate its effect on the yield of FAME. Fig. 5 demonstrates that the yield of FAME increases from second stage to third stage upto 99.99 % and then it remains constant .Thus reaction zone can be reduced to 2nd and 3rd stage for high yield.
2) *Effect Of Methanol Feed Location :* Methanol is the lightest among other components with low boiling point (high volatility) .The determination of its feed stage in the column is worth significant as it influences the reaction kinetics and mass transfer . For sensitivity analysis ,methanol was fed at the top ,bottom and mid of the reaction zone and a graph was plotted to observe its effect on product (FAME) composition. As seen in the fig. 6 methanol when fed at top with oil gives higher conversion and more amount of FAME is produced .Moreover ,introducing methanol

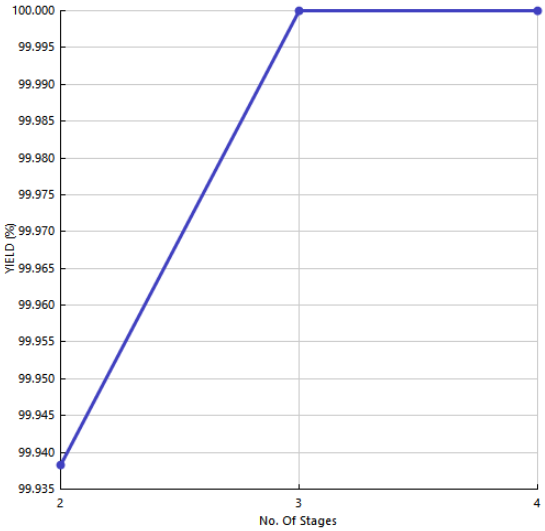

Figure 5. Effect of no of stages of reaction zone

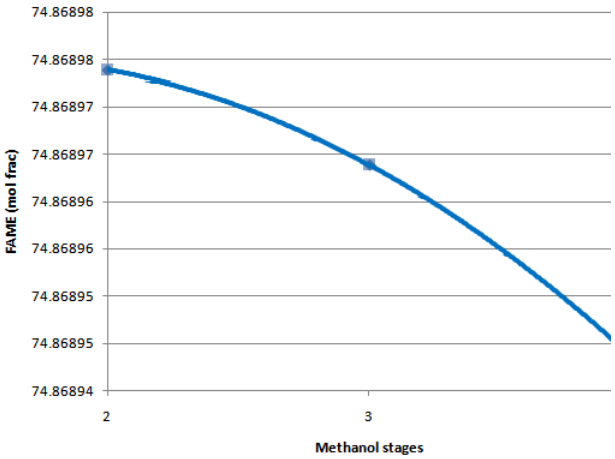

Figure 6. Effect of methanol feed stage

from the top reduces the reboiler duty as well. Fig. 7 demonstrates the effect of methanol feed stage on reboiler duty and it is clearly observed that reboiler duty is minimum when methanol is fed at the top and increases gradually as reaction zone increases.

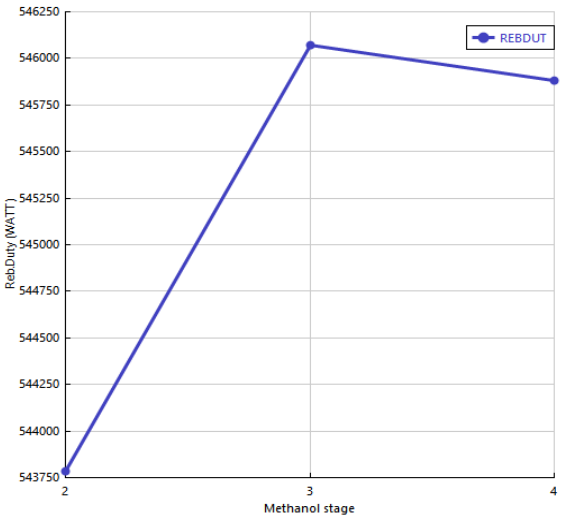

Figure 7. Effect of methanol feed stage on reboiler duty

3) *Effect Of Fresh Methanol Flow Rate In Feed:* One of the key design parameters on the performance of reactive distillation column is entering methanol to oil feed molar ratio. In the simulation, the flow rate of fresh methanol was determined to maintain the optimal value of this ratio at which greater amount of biodiesel would produce but keeping the bottom stage temperature below degradation temperature of biodiesel (275 °C).Fig .8 demonstrate that FAME concentration increases as fresh methanol amount increase but beyond 13.7 kmol/hr a decreasing trend is observed due to dilution effect of excess methanol in the

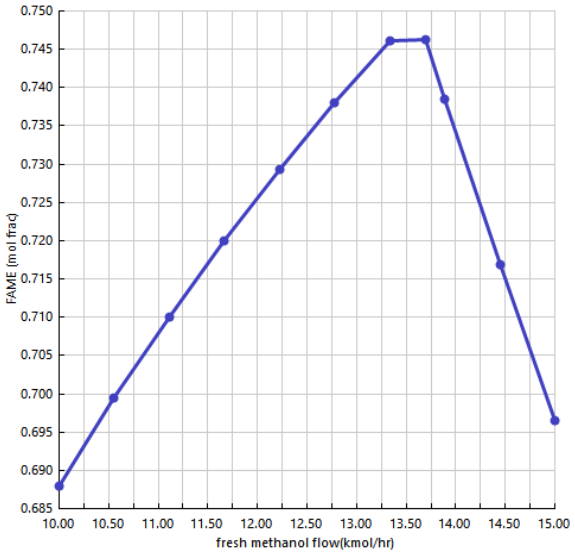

Figure 8. Effect of fresh methanol flow rate on composition

column .On the other hand, fig 9 illustrates that bottom stage temperature falls as more fresh methanol is introduced .As a result ,fresh methanol should be fed at 13.7 kmol/hr wich favors high FAME concentration keeping the bottom stage temperature below 275 ^{o}C with methanol to oil ratio 3.6:1 as entering feed for the column.

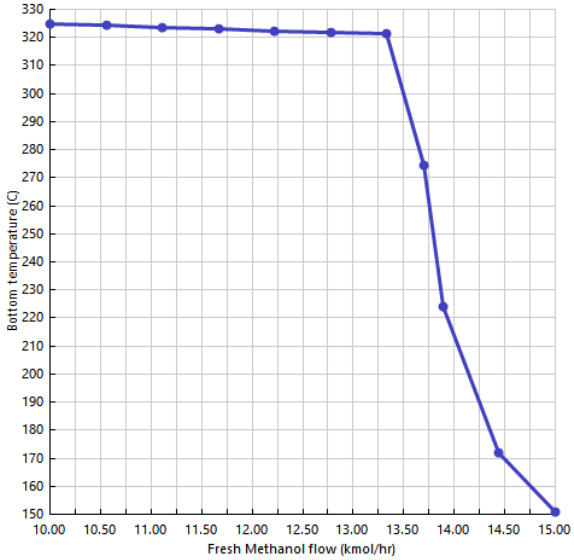

Figure 9. Effect of fresh methanol flow rate on bottom stage temperature

5 CONCLUSION

From the optimized results of simulation, it is found that reactive distillation column should consist of 2 reactive stages, the methanol to oil ratio should be 3.6:1 with fresh methanol being fed at 13.7 kmol/hr . The column should be operated at 1 atm .The reactants should be fed at the top of column to give a high conversion of Jatropha oil and methanol.

In conclusion, the results obtained are very promising and it is found that reactive distillation technique is highly feasible to produce biodiesel .The model developed for reactive distillation in Aspen plus ® has more flexibillty which can accommodate higher flow rates for scale-up of operations, add or remove stages of operation, and predict associated capital and production costs

REFERENCES

1. Yu-Cheng Chang , Wen-Jhy Lee , Effects of waste cooking oil-based biodiesel on the toxic organic pollutant emissions from a diesel engine, Applied Energy 113 (2014) 631–638
2. Leslie R. Rudnick ,Synthetics, Mineral Oils, and Bio-Based Lubricants: Chemistry and Technology, Second Edition, CRC Press,Taylor & Francis Group,2013
3. Ayhan Demirba ,Biodiesel: A Realistic Fuel Alternative for Diesel Engines, Springer, 2008 pp.8-12
4. Mushtaq Ahmed ,Mir Ajab khan,M.Zafar ,Shazia Sultana,Practical Handbook on Biodiesel Production and properties,CRC Press,Taylor & Francis Group,2013,pp.11-35
5. Zayed Al-Hamamre , Jehad Yamin , Parametric study of the alkali catalyzed transesterification of waste frying oil for Biodiesel production,
6. Energy Conversion and Management 79 (2014) 246–254
7. Pedro Lisboa ,Ana Rita Rodrigues et al ,Enzymatic transesterification using supercritical carbondioxide, J.of Supercritical Fluids 85 (2014) 31–40
8. Shihong Liu ,Kaili Nie,Xin et al ,Kinetic study on lipase-catalyzed biodiesel production from waste cooking oil, Journal of Molecular Catalysis B:Enzymatic 99 (2014) 43–50
9. Zahira Yaakob et al ,Overview of the production of biodiesel from Waste cooking oil, Renewable and Sustainable Energy Reviews,18 (2013),184-193
10. Yuan-Chung Lin, Po-Ming Yang, Shang-Cyuan Chen, Jia-Fang Lin,Improving biodiesel yields from waste cooking oil using ionic liquids as catalysts with a

microwave heating system, Fuel Processing Technology 115 (2013) 57–62
11. Sérgio Morais , Teresa M. Mata , António A. Martins , Gilberto A. Pinto c, Carlos A.V. Costa ,Simulation and life cycle assessment of process design alternatives for biodiesel production from waste vegetable oils, Journal of Cleaner Production 18 (2010) 1251-1259
12. Meisam Hasheminejad , Meisam Tabatabaei ,, Yaghoub Mansourpanah ,Mahdi Khatami far , Azita Javani ,Upstream and downstream strategies to economize biodiesel production, Bioresource Technology 102 (2011) 461–468
13. Marta G. Varanda, G. Pinto, F. Martins ,Life cycle analysis of biodiesel production, Fuel Processing Technology 92 (2011) 1087–1094
14. Aashish Gaurav, Mateus Lenz Leite, Flora T. T. Ng, and Garry L. Rempel ,Transesterification of Triglyceride to Fatty Acid Alkyl Esters(Biodiesel): Comparison of Utility Requirements and Capital Costs between Reaction Separation and Catalytic Distillation Configurations Energy Fuels 2013, 27, 6847 − 6857
15. A.A Kiss, Advanced Distillation Technologies, Design, Control and Applications, John Wiley & Sons Ltd,2013
16. William L. Luyben, Cheng-Ching Yu, Reactive Distillation Design and Control, John Wiley & Sons Ltd,2008
17. R.Taylor, & R. Krishna, Modelling Reactive Distillation., Chemical Engineering Science 55 (2000) 5183-5229
18. J.M. Nzikou, L. M atos, F. M bemba, C.B. Ndangui, N.P.G. Pambou-Tobi, Characteristics and Composition of Jatropha curcas Oils, Variety Congo-Brazzaville, Research Journal of Applied Sciences, Engineering and Technology 1(3): 154-159, 2009 ISSN: 2040-7467,2009
19. A.A Refaat, Biodiesel production using solid metal oxide catalysts, Int. J. Environ. Sci. Tech., 8 (1), 203-221, Winter 2011
20. Zhang, Y,. Biodiesel production from waste cooking oil: 1. Process design and technology assessment. Bioresoure. Technol. 89 (1), 1–16,2003
21. Haruna Ibrahim, Abdulkareem S. Ahmed , Idris M. Bugaje, Ibrahim A. Muhammed-Dabo ,Simulation and Design of Continuous Heterogeneous Catalytic Biodiesel Production, Asian Journal of Engineering and Technology (ISSN: 2321 – 2462) Vol. 1,2013

TEMPERATURE PREDICTION OF A SOLID BODY BY TWO-COLOR METHOD USING IMAGE-PROCESSING TECHNIQUE

Sohaib Z Khan[1,*], Muhammad A Khan[1], Hamza Ahmed[1], Ali ZainUl Abedeen[1], Tayyab Gulfaraz[1], Hassaan Ul Haq[1]

[1] Department of Engineering Sciences, PN Engineering College, National University of Sciences and Technology, Karachi, Pakistan

[*]Corresponding author. Tel.: +92-21-9924-0752; fax: +92-21-99240112
E-mail address: Sohaib.Khan@pnec.nust.edu.pk(Sohaib Z Khan)

ABSTRACT

Temperature measurement is a critical industrial requirement. In many industrial processes, determining temperature at a given instance on all points of a heat source is gaining importance. Typical temperature measurement methods are limited in this aspect. A two-color methodhas been developed for the temperature prediction of a heat source, which is based on comparing intensity of images taken at two different wavelengths. In this work, the two-color method has been used and images of an active furnace were taken using two narrow band pass filters. The wavelengths of the filters were 940nm and 850nm. A simple CMOS camera was used for image acquisition. These images were further processed in MATLAB image-processing toolbox. A Series of experiments were conducted at different temperatures on two separate furnaces. Temperature predicted by this method was validated by the reading of thermocouple installed on the furnaces.

Keywords: Furnace; image-processing; Matlab; two-color method; temperature

1 INTRODUCTION

Temperature measurement has always been an important requirement in many industrial processes. Conventional techniques used to measure temperature involve contact type devices. Physical probes such as thermocouples are being used in most of the industry. In general, the contact method has certain difficulties in application. For example, measurement of flame temperature has disadvantages including single point measurement, degradation due to physical contact and its intrusive nature [1].

Non-contact temperature measurement techniques are being researched upon and developed as a result. Infrared pyrometers convert the energy radiated by the target to electrical signals which are then interpreted as temperature values [2]. Work has been done on measuring emitted intensity of source at different wavelengths and then calculating the emissivity and temperature by using least squares curve fitting techniques [3].

Most of the heat sources emit light as a function of temperature. The image can be acquired to get the temperature distribution of the heat source. The color-temperature relationship can used to characterize the heat source. The red, green and blue color properties are obtained from individual pixels. The color histogram can be obtained to show the color distribution of the image and hence the temperature distribution of the heat source [4].

The distribution of temperature can be calculated from the ratio between the grey-scale levels of corresponding pixels within two images captured at selected wavelengths [5]. This is commonly known as two-color method. The main advantage of this technique is the emissivity-free measurement as the ratio of the emissivity at two different wavelengths is considered [6]. Hottel and Broughton [7] first introduced the two-color technique and utilized it to measure the flame temperature in utility furnaces. Extensive applications of this technique were found in combustion engines where flame temperature, as well as soot concentrations were calculated [8, 9]. This technique has improved over the years and expanded to various types of flames, i.e. premixed and diffusion flames [10, 11].These provide the detailed temporal and/or spatial information [12-15]. Digital processing of images from monochrome CCD cameras can be used to measure certain flame parameters such as geometrical and luminous parameters [16-18] and statistical parameters [19].In other research works, the technique was successfully implemented to predict temperatures on a brake disc [20] and the die casting tooling surface [21].

In this paper, the two-color temperature measurement method is used to predict the temperature of active furnaces operating at high temperature. In contrast to previous efforts, the developed method is simple to use and only involve less-expensive equipment.

2 THEORETICAL BACKGROUND

The radiation of an object is governed by Planck's radiation law:

$$M(\lambda,T) = \varepsilon_\lambda \frac{C_1}{\lambda^5}\left(e^{C_2/\lambda T}-1\right)^{-1} \quad (1)$$

Where $M(\lambda,T)$is the monochromatic exitance, namely monochromatic radiation emitted in energy per unit time per unit area $Wm^{-2}\mu m^{-1}$,λ is the wavelength of the radiation (μm), T is absolute temperature (K), ε_λ is monochromatic emissivity, and C1 and C2 are first and second Planck's constants. Planck's law can be replaced by Wien's radiation law:

$$M(\lambda,T) = \varepsilon_\lambda \frac{C_1}{\lambda^5} e^{-C_2/\lambda T} \quad (2)$$

The ratio of the grey levels at wavelengths λ_1 and λ_2 is given by:

$$\frac{G(\lambda_1,T)}{G(\lambda_2,T)} = \frac{S_{\lambda1}}{S_{\lambda2}}\frac{\varepsilon_{\lambda1}}{\varepsilon_{\lambda2}}\left(\frac{\lambda_2}{\lambda_1}\right)^5 \exp\left[\frac{C_2}{T}\left(\frac{1}{\lambda_2}-\frac{1}{\lambda_1}\right)\right] \quad (3)$$

Where,

ε= Emissivity.

G (λ, T) = Grey level intensity value at a given wavelength and temperature.

S= Spectral response of the camera.

$S_{\lambda1}$and $S_{\lambda2}$ are the spectral responses of the camera at wavelengths $\lambda_1$and λ_2.The ratio between the spectral sensitivities $S_{\lambda1}$and $S_{\lambda2}$is known from the spectral response performance of the camera. This ratio can be called the instrument factor [22].

2.1 Explanation of Spectral Response of Camera (Instrument Factor)

For the sake of understanding, the spectral response plot of a digital CMOS camera (C11440-52U) has been shown in the figure below [23].

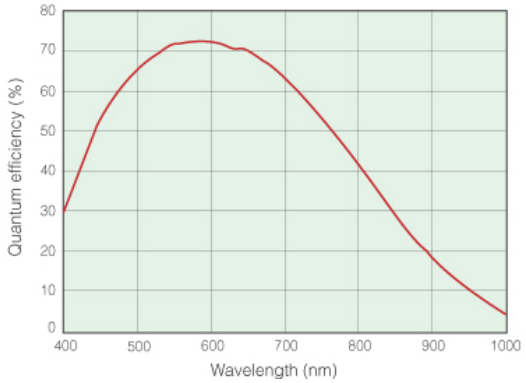

Figure 1. Spectral response of a digital CMOS camera [4].

In Figure 1, the quantum efficiency of the CMOS chip can be seen at different wavelengths.Where, quantum efficiency is simply the ratio of converted electrons and incident photons.For example, if $S_{\lambda1}$=1000nm and $S_{\lambda2}$=780nm,then the ratio of quantum efficiency at these wavelengths will give the instrument factor: $S_{\lambda2}/S_{\lambda1}$= 0.45/0.05= 9.

Rearranging Eq. (3) yields:

$$T = \frac{C_2\left(\frac{1}{\lambda_2}-\frac{1}{\lambda_1}\right)}{\left[\ln\frac{G(\lambda_1,T)}{G(\lambda_2,T)} + \ln\frac{S_{\lambda2}}{S_{\lambda1}} + \ln\frac{\varepsilon_{\lambda2}}{\varepsilon_{\lambda1}} + \ln\left(\frac{\lambda_1}{\lambda_2}\right)^5\right]} \quad (4)$$

The difference between $\varepsilon_{\lambda1}$and $\varepsilon_{\lambda2}$ is negligible which means

$$\varepsilon_{\lambda1} \approx \varepsilon_{\lambda2}$$

Therefore, $\frac{\varepsilon_{\lambda1}}{\varepsilon_{\lambda2}}$=1

we know that ln (1) =0, Hence ln ($\frac{\varepsilon_{\lambda1}}{\varepsilon_{\lambda2}}$) =0.

Flower [7] proved that, when assuming the soot particles in the flame are homogeneous, optically thin, isothermal along a horizontal line through the flame, and small relative to the used wavelength, the spectral emissivity is inversely proportional to the wavelength, i.e., ε_λ α $1/\lambda$. Therefore, another formulation for gaseous flames in this study is obtained by substituting $\varepsilon_{\lambda1}$and $\varepsilon_{\lambda2}$ into Eq. (4):

$$T = \frac{C_2\left(\frac{1}{\lambda_2}-\frac{1}{\lambda_1}\right)}{\left[\ln\frac{G(\lambda_1,T)}{G(\lambda_2,T)} + \ln\frac{S_{\lambda2}}{S_{\lambda1}} + \ln\left(\frac{\lambda_1}{\lambda_2}\right)^6\right]} \quad (5)$$

Where, C_2 = Second Radiation Constant = 1.4388*107 (m·K)

λ_1= Wavelength of first filter =850 nm

λ_2= Wavelength of second filter = 940 nm

G ($\boldsymbol{\lambda}$, T) = Greyscale intensity value at a given wavelength and temperature

$\frac{S_{\lambda2}}{S_{\lambda1}}$= ratio of the spectral responses of the camera (instrument factor)

Eq. (5) is the final expression which was used in MATLAB code in order to predict temperature.

3 EXPERIMENTAL PROCEDURE

Experiments were conducted to predict the inside temperature of two different electric furnaces as shown in Figure 2. The maximum temperature of the Furnace A is 1100 °C and furnace B is 1280C. Both furnaces have thermocouples attached and a digital temperature display as shown in Figure 3. The thermocouple measures the average temperature of the back wall of the furnace. Images of the same wall has been taken for temperature prediction.

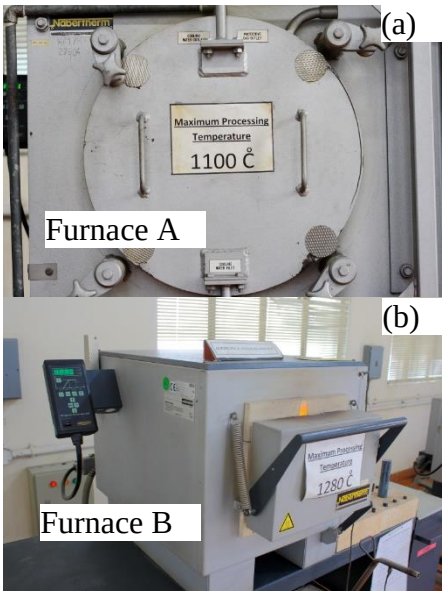

Figure 2. Electrical furnaces to measure inside wall temperature (a) Furnace A with maximum temperature of 1100C and (b) Furnace B with maximum temperature of 1280C.

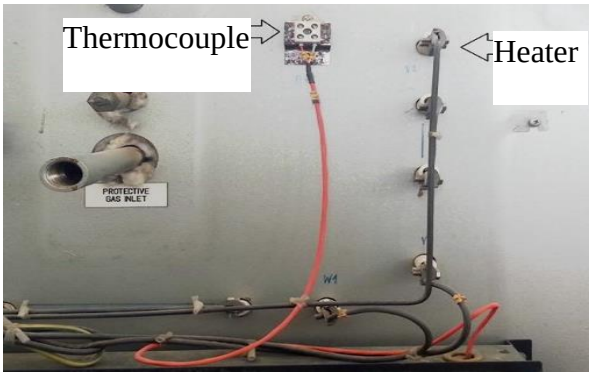

Figure 3. Thermocouple attachment at the Furnace B.

The furnace was heated first to the maximum temperature and then held for some time to achieve uniform temperature inside the furnace. The door of the furnace was opened to allow the view of the inside of the furnace. The pictures are taken during cooling, once the predefined temperature was shown on the digital display meter. Multiple pictures were taken at the given temperature by re-heating the furnace.

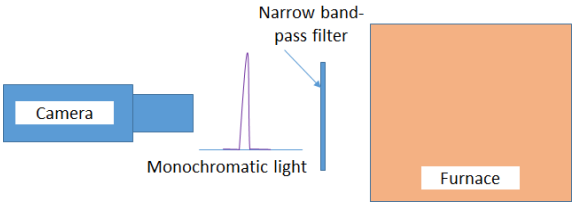

Figure 4. Schematic diagram of the experimental setup.

The camera used in this work was Canon Rebel XTi which has 10.1 megapixel CMOS sensor. This camera has good spectral resolution in infrared region. Al the images were taken at f-number of 5, exposure time of 1sec, ISO-800 with no flash. It should be noted that to allow large amount of light to reach to the CMOS sensor lower f-number and higher exposure time was selected. The selection of these values are important so that there should be no saturation in the image. Saturated images will lead to wrong calculations. Two different narrow-band pass filters were placed separately in front of the camera to capture a monochromatic image. The setup is shown in Figure 4. The narrow band-pass filters allowed to pass only the wavelengths of850±10 nm and 940±10 nm.

4 RESULTS AND DISCUSSION

Once the images are taken they are read and calculated according to the equations mentioned above. The first step was to read the two different RGB images in Matlab. These images were then converted to the gray-scale level images. The region of interest can be defined to save processing time. This allowed no calculation on the pixels outside the furnace. After that the intensity ratio of both gray images were calculated.

Finally, instrument correction factor and other constants are applied to each pixel to predict the temperature. These values can be plotted in 3D graph for spatial temperature distribution.The complete work flow of the image processing in Matlab is shown in Figure 5.

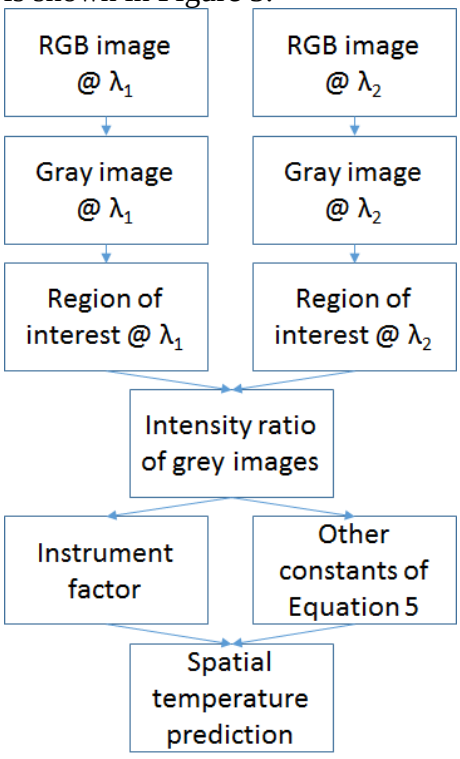

Figure 5. The work flow of the image processing in Matlab.

4.1 Furnace A

On furnace A, three experiments were performed at the temperature of 1000°C, 1050°C and 1100°C, respectively. The stepwise procedure to predict the furnace A temperature from images taken at temperature 1100°C is shown in details from Figure 5 to Figure 7. Figure 6 shows the direct images captured by the camera at two different wavelengths. Figure 7 shows the 2D intensity profile after implementing the instrument factor. Figure 8 shows 3D intensity distribution of the both monochromatic images. The spatial temperature prediction is shown in Figure 9.

It can be seen that most of the wall is at the same temperature and two-color method was able to find the temperature close to the temperature measured by the thermocouple. The temperature prediction of furnace A at other readings are summarized in Table 1.

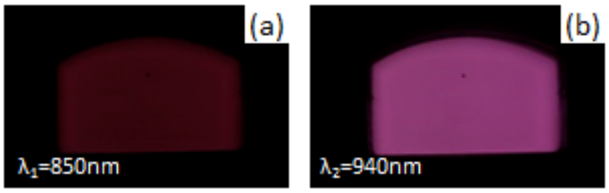

Figure 6.Monochromatic images of FurnaceA at 1100°C with wavelengths of (a) λ_1=850nm and (b) λ_2=940nm.

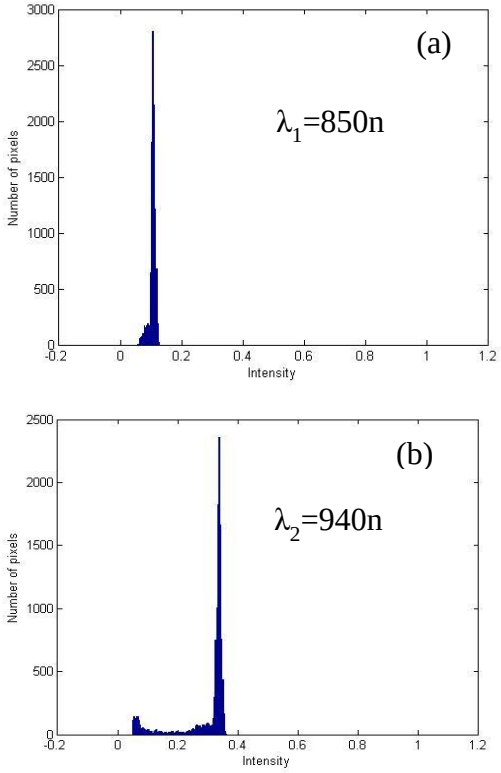

Figure 7. 2D intensity graph of monochromatic images of Furnace A at 1100°C with wavelengths of (a) λ_1=850nm and (b) λ_2=940nm.

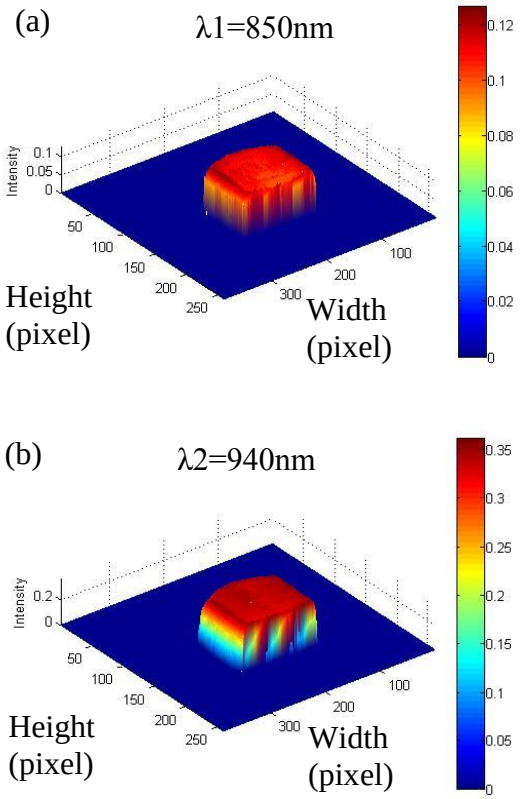

Figure 8. 3D intensity representation of monochromatic images of Furnace A at 1100°C with wavelengths of (a) λ_1=850nm and (b) λ_2=940nm.

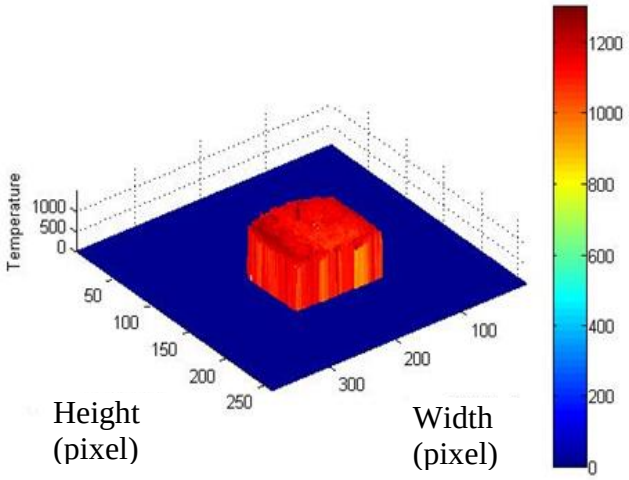

Figure 9. 3D representation of the temperature of the Furnace A at 1100°C.

4.2 Furnace B

Four experiments were performed at the temperature of 1110°C, 1156°C, 1210°C and 1280°C, respectively. The monochromatic images taken directly by the camera using narrow band-pass filters are shown in Figure 10. Similar procedure was adopted for the furnace B and the spatial temperature distribution of the inner wall of

the furnace B is shown in Figure 11. The temperature prediction of furnace B at other readings are summarized in Table 1.

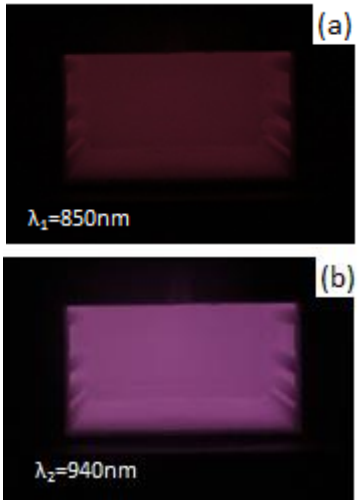

Figure 10. Monochromatic images of Furnace A at 1110°C with wavelengths of(a) λ_1=850nm and (b) λ_2=940nm.

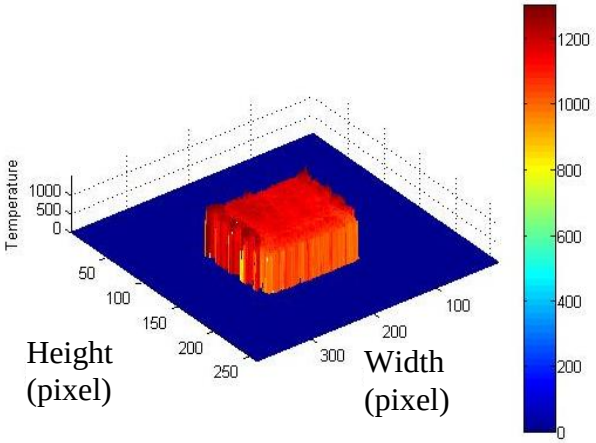

Figure 11. 3D representation of the temperature of the Furnace Bat 1110°C.

Table 1.Measured and Average Predicted Temperatures Using Two-Color Technique.

Measured Temperature °C	Average Predicted temperature °C
Furnace A	
1000	1006
1050	1061
1100	1114
Furnace B	
1110	1118
1150	1042
1210	1191
1280	1272

In this study, the two-color method was used with the MATLAB to predict the temperature of the hot surface. Results have shown that the method is good enough for industrial application. The use of this technique can be beneficial in industries where temperature measurement is an imperative requirement. This may provide a long-term solution to the industry as a non-contact technique and the system would have high working life than ordinary contact techniques. However, error in predicted results can be reduced by taking the images from both filters simultaneously.

Since, in this technique knowledge of emissivity value is not required, it represents a better solution where finding an emissivity value is challenging. Especially, when the temperature variation is large and fluctuating. It can also provide an alternate solution with relatively low cost thermographic cameras. However, it should be noted that the narrow band-pass filters are not cheap and for different application different band-pass filters would be required.

5 CONCLUSION

It can be concluded that a non-contact technique has been developed for temperature measurement. Results have been validated by comparing with thermocouple readings of active furnaces working at high temperature. The overall maintenance work and cost of this technique is low as the instrument does not come in contact during the temperature measurement. To further improve this technique for more industrial applications a near real-time in-situ solution is required which can provide instant spatial temperature distribution of objects at high temperature.

REFERENCES

[1] Fan Jiang, Shi Liu, Shiqiang Liang, Zhihong Li, Xueyao Wang and Gang Lu, *Journal of Thermal Science*, Vol.18, No.3 ,284−288, 2009.

[2] Wang Huajian, Huang Zhifeng, et al., Measurements on flame temperature and its 3D distribution in a 660 MWe arch-fired coal combustion furnace by visible image processing and verification by using an infrared pyrometer, *Journal of Measurement and Science Technology*, 18, 2009.

[3] Mansoor A. Khan, Charly Allemand and Thomas W. Eagar, Noncontact temperature measurement. II. Least squares based techniques, *Rev. Sci. Instrum*. 62, 403, 1991

[4] M. Vrhel, H. J. Trussell, *IEEE Signal Magazine*, 22, p. 14-22, 2005.

[5] M. Vrhel, H. J. Trussell, *IEEE Signal Magazine*, 22, p. 23-33, 2005.

[6] K.-P. Möllmann, F. Pinno and M. Vollmer, Application Note for Research & Science. Two-Color or Ratio Thermal Imaging – Potentials and Limits, *FLIR Technical Series*, 2010.

[7] Hottel HC, Broughton FP, Determination of true temperature and total radiation from luminous gas flames. *Ind Eng Chem (Anal Ed)*, 4(2), 166–75, 1932.

[8] Matsui Y, Kamimoto T., A study on the time and space resolved measurement of flame temperature and soot concentration in a D.I. diesel engine by the two color method, *Society of Automotive Engineers Publication*, 1979, Paper No.790491, 1971.

[9] Quoc HX, Vignon JM, Burn M. , A new approach of the two-color method for determining local Instantaneous soot concentration and temperature in a D.I. diesel combustion chamber, *Society of Automotive Engineers Publication*, 1991, Paper No.910736, 1991.

[10] Flower WL, Optical measurements of soot formation in premixed flames. *Combust Sci Technol*, 1983, 33:17–33, 1983.

[11] Flower WL. Soot particle temperatures in axisymmetric laminar ethylene–air diffusion flames at pressures up to 0.7 MPa. *Combust Flame*, 1989; 77: 279–93, 1989.

[12] Chun Lou, Huai-Chun Zhou , Peng-Feng Yu, Zhi-Wei Jiang, Measurements of the flame emissivity and radiative properties of particulate medium in pulverized-coal-fired boiler furnaces by image processing of visible radiation, *Proceedings of the Combustion Institute,* 31 (2007), 2771–2778, 2007.

[13] Chun Lou, Huai-Chun Zhou, Deduction of the two-dimensional distribution of temperature in a cross section of a boiler furnace from images of flame radiation, *Combustion and Flame,* 143:97–105, 2005.

[14] Huai-Chun Zhoua,, Chun Loua, Qiang Chenga, Zhiwei Jianga, Jin Heb, Benyuan Huangb, Zhenlin Peib, Chuanxin Lu, Experimental investigations on visualization of three-dimensional temperature distributions in a large-scale pulverized-coal-fired boiler furnace, *Proceedings of the Combustion Institute,* 30:1699–1706, 2005.

[15] Zhuoyong Yan, Qinfeng Liang, Qinghua Guo, Guangsuo Yu, Zunhong Yu, Experimental investigations on temperature distributions of flame sections in a bench-scale opposed multi-burner gasifier, *Applied Energy,* 86 (2009) 1359–1364, 2009.

[16] Y. Yan et al., Monitoring and characterization of pulverised coal flames using digital imaging techniques, *Fuel,* 81, 2002.

[17] Gang Lu, Yong Yan, and Mike Colechin, A Digital Imaging Based Multifunctional Flame Monitoring System, *IEE Transactions on instrumentation and measurement*, vol.53, n. 4, 2004.

[18] G Gilabert, G Lu and Y Yan, Three dimensional visualisation and reconstruction of the luminosity distribution of a flame using digital imaging techniques, *Journal of Physics: Conference Series*,15 (2005), 167–171, 2005.

[19] R. Hernandez, J. Ballester, Flame imaging as a diagnostic tool for industrial combustion, *Combustion and flame*, 155, 509-528, 2008.

[20] J. Thevenet, M. Siroux and B. Desmet, Brake disc surface temperature measurement using a fiber optic two-color pyrometer, 9th *International Conference on Quantitative InfraRed Thermography*, July 2-5, 2008, Krakow, Poland, QIRT Journal, 2008.

[21] H. Kourous, B. N. Shabestari, S. Luster, and J.Sacha; On-line Industrial Thermography of Die Casting Tooling using Dual-Wavelength IR imaging; *Thermosense XX, Proc. of SPIE*, Vol. 3361, p. 218-227, 1998.

[22] Y. Huang, Y. Yan, G. Riley, Vision-based measurement of temperature distribution in a 500-kW model furnace using the two-color method, *Chatham, Kent ME4 4TB,* Elsevier, UK January 2008.

[23] Hamamatsu, Board level digital CMOS camera, Hamamatsu Photonics K.K, January 2002. [Online] Available: http://www.hamamatsu.com/us/en/product/alpha/C/C11440-52U/index.html. [Accessed October 2014].

UNSTEADY MOTION OF FRACTIONALIZED SECOND GRADE FLUID WITH SLIP EFFECTS

Muhammad Jamil[1,*], Sanaullah Dehraj[2]

[1] Department of Mathematics, NED University of Engineering & Technology, Karachi-75270, Pakistan.

[2] Department of Mathematics and Statistics, Quaid-e-Awam University of Engineering, Science and Technology, Nawabshah, Pakistan.

[*]Correspondence author. jqrza26@yahoo.com

Abstract

The purpose of this paper is to provide exact analytical solutions for second grade fluids with fractional derivative approach. More precisely, our aim is to find the velocity field $u(y,t)$ and the shear stress $\tau(y,t)$ corresponding to the motion of a fractionalized second grade fluid due to accelerated plane, where no-slip assumption is no longer valid. The general solutions are obtained using the discrete Laplace transform. They are presented in series form in the terms of the Wright generalized hypergeometric function ${}_p\psi_q$ and presented as sum of the slip contribution and the corresponding no-slip contribution. The similar solutions for ordinary second grade and Newtonian fluids can easily be obtained as limiting cases of general solutions. Furthermore, the solutions for fractionalized and ordinary second grade fluid, when slip effect is not present are also obtained as special cases. Finally, the impact of the material, slip and fractional parameters on the motion of fractionalized second grade fluids is demonstrated by graphical illustrations. The difference among fractionalized second, ordinary second grade and Newtonian fluid models is also elaborated.

Keywords: Second grade fluid, fractional derivative, slip effects, oscillating flows, exact solutions, velocity field, shear stress, Laplace transform.

1 INTRODUCTION

Polymer solutions, blood and certain oil are non-Newtonian fluids, play very important role in modern technological applications and industries. The wide applications of these fluids in many areas of life attract researcher and scientist to study them and describe their behaviors. Generally non-Newtonian fluids divide in rate, differential and integral types. One of the most popular differential type non-Newtonian fluid is the second-grade fluids [1], Moreover, the second grade fluid is the subclass of non-Newtonian fluids for which one can reasonably hope to obtain exact solutions. For many reason exact solutions are very important. For example they provide a standard for checking the accuracies of many approximate solutions. They can also be used as tests for verifying numerical schemes that are developed for studying more complex flow problems. Therefore describing the behavior of non-Newtonian fluids, exact solutions are necessary. Therefore, various researches [2-7] in the field are engaged in obtaining such solutions. Nowadays fractional calculus, which is the branch of Mathematics that deals arbitrary order of differentiation and integration, became important and popular due to its successful applications in science and engineering. On the other hand fractional differential equations are increasingly used to model problems in fluid flow, rheology, biorheology, diffusion, relaxation, oscillation, anomalous diffusion, reaction–diffusion, turbulence, diffusive transport akin to diffusion, electric networks, polymer and chemical physics, electrochemistry of corrosion, relaxation and retardation processes in complex systems, propagation of seismic waves, dynamical processes in self-similar and porous structures and many other physical and engineering processes [8, 9] . The most important advantage of using fractional differential equations in these and other applications is their non-local property. It is well known that the integer order differential operator is a local operator but the fractional order differential operator is non-local. This means that the next state of a system depends not only upon its current state but also upon all of its historical states. This is more realistic and it is one reason why fractional calculus has become more and more popular [8,10]. In formulation and solution of such fluid flows fractional calculus approach has been extensively utilized in the last few decades. The time derivative of integer order in the constitutive equation is replaced by so called Reimann/Caputo operator. In particular, it has been proved to be a valuable tool for handling viscoelastic properties. Bagley [11], Friedrich [12], Junqi *et al.*[13], Guangyu *et al.*[14], Xu and Tan [15,16] and Tan *et al.*[17-22] have sequentially introduced the fractional calculus approach. Here we mention only those contributions which regard with the viscoelastic type studies [4, 17, 18, 23-25] and the references therein. In the literature, much attention has been drawn on the flow problems with no-slip condition. No-slip condition is no longer valid for thin films problems, problems involving multiple interfaces and the flow of rarefied fluids are considered. Many polymeric fluids slip or stick-slip on solid boundaries

and hence no-slip condition is no-longer valid. Experimentalists usually associate "Spurt" with slip at the wall [26]. The inadequacy of the no-slip condition is quite evident in polymer melts which often exhibit microscopic wall slip. The slip condition plays an important role in shear skin, spurt and hysteresis effects. Though many flow problems concerning Newtonian and non-Newtonian fluids have been solved under the no-slip condition, the fluid slippage might occur at the solid boundary [27-32]. We give some investigations for existence of slip at the solid boundary [33, 34]. In 1823, first time the possibility of fluid slip at solid boundary indicated by Navier as a general boundary condition. This boundary condition assumes that the tangential velocity of the fluid relative to the solid at a point on its surface is proportional to the tangential stress acting at that point [35].

2 MATHEMATICAL MODEL OF PROBLEM

The equations governing the flow of an incompressible fluid include continuity equation and momentum equation. In the absence of body forces

$$\nabla\cdot\mathbf{V}=0 \qquad \nabla\cdot\mathbf{T}=\rho\frac{\partial\mathbf{V}}{\partial t}+\rho\left(\mathbf{V}.\nabla\right)\mathbf{V}, \tag{1}$$

where ρ is the fluid density, **V** is the velocity field, t is the time and ∇ represents the del or nabla operator. The Cauchy tensor **T** in an incompressible homogeneous fluid of second grade is related to the fluid motion in the following manner [36-41].

$$\mathbf{T}=-p\mathbf{I}+\mathbf{S},\ \mathbf{S}=\mu\mathbf{A}_1+\alpha_1\mathbf{A}_2+\alpha_2\mathbf{A}_1^2. \tag{2}$$

where p is hydrostatic pressure, $\mathbf{I}$ is unit tensor identity, $-p\mathbf{I}$ is the indeterminate part of the stress or spherical stress due to the constraint of incompressibility, **S** is the extra-stress tensor, μ is the dynamic viscosity, α_1 and α_2 are the normal stress moduli or material moduli, and $\mathbf{A}_1$ and $\mathbf{A}_2$ are the kinematic tensors or first two Rivilin-Ericksen tensor defined through

$$\mathbf{A}_1=\left(\nabla\mathbf{V}\right)+\left(\nabla\mathbf{V}\right)^T,\ \mathbf{A}_2=\frac{d\mathbf{A}_1}{dt}+\mathbf{A}_1\left(\nabla\mathbf{V}\right)+\left(\nabla\mathbf{V}\right)^T\mathbf{A}_1. \tag{3}$$

For the problem under consideration, we shall assume a velocity field of the form

$$\mathbf{V}=\mathbf{V}\left(y,t\right)=u\left(y,t\right)\boldsymbol{i},\quad \mathbf{S}=\mathbf{S}\left(y,t\right), \tag{4}$$

where $\boldsymbol{i}$ is the unit vector along the x-direction of the Cartesian coordinate system. For these flows constraint of incompressibility is automatically satisfied for these flows. If the fluid is at rest up to moment $t=0$ then

$$\mathbf{V}=\mathbf{V}\left(y,0\right)=\mathbf{0},\quad \mathbf{S}=\mathbf{S}\left(y,0\right)=\mathbf{0}, \tag{5}$$

Eqs. (1)-(5) yields meaningful mathematical model of problem is represented by the following partial differential Eqs.

$$\frac{\partial u\left(y,t\right)}{\partial t}=\left(\nu+\alpha\frac{\partial}{\partial t}\right)\frac{\partial^2u\left(y,t\right)}{\partial y^2},$$
$$\tau\left(y,t\right)=\left(\mu+\alpha_1\frac{\partial}{\partial t}\right)\frac{\partial u\left(y,t\right)}{\partial y}, \tag{6}$$

where $\tau\left(y,t\right)=S_{xy}\left(y,t\right)$ is the non-zero shear stress and $\nu=\frac{\mu}{\rho}$ is the kinematic viscosity and $\alpha=\frac{\alpha_1}{\rho}$ the viscoelastic parameter of the second grade fluid. The governing equations corresponding to an incompressible fractionalized second grade fluid, performing the same motion in the absence of pressure gradient in the flow direction are [21]

$$\frac{\partial u\left(y,t\right)}{\partial t}=\left(\nu+\alpha D_t^{\beta}\right)\frac{\partial^2u\left(y,t\right)}{\partial y^2},$$
$$\tau\left(y,t\right)=\left(\mu+\alpha_1D_t^{\beta}\right)\frac{\partial u\left(y,t\right)}{\partial y}, \tag{7}$$

where $0<\beta<1$ is the fractional parameter. Of course, the new material constant α_1, although for the simplicity we keep same notations, tends to the original α_1 as $\beta\to1$. The fractional differential operator so called Caputo fractional operator D_t^{β} defined by

$$D_t^{\beta}f\left(t\right)=\begin{cases}\frac{1}{\Gamma\left(1-\beta\right)}\int_0^t\frac{f'\left(\tau\right)}{\left(t-\tau\right)^{\beta}}d\tau, & 0\le\beta<1,\\ \frac{df\left(t\right)}{dt}, & \beta=1,\end{cases} \tag{8}$$

and $\Gamma(\bullet)$ is the gamma function. The system of partial differential Eqs.(7) with appropriate initial and boundary conditions, will be solved by the means of discrete Laplace transform. In order to avoid lengthy calculations of residues and contour integrals, the discrete inverse Laplace transform method will be used [6, 19-23, 25 45-46].

3 FORMATION OF INITIAL AND BOUNDARY CONDITIONS

Consider an incompressible fractionalized second grade fluid occupying the space lying over an infinitely extended plane which is situated in the xz - plane and perpendicular to the y -axis. Initially, the fluid is at rest and at the moment $t=0^+$ the plane start to move in its own plane. Here we assume the existence of slip boundary between the velocity of the fluid at the plane $u\left(0,t\right)$ and the speed of the plane, the relative velocity between $u\left(0,t\right)$ and the plane is assumed to be proportional to the shear rate at the plane. Due to the shear, the fluid above the plane is gradually moved. Its velocity is of the form $(4)_1$, while the governing equations are given by Eqs. (7). The appropriate initial and boundary conditions are

$$u\left(y,0\right)=0 \quad y>0, \tag{9}$$

$$u\left(0,t\right)=UH\left(t\right)t^n+\theta H\left(t\right)\left.\frac{\partial u\left(y,t\right)}{\partial y}\right|_{y=0}, \tag{10}$$

where $H(t)$ is the Heaviside function and θ is the slip strength or slip coefficient. If $\theta = 0$ than the general solution without slip effect will be obtained. If θ is finite, fluid slip occurs at the plane but its effect depends upon the length scale of the flow. Furthermore, the natural condition is as under

$$u(y,t) \to 0 \text{ as } y \to \infty \text{ and } t > 0, \tag{11}$$

have to be satisfied. They are consequence of the fact that the fluid is at rest at infinity and there is no shear in the free stream.

4 CALCULATION OF THE VELOCITY FIELD

In order to find exact analytical solution for velocity field, we apply the Laplace transform formula to Eq. $(7)_1$ for a sequential fractional derivative and taking into account initial condition (9) we find that

$$\left(\frac{\partial^2}{\partial y^2} - \frac{q}{\nu + \alpha q^{\beta}}\right)\bar{u}(y,q) = 0, \tag{12}$$

where $\bar{u}(y,q)$ is the image funciton of $u(y,t)$ and q is a transform parameter. Furthermore, the discrete Laplace of boundary condition (10) and natural condition (11) is as under

$$\bar{u}(0,q) = \frac{Un!}{q^{n+1}} + \theta \frac{\partial \bar{u}(y,q)}{\partial y}\Big|_{y=0}, \tag{13}$$

and

$$\bar{u}(y,q) \to 0 \text{ as } y \to \infty, \tag{14}$$

solving Eq.(12) under the boundary condition (13) and natural condition (14), we get

$$\bar{u}(y,q) = \frac{Un!}{q^{n+1}\left[1 + \theta\sqrt{\frac{q}{\nu + \alpha q^{\beta}}}\right]} \exp\left\{-\left(\frac{q}{\nu + \alpha q^{\beta}}\right)^{\frac{1}{2}} y\right\}. \tag{15}$$

In order to obtain $u(y,t) = L^{-1}\{\bar{u}(y,q)\}$ and to avoid the lengthy and burdensome calculations of residues and contours integrals, we apply the discrete inverse Laplace transform method [6,19-23,25,45-46]. Before applying discrete inverse Laplace transform, firstly we rewrite (15) in series form and using the fact

$$(-1)^k \frac{\Gamma(m+1)}{\Gamma(m-k+1)} = \frac{\Gamma(k-m)}{\Gamma(-m)}, \tag{16}$$

We get

$$\bar{u}(y,q) = \frac{Un!}{q^{n+1}} + Un!\sum_{k=1}^{\infty}\left(\frac{-\theta}{\sqrt{\alpha}}\right)^k \sum_{n=0}^{\infty} \frac{\Gamma\left(n+\frac{k}{2}\right)}{n!\Gamma\left(\frac{k}{2}\right)}\left(\frac{-\nu}{\alpha}\right)^n \frac{1}{q^{(\beta-1)\left(\frac{k}{2}\right)+n(\beta+1)+1}}$$

$$+Un!\sum_{k=0}^{\infty}\left(\frac{-\theta}{\sqrt{\alpha}}\right)^k \sum_{m=1}^{\infty}\left(\frac{-y}{\sqrt{\alpha}}\right)^m \frac{1}{m!}\sum_{n=0}^{\infty} \frac{\Gamma\left(n+\frac{m+k}{2}\right)}{n!\Gamma\left(\frac{m+k}{2}\right)}\left(\frac{-\nu}{\alpha}\right)^n \frac{1}{q^{(\beta-1)\left(\frac{m+k}{2}\right)+(\beta+1)n+1}}. \tag{17}$$

Inverting (17) by means of discrete inverse Laplace transform, we find that

$$u(y,t) = UH(t)t^n + UH(t)n!\sum_{k=1}^{\infty}\left(\frac{-\theta}{\sqrt{\alpha}}\right)^k$$

$$\times\sum_{n=0}^{\infty} \frac{\Gamma\left(n+\frac{k}{2}\right)\left(\frac{-\nu t^{\beta+1}}{\alpha}\right)^n}{n!\Gamma\left(\frac{k}{2}\right)\Gamma\left((\beta-1)\frac{k}{2}+n(\beta+1)+1\right)} t^{(\beta-1)\frac{k}{2}}$$

$$+Un!H(t)\sum_{k=0}^{\infty}\left(\frac{-\theta}{\sqrt{\alpha}}\right)^k \sum_{m=1}^{\infty}\left(\frac{-y}{\sqrt{\alpha}}\right)^m \frac{1}{m!}$$

$$\times\sum_{n=0}^{\infty} \frac{\Gamma\left(n+\frac{m+k}{2}\right)\left(\frac{-\nu t^{\beta+1}}{\alpha}\right)^n}{n!\Gamma\left(\frac{m+k}{2}\right)\Gamma\left((\beta-1)\frac{m+k}{2}+n(\beta+1)+1\right)} t^{(\beta-1)\left(\frac{m+k}{2}\right)} \tag{18}$$

The wright generalized hypergeometric funciton is defined as below

$${}_p\Psi_q\left[z\left|\begin{matrix}(a_1,A_1),\ldots(a_p,A_p)\\(b_1,B_1),\ldots(b_q,B_q)\end{matrix}\right.\right] = \sum_{n=0}^{\infty}\frac{z^n\Pi_{j=1}^{p}\Gamma(a_j+A_jn)}{n!\Pi_{j=1}^{q}\Gamma(b_j+B_jn)}. \tag{19}$$

In terms of wright generalized hypergeometric function (19) we write velocity field expression (18) as a simple form

$$u(y,t) = UH(t)t^n + n!UH(t)\sum_{k=1}^{\infty}\left(\frac{-\theta}{\sqrt{\alpha}}\right)^k$$

$$\times_1\Psi_2\left[\frac{-\nu t^{\beta+1}}{\alpha}\left|\begin{matrix}\left(\frac{k}{2},1\right)\\\left(\frac{k}{2},0\right),\left((\beta-1)\frac{k}{2}+1,\beta+1\right)\end{matrix}\right.\right] t^{(\beta-1)\frac{k}{2}}$$

$$+n!UH(t)\sum_{k=0}^{\infty}\left(\frac{-\theta}{\sqrt{\alpha}}\right)^k \sum_{m=1}^{\infty}\left(\frac{-y}{\sqrt{\alpha}}\right)^m \frac{1}{m!}$$

$$\times_1\Psi_2\left[\frac{-\nu t^{\beta+1}}{\alpha}\left|\begin{matrix}\left(\frac{m+k}{2},1\right)\\\left(\frac{m+k}{2},0\right),\left((\beta-1)\frac{m+k}{2}+1,\beta+1\right)\end{matrix}\right.\right] t^{(\beta-1)\frac{m+k}{2}} \tag{20}$$

5 CALCULATION OF SHEAR STRESS

In order to obtain shear stress $\tau(y,t)$, apply discrete Laplace transform to Eq. $(7)_2$, we find that

$$\bar{\tau}(y,q) = \left(\mu + \alpha_1 q^{\beta}\right)\frac{\partial \bar{u}(y,q)}{\partial y}, \tag{21}$$

where $\bar{\tau}(y,q) = L\{\tau(y,t)\}$ and q is transform parameter. Using equation (15) into Eq. (21) we get

$$\bar{\tau}(y,q) = \frac{-\rho\sqrt{q}n!U\sqrt{\nu+\alpha q^{\beta}}}{q^{n+1}\left[1+\theta\sqrt{\frac{q}{\nu+\alpha q^{\beta}}}\right]} \times \exp\left\{-\left(\frac{q}{\nu+\alpha q^{\beta}}\right)^{\frac{1}{2}} y\right\}. \tag{22}$$

Furthermore Eq. (22) can be rewritten in series form as under

$$\bar{\tau}(y,q) = -\sqrt{\alpha}\rho n!U\sum_{k=0}^{\infty}\left(\frac{-\theta}{\sqrt{\alpha}}\right)^k \sum_{m=0}^{\infty}\left(\frac{-y}{\sqrt{\alpha}}\right)^m \frac{1}{m!}.$$

$$\times\sum_{n=0}^{\infty}\frac{\Gamma\left(n+\frac{m+k-1}{2}\right)\left(\frac{-\nu}{\alpha}\right)^{n}}{n!\Gamma\left(\frac{m+k-1}{2}\right)q^{(\beta-1)\left(\frac{m+k-1}{2}\right)+n(\beta+1)+1}} \tag{23}$$

To obtain shear stress apply discrete inverse Laplace transform to Eq. (23) we get

$$\tau(y,t)=-\sqrt{\alpha}\rho n!UH(t)\sum_{k=0}^{\infty}\left(\frac{-\theta}{\sqrt{\alpha}}\right)^{k}\sum_{m=0}^{\infty}\left(\frac{-y}{\sqrt{\alpha}}\right)^{m}\frac{1}{m!}$$
$$\times\sum_{n=0}^{\infty}\frac{\Gamma\left(n+\frac{m+k-1}{2}\right)\left(\frac{-\nu t^{\beta+1}}{\alpha}\right)^{n}t^{(\beta-1)\left(\frac{m+k-1}{2}\right)}}{n!\Gamma\left(\frac{m+k-1}{2}\right)\Gamma\left((\beta-1)\left(\frac{m+k-1}{2}\right)+n(\beta+1)+1\right)} \tag{24}$$

Eq. (24) can be written in simple form by using wright generalized hypergeometric function (19) we have

$$\tau(y,t)=-\sqrt{\alpha}\rho n!UH(t)\sum_{k=0}^{\infty}\left(\frac{-\theta}{\sqrt{\alpha}}\right)^{k}\sum_{m=0}^{\infty}\left(\frac{-y}{\sqrt{\alpha}}\right)^{m}\frac{1}{m!}$$

$$\times_1\Psi_2\left[\frac{-\nu t^{\beta+1}}{\alpha}\middle|\begin{matrix}\left(\frac{m+k-1}{2},1\right)\\ \left(\frac{m+k-1}{2},0\right),\left((\beta-1),\left(\frac{m+k-1}{2}\right)+1,\beta+1\right)\end{matrix}\right]t^{(\beta-1)\left(\frac{m+k-1}{2}\right)}. \tag{25}$$

6 SPECIAL CASES

6.1 Ordinary second grade fluid with slip effects $\beta\to 1$

Letting $\beta\to 1$ into Eqs. (20) and (25), we find the velocity field and the shear stress corresponding to ordinary second grade fluid with slip effects.

6.2 Fractionalized second grade fluid without slip effect for $\theta\to 0$

Letting $\theta\to 0$ in Eqs. (20) and (25), respectively we gvet

$$u(y,t)=UH(t)t^{n}+n!UH(t)\sum_{m=1}^{\infty}\left(\frac{-y}{\sqrt{\alpha}}\right)^{m}\frac{1}{m!}$$

$$\times_1\Psi_2\left[\frac{-\nu t^{\beta+1}}{\alpha}\middle|\begin{matrix}\left(\frac{m}{2},1\right)\\ \left(\frac{m}{2},0\right),\left((\beta-1)\frac{m}{2}+1,\beta+1\right)\end{matrix}\right]t^{(\beta-1)\frac{m}{2}} \tag{26}$$

$$\tau(y,t)=-\sqrt{\alpha}\rho n!UH(t)\sum_{m=0}^{\infty}\left(\frac{-y}{\sqrt{\alpha}}\right)^{m}\frac{1}{m!}$$

$$\times_1\Psi_2\left[\frac{-\nu t^{\beta+1}}{\alpha}\middle|\begin{matrix}\left(\frac{m-1}{2},1\right)\\ \left(\frac{m-1}{2},0\right),\left(\beta-1\left(\frac{m-1}{2}\right)+1,\beta+1\right)\end{matrix}\right]t^{(\beta-1)\left(\frac{m-1}{2}\right)}, \tag{27}$$

the velocity field and shear stress corresponding fractionalized second grade fluid without slip effects.

6.3 Ordinary second grade fluid without slip effects $\beta\to 1$

Taking $\beta\to 1$ into Eqs. (26) and (27), we find the velocity field and shear stress corresponding to ordinary second grade fluid without slip effects.

6.4 Newtonian fluid with slip effect $\alpha\to 0$

For $\alpha\to 0$, Eq. (15) reduces as under

$$\bar{u}(y,q)=\frac{Un!}{q^{n+1}\left[1+\theta\sqrt{\frac{q}{\nu}}\right]}\exp\left\{-\left(\sqrt{\frac{q}{\nu}}\right)y\right\}. \tag{28}$$

Rewrite Eq. (28) in series form as below

$$\bar{u}(y,q)=Un!\sum_{m=0}^{\infty}\left(\frac{-y}{\sqrt{\nu}}\right)^{m}\frac{1}{m!}\frac{1}{q^{1+n-\frac{m}{2}}}+Un!\sum_{k=1}^{\infty}\left(\frac{-\theta}{\sqrt{\nu}}\right)^{k}$$
$$\times\sum_{m=0}^{\infty}\left(\frac{-y}{\sqrt{\nu}}\right)^{m}\frac{1}{m!}\frac{1}{q^{1+n-\left(\frac{m+k}{2}\right)}} \tag{29}$$

Inverting (29) by means of discrete Laplace transform we get

$$u(y,t)=Un!t^{n}H(t)\sum_{m=0}^{\infty}\left(\frac{-y}{\sqrt{t\nu}}\right)^{m}\frac{1}{m!\Gamma\left(1-\frac{m}{2}+n\right)}$$
$$+t^{n}Un!H(t)\sum_{k=1}^{\infty}\left(\frac{-\theta}{\sqrt{t\nu}}\right)^{k}\sum_{m=0}^{\infty}\left(\frac{-y}{\sqrt{t\nu}}\right)^{m}\frac{1}{m!}$$
$$\times\frac{1}{\Gamma\left(1-\left(\frac{m+k}{2}\right)+n\right)} \tag{30}$$

Since wright function is defined as

$$W_{a,b}(z)=\sum_{n=0}^{\infty}\frac{z^{n}}{n!\Gamma(an+b)},\ a>-1,\ \text{and}\ b\in\mathbb{C}, \tag{31}$$

Simple form of Newtonian fluid with slip effect can be obtained using wright function (31) as below

$$u(y,t)=n!t^{n}UH(t)$$
$$\times\left[W_{\frac{-1}{2},1+n}\left(\frac{-y}{\sqrt{t\nu}}\right)+\sum_{k=1}^{\infty}\left(\frac{-\theta}{\sqrt{t\nu}}\right)^{k}W_{-\frac{1}{2},n+1-\frac{k}{2}}\left(\frac{-y}{\sqrt{t\nu}}\right)\right]. \tag{32}$$

Similarly for finding shear stress $\tau(y,t)$ for Newtonian fluid with slip effect put $\alpha\to 0$, into Eq. (22) we get

$$\bar{\tau}(y,q)=\frac{-\rho\sqrt{q}n!U\sqrt{\nu}}{q^{n+1}\left[1+\theta\sqrt{\frac{q}{\nu}}\right]}\exp\left\{-\left(\frac{q}{\nu}\right)^{\frac{1}{2}}y\right\}, \tag{33}$$

For finding $L^{-1}\left\{\bar{\tau}(y,q)\right\}=\tau(y,t)$ we rewrite (33) in series form as below

$$\bar{\tau}(y,q)=-n!U\sqrt{\rho\mu}\sum_{k=0}^{\infty}\left(\frac{-\theta}{\sqrt{\nu}}\right)^{k}$$
$$\times\sum_{m=0}^{\infty}\left(\frac{-y}{\sqrt{\nu}}\right)^{m}\frac{1}{m!}\frac{1}{q^{n-\left(\frac{m+k-1}{2}\right)}}. \tag{34}$$

Inverting (34) by means of discrete inverse Laplace transform we get

$$\tau(y,t) = -n!UH(t)t^{n-\frac{1}{2}}\sqrt{\rho\mu}\sum_{k=0}^{\infty}\left(\frac{-\theta}{\sqrt{tv}}\right)^{k} \times\sum_{m=0}^{\infty}\left(\frac{-y}{\sqrt{tv}}\right)^{m}\frac{1}{m!}\frac{1}{\Gamma\left(n-\left(\frac{m+k-1}{2}\right)\right)}. \quad (35)$$

Using wright function (35) can be written as

$$\tau(y,t) = -n!UH(t)t^{n-\frac{1}{2}}\sqrt{\rho\mu} \times\sum_{k=0}^{\infty}\left(\frac{-\theta}{\sqrt{tv}}\right)^{k} W_{\frac{-1}{2},\frac{n-k+1}{2}}\left(\frac{-y}{\sqrt{tv}}\right). \quad (36)$$

6.5 Newtonian fluid without slip effect $\theta \to 0$

Finally taking $\theta \to 0$ in Eqs. (32) and (36) the solution for Newtonian fluids without slips effects are obtained.

7 NUMERICAL RESULTS AND DISCUSSION

In the last sections, we have determined exact analytical solutions for fractionalized second grade fluid moving over the plane. In order to discuss some relevant physical aspects of the obtained results, many graphs are sketched in the present section. Attention has been focused on analyzing the difference between the velocity and shear stress profiles of fractionalized second grade fluid for the flow induced by a moving plane. We interpret these results with respect to the variations of emerging parameters of interest. The diagrams of the velocity field $u(y,t)$and, the shear stresses $\tau(y,t)$ have been drawn against y for different values of time t and the material constants $\alpha, \nu, \theta,$ the power n and fractional parameter β. For the sake of simplicity, all graphs are plotted by taking$U=1$, $\nu=0.295$, $\mu=26$, $\alpha=0.5$, $\beta=0.2,$ and using Mathcad software. It is also note effects of material parameters on shear stress $\tau(y,t)$ profiles are discussed in absolute sense. In Figs.1, the diagrams of the velocity and the shear stress at three different times for fractionalized second grade fluid are presented. It is clear that, both the velocity and the shear stress are increasing functions with respect to time t and decreasing ones with respect to the height y . Fig. 2 provides the graphical illustration for the effect of material parameter α on the two entities. The velocity as well as shear stress are increased with the increase of material parameter α. The influence of the kinematic viscosity ν on the fluid motion is shown in Figs.3. Again both the velocity and the shear stress are increasing functions with respect to kinematic viscosity ν. The variation of fractional parameter β on fluid motion is shown in Figs. 4. The velocity filed $u(y,t)$ and the shear stress $\tau(y,t)$ have opposite behavior when fractional parameter β increases. The velocity field increases and shear stress decreases with regard to fractional parameter β. Figs.5 are prepared to show the effect of the slip parameter θ on the fluid motion. As it was to be expected, both the velocity and the shear stress are decreasing functions with regard to the slip parameter θ and this effect is clear near the moving plane. Fig.6 is established to show the behavior of the parameter n . It is observed that both entities are increasing function of the parameter n . The velocity field and shear stress decrease as we move up form the plane. This phenomenon is clear from Figs.7. Finally, for comparison, the profiles of the velocity and the shear stress corresponding to the four models (fractionalized second grade for $\beta=0.2,0.5$, ordinary second grade $\beta=1,$ Newtonian) are together depicted in Fig.8 and 9. For two different values of t =4s, 10s and of the common material constants. It is clearly seen from these diagrams that, that the fractionalized second grade fluids have largest values and Newtonian fluid is smallest for both entities of interest. The select the reasonable value of the fractional parameter β, corresponding to the optimum dynamical system, results by comparison with the experimental results. The units of the material constants in all figures are SI units.

8 CONCLUDING REMARKS

In this paper, the unsteady flow of a fractional second grade fluid over an infinite plane where no-slip assumption is no longer valid is studied by means of the discrete Laplace transforms and infinite series. The motion of the fluid is due to the plane that at time $t=0^{+}$ is moved with a velocity $UH(t)t^{n}$ in its plane. The general analytical solutions are obtained for the velocity $u(y,t)$ and the shear stress $\tau(y,t)$ under series form in terms of the Wright generalized hypergeometric function ${}_{p}\Psi_{q}$, and presented as sum of the slip contribution and the corresponding no-slip contribution, satisfy all imposed initial and boundary conditions. The similar solutions for ordinary second grade and Newtonian fluids, can easily be obtained as limiting cases of general solutions. Furthermore, the solutions for fractionalized and ordinary second grade fluid, when slip effect is not present are also obtained as a special cases. Finally, the influence of the material, slip and fractional parameters on the motion of fractionalized second grade fluids is underlined by graphical illustrations. The difference among fractionalized second, ordinary second grade and Newtonian fluid models is also highlighted. The important conclusions from present study are the following.

- The general solutions (20) and (25) are presented as a sum of the slip and the corresponding no-slip contribution. These solutions can be easily particularized to give the similar solutions for ordinary second grade fluid.

- Both velocity field $u(y,t)$ and the shear stress $\tau(y,t)$, are increasing functions with respect to the time, material parameter α and kinematic viscosity ν .
- The fractional parameter β has strong influence on the fluid motion. It is noted that fractional parameter have opposite effect on velocity and shear stress profiles.
- The increasing values of slip parameter θ slow down the fluid motion.
- As expected, the increasing values of n and the height y increases and decreases the fluid motion respectively. It is also observed that all pertinent parameters have clear effects near the moving plane.
- The fractionalized second grade fluid moving fast in comparison to ordinary second grade and Newtonian fluids.

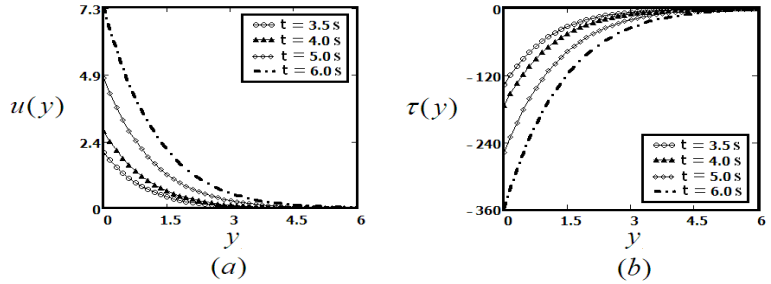

Figure 1: Profiles of the velocity field $u(y,t)$ and the shear stress $\tau(y,t)$ for fractionalized second grade fluid given by Eqs. (20) and (25), for $U=1$, $\nu=0.295$, $\mu=26$, $\alpha=0.5$, $\beta=0.2$, $\theta=5$, $n=2$ and different values of *t*.

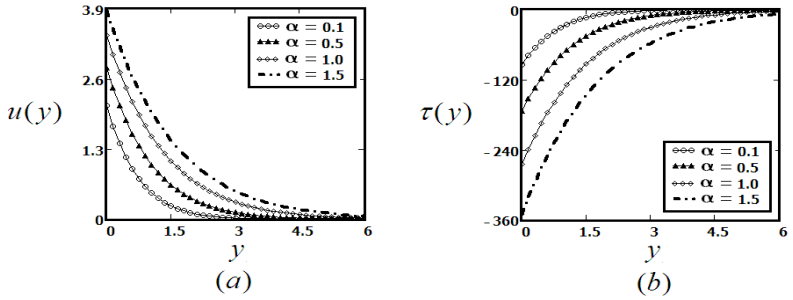

Figure 2: Profiles of the velocity field $u(y,t)$ and the shear stress $\tau(y,t)$ for fractionalized second grade fluid given by Eqs. (20) and (25), for $U=1$, $\nu=0.295$, $\mu=26$, $\beta=0.2$, $\theta=5$, $n=2$, $t=4s$ and different values of α .

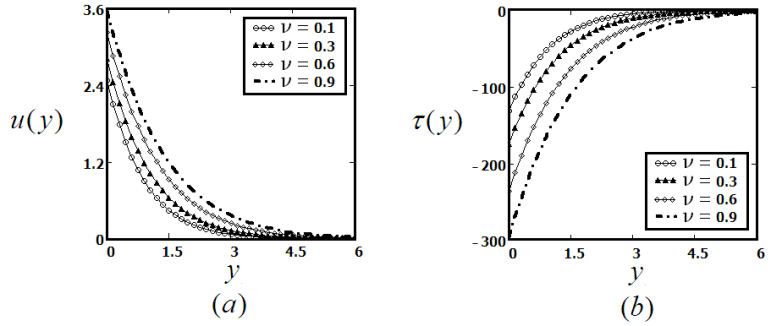

Figure 3: Profiles of the velocity field $u(y,t)$ and the shear stress $\tau(y,t)$ for fractionalized second grade fluid given by Eqs. (20) and (25), for $U=1$, $\rho=88$, $\alpha=0.5$, $\beta=0.2$, $\theta=5$, $n=2$, $t=4s$ and different values of ν .

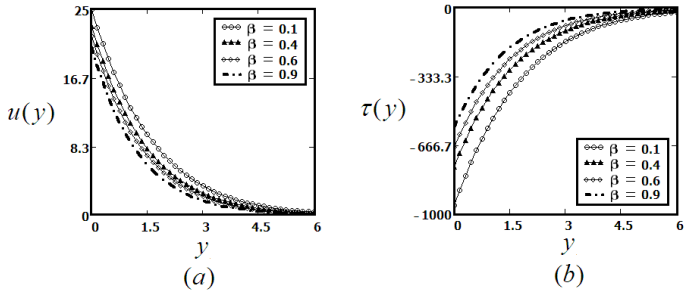

Figure 4: Profiles of the velocity field $u(y,t)$ and the shear stress $\tau(y,t)$ for fractionalized second grade fluid given by Eqs. (20) and (25), for $U=1$, $\nu=0.295$, $\mu=26$, $\alpha=0.5$, $\theta=5$, $n=2$, $t=4s$ and different values of β.

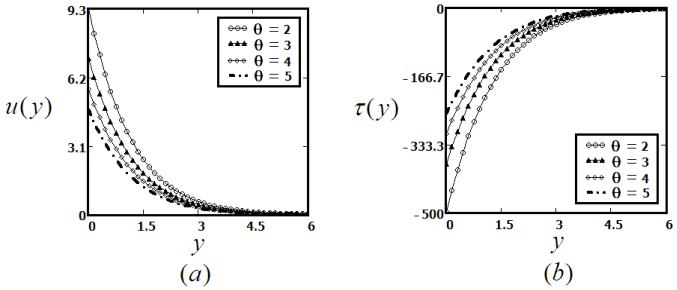

Figure 5: Profiles of the velocity field $u(y,t)$ and the shear stress $\tau(y,t)$ for fractionalized second grade fluid given by Eqs. (20) and (25), for $U=1$, $\nu=0.295$, $\mu=26$, $\alpha=0.5$, $\beta=0.2$, $n=2$, $t=5s$ and different values of θ.

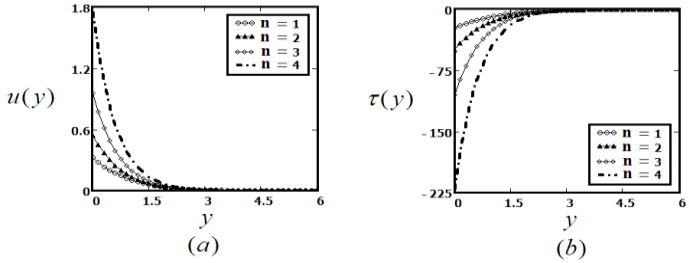

Figure 6: Profiles of the velocity field $u(y,t)$ and the shear stress $\tau(y,t)$ for fractionalized second grade fluid given by Eqs. (20) and (25), for $U=1$, $\nu=0.295$, $\mu=26$, $\alpha=0.5$, $\beta=0.2$, $t=2s$ and different values of n.

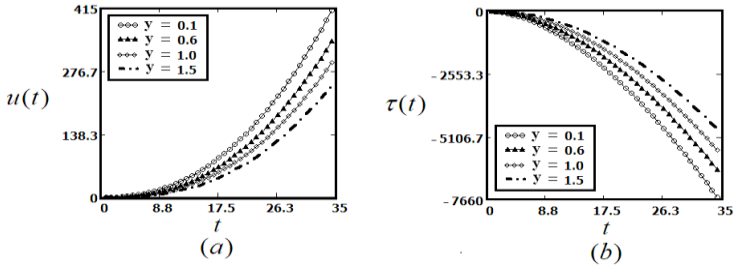

Figure 7: Profiles of the velocity field $u(y,t)$ and the shear stress $\tau(y,t)$ for fractionalized second grade fluid given by Eqs. (20) and (25), for $U=1$, $\nu=0.295$, $\mu=26$, $\alpha=0.5$, $\beta=0.2$, $\theta=5$, $n=2$ and different values of y.

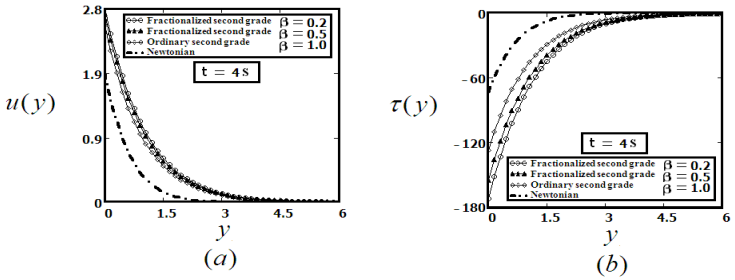

Figure 8: Profiles of the velocity field $u(y,t)$ and the shear stress $\tau(y,t)$ for fractionalized second grade, ordinary second grade and Newtonian fluids given for $U=1$, $\nu=0.295$, $\mu=26$, $\alpha=0.5$, $\beta=0.2, 0.5 \& 1$, $\theta=5$, $n=2$ and $t=4s$.

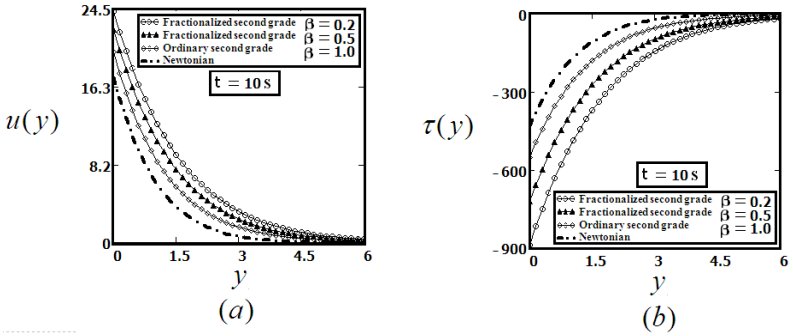

Figure 9: Profiles of the velocity field $u(y,t)$ and the shear stress $\tau(y,t)$ for fractionalized second grade, ordinary second grade and Newtonian fluids given, for $U=1$, $\nu=0.295$, $\mu=26$, $\alpha=0.5$, $\beta=0.2, 0.5 \& 1$, $\theta=5$ and $t=10s$.

REFERENCES

[1] K.R. Rajagopal, Kaloni, Continuum Mechanics and its Applications, Washigton, DC, Hemisphere Press (1989).

[2] Corina Fetecau, M. Jamil, C. fetecau, D. Vieru, The Rayleigh-Stokes problems for an edge in a generalized Oldroyd-B fluid, Zeitschrift frangewandte Mathematik und Physik (ZAMP), 60 (2009) 921 – 933.

[3] M. Jamil, First problem of Stokes' for generalized Burgers' fluids, ISRN Mathematical Physics, (2012) Article ID 831063.

[4] M. Jamil, N. A. Khan, A. Rauf, Oscillating flows of fractionalized second grade fluid, ISRN Mathematical Physics, (2012) Article ID 908386.

[5] K. Khandelwal , V. Mathur, Exact Solutions for an Unsteady Flow of Viscoelastic Fluid in Cylindrical Domains Using the Fractional Maxwell Model, Int. J. Appl. Comput, Math DOI 10.1007/s40819-014-0018-2.

[6] Y. Liu, L. Zheng, X. Zhang, Unsteady MHD Couette flow of a generalized Oldroyd-B fluid with fractional derivative, Comput. Math. Appl., 61 (2011) 443-450.

[7] D. Tripathi, P. K. Gupta, and S. Das, Influence of slip condition on peristaltic transport of a viscoelastic fluid with fractional Burgers' model, Thermal Science,15 (2011) 501–515.

[8] D. Kumar, J. Singh, S. Kumar, A fractional model of Navier–Stokes equation arising in unsteady flow of a viscous fluid, Journal of the Association of Arab Universities for Basic and Applied Sciences (2014).

[9] D. Valério, J. T. Machado, V. Kiryakova, Some pioneers of the applications of fractional calculus, Fractional Calculus and Applied Analysis, 17 (2014) 552-578.

[10] S. Gupta, D. Kumar, J. Singh, Numerical study for systems of fractional differential equations via Laplace transform, Journal of the Egyptian Mathematical Society (2014), doi.org/10.1016/j.joems.2014.04.003.

[11] R. L. Bagley, A theoretical basis for the application of fractional calculus to viscoelasticity, Journal of Rheology, 27 (1983) 201-210.

[12] C. H. R. Friedrich, Relaxation and retardation function of the Maxwell model with fractional derivatives, Rheological Acta, 30 (1991) 151-158.

[13] H. Junki, H. Guangyu, L. Ciqun, Analysis of general second order fluid flow in double cylinder rheometer, Science in China Series A, 40 (1997) 183-190.

[14] H. Guangyu, H. Junki, L. Ciqun, General second order fluid flow in a pipe, Appl. Math. Mech. (English Ed.), 16 (1995) 825-831.

[15] M. Y. Xu, W. Tan, Theoretical analysis of the velocity field, stress field and vortex sheet of

generalized second order fluid with fractional anomalous diffusion, Sci. China Ser. A, 44 (2001) 1387-1399.

[16] M. Y Xu, Tan W. C, Representation of the constitutive equation of viscoelastic materials by the generalized fractional element networks and its generalized solution, Sci. China Ser. G., 46 (2003) 145-157.

[17] M. Jamil, N. A. Khan, M. I. Asjad, New exact solutions for an Oldroyd-B fluid with fractional derivatives, Stokes' first problem, Int J Nonlinear Sc & Num Simulation, 14 (2013) 443-451.

[18] M. Jamil, N. A. Khan, N. Shahid, Fractional MHD Oldroyd-B fluid over an oscillating plate, Thermal Science, 17 (2013) 997-1011.

[19] W. C. Tan, W. X. Pan, M. Y. Xu, A note on unsteady flows of a viscoelastic fluid with fractional Maxwell model between two parallel plates, Int. J. Non-linear Mech., 38 (2003) 645-650.

[20] W. C. Tan, F. Xian, L. Wei, An exact solution of unsteady Couette flow of generalized second grade fluid, Chinese Science Bulletin, 47 (2002) 1783-1785.

[21] W. C. Tan., M. Y. Xu, The impulsive motion of flat plate in a generalized second grade fluid, Mech. Res. Comm., 29 (2002) 3-9.

[22] W. C. Tan, M. Y. Xu, Unsteady flows of a generalized second grade fluid with the fractional derivative model between two parallel plates, Acta Mech Sin., 20 (2004) 471-476.

[23] M. Jamil, A. Rauf, A. A. Zafar, N. A. Khan, New exact analytical solutions for Stokes' first problem of Maxwell fluid with fractional derivative approach, Comput. Math. Appl., 62 (2011) 1013-1023.

[24] M. Khan, S. Wang, Flow of a generalized second-grade fluid between two side wall perpendicular to a plate with a fractional derivative model, Nonlinear Analysis: Real World Applications, 10(1)(2009) 203–208.

[25] L. Zheng,Y. Liu, X. Zhang, Slip effects on MHD flow of a generalized Oldroyd-B fluid with fractional derivative, Nonlinear Anal., Real World Appl., 13 (2012) 513-523.

[26] I. M. Eldesoky, Influence of slip condition on peristaltic transport of a compressible Maxwell fluid through porous medium in a tube, Int. J. of Appl. Math and Mech., 8 (2012) 99-117.

[27] E. A. Ashmawy, Unsteady couette flow of a micropolar fluid with slip, Meccanica, 47(1) (2012) 85–94.

[28] R. Ellahi, Effects of the slip boundary condition on non-Newtonian flows in a channel,Comms in Nonlinear Science and Numerical Simulation,14 (2009) 1377–1384.

[29] M. Jamil, N. A. Khan, Slip effects on fractional viscoelastic fluids, International Journal of Differential Equations, (2011) Article ID 193813.

[30] T. Hayat, R. Ellahi, S. Asghar, A. M. Siddiqui, Flow induced by a non-coaxial rotation of a porous disk executing non-torsional oscillations and a second grade fluid at infinity, Appl. Math. Model. 28 (2004) 591-605.

[31] S. Richardson, on the no-slip boundary condition, Journal of Fluid Mechanics, 59(1973) 707–719.

[32] P. A. Thompson, S. M. Troian, A general boundary condition for liquid flow at solid surfaces,Nature, 389 (1997) 360–362.

[33] A. B. Basset, A Treatise on Hydrodynamics, Dover, New York, NY, USA, 2 (1961).

[34] M. E. O.'Neill, K. B. Ranger, H. Brenner, Slip at the surface of a translating-rotating sphere bisected by a free surface bounding a semi-infinite viscous fluid, removal of the contact line singularity, Physics of Fluids, 29 (1986) 913–924.

[35] M. Devakar, D. Sreenivasu, B. Shankar, Analytical solutions of some fully developed flows of couple stress fluid between concentric cylinders with slip boundary conditions, International Journal of Engineering Mathematics, 2014, Article ID 785396.

[36] C. Fetecau, Corina Fetecau, Starting solutions for some unsteady unidirectional flows of a second grade fluid, Int. J. Eng. Sci., 43 (2005) 781-789.

[37] C. Fetecau, Corina Fetecau, Starting solutions for the motion of second grade fluid due to longitudinal and torsional oscillations of a circular cylinder, Int. J. Eng.Sci., 44 (2006) 788-796.

[38] C. Fetecau, Corina Fetecau, J. Zierep, Decay of potential vortex and propagation of a heat wave in a second grade fluid, Int. J. Non-linear Mech., 37 (2002) 1051-1056.

[39] T. Hayat, M. Khan, M. Ayub, Some analytical solutions for second grade fluid flows for cylindrical geometries, Math. and Comput. Modelling., 43 (2006) 16-29.

[40] T. Hayat, S. Najam, M. Sajid, M. Ayub, S. Mesloub, On exact solutions for oscillatory flows in a generalized burgers fluid with slip condition, Z. Naturforsch. 65 (2010) 381 - 391.

[41] K. R. Rajagopal, On the creeping flow of the second order fluid, J. of Non Newtonian Fluid Mech., 15 (1984) 239-246.

[42] Y. Luchko, Algorithms for Evaluation of the wright function for the real arguments values, Fractional Calculus and Applied analysis, (2008).

[43] F. Mainardi, Frcational calculus and waves in linear viscoelasticity, An introduction to mathematical models, Imperial College Press, London, (2010).

[44] I. Petras, Fractional Derivatives, Fractional Integral and Fractional Differential Equations in Matlab, Engineering Education and Research using MATLAB, (2011).

[45] C. Fetecau, A. Mahmood, M. Jamil, Exact solutions for the flow of Visco-elastic fluid induced by a circular cylinder subject to a time dependent shear stress, Commun Nonlinear Sci Numer Simulat, 15 (2010) 3931 - 3938.

[46] M. Jamil, N. A. Khan, A. A. Zafar, Translational flows of an Oldroyd-B fluid with fractional derivatives, Comput. Math. Appl., 62 (2011) 1013-1023.

EFFECT OF TEMPERING TEMPERATURE ON SUSCEPTIBILITY OF INTERGRANULAR CORROSION OF AUSTENITIC STAINLESS STEEL (AISI 304)

M.Rizwan[1,*], Iftikhar A[2], M.Ali[3], Muzammil Y[4]

[1,2,3]Metallurgical Engineering Department, NED University of Engineering & Technology, Karachi, Pakistan

[4]Byco Petroleum Pakistan Limited

[*]Corresponding author. Tel: +923333657963; Email address: materialist.riz@gmail.com

ABSTRACT

Austenitic stainless steels undergo intergranular corrosion, when they are heated in the range of 500°C to 850°C, and then slowly cooled. Intergranular corrosion is the cause of many failures in Austenitic stainless steel which causes the material to fail in a brittle manner. Electrochemical Potentiokinetic Reactivation test is the latest Non- Destructive tool to analyze the sensitization behavior of materials. In this research, the effect of tempering temperature on susceptibility to intergranular corrosion was examined in AISI 304 Stainless Steel by Double loop electrochemical potentiokinetic reactivation (DLEPR) test according to ASTM standard G108. Microscopic examination is carried out by oxalic etch test according to ASTM standard A262 Practice A, to validate the results obtained from DLEPR test. Potentiostat samples were initially Solution annealed and then quenched to produce a homogenized structure. These samples were then tempered (heated) at several temperatures to induce different levels of sensitization in samples. The degree of Sensitization (DOS) was measured with the help of DLEPR and the results were validated by microstructural analysis.

Keywords: Intergranular Corrosion, AISI 304, Solution Annealing, DLEPR, Sensitization.

1 INTRODUCTION

Austenitic stainless steels show outstanding mechanical properties as well as unmatched Corrosion resistance that make them an ideal material for petrochemical, fertilizer and nuclear industries. [1]

Austenitic stainless steels are designated as AISI 200 and 300 series that are non-Magnetic ferrous alloys. AISI 304 and AISI 316 are the most common grades of Austenitic Stainless steels. [2]

In aqueous environment a passive film of Cr_2O_3 is formed on the surface, which gives it excellent corrosion resistance. [3]

These steels, when heated in the temperature range of 500-850°C, Chromium precipitates out and forms Chromium carbide along grain boundaries. This Chromium carbide results in Chromium depletion in the region around grain boundaries. This depletion causes percentage of Chromium to decreases well below 12% (which is minimum amount of Chromium, necessary to make Stainless Steel) in nearby material. In this region material does not behave as Corrosion resistant. This material is known as ‘‘sensitized material’’. This sensitized material when exposed to corrosive environments, Chromium depleted region dissolves leading to Intergranular Corrosion (IGC). This is only possible when the region around grain boundary has less than 12% chromium, because steels having chromium greater than 12% possess passivity.

Carbon is generally considered as an undesirable impurity in primary solid solution of Chromium steels. While it stabilizes the primary solid solution structure, it has a good affinity for Chromium (Cr), due to this affinity, Cr carbides, $M_{23}C_6$ form whenever carbon reaches levels of supersaturation in primary solid solution, and diffusion rates are adequate for carbon and Cr to segregate into precipitates. The solubility of carbon in primary solid solution is over 0.4% at activity however decreases greatly with decreasing temperature [2].

The equilibrium diagram for carbon in a basic 18%Cr10%Ni alloy is shown in Fig 1. At ambient temperature, little or no carbon is soluble in Austenite; even the 0.03% of L grades is mostly in a supersaturated solution. The absence of carbides in solid solution stainless-steel is because of the slow diffusion of carbon and therefore the even slower diffusion of Cr in solid solution. At a carbon level of 0.06%, which is found in most 304, supersaturation is reached below about 850°C. Below this temperature, supersaturation increases exponentially, while diffusion decreases exponentially. This results in precipitation rates that vary with temperature and carbon level as shown in Fig 1.

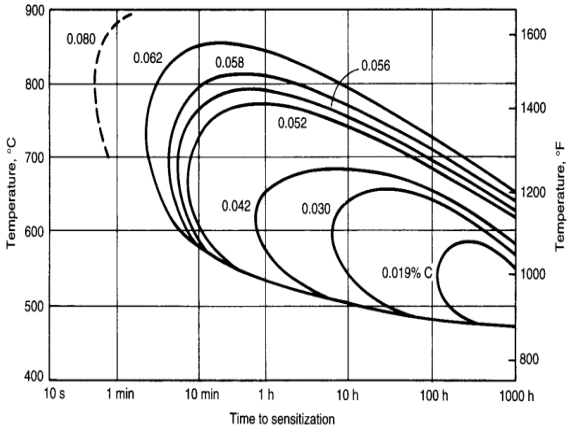

Figure 1. Time-Temperature-Sensitization curve. [4]

Desensitization of a Sensitized material can be achieved by Solution treatment at a temperature of 1050ºC to 1150ºC which dissolves chromium carbides again into solution. Time-Temperature-Sensitization (TTS) diagram is referred to study the effect of tempering temperature on Austenitic stainless steel. This diagram illustrates time required for isothermal sensitization at different temperatures. [1]

There are various standard methods, like oxalic acid test, Strauss test, Huey test, Streicher test, and Copper–Copper Sulfate-50 % sulphuric acid test, that can be used to analyze the susceptibility to intergranular corrosion in accordance with ASTM A-262 [5]. All of the above mentioned tests are time consuming and none of these is a quantitative and non-destructive method.

The research has been carried out for last many years to develop electrochemical potentiokinetic reactivation tests (EPR); these tests (single and double loop) have been broadly used to determine the degree of sensitization of stainless steels. The aim of EPR tests is to reveal the adjacent areas of the precipitates, where the chromium concentration decreases below a critical value in order to obtain quantitative electrochemical parameters of the degree of sensitization. [6]

In this study the effect of tempering temperature on susceptibility to intergranular corrosion is observed. ASTM A-262 Practice A, test was used to investigate intergranular corrosion with the help of microstructures. Degree of sensitization was also calculated by using Double loop electrochemical potentiokinetic reactivation (DLEPR) test.

Table 1. Chemical compositions of AISI 304 type stainless steel (WT %), Iron as balance

Elements	C	Si	Mn	P	S	Ni	Cr
Compos-ition	0.065	0.43	1.83	0.027	0.024	8.02	18.60

2 EXPERIMENTAL WORK

2.1 Material Selection

A square cross-sectional bar of AISI 304 stainless steel having a cross-section of 16mm x16mm is purchased with the assurance of the Mill test certificate. The Chemical composition of the material purchased is shown in Table 1.

2.2 Sample preparation

Three types of sample were prepared, for testing of sensitization by Double loop EPR test, oxalic etch and impact test for the validation of results.

For DLEPR six cylindrical samples with 7 mm diameter and 70 mm length are prepared. On one side; the surface of rod is made flat for the purpose of clamping.

For oxalic etch test six samples were cut from the DLEPR samples for observation of microstructure. The samples were first soldered with a piece of wire to give electrical connection and mounted (cold mounting) and then ground on P240, P320, P400, P600, P800, P1000 Silicon carbide papers following polishing with Alumina paste.

2.3 Heat Treatment

Heat treatment cycles are designed according to the sensitization range of AISI 304 stainless steel. All the samples are solution annealed to 1050°C for 40minutes followed by water quenching. These samples are then tempered at 600°C, 625°C, 675°C, 700°C and 750°C for 40 minutes followed by air cooling in order to simulate different degrees of sensitization.

2.4 DLEPR Tests

For detecting degree of sensitization to intergranular corrosion, first the test solution (1L of 0.5M H_2SO_4 + 0.01M KSCN + distilled water) [5] has to be prepared freshly under a ventilated hood. Firstly, the specimen was subjected to open circuit condition (during which cell was off) for 2 min so that E_{corr} (open circuit potential) develops. Then sample is polarized and voltage is scanned anodically from E_{corr} to + 0.3 V vs SCE (reference) with the regarding scan rate (i.e., 1.667 mv/sec), after which it is reversed back at the same scan rate to $E_{corr.}$ [4] The polarization curves forms were then

examined to determine peak current. %DOS is then calculated from Ir:Ia ratio.

2.5 Oxalic etch test

The test sample was connected to the positive terminal of the DC Power and a cylindrical piece of stainless steel is made as cathode (connected to negative terminal). The electrolyte is a solution of 10gram oxalic acid ($H_2C_2O_4.2H_2O$) crystals dissolved in 100ml water. The samples were etched at a current density of 1 Amp/cm^2 for 1.5 min according to ASTM A262. The etched surfaces were examined under metallurgical microscope at 400X.

3 RESULTS AND DISCUSSION

3.1 EPR test results

The samples were polarized and the voltage was scanned anodically from E_{corr} vs SCE (reference electrode) with the scan rate of 1.667 mv/sec. Later on, it was reversed back at the same scan rate to E_{corr}. The degree of sensitization is determined by eqn(1):

$$DOS = \frac{Ir}{Ia} x\ 100 \qquad (1)$$

Table 2 shows the DLEPR results of the AISI 304 samples immersed in test solution at different tempering temperatures. It is evident from this table that the corrosion rates of 304 ASS samples are increasing as temperature increases as cited by Ayo S. Afolabi et al. [7]. This trend of results is also similar to the Oxalic etch test results discussed. It can also be seen from the table 2 that reactivation current (Ir) values to move to more positive values as tempering temperature increases.

Table 2. DLEPR test results for AISI 304 type stainless steel.

S. No.	TEMPERA-TURES (in ^oC)	TIME (mins)	Ia mA	Ir mA	%DOS (Ir/Ia) x100
1	Solution annealed	40	148	2.1	1.46
2	600^{o}C	40	209	5.0	2.4
3	675^{o}C	40	171	23	13.8
4	750^{o}C	40	211	39	18.8
5	800^{o}C	40	189	39	20.6

This indicates that dissolution of the metal at grain boundaries takes place with increase in tempering temperatures, as shown in Figure 2.

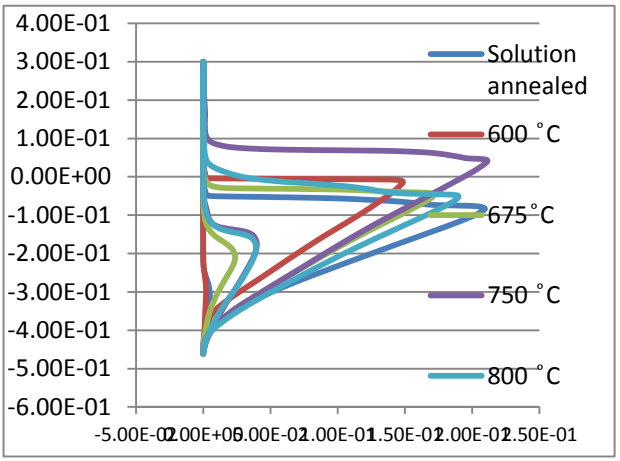

Figure 2: DLEPR curves for all the samples.

3.2 Oxalic acid etch test results

All micrographs obtained after Oxalic acid etch test show that there are several black spots present on the surface of samples. These black spots indicate the existence of pits on the samples. The reason behind the pitting of samples is that during the electrochemical test, KSCN was used as an activator. It is used for breaking of passivation layer and to corrode the samples. Drawback of using KSCN is that it introduces pitting corrosion in the sample which permanently remains on the samples. After oxalic etching, these pits are clearly visible.

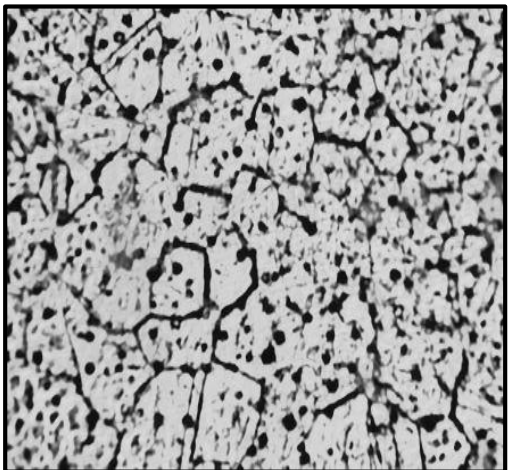

Figure 3. Micrograph of AISI 304 sample, Tempered at 800^{o}C at 400x.

4 CONCLUSION

In this study, the effect of different tempering temperatures on susceptibility to intergranular corrosion of AISI 304 stainless steel has been examined. Based on the results obtained, following conclusion can be made.

The DLEPR test results showed that the degree of sensitization increases with increase in tempering temperature. This increase in sensitization is due to

higher mobility of Carbon as a result of increasing temperature. Sensitization occurs due to the precipitation of Carbides (particularly Chromium carbide) along the grain boundaries.

This linear behavior of Carbide precipitation has also been observed with the help of Optical microscope. Samples sensitized at several temperatures were observed on microscope after etching them in Oxalic Acid. These micrographs confirmed that, in this temperature range, DOS for AISI 304 Stainless steel follow linear behavior.

ACKNOWLEDGEMENTS

Authors would like to thank every individual who provided his assistance during any phase of this research and particularly to Mr. Zeeshan Hassan who as a Technician at Materials Deterioration lab, Department of Metallurgical Engineering, provided his assistance on numerous occasions.

REFERENCES

[1] N. Parvathavarthini: Corrosion of Austenitic Stainless Steels: Mechanism, Mitigation and Monitoring, ed. by H. S. Khatak and Baldev Raj, Woodhead Publishing House, Cambridge, England, (2002), 287.

[2] Aydogdu, G.H., 2004. Determination of Susceptibility to Intergranular Corrosion in AISI 304l and 316l Type Stainless Steels, *Journal of Corrosion science 48 (2006) 3565–3583.*

[3] ASTM G108: Standard Test Method for Electrochemical Reactivation (EPR) for Detecting Sensitization of AISI Type 304 and 304L Stainless Steels.

[4] Michael F. Mc Guire, Stainless steel for design engineers, American Society for Metals, Metals Park, OH,2008.p.76-77.

[5] Schluter, J.M., Chivinsky, J.A., 1985. ASTM A 262, in: Laboratory Corrosion Tests and Standards: A Symposium by ASTM Committee G-1 on Corrosion of Metals, Babel Harbor, FL 14-16 Nov. 1993. p. 455.

[6] Leiva-García, R., Muñoz-Portero, M.J., García-Antón, J., 2011. In-Situ Study of Single and Double Loop Reactivation Methods during the Characterization of the Degree of Sensitization of a Duplex Stainless Steel (UNS 1.4462) Using a Minicell and a Confocal Microscope. *Int. J. Electrochem. Sci 6, 830–846.*

[7] Afolabi, A.S., Potgieter, J.H., Abdulkareem, A.S., Fungura, N., 2011. Effect of tempering temperature and time on the corrosion behavior of 304 and 316 austenitic stainless steels in oxalic acid. *International Science Index Vol:5, No:7, 2011 waset.org/Publication/518.*

SILVER NANOPARTICLES - SYNTHESIS, CHARACTERISATION AND THEIR APPLICATION AS POLYMER REINFORCEMENT

Humair Ahmed[1*], S.M Mohsin[2] and M. Faizan[3]
[1,2,3] Materials Engineering Department, NED University of Engineering & Technology, Karachi, Pakistan

[*]Corresponding author. Tel.: +92 345-3116249
E-mail address: *ahumair@hotmail.com* (Humair Ahmed)

Abstract

In this study, Chemical reduction route of synthesis of Silver Nanoparticles by Glucose was used. The reaction proceeded with the solution turning colorless to brown and showed UV–visible spectra characteristic of silver nanoparticles (λmax= 420 nm). Scanning electron microscope (SEM) observations showed the presence of silver nanosized crystallites after short incubation period. When the reaction mixture was left for longer period, very few micro-aggregates were also observed. Synthesised Silver Nanoparticles were added in Polyester Resin as Nano fillers and the mechanical properties of modified and unmodified resins were evaluated. Modification by silver nanoparticles, found to have a direct relation with the mechanical properties of resin as an increase in both shore hardness and tensile strength was observed.

Keywords: Silver Nanoparticles, Nobel metals, Silver, Nanotechnology, Modified resin, Polyester.

1 INTRODUCTION

Noble metal nanoparticles such as Gold (Ag) and Silver (Au) nanoparticles have always been a basis of great curiosity due to their novel electrical, optical, physical, chemical and magnetic properties and for their attractive biophysical, biochemical, and biotechnological applications. Apart from excellent chemical stability, Gold and silver nanoparticles also exhibit Raman scattering (SERS) in the range of visible spectrum. The resonance frequencies are typically the function of particle shape and size as well as of optical properties of the material [1]. Nobel metal Silver, for instance, has been used as a disinfectant; while its pronounced role as a catalyst cannot be challenged [1,2]. On the other side, Gold nanoparticles have developed considerable attention in last few years for potential applications in medicine and pharmacy as their electronic, chemical, optical properties are depended upon the size of the particle, due to this scientists are hopeful for targeted cancer treatments such as radiotherapy and thermal therapy by using gold nanoparticles[3] Chemical methods are usually preferred to synthesis of Silver nanoparticles (Ag NPs) and among them chemical reduction is an appropriate choice of making stable, colloidal solution of silver in water or organic solvents. However, there is no restriction in synthesising Ag NPs using other chemical methods [4]. Polyols, $NaBH_4$, N_2H_4, sodium citrate etc are some of the typical reducing agents [5]. For higher reaction rates, elevated temperature methods of synthesising Ag Nps are mostly used, however there also some methods ot synthesize them at room temperature. Sodium dodecyl sulphate (SDS), polyvinyl pyrrolidone (pvp), tri-sodium citrate is some capping agents to prevent agglomeration of Ag Nps. [6]. Typical Thermal methods include a reduction of Ag+ by dextrose [5], hydrazine [7] and/or formaldehyde sulphoxylate (SFS) [8] as a reduction agent.

Size and morphology of Silver Nanoparticles are a function of temperature of reaction. Some researchers were able to synthesise both disk and globular morphology of Ag Nps, using silver-mirror reaction [9]. Some researchers focused on the large scale preparation of Silver Nanopowder, for example, Khanna et al, were able to device a large scale process of preparation of silver nanoparticle of size less than 50 nm by using tri-sodium citrate which was used as initial surfactant-cum-reducing agent followed by sodium formaldehyde sulphoxylate (SFS), a secondary reducing agent.

The sole purpose of this study was to synthesise silver nanoparticles using optimum parameters and conditions (structured synthesis of Silver Nanoparticles). Considering the wide application range of silver nanoparticles, the synthesised silver nanoparticles were then employed in modification of unsaturated Polyester resin. The effects of this modification were verified through mechanical testing.

2 EXPERIMENTAL WORK

2.1 Materials and Methods

AgNO3 (99%, Merck), Glucose and Diethyl Amine were used without further purification. All the experimental work is carried out in deionised water. Sterilised syringes were used for handling

colloidal solutions. The labware and glassware used in the experiments were washed using deionised water, rinsed thoroughly with Acetone.

2.1.1 Preparation of Silver Nanoparticles:

Initially, aqueous solutions of Silver Nitrate and Glucose were prepared with predefined molarities of 3mM and 5mM respectively. These solutions were mixed and stirred using Magnetic Stirrer for 2 hours to obtain a homogeneous solution. After which an aqueous solution of Diethyl Amine (DEA) of a pre-defined molarity of 115mM was added to it and stirred vigorously. This addition triggered the reduction process and the color of the solution changed to brown and lastly green colored precipitates were obtained. Decantation and washing was then carried out several times with deionised water, the precipitates then collected were dried in air at 60^{o}C.

The governing Equations are:

$$NH(C_2H_5)_2(DEA) + H_2O \rightarrow NH_2(C_2H_5)_2 + OH^-$$

$$R\text{-}CHO + 2OH^- \rightarrow R\text{-}COOH + H_2O + 2e^-$$

$$Ag^+ + e^- \rightarrow Ag + 2NH(C_2H_5)_2$$

The final dried powder (green colored) was taken to further characterisation. Schematic of process is presented in **Figure 1**.

2.1.2 Modification of Polyester Resin:

Unsaturated Polyester Resin (Industrial Grade), Methyl Ethyl Ketone Peroxide (MEKP), hardener of Polyester, Cobalt Octoate (2%) and Synthesised Silver Nanoparticles were used without further purification. Sterilised syringes were used for handling hardener and Cobalt Octoate. The labware and glassware used in the experiments were washed using Deionised water, rinsed thoroughly with Acetone. A Glass mould (203.2 x 20.32 mm) was initially prepared, which was used to cast the rectangular tensile test specimens. A common practice of cleaning mould using acetone and then applying a fine layer of wax was employed when needed. Polyester resin (15 ml) was taken in a graduated cup, MEKP (1% by volume of resin) resin was added, Manual mixing was carried out for at least 3 minutes followed by addition and mixing of Cobalt Octoate (4-6 drops). The resin was then poured into the mould and left for 12 hours in an ambient environment. Similarly another experiment was carried out in which 1% AgNPs Solution was added with Cobalt Octoate.

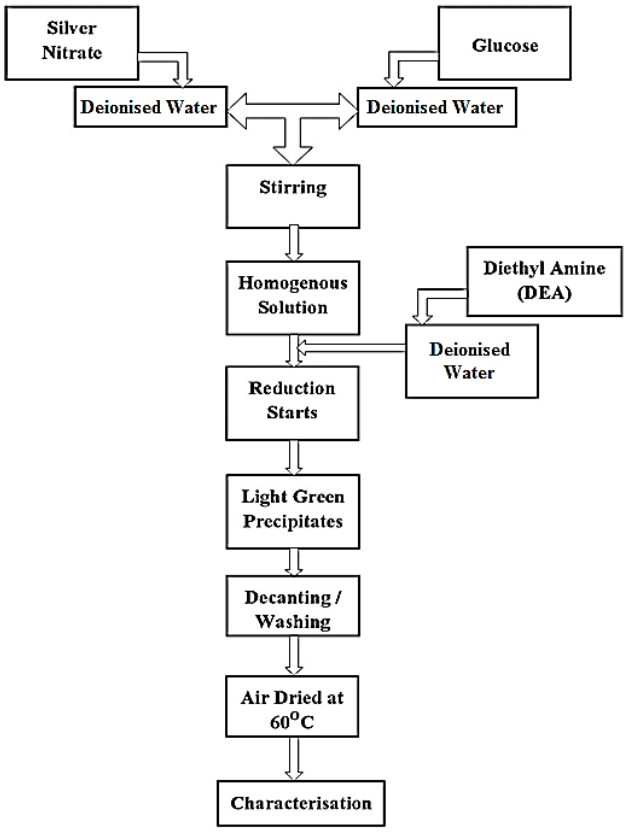

Figure 1. Process layout for Synthesis of Silver Nanoparticles

3 CHARACTERISATION

3.1 Silver Nanoparticles:

The dried powder was characterised using number of techniques. The powder was tested for initially, for its optical absorption property using a Spectrum Lab, UV–Visible spectrometer, to confirm the formation of Nano silver. For this test, Powder was dispersed using stirring to obtain a colloidal solution, which was further subjected to sonication. The powder samples were subjected to X-ray diffraction (XRD) studies on a Philips, PANALYTICAL XRD to understand their chemistry and structure. Morphological studies along with size and shape of particles were carried out using a Quanta 200 Scanning Electron Microscope equipped with EDAX.

3.2 Modified Polyester:

After curing, Mechanical characterisation was carried out. Tensile testing was done on Super L60, Tinius Olsen Tensile testing Machine, while Shore hardness testing machine was employed for hardness testing (Scale D).

4 RESULTS AND DISCUSSION

4.1 Silver Nanoparticles

4.1.1 Visual observations and UV–visible spectroscopy:

When synthesis of Silver Nanoparticles was carried out using Glucose and Diethyl Amine (DEA), the reaction was actually dependent upon the mixing of Precursors, after incorporation of all precursors the solution remained unchanged i.e. no colour variation was observed, however as the vigorous mixing proceeded, the colour started to change from colourless to yellow then light brown, dark brown finally green colour solution was obtained with silver patches in the beaker which are characteristic of presence of Silver in the solution. Consider **figure 2**.

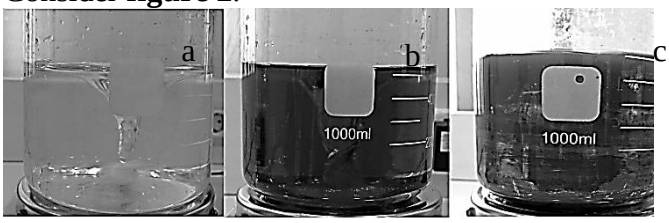

Figure 2 a, b, c. Mixing of Precursors (a) Colorless Solution (b) Reduction Started as color started to change (c) Silver patches started to appear on walls of beaker

Control silver nitrate solutions (without Glucose) can never develop changes of brown color nor can they display the spectrum peak. These results indicated that abiotic reduction of silver nitrate did not occur under the reaction conditions that were used. The Viscosity of DEA was (on Avg.) 350 cps. The UV–visible spectra of reaction mixture, depicted in **Figure 3**, has surface plasmon peak for silver nanoparticles, a smooth and narrow absorption band in between 410 - 418 nm was observed which is typical of monodispersed (spherical) nanoparticles. The exact wavelength at which there is the maximum absorbance depends on several system features, for example it depends on the size, shape and distribution of nanoparticles, and it also depends on the dielectric behavior of the nanoparticles in its surrounding medium.

The colloidal solution forms were stable up to longer period of time and are virtually unaffected by minor temperature variations, however it is recommended to use Proper Dispersant and Surfactant, when synthesising Silver Nanoparticles.

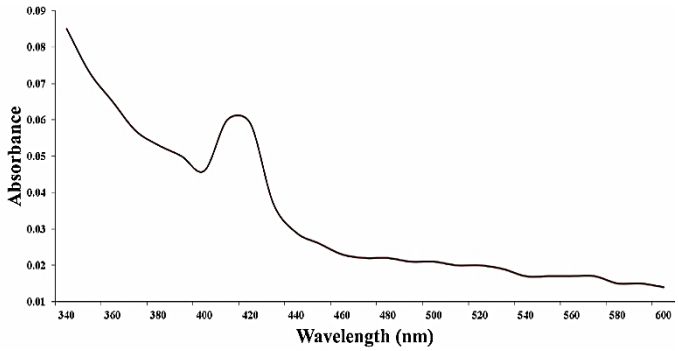

Figure 3. UV–visible spectra of Silver Nanoparticles having a smooth and narrow absorption band in between 410 - 418 nm

4.1.2 XRD studies:

The crystalline nature of silver nanoparticles was confirmed from XRD analysis. Figure. 4 shows the XRD pattern of Ag nanoparticles obtained. The diffraction peaks appeared at 38.3◦, 44.5◦ and 64.6◦ correspond to the (1 1 1), (2 0 0) and (2 2 0) facets of the face centered cubic crystal structure, respectively.

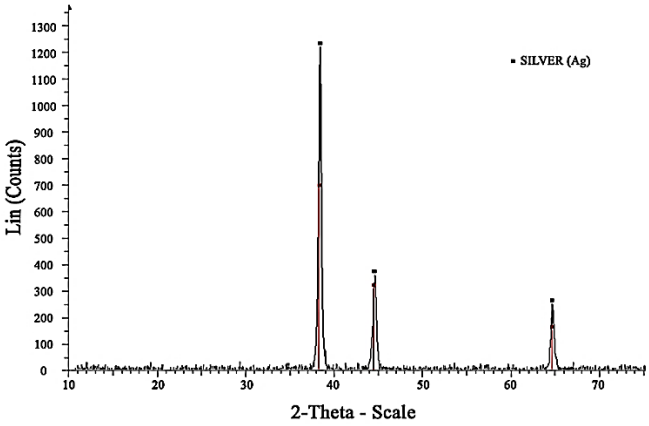

Figure 4. XRD Pattern of Silver Nanoparticles synthesised using Chemical Reduction route

From this study, considering the peak at degrees, average particle size has been estimated by using Debye-Scherrer formula

$$D = \frac{0.9\,\lambda}{\beta \cos\theta}$$

[10]

Where ‘λ’ is wave length of X-Ray (0.1541 nm), ‘β’ is FWHM (full width at half maximum), ‘θ’ is the diffraction angle and ‘D’ is particle diameter size.

The particles size calculated from XRD Pattern by using the Scherrer’s equation predicts the nanopowder may have the uniformed size less than 30nm.

4.1.3 Scanning Electron Microscopic Studies:

A scanning electron microscope was used to analyse the structure of the nanoparticles that were formed. **Representative** SEM micrographs are

shown in **Figure. 5** a, b and c, respectively. From the **figure 5** a, it was evident that the silver nanoparticles coalesced to nano-clusters. When reaction mixtures were incubated for longer periods, some nanoparticles aggregated into micro particles.

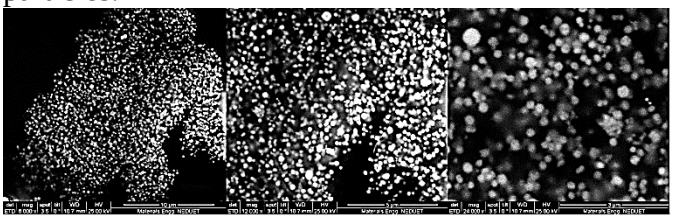

Figure 5 a, b, c. Scanning Electron Microscopy of Silver Nanoparticles (a) Cluster of Nanoparticles (b, c) Silver Nanoparticles with different particles sizes.

It was noted that leaving solution for longer period of time will settle down majority of Particles, leaving a homogenous colloidal solution of Silver Nanoparticles, Moreover in all experiments any sort of Surfactant was not used, so clustering of Nanoparticles was predominant in all experiments. SEM micrograph depicted the presence of Silver Nanoparticles were of spherical in shape.

4.2 Effect of Silver Nanoparticles as Nano Fillers

4.2.1 Visual observations:

The resin in its mixing stages with 1% AgNPs, changes its colour to green, however after curing the resin had lost considerable amount of its transparency. Silver nanoparticles were homogenously dispersed in the resin. Beside the transparency, loss of toughness was also evident as depicted in figure 6a, i.e. a fractured sample of an unmodified resin shows a shear fracture morphology which proves the presence of ductility in unmodified resin. However as in figure 6b, the flat shiny fractured surface proves complete brittle fracture in modified resin.

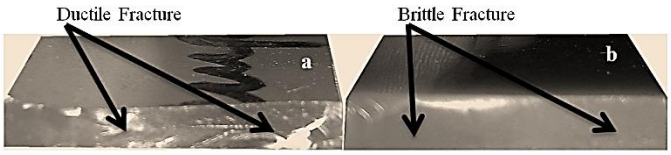

Figure 6. Visual observation of fractured sample a) Unmodified Resin b) Modified resin

4.2.2 Tensile and Hardness Studies:

Effects of AgNPs on the Polyester tensile properties are shown in **figure 7**. Modification by 1% showed a remarkable, approx. 39%, increase in the tensile strength of Polyester resin.

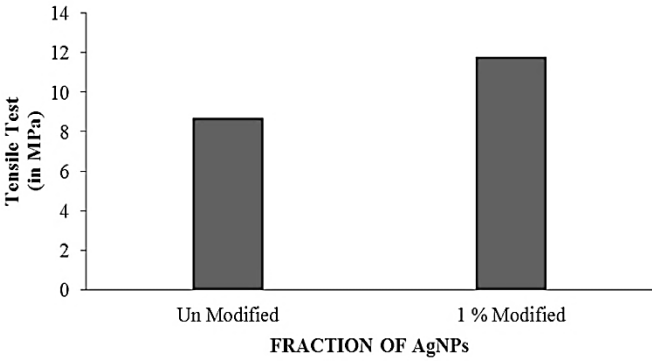

Figure 7. Comparison of Tensile properties of modified resin with unmodified

In general, it was observed that inclusion of a small percentage of submicron and nano particles (around 1%) improves all tensile properties of the cured Polyester resin system under investigation. Literature review revealed that the nano particles (under 10 nm) are used as toughening agent in the Polyester resin, its ultimate tensile strength (UTS) can be improved, more than what could have been achieved by using submicron particles (250 nm). The crystallinity of Polymer is associated with the folding of Molecular chains, however in this case it must be established that the presence of Nano clusters of Silver had forced molecular chains of Polyester to come close to each other and align in a pattern. This behaviour of Polymer was of prime importance when synthesising a composite having reinforcement other than particles. The resultant composite may have much improved Tensile Strength and required Toughness as well.

Modification considerable increased the hardness of the resin, which is certainly associated with the presence of crystallinity and the rigid network created by Nanoparticles. The comparison of hardness values is presented in **figure 8**, which shows more than 100% increment in the hardness value of Polyester resin.

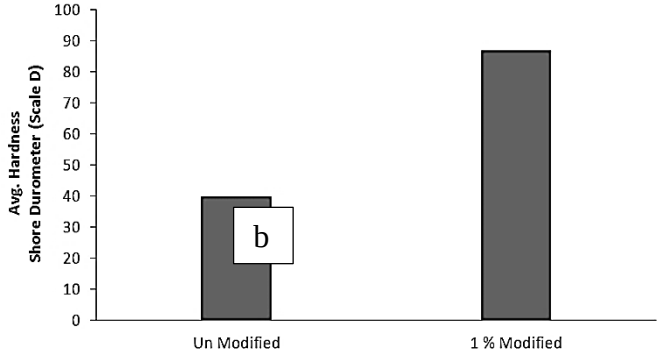

Figure 8. Comparison of Hardness of modified resin with unmodified one.

5 CONCLUSIONS

Following conclusion can be drawn from the result of this study:

1. Test results showed that the one of the easiest method of synthesis of Silver Nitrate is Reduction by using DEA and Glucose. The colloidal solution forms are stable up to longer period of time and are virtually unaffected by minor temperature variations.
2. XRD results confirmed the formation of Silver nanoparticles, moreover XRD pattern was utilised to find the particle size, which is found to be under 30nm.
3. SEM micrograph depicted the presence of Silver Nanoparticles were of spherical in shape.
4. As Nano fillers, AgNPs were proven to be handy in increasing strength by inducing crystallinity. Additions of 1% showed a remarkable increase in Strength (approx. 39%).
5. Hardness was also increased as Nano clusters of Silver had forced molecular chains of Polyester to come close to each other and align in a pattern.

ACKNOWLEDGEMENT

The support rendered by the Prof. Dr. Tufail, Dean Chemical and Process Engineering, Prof. Dr. Ashraf Ali, NED University, Engr. Usman Niaz for Scanning Electron Microscopy, faculty and Staff of Department of Materials Engineering, NED University of Engineering and Technology, throughout the experimentation is gratefully acknowledged. The author would also like to thank Pakistan Council of Scientific and Industrial Research, for their support during characterisation of samples.

REFERENCES

[1] Khalaf Ali Abdul Rahman, Raouf Dayah N. "*Preparation of Silver Nanoparticles by Pulsed Laser Ablation in Liquid Medium*" Engg. & Tech. Journal. **29** (2011) 3058-3066.

[2] Chargot M.S., Gruszecka A., A. Cytawa Smolira, J., MichalaL. k "*Mass- spectrometric investigations of the synthesis of silver nanoparticles via electrolysis*" Vacuum. **82** (2008) 1088–1093

[3] Kumar U., Nayak P.L. "*Biomedical Applications of Gold Nanoparticles: Opportunity and Challenges*" World Journal of Nano Science & Technology.**1(2)** (2012) 10–25

[4] El-Sheikh M. A., El-Rafie S. M., Abdel-Halim E. S., El-Rafie M. H. "*Green Synthesis of Hydroxyethyl Cellulose-Stabilised Silver Nanoparticles*" Journal of Polymers. **2013** (2013) 1–11

[5] Reza Ghorbani H., Akbar Safekordi A., Attar H., and Rezayat Sorkhabadi S. M. "*Biological and Non-biological Methods for Silver Nanoparticles Synthesis*" Chem. Biochem. Eng. Q. **25 (3)** (2011) 317–326

[6] Van Dong Pham, Hoang Ha Chu, Tran Binh Le and Kasbohm Jörn "*Chemical synthesis and antibacterial activity of novel-shaped silver nanoparticles*" International Nano Letters (2012) 2-9

[7] Guzmán M. G., Dille J., Godet S. "*Synthesis of silver nanoparticles by chemical reduction method and their antibacterial activity*" International Journal of Chemical and Biological Engineering **2:3**(2009) 104-111

[8] Khanna P. K., Singh Narendra, Kulkarni Deepti, Deshmukh S., Charan Shobhit, and P. V. Adhyapak. "*Water based simple synthesis of re-dispersible silver nano-particles*" Materials Letters **61(16)** (2007) 3366-3370

[9] Sarkar, Sougata et al. "Facile Synthesis Of Silver Nano Particles With Highly Efficient Anti-Microbial Property". Polyhedron 26.15 (2007): 4419-4426.

[10] Theivasanthi T. and Alagar M.. "Nano Biomedicine and Engineering Electrolytic synthesis and characterization of silver nanopowder" Nano Biomedicine and Engineering 01 (2012):58-65.

SYNTHESIS OF ALUMINA - ALUMINUM TITANATE NANO COMPOSITE BY REACTION SINTERING AND ITS CHARACTERISATION

S. M. Mohsin Jafri[1,*] M. Faizan[2] and Humair A. Siddiqui[3]
[1,2,3] Materials Engineering Department, NED University of Engineering & Technology, Karachi, Pakistan

[*]Corresponding author. Tel.: +92-346-2670596;
E-mail address: m.jafri0607@gmail.com

Abstract

This paper presents the synthesis of Alumina-Aluminium Titanate nano composite by reaction sintering and its characterisation. Alumina – Aluminium Titanate nano composite has a very good thermal stability and a very low thermal expansion which makes it suitable for use at high temperature without appreciable change in its dimensions. The paper describes the formation of Alumina 20% Titania nano composite, which includes 99% pure Alumina & Titania. These materials were ball milled for forty hours, with ethanol as dispersant in high energy ball mill. 2% Poly Vinyl Acetate had been added for binding purpose. Mixing of binder was done for 10 hours in Four Jar Mixer. Afterwards samples were compacted at different pressures in uniaxial press. Reaction sintering was done in Muffle furnace at 1350 °C and the samples were cooled in air. The tablets were analysed using Optical Microscopy for surface analysis, Scanning Electron Microscopy for phase interaction and grain boundary study with in the composite. X-Ray Diffraction studies were done for phase analysis. Hardness of the samples was taken on Micro Vickers Hardness Tester. Further characterisation includes the porosity analysis of the samples.

Keywords: Reaction sintering, Optical Microscopy, Scanning Electron Microscopy, Macro Vickers Hardness Tester, XRD.

1 INTRODUCTION

From the mechanical point of view, unlike to the brittle micro-grained ceramics, nanometer-grained ones are normally capable of putting up with important elongation before breaking at moderate temperatures (~0.5 Tm) [1]. The narrow grain size and the enormous amount of grain boundaries also result in unusual (thermo-) mechanical properties, e.g. super-plasticity and extreme hardness [2] . The high thermal shock resistance due to the negligible thermal expansion coefficient, additional to its low thermal conductivity and good chemical resistance makes the aluminum titanate (Al_2TiO_5) a suitable material for different technological applications [3,4,10]. Aluminum titanate exhibit two allotropic forms α and β, where β-AT is the stable phase [5]. Aluminum titanate presents two major problems: the thermodynamics instability of the Al_2TiO_5 below 1280 °C and its poor mechanical resistance related to an extensive micro-cracking which is, in turn, responsible for the low thermal expansion. Cooling from the sintering temperature results in micro-cracking in AT [6,11]. Alumina based composite are prone to fracture due to its low fracture toughness. Improved flaw tolerance has been observed as a result of addition of AT due to induced residual stresses by virtue of thermal expansion mismatch between alumina and aluminium titanate [6]. In this work the concept of reaction sintering is utilised to form Alumina-Aluminium Titanate nano composite in order to enhance the properties of the composite.

2 EXPERIMENTAL

2.1 Materials and Methods

The materials used for the manufacturing of composite were Alumina (99.99 % pure Alpha Alumina, Merck). Titania that was utilised in the manufacturing of composite was (99.9 % pure, rutile and anatase, Merck).

2.2 Manufacturing of composite

The purity of powders was checked by X-Ray Diffraction analysis. The initial size of precursor was found to be 5000 nm of that of Alumina and 370nm of that of Titania using Laser Particle Size Analyser (BT 9300, Better size Instrument limited). Scanning Electron Microscope (FEI Quanta 200) was used to confirm the particle size of Alumina and Titania.

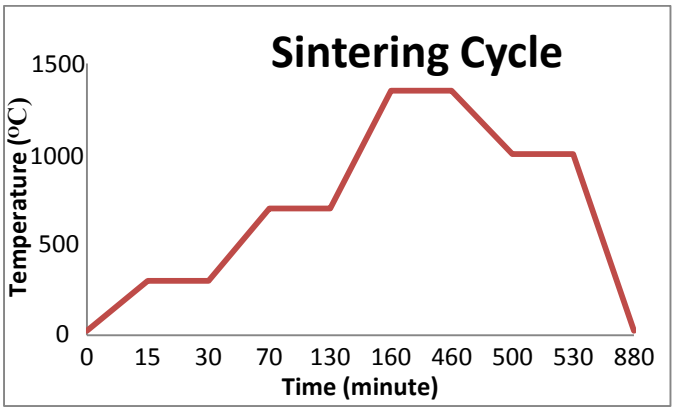

Figure 1. Sintering cycle for Al_2O_3-AT composite

The initial powders ratio was 80% Alumina and 20 % Titania, blended in a ball-mill uniformly, in Bench-Top Planetary Automatic ball mill (EQ-MJ-500) with Alumina jars and yittria stabilized Zirconia balls for 40 hours with fixed speed of 400rpm and the ball to powder ratio was 10:1. Methanol was used as a dispersant medium in the experiment. After ball milling, drying was done in Gravity Convection Drying Oven with Digital Temperature Controller (EQ-DHG-9015-220) for 10 hours. 2% Polyvinyl acetate (PVA) was used as a binding material for making ceramic tablets. Mixing of binder was done in Desk-Top Vertical Automatic Mixer with 4 x1 Liter Nylon Tank (MSK-SFM-2).

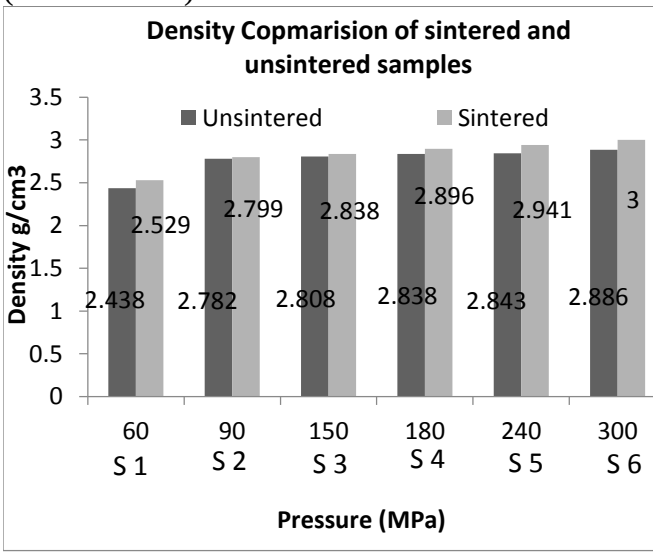

Figure 2. Density comparison between unsintered and sintered samples

Pressing of powder under various loads was done in Hydraulic Heavy Duty 100 Tons Manual Hydraulic Dry press. Drying was done in 12L Gravity Convection Drying Oven for 6 hours at 150 °C. Binder burn off for the samples was carried out at 700 °C for one hour in air atmosphere in the electrically fired furnace (Protherm PLF 1400). Before going to 700 °C, the samples were hold at 300 °C for 15 minutes in order to avoid the thermal shock. Sintering temperature was achieved without cooling the sample from binder burn off. Sintering temperature was 1350 °C Figure 1 shows sintering cycle.

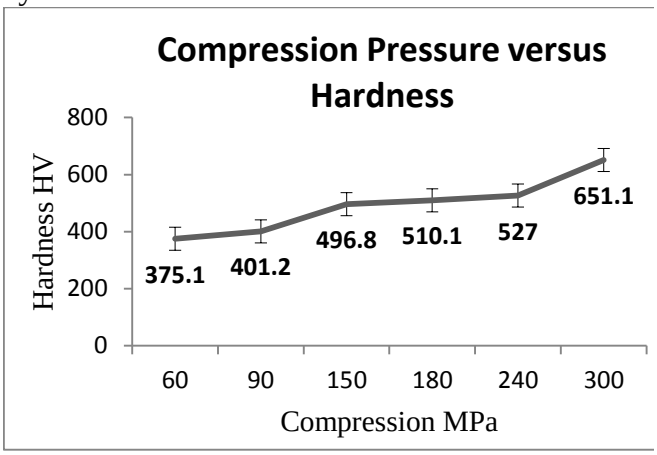

Figure 3. Compression pressure and harness relationship

Characterization of samples was performed by X-Ray Diffraction (Panalytical X'pert Pro MPD system). Microstructure of the samples was determined by Scanning Electron microscope (FEI Quanta 200) with EDX detector. Hardness of the samples was determined by Micro Vickers Hardness Tester (Wolpert 402 MVD), hardness was calculated using Eq.(1) according to American society of testing and Materials (ASTM) C 1327.

$$H = 1.854\frac{P}{d^2} \qquad (1)$$

Where H is the hardness of the material, P is the load and d is the length of diagonal impression of pyramid indenter. 200gf was applied when calculating harness of samples.

3 RESULTS AND DISCUSSION

Initial particle size was analysed using laser particle size analyser Figure 5 and Scanning electron microscope Figure 4. The initial particle size of Alumina was found to be 1000 nm. In order to reduce the particle size, the particles were ball milled in high energy ball mill. Laser particle size analyser was used to get the particle size distribution of alumina and Titania Figure 4.

XRD of initial precursor was performed in order to find phases present in the sample. The XRD analysis of particles shows a high amount of Rutile phase in the initial TiO_2 powder Figure 6. XRD of Alumina shows α-Alumina in excess The XRD pattern of Alumina is shown in the Figure 7, this was favorable for sintering. The XRD pattern of unsintered Alumina and Titania is shown in Figure 8. The XRD pattern confirms the presence of Titania and alumina in the mixture.

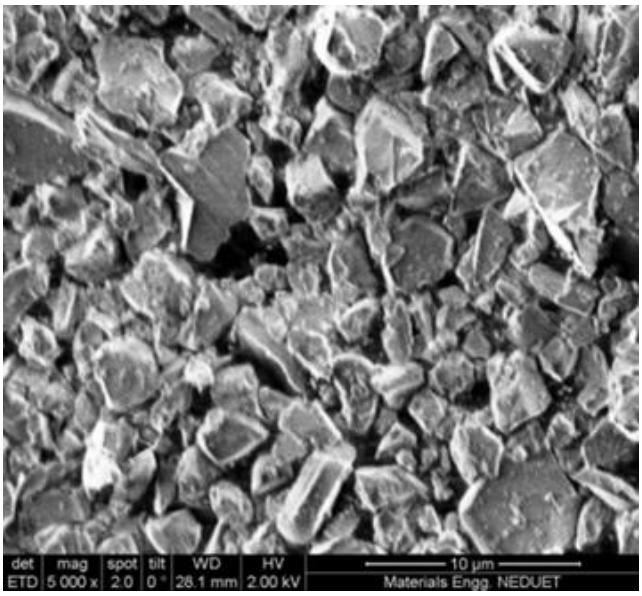

Figure 4. Particle size analysis of Alumina by Scanning Electron Microscope.

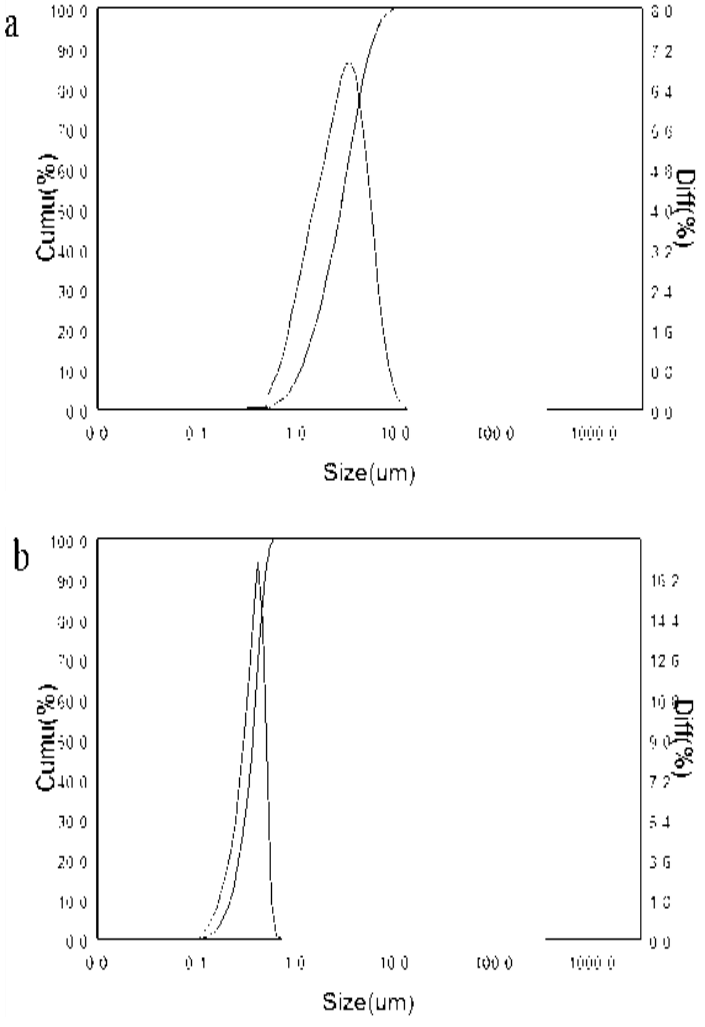

Figure 5. Initial particle size of (a) Alumina (b) Titania by Laser Particle Size Analyser

.

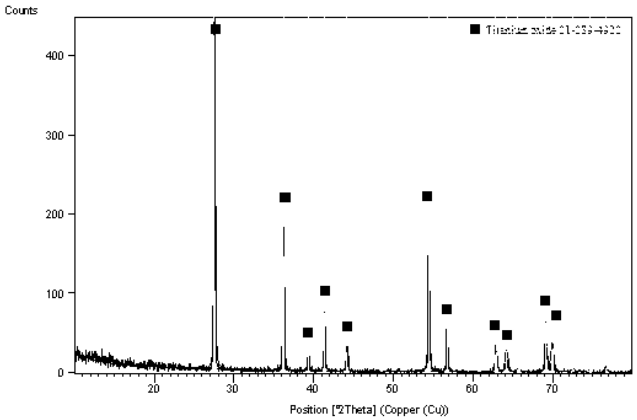

Figure 6. XRD of Titania. Figure shows Rutile phase in excess

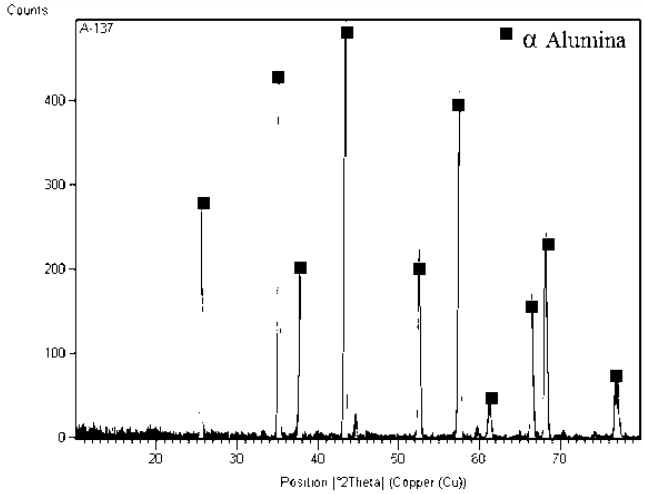

Figure 7. XRD results of α-Alumina

Powder compressibility is known to be as one of the most critical factors in getting the compact and dense ceramic materials. This directly affects the green density and the fired density. Compaction mechanism of brittle powder can be divided in three stages. (I) Sliding and rearrangement of particles, (II) Fragmentation of brittle solids, (III) elastic deformation of bulk compacted power [7,9]. The stage includes the compaction of the particles, sliding and rearrangement of the agglomerated particles. With the increase in the pressure the movement of the particles is constrained, this exerts force on particles which results in disintegration process and frictional loses [8]. Figure 9 reveals the XRD results of Alumina Aluminium Titanate composite after sintering that only two phase has been detected. These phases are of Alumina and AT. The XRD analysis of sintered samples reveals that there were very little peaks of Titania, giving indication that the most of the Titania is consumed in the conversion of Alumina into Aluminum Titanate.

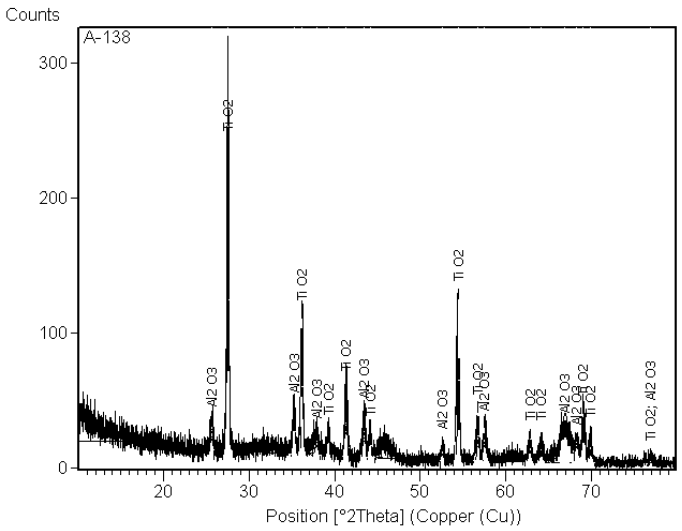

Figure 8. XRD analysis results of Alumina and Titania before sintering

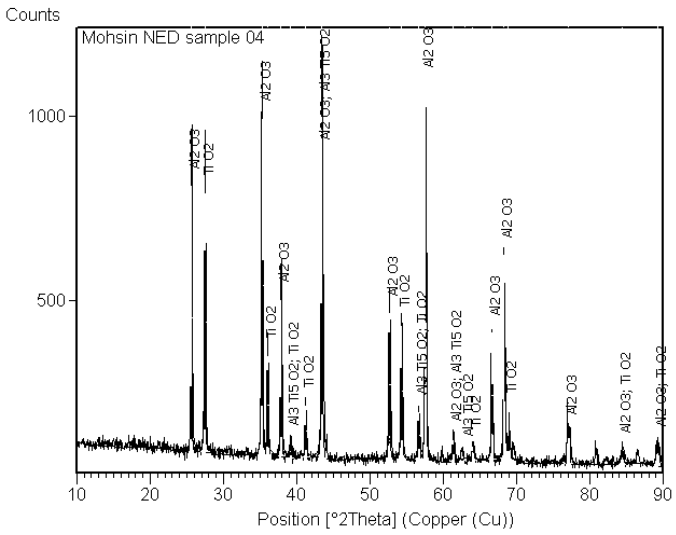

Figure 9. XRD Analysis of Alumina and AT composite after sintering

The XRD pattern was taken form 10° - 90° with special consideration on 25° - 35°. XRD analysis was taken for different pressure. Analysis of density was carried out for different compaction pressure. The density of increased from 2.529 g/cm3 to 3.00 g/cm3 i.e. 64 % to 76.92 % respectively [13]. Scanning Electron Microscope (SEM) analysis showed that the nano powders diffuse in each other upon sintering. Nano powders give higher contact points which eventually result decrease in the diffusion path. Hence sintering in this regard is increased due to the increase in coordination number. Mechanical properties were analysed using Micro Vickers Hardness testing machine . The hardness test showed that the same trend as observed between compaction pressure and the density of the composite. Same trend was repeated here which showed the increase in hardness with the increase in pressure. Scanning electron microscope images were taken on the polished samples in order to reveal the surface morphology and cracking present if any. The addition of AT in the Al_2O_3 is very beneficial. This addition results in the control of grain growth of both Aluminum Titanate and Alumina. The surface analysis reveals no micro cracking in the sample representing the absence of abnormal growth of AT in the sample. Further analysis of sample in Scanning Electron Microscope at higher magnification reveals that there was a proper interface in between Alumina and AT grains as mentioned by Lu Hong-xia in [12,14]. SEM analysis additionally reveals that the particles were homogenously dispersed in the matrix and grain boundaries Figure 10.

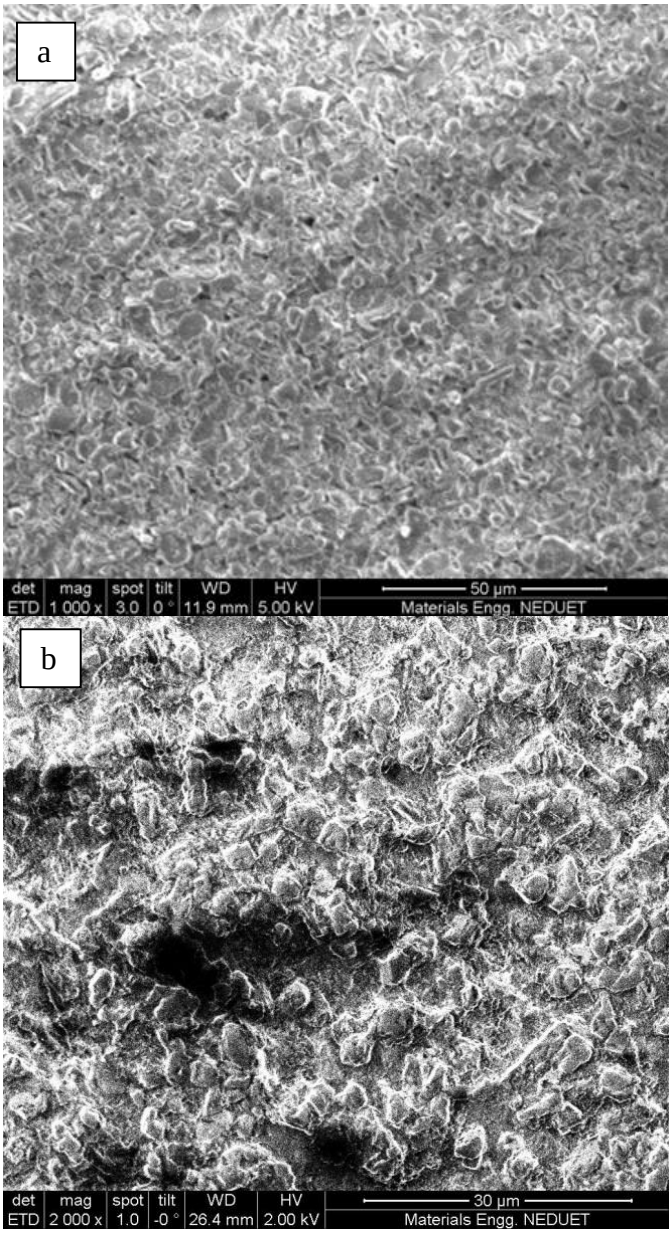

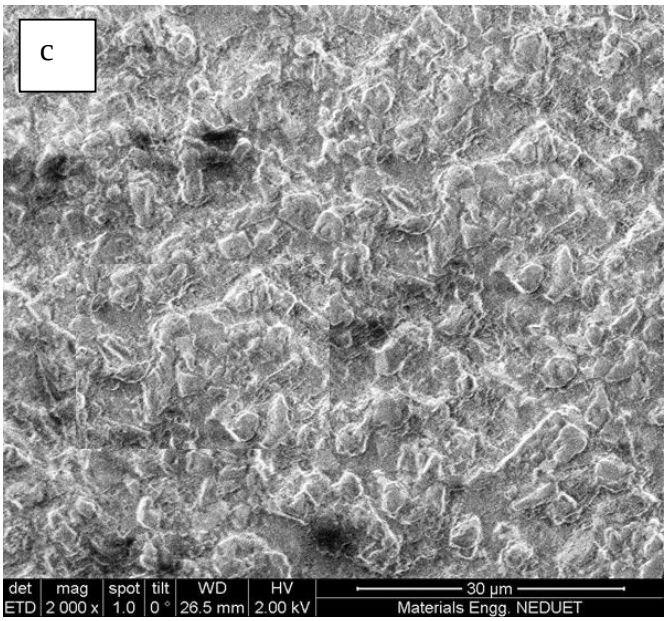

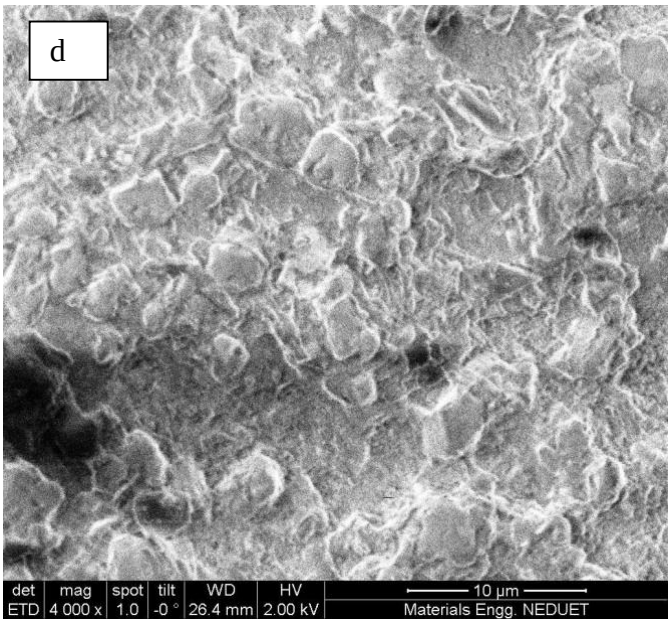

Figure 10: Scanning Electron Microscope images of the composite after sintering (a) shows the composite slightly less magnified, the micrograph shows grains interlocked in each other. (b) & (c) Images are at higher magnification which shows a higher magnification the phase boundaries and phase interaction (d) Image shows that samples are quite dense, homogenous and compact.

4 CONCLUSION

Al_2O_3-20 wt % AT composites was prepared by reaction sintering of Titania and Alumina at different compaction pressure. The relative density was 76.92 % which was observed. XRD pattern revealed the Al_2O_3 and AT phases present in the sample.

5 ACKNOWLEDGEMENTS

The authors wish to acknowledge the support provided for this research by Prof. Dr. M. Tufail Dean Chemical and Process Engineering, NED University, Prof. Dr. Ashraf Ali NED University and Engr Usman Niaz for Scanning Electron Microscope Facilities.

6 REFERENCES

[1] Mazaheri . Mehdi *, Zahedi A.M., Haghighatzadeh M. and Sadrnezhaad S.K. , "Sintering of titania nanoceramic: Densification and grain growth", *Ceramics International*, vol 35, 2009, pp 685–691.

[2] Vaben R. and Stover D., "Processing and properties of nanophase ceramics", *Journal of Materials Processing Technology*, vol 92-93, 1999, pp 77-84.

[3] Anderson Marc A., Gieselmann Mary J. and Xu Qunyin , "Effect of TiO_2 on initial sintering of Al_2O_3", *Journal of the American Ceramic Society*, Vol 53, Issue 3, 1970, pp 136–141.

[4] Lakshmanan Arunachalam Irene Barrios de Arenas (2012). *Reactive Sintering of Aluminum Titanate, Sintering of Ceramics – New Emerging Techniques*, (Ed.), ISBN: 978-953-51-0017-1,

[5] Prasadarao A.V., Selvaraj U., Komarneni S., Bhalla A.S. and Roy R., "Enhanced densification by seeding of sol–gel-derived aluminum titanate", *Journal of the American Ceramic Society*, Vol 75, 1992, pp 1529–1533.

[6] Padture N.P., Runyan J.L., Bennison S.J., Braun L.M. and Lawn B.R., "Model for toughness curves in two-phase ceramics, II: microstructural variables", *Journal of the American Ceramic Society* Vol 76, 1993, pp 2241–2247.

[7] Bowen P. and Carry C., "From powders to sintered pieces: forming, transformations and sintering of nanostructuredceramic oxides", *Powder Technology*, Vol 128, 2002, pp 248-255.

[8] GrootZevert W.F.M., Winnubst A.J.A., Theunissen G.S.A.M. and Burggraaf A.J., "Powder preparation and compaction behavior of fine grained YTZP", *Journal of Materials Science*, Vol 25, 1990, pp 3449 –3455.

[9] Buscagliaa V., Nannib P., Battilanaa G., Aliprandic G. and Carryd C., "Reaction sintering of aluminium titanate: II—Effect of different alumina powders", *Journal of the European Ceramic Society*, Vol 13, Issue 5, 1994, pp 419–426.

[10] Anderson Marc A., Gieselmann Mary J. and Xu Qunyin, "Effect of TiO_2 on initial sintering of Al_2O_3", *Journal of the American Ceramic Society*, Vol 53, Issue 3, 1970, pp 136–141.

[11] Miranzo P., Pena P., Moya J. S. and Aza S. De, "Multicomponent toughened ceramic materials

obtained by reaction sintering", *Journal of Materials Science,* Vol 20, Issue 8, 1985, pp 2702-2710).

[12] Lu Hong-xia, Hu Jie, Chen Chang-ping, Sun Hong-wei, Hu Xing and Yang De-lin, "Characterization of Al_2O_3–Al nano-composite powder prepared by a wet chemical method". *Ceramics International,* Vol 31, 2005, 481–485.

[13] Stanciu Lia, Groza Joanna R., Stoica Ligia and Plapcianu Carmen, "Influence of Powder Precursors on Reaction Sintering of Al_2TiO_5", *Scripta Materialia*, 2003.

[14] Wang Jenqdaw and Raj Rishi, " Estimate of the Activation Energies for Boundary Diffusion from Rate-Controlled Sintering of Pure Alumina, and Alumina Doped with Zirconia or Titania", *Journal of the American Ceramic Society*, Vol 73, Issue 5, 1990, pp 1172–1175.

DETERMINATION OF PITTING POTENTIALS OF PASSIVATING MATERIAL IN CHLORIDE ION CONTAINING ENVIRONMENT

Muhammad Faizan[1*],Humair Ahmed[2], S. M Mohsin Jafri[3]

[1,2,3] Department of Materials Engineering, NED University of Engineering & Technology
*Corresponding author. Tel.: +92-21-9261261 (E: 2653); fax: +92-21-99261255
E-mail address: mfaizan@neduet.edu.pk

Abstract

Corrosion causes a variety of problems, depending on the conditions under which engineering alloys applied. Stainless steels are generally very good corrosion resistant material and will perform satisfactorily in most environments. The electrochemical behaviour of passivating material has been studied in chloride containing environment in which they corroded locally. The Cyclic Polarization curves were obtained for passivating materials i.e. Stainless Steel in Chloride containing environments. The pitting potential, corrosion potential and passivating potential were analysed with respect to the chloride ion concentration. It is observed that in chloride containing environments the pitting starts at lower potentials as compared to the environments that contain less or no chloride ion contents. Results obtained establish the dynamic relationship and interaction between the chloride ion concentration and electrochemical potentials in the corrosion behaviour of the ferrous alloy at ambient temperature. It concludes that the higher the molar concentration of the electrolyte lower the potential required for Passivation and Pitting.

Keywords: Passivation Potential, Pitting Potential, Cyclic Polarization Curve

1 INTRODUCTION

Pitting is one of the most insidious and destructive forms of localized attack on engineering structures. Stainless steels, like other passivating metals and alloys, are prone to pitting in halide ion-containing electrolytes [1]. It is long known that pit potentials can be rapidly measured also by the galvanostatic anodic polarization method[2].Without any doubt, the most common electrochemical technique used for determining such pit potentials is the cyclic slow potentiodynamic anodic polarization test which forms the basis of the ASTM G-61 test method applicable to iron-, nickel-, and cobalt-based alloys for quality control and/or acceptance of materials [3].Corrosion causes a variety of problems, depending on the conditions under which engineering alloys applied. Steel corrosion is an electrochemical process, initiated by certain electrolytic conditions in the proximity of the steel member. Stainless steels are generally very corrosion resistant and will perform satisfactorily in most environments. The limit of corrosion resistance of a given stainless steel depends on its constituent elements when exposed to a corrosive environment; however under exposure in certain industrial conditions stainless steel corrodes in the form of localized attacks (pitting), due to inclusions or a breakdown of the passive film. Pit type corrosion is simple galvanic corrosion, occurring as the small active area is being attacked by the large passivated area. This difference in relative areas accelerates the corrosion, causing the pits to penetrate deeper. It is most aggressive in solutions containing chloride, bromide or hypochlorite ions; iodides and fluorides are much less harmful. However, in the presence of oxygen, all chlorides become dangerous. This form of corrosion is often more detrimental than general corrosion, due to local dissolution which can cause rapid penetration of the metal thickness. Austenitic S.S has good corrosion resistance due to the formation of passive film of chromium oxide. The film is stable, invisible, thin, durable, extremely adherent and self-repairing. Passivation reduces the anodic reaction involved in the corrosion process, but quite severe pitting corrosion can occur in acidic environments [4]. The polarization curves show a spontaneously passive material, meaning that a protective passive film is present on the metal surface at the different passivation potentials (E_{pp}). During upward scanning, breakdown occurs, and a stable pit starts growing at the pitting potential (E_{pitt}) in the transpassive region of the polarization curve, where the current increases sharply from the passive current level [5,6]. Meguid and Mahmoud [7] studied the effect of different sulphur containing anions added to chloride on pitting corrosion of 304SS, and found that 10−2 mol/L$Na_2S_2O_3$ or 0.1 mol/L NaCl strongly reduced the pitting induction time.

This study is related to the corrosion i.e. Pitting Corrosion of the passivating materials i.e. Stainless Steel in different molar concentration of chloride ions. By this study the passivation potential, pitting potential and corrosion potential of stainless steel in corrosive environment detected.

2 EXPERIMENTS

Commercially available Type 304 austenitic stainless steel was used for all experiments of average nominal composition; 0.08%C, 0.03%S, 1.33%Mn, 9.88%Ni, 2.44%Mo, 16.72% Cr. The material is in the shape of rectangular plate. The electrodes were prepared by mounting the metal in Epoxy, and dried the samples for one day. The sample was then grinded using series of grinding papers (180, 220, 800 and 1000 grits) on MOPAO 260 E Grinder Machine. Samples were polished using Benetec Polishing Machine to remove all kinds of grinding marks, washed with de-ionized water, rinsing with acetone before drying and stored in a desiccator. Figure 1: is the working electrode shows the soldering of copper wire onto the Stainless Steel sample surface, the soldered sample then cold mounted in epoxy. After mounting the sample, thermal conductivity of sample is carried out to check the continuity of electrical connection of the sample through digital multi meter. After the working electrodes were prepared, measurement of sample was conducted; sample area was measured by using Stereo Microscopy. Area determination is very important for the current density of the material. The sample of Stainless Steel is grinded and polished for XRF-analysis. After mounting we ground our samples through emery paper ranges 180, 220, 320, 400, 600, 800, 1000, 1200 mesh size for XRF analysis and for Cyclic Polarization. The prepared samples are then analysed in the Computerized Potentiostat G750-350 series. The corrosion cell contains of three electrodes (i) the working electrode (ii) the counter electrode and (iii) the reference electrode, here the working electrode is of Stainless Steel, the counter electrode is of Graphite and the Reference electrode is of Saturated calomel electrode and these three electrodes are immersed in the electrolyte i.e. HCl solution.

Micrograph analysis is carried out via Olympus GX51 for the determination of pit formation on the sample in chloride ion containing electrolyte.

3 RESULTS AND DISCUSSION

Figure 2: shows the variation of potential (E) with Current (I) for stainless steel 304 in dilute hydrochloric acid. The line AB represents the cathodic behaviour of the sample. Line BC is the active zone (anodic dissolution reaction). At potentials more positive than B, corrosion rate increases, and reaches a maximum at the passivation potential point C, which is often given the symbol, Ep. The transition from active dissolution occurs in the region C to D. A protective film begins to form and causes a sudden drop in corrosion current density. At D (pitting potential E_{pitt}), breakdown of the protective film begins. It is here that the likelihood of pitting is greatest, and consequently specimen failure.

Figure 3: is the polarization curve between current (I) Vs Potential (E). In this curve different points found, i.e. the corrosion potential (E_{corr}) is found to be -217.5 mV, passivation potential (E_p) is 856 mV & the pitting potential (E_{pitt}) is 7.141 mV. In figure 4: the corrosion potential (E_{corr}) is found to be -205.6 mV, passivation potential (E_p)is 808 mV & the pitting potential (E_{pitt}) is -10.87 mV. In figure 5: the corrosion potential (E_{corr}) is found to be -194 mV, passivation potential (E_p)is 760 mV & the pitting potential (E_{pitt}) is -84 mV. In figure 6: the corrosion potential (E_{corr}) is found to be -165 mV, passivation potential (E_p) is 689 mV & the pitting potential (E_{pitt}) is -145 mV. In figure 7: the corrosion potential (E_{corr}) is found to be -151.8 mV, passivation potential (E_p) is 600 mV & the pitting potential (E_{pitt}) is -161.8 mV.

Figure 8: shows that, as the molar concentration of the electrolyte increased the passivation potential decreases, that are as the solution concentration enhances the potential required to passivate the material decreases. Table 2: is between pitting potential and HCl concentration, the pitting potential measured here in mV and the concentration is in Molar strength. It is showing that as the molar strength is increasing the potential required to pit decreases. Table 1: is between the passivation potential and HCl concentration, showing that as we are increasing HCl strength the passivating potential decreases. From the figure 9: it is concluded that as the molar concentration of the electrolyte increased the pitting potential decreases, that is as the solution concentration enhances the potential required to pitting the material decreases.

4 MICROSCOPIC ANALYSIS

Figure 10: showing the micrographs of pitting behaviour of stainless steel. It is confirming that the pitting attack happening on the surface of Stainless Steel in chloride ion solution. Figure 10: is captured at 500X and 1000X. From the figure 10: it is

proving that at pitting potentials the pits are forming. Pits are forming due to the accumulation of positive charges in the form of Fe^{2+} then attract negatively charged chloride ions. The resulting ferrous chloride hydrolyses to produce insoluble ferrous hydroxide plus excess hydrogen and chloride ions, these ions accelerate the corrosion at the bottom of the pit as described by Loto [2].

5 FIGURES AND TABLES

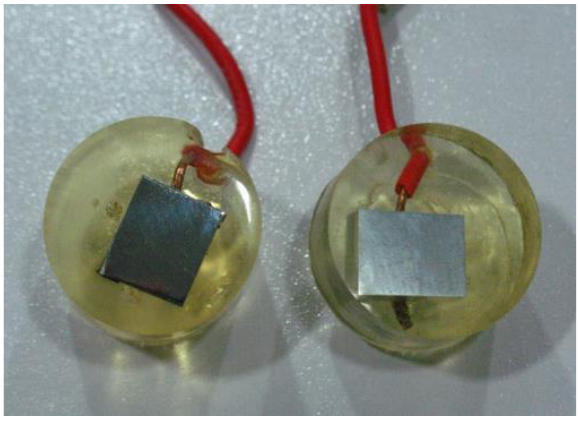

Figure 1. Mounted Sample for Potentiostat

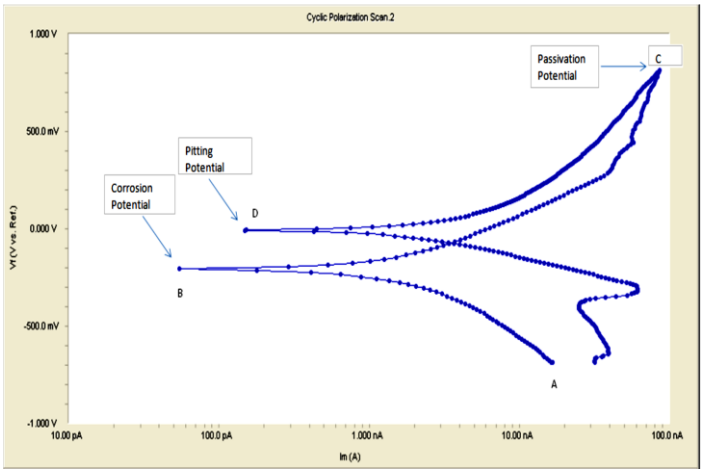

Figure 2. Cyclic Polarization curve (E vs I)

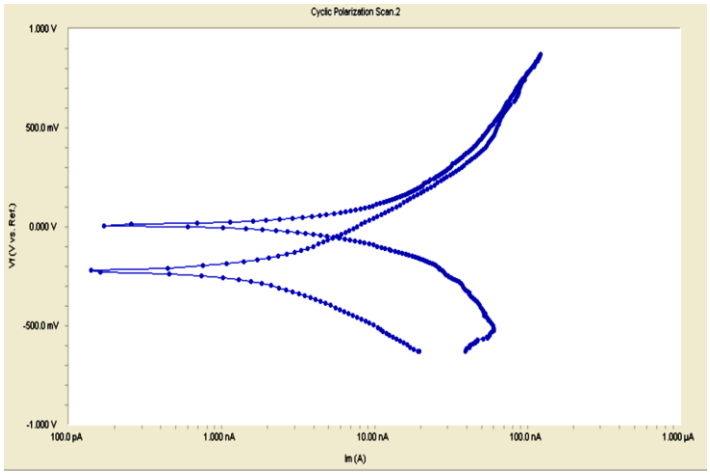

Figure 3. Cyclic Polarization Curve of Stainless Steel Sample 1, in 0M HCl

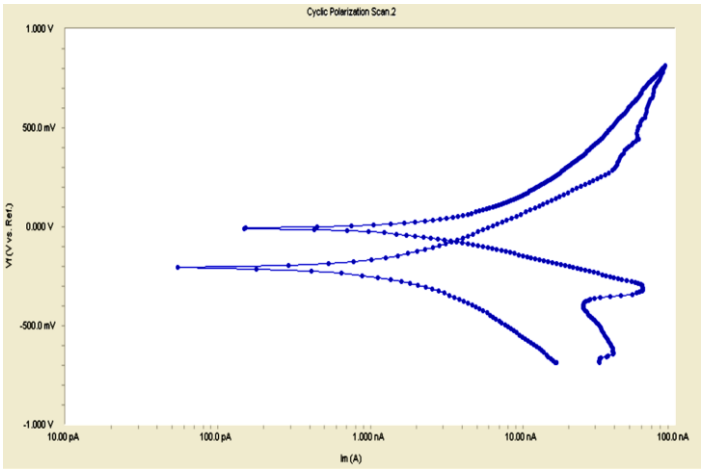

Figure 4. Cyclic Polarization Curve of Stainless Steel Sample 2, in 2M HCl

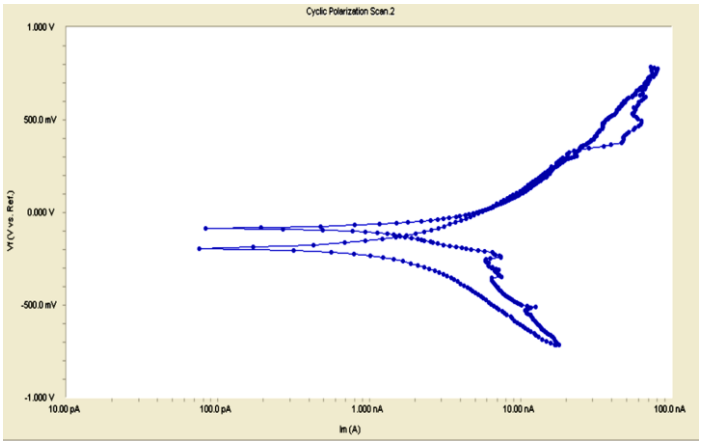

Figure 5. Cyclic Polarization Curve of Stainless Steel Sample 3, in 3M HCl

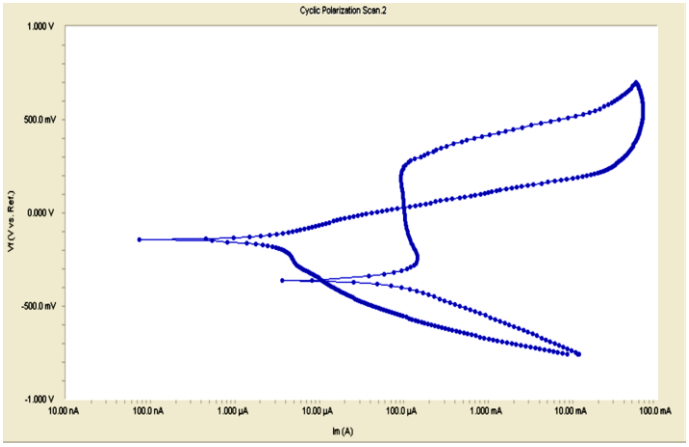

Figure 6. Cyclic Polarization Curve of Stainless Steel Sample 4, in 4M HCl

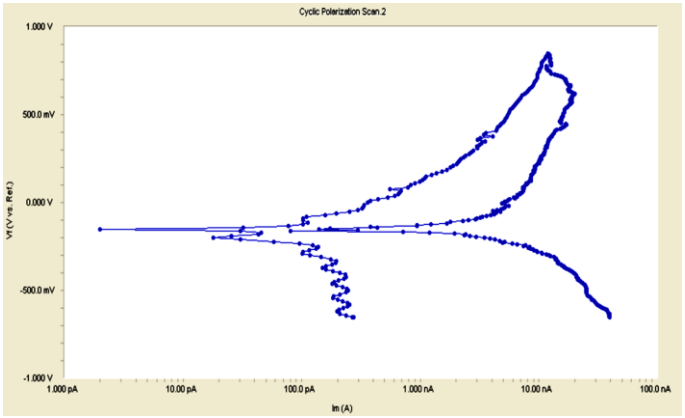

Figure 7. Cyclic Polarization Curve of Stainless Steel Sample 5, in 5M HCl

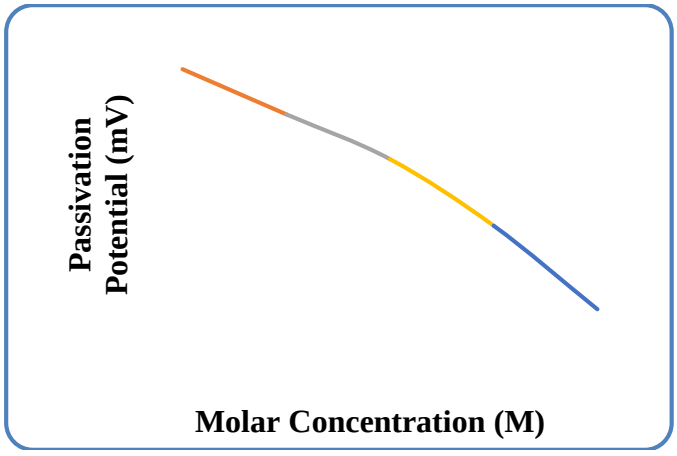

Figure 8. Variation of Passivation Potentials with Chlorine Concentrations

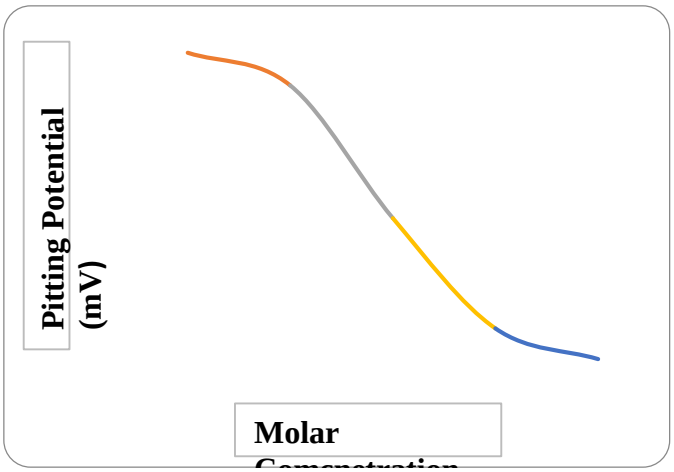

Figure 9. Variation of Pitting Potentials with Chloride Concentration

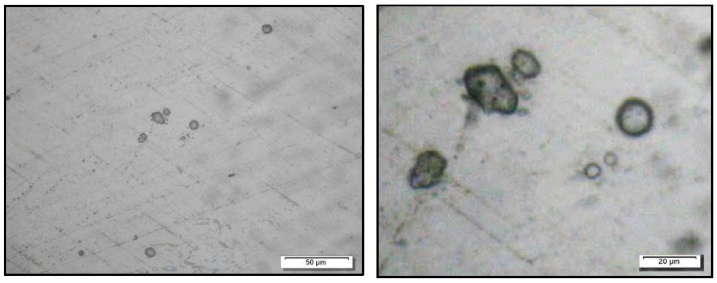

Figure 10. Micrograph of a Pitted Sample in Chloride Ion Environment at 500X & 1000X

Table 1. Values of Passivation Potentials and Hydrochloric acid Concentration for the Investigation of samples of Stainless Steel.

Sample	Passivation Potential (mV)	HCl Concentration (M)
1	856	0
2	808	2
3	760	3
4	689	4
5	600	5

Table 2. Values of Pitting Potentials and Hydrochloric acid Concentration for the Investigation of samples of Stainless Steel.

Sample	Pitting Potential (mV)	HClComcnetration (M)
1	7.141	0
2	-10.87	2
3	-84.02	3
4	-144.9	4
5	-161.8	5

6 CONCLUSION

Pitting potential (E_{pitt}) is the potential at which pitting starts and this is noticed when the current of the polarization curve suddenly rises. The E_{pitt} for stainless steel occurs at the point when the anodic current increases sharply as shown in the polarization curves figure: 4 to 8 the E_{pitt} values decreases with increase in chloride ion concentration from sample 1 to 5. The pH of the electrolyte inside the pit decreases which causes

further acceleration of the corrosion process. A large ratio between the anode and cathode areas favours increase of the corrosion rate. This is shown in the figure 11

ACKNOWLEDGEMENTS

The authors wish to acknowledge the support provided for this research by Prof. Dr. M. Tufail Dean CPE, Dr. Ashraf Ali Chairman Materials Engineering Department and Mr. Ghani Chishty.

REFERENCES

[1] Frangini S.,De CristofaroN., "Analysis of the Galvanostatic Polarization Method for Determining Reliable Pitting Potentials on Stainless Steels in Crevice-free Conditions", Corrosion Science, vol. 45, 2003,pp. 2769–2786

[2] Szklarska-SmialowskaZ., Janik-CzachorM., "*Effect of Chloride Ion Concentration on the Anodic Dissolution Behavior of Nickel*", Corrosion Science,vol. 11, 1971,p. 901

[3] ASTM, Standard Test Method for Conducting Potentiodynamic Polarization Measurements for Localized Corrosion Susceptibility of Iron-, Nickel-, or Cobalt-Based Alloys, ASTM G 61-86, Annual Book of ASTM Standards, vol. 3, 1986, pp. 223–227.

[4] Fossati A., Borgioli F., Galvanetto E., Bacci,"*Corrosion resistance steel in NaClsolutions*"Corrosion Science, vol 48, 2006, pp. 1513-1527

[5]LotoR.T.,"Pitting Corrosion Evaluation of Austenitic Stainless Steel type 304 in Acid Chloride Media", J. Mater. Environmental Science, vol. 4,2013,pp. 448-459

[6] Strehblow H.H., "*Corrosion Mechanisms in Theory and Practice*", P. Marcus and J. Oudar, Editors, Marcel Dekker, Inc., New York vol. 27,1995, pp. 201

[7] Abd El MeguidE. A., MahmoudN. A., AbdelRehimS. S.,"*Effect of Different Sulphur Containing Anions Added to Chloride on Pitting Corrosion of 304SS*", Mater. Chem. Phys., vol. 63,2000,pp. 67-74.

DETERMINATION OF ACCURATE MACHINE-SETTINGS FOR THE FACE-MILLING OF HYPOID GEAR

M. Wasif[1,*], M. Rababah[2], S.M. Hasan[1] and S.A. Iqbal[1]

[1]Department of Industrial & Manufacturing Engineering, NED University of Engineering & Technology, Karachi, Pakistan.

[2]Mechanical Engineering Department, Hashemite University, Zarqa, Jordan.

[*]Corresponding author. Tel.: +9221-992616261-8 Ext. 2462; fax: +9221-99261255

E-mail address: wasif@neduet.edu.pk (M. Wasif)

Abstract

A mathematical model for the machine settings of hypoid gears is developed, which is based on accurate blade geometries of a face-milling cutter system. Blades of the cutter system considered in this research, includes rake and relief angles, which are necessary for the efficient metal cutting.

In this research, cutter system orientation on the gear root tangent plane is determined by the root angle, which is calculated for the given spiral angle at the mean point projection of the gear teeth. Whereas, for the position of the cutter system and the gear blank, the tangency between the cutter sweep envelope and the gear teeth at the mean point projection are considered. Considering the tangency and common geometrical entities, a machine reference system is developed.

Keywords: hypoid gears; machine settings; face milling; accurate blade

1 INTRODUCTION

In face milling of hypoid gears, the gear tooth surface is formed by the sweep envelope of the rotating cutter head, which is fed perpendicular to the root cone of the gear blank. In face milling of hypoid gears, the tooth surface is complimentary copy of the cutter sweep surface [1]. Since the gear tooth is the copy of cutter sweep envelope; gear tooth forms the same unit normal and the principal directions as that of the cutter sweep surface as shown in the Fig. 1.

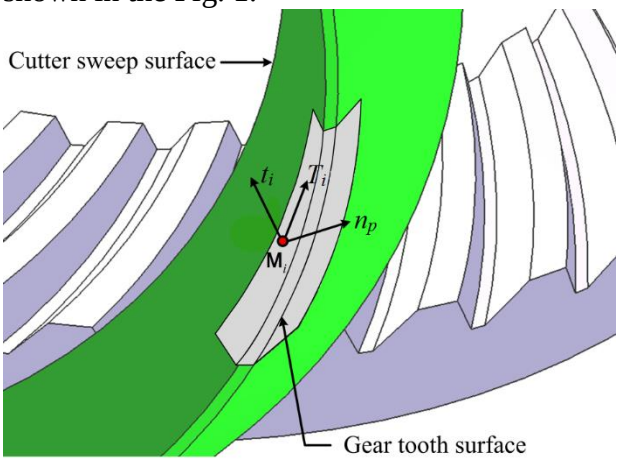

Figure 1. Gear tooth engagement with the cutter sweep envelope during the FORMAT machining

Cutter head of the face milling process contains several groups of inside and outside blades. These blades are arranged to machine the convex and the concave sides of the gear tooth, with the prescribed land width as shown in the Fig. 2.

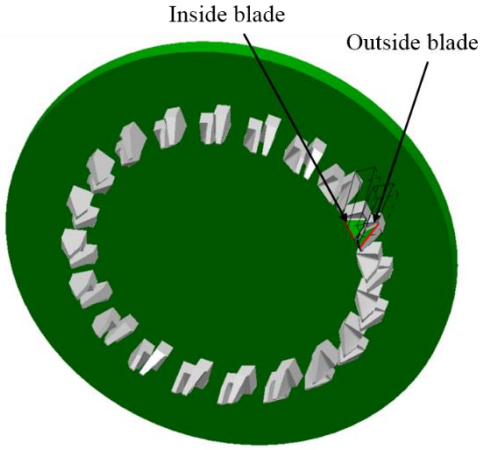

Figure 2. Cutter head assembly containing inside and outside blades

The location and position of the cutter system and the gear blank in the machine reference system are defined by the five geometric parameters called machine settings. Machine settings of the hypoid gear and pinion are based on the cutter system and the gear teeth specifications, which are known for the determination of the machine settings. Since machine settings are based on the cutter system and gear geometry, therefore, the gear and cutter system geometries are defined in following sections and then the machine settings are discussed and explained in section 4.

Several researches have been published to determine the accurate machine settings.

Litvin presented the machine setting settings for the FORMATE® and the Helixform® Methods, using the tilted cutter head and the local syntheses

method [1-2]; Litvin also proposed the cutter tilt mechanism and the machine-setting model [3]. Krezner proposed the computer aided corrections in the machine-setting, based on the first order surface deviations, and claimed that the second order surface deviations are minor [4]. Gosselin et al. proposed the correction methods in machine setting based on the tooth contact analysis (TCA) and performed the numerical regression method until satisfactory machine setting achieved [5-7]. Simon proposed an algorithm to calculate the machine setting corrections to reduce the sensitivity of the gear pair misalignments; moreover, equivalent machine settings for the universal hypoid generator are also calculated [8-11]. Perez et al. presented the analytical method for the determination of machine settings of the bevel gears based on three different geometry of the gear [12].

In gear machining industry, basic machine settings are calculated using the gear cutter and the gear tooth geometry, pilot gears are produced, and then corrected machine settings are calculated based on the surface deviation between the theoretical and the machined gear surfaces [5-7]. Deviations between the theoretical and machined surfaces exist due to the errors caused by the modelling approximation of the teeth surfaces [13].

In the previous research, simplified blade models in cutter systems are considered, in which rake and relief angles of the blades are neglected. The side cutting edge of the blade is assumed to be laid on the normal plane of the cutter [1-3]. Whereas, in the practical gear machining, the top and the side cutting edge of the blade lay on the rake plane of the blade [13] and hence it is called accurate blade model in this article.

In current research, mathematical model for the machine settings of hypoid gears produced by the face milling process is presented. The machine settings in this research are based on; accurate blade model of the cutter system and a spiral angle at the mean point projection of the gear tooth. For the given spiral angle at the mean point, root spiral angle on the root cone tangent plane of the gear is calculated, which decides the cutter orientation on that plane. Machine settings are determined, based on the relative position of the gear teeth and the cutter system, tangent to each other at the mean point projection on the driving side of the gear teeth, which bears the largest pressure during the gear meshing. Mean point **M** is located at the middle of the face width, just above the middle of tooth land, at a height h_M equal to the average of gear and pinion dedendums in that plane [14].

Using the cutter and gear engagement at the mean point projection of the gear tooth, the machine centre is introduced in the system, which lies at the point of intersection of the gear rotation axis and cutter face plane.

This article consists of six sections, first section is the preamble of this research article, second section described the geometry of the cutter sweep envelop and the gear. It includes the relationship between the two geometries. Next two sections address the mathematical model for the root spiral angle at the mean point and the machine setting of hypoid gears. Numerical results and the comparison between the previous and the current research are discussed in the last two sections.

2 GEAR TOOTH AND CUTTER SYSTEM GEOMETRIES GEAR TOOTH PROFILE

Consider the mean normal cross-section of the gear tooth, located at the middle of the face width. It is defined by the unit normal n_p , and the principal direction t_i along the tooth height, at a point $\mathbf{M}_i$ on the tooth, as shown in the Fig. 3(a). This cross section is called "gear tooth profile".

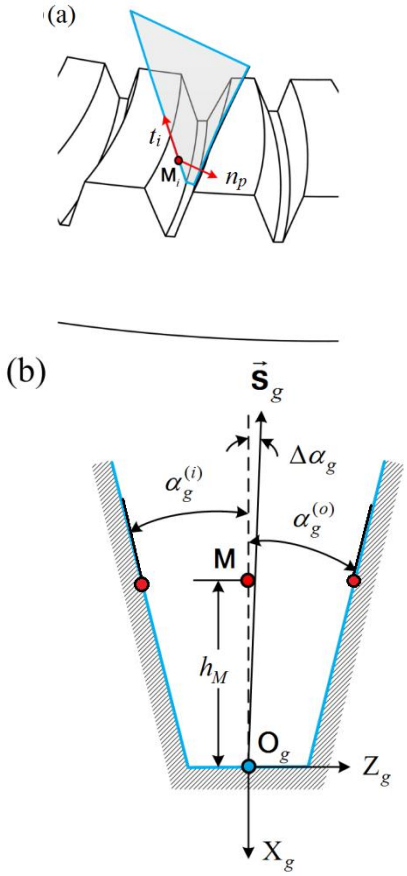

Figure 3. (a) Mean normal cross-section, (b) gear tooth profile

In this profile, consider a coordinate system $\mathbf{O}_g$, attached at the middle of the tooth land, such that the X_gZ_g - plane coincide with the gear tooth profile, where, X_g-axis is perpendicular to the land at $\mathbf{O}_g$, as shown in the Fig. 3(b).

The point **M** lies along the negative X_g-axis at a height h_M as shown in the Figure 3(b).

The flank of the gear tooth formed by the accurate blades in the cutter system are hyperbolic profile rather than straight as assumed in the previous researches. Therefore, the angle between the tangents on the tooth flank at the height h_M and the X_g-axis are called flank angles α_g, as shown in the Figure 3(b). Where, superscripts *(i)* and *(o)* denote the flank angles of the convex and concave sides of the gear teeth.

From the research [13], unit parametric representation of the side cutting edge of the inside and outside blade are given as the function of blade angle α_b, back rake angle α_o, side rake angle α_f, and relief angles γ_f, which is mathematically given by;

$$\vec{\mathbf{SCE}}_k\left(u_k,\alpha_o^{(k)},\alpha_b^{(k)},\alpha_f^{(k)},\gamma_f^{(k)}\right)=u_k.\vec{\mathbf{sce}}_k \qquad (1)$$

Where, k can be replaced with either i or o to mention these parameters for the inside or outside blade respectively, u_k be the parameter of the side cutting edges.

Arrangement of inside and outside blade coordinate systems ($\mathrm{O}_b^{(i)}$ and $\mathrm{O}_b^{(o)}$) are shown in Fig. 4.

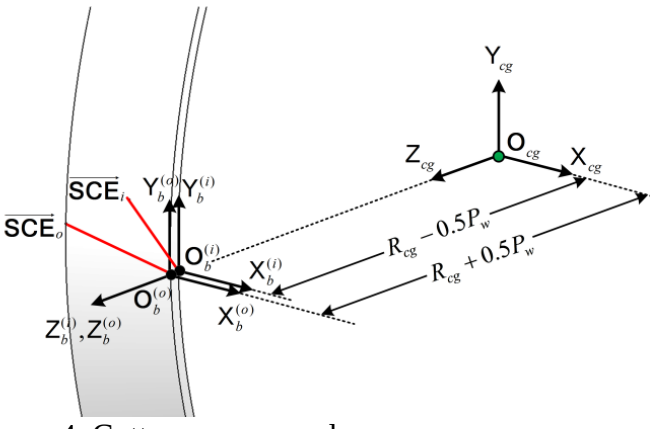

Figure 4. Cutter sweep envelope.

Introducing a cutter head coordinate system O_{cg} which is rigidly attached with the centre face of the cutter head, X_{cg}-axis of the cutter is the roatation axis. O_{cg} have all axes parallel to the $\mathrm{O}_b^{(i)}$ coordinate system and is located along negative $Z_b^{(i)}$ axis at a distance, equal to the inside point radius $R_{cg}-0.5P_w$, where R_{cg} is the average cutter radius, measured from the centre of point width P_w to the point O_{cg}. Cutter sweep envelope is formed by revolving the side cutting edges $\vec{\mathbf{SCE}}_k$ of the blades about the X_{cg}-axis of the cutter, as shown in the Fig. 4. Mathematically, the cutter sweep surface is given by;

$$\vec{\mathbf{S}}_k^{cg}\left(u_k,\theta_{cg}\right) = \mathrm{Rot}\left(X_{cg},\theta_{cg}\right).\mathrm{Tr}\left(Z_b,R_{cg}\mp 0.5P_w\right).\vec{\mathbf{SCE}}_k \qquad (2)$$

Where, θ_{cg} be the angular parameter of the cutter sweep surfaces. Intersection between the cutter sweep surfaces and the $X_{cg}Y_{cg}$ - plane of the cutter, provides two sets of coordinates $\mathbf{P}_i^{cg}(u_i,\theta_{cg})$ and $\mathbf{P}_o^{cg}(u_o,\theta_{cg})$, which can be generally represented as $\mathbf{P}_k^{cg}(u_k,\theta_{cg})$. Using the least square B-spline regression, cubic B-spline curves are fitted on each set of coordinates with the knot vector $\vec{\mathbf{U}}_k$, where knot vector is generated by average sum method. The curves, fitted on the intersection points of the cutter sweep surfaces are called *equivalent cutting edges* or simply *ECE*, which are shown in the Fig. 5. These *ECEs* are denoted by $\vec{\mathbf{P}}_k^{cg}(v_k)$, where v_k be the B-spline parameters and are bounded within the knot vector.

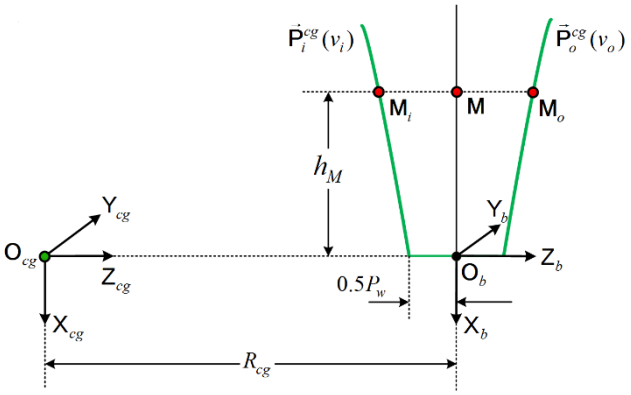

Figure 5. *ECE* in cutter coordinate system

Coordinates of the mean point **M** in cutter coordinate system O_{cg} is given by;

$$\mathbf{M}^{cg}=\begin{bmatrix}-h_M & 0 & R_{cg} & 1\end{bmatrix}^T \qquad (3)$$

Consider another coordinate system $\mathbf{O}_b$, which is attached at the centre of the point width, having same orientation as that of cutter coordinate system as shown in the Figure 5. To develop mathematical expression for the spiral angle at the point $\mathbf{M}_i$, it is desired to calculate the coordinates of mean point projections $\mathbf{M}_k$ on the inside and the outside *ECE*. Therefore, transforming *ECEs* from cutter

coordinate system to the $\mathbf{O}_b$ coordinate system. Mathematically, the ECE in $\mathbf{O}_b$ coordinate system are given by;

$$\vec{\mathbf{P}}_k^b = \mathbf{M}_{b,cg}.\vec{\mathbf{P}}_k^{cg} = \mathrm{Tr}\left(Z_{cg}, -R_{cg}\right).\vec{\mathbf{P}}_k^{cg} \quad (4)$$

The points $\mathbf{M}_k$ on the ECE are calculated by taking the x-components of the ECE equal to the mean height, which determines the parameter v_k. The parameters are then substituted into the B-splines equation to calculate the z-components of the curves. Mathematically, the mean point projections are given by;

$$\begin{aligned}\mathbf{M}_k &= \vec{\mathbf{P}}_k^b\left(v_k^M\right)\\ &= \left[\mathbf{x}\left(v_k^M\right) \quad 0 \quad \mathbf{z}\left(v_k^M\right) \quad 1\right]^T\\ &= \left[-h_M \quad 0 \quad \mathbf{z}\left(v_k^M\right) \quad 1\right]^T\end{aligned} \quad (5)$$

3 ROOT SPIRAL ANGLE

As mentioned above, the spiral angle β_i controls the curvature of the gear teeth. It is necessary to provide appropriate spiral angle on the driving tooth of the gear for smooth and noiseless operation. Spiral angle is defined on the driving teeth at a height of h_M from the land. It is the angle between the pitch cone generatrix to the point $\mathbf{M}_i$ and the unit normal n_p as shown in the figure 6. On the other hand, root spiral angle defines the orientation of cutter on the gear root cone tangent plane. It is the angle between the root cone generatrix at the point $\mathbf{O}_g$ and the unit normal n_p as shown in the figure 6. For the desired spiral angle β_i, the cutter orientation or root spiral angle β_r is to be calculated.

To acquire the desired shape of the gear teeth, it is required to align the *ECE* with the gear tooth cross section such that the coordinate systems $\mathbf{O}_b$ and $\mathbf{O}_g$ and the symmetric axis are coincided [1] as shown in Figure 7.

The root spiral angle is calculated using an iterated way. Therefore, these two spiral angles can be related as;

$$\beta_i = f(\beta_r) \quad (6)$$

Due to the unavailability of the blades, cutter head is titled with an anlge of θ_g about the Y_b axis (case 2) to coincide the symmetric axes of the cutter sweep profile with the gear teeth profile.

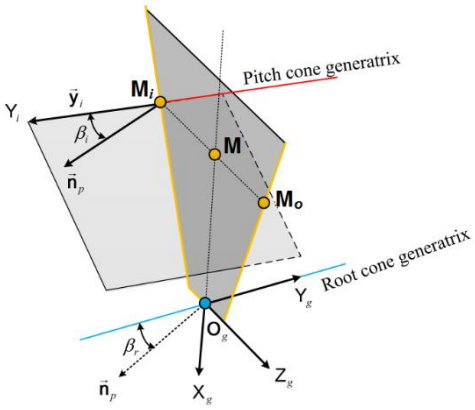

Figure 6. Relationship between the spiral angle at a point, and the root spiral angle

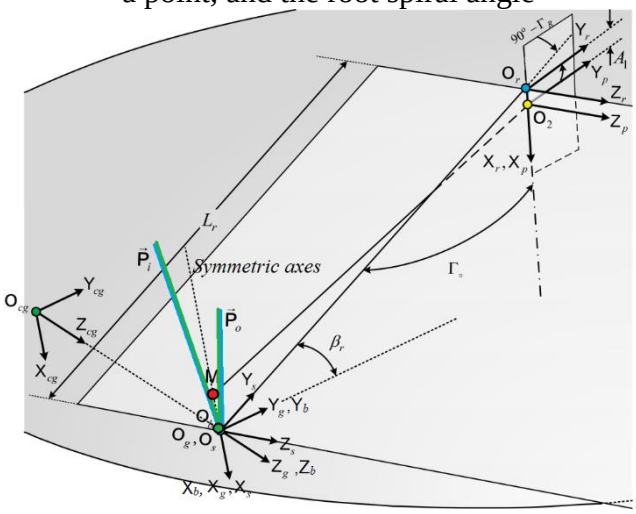

Figure 7. Root spiral angle

To build the relationship between the two spiral angles, it is necessary to relate the pitch cone generatrix, root cone generatrix and unit normal n_p in a single coordinate system. Therefore, the relationship is built by transformation from the $\mathbf{O}_b$ coordinate system to the $\mathbf{O}_2$ coordinate system.

Cutter head is rotated with an angle of β_r about the X_g axis, it from a new coordinate system $\mathbf{O}_s$, as shown in the Figure 7. Where, the Y_s axis forms the generatrix of the root cone, and the X_s axis is parallel to X_g axis. Apex of the root cone $\mathbf{O}_r$ lies at a distance of L_r from the $\mathbf{O}_s$ along the Y_s axis. The orientation of root cone coordinate system $\mathbf{O}_r$ form an angle of $90^\circ - \Gamma_R$ about the Z_r axis. The X_r axis of the coordinate system $\mathbf{O}_r$ is directed along the gear rotation axis, where Γ_R be the root angle as shown in Figure 7. Pitch cone coordinate system $\mathbf{O}_2$ lies at a distance of A_1 along the X_r axis, having same orientation as $\mathbf{O}_r$. Distances L_r and A_1 are determined by the AGMA standards [16].

The vectors n_p and $\mathbf{M}_i$ are transformed to the coordinate system $\mathbf{O}_2$.

$$\vec{n}_p^2 = \mathbf{M}_{2,g}.\vec{n}_p^g \quad (7)$$

$$\mathbf{M}_i^2 = \mathbf{M}_{2,g}.\mathbf{M}_{g,b}.\mathbf{M}_i \quad (8)$$

Transformation from $\mathbf{O}_g$ to the $\mathbf{O}_2$ is mathematically given by;

$$\mathbf{M}_{2,g} = \mathrm{Tr}(\mathsf{Z}_r,-A_1).\mathrm{Rot}(\mathsf{Z}_s,90^\circ-\Gamma_R).\mathrm{Tr}(\mathsf{Y}_s,-L_r).\mathrm{Rot}(\mathsf{X}_g,\beta_r) \quad (9)$$

$$\mathbf{M}_{g,b} = \mathrm{Rot}(\mathsf{Y}_b,\theta_g).\mathrm{Tr}(\mathsf{X}_g,a).\mathrm{Tr}(\mathsf{Z}_g,b) \quad (10)$$

Where, θ_g be the tilt angle of the cutter, whereas, a and b be the tilt corrections (case 2), as discussed in the previous article [14]. For the exact cutter head with out tile (case 1), $\mathbf{M}_{g,b}$ is a unity matrix.

A unit vector y_i, emerging from the pitch cone generatrix $\mathbf{O}_2$ to the point $\mathbf{M}_i$ is considered, as shown in the Figure 6.

Therefore, the spiral angle at this point is given by,

$$\beta_i = \cos^{-1}\left(\vec{\mathbf{n}}_p.\vec{\mathbf{y}}_i\right) \quad (11)$$

Single variable optimization is used to calculate the root spiral angle for the given spiral angle at the driving mean point projection, which is shown in the Figure 8.

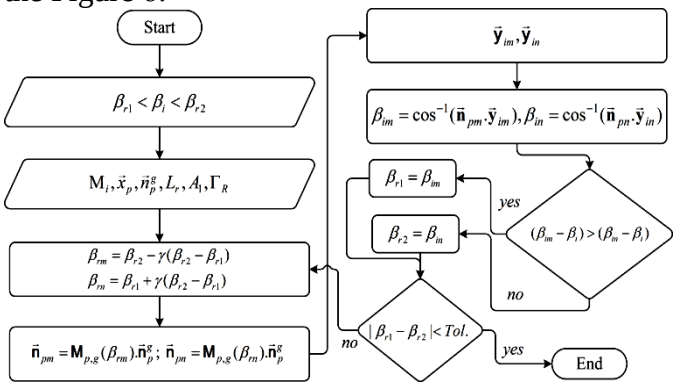

Figure 8. Algorithm for the root spiral angle

Initial guess values of the β_r are provided around the given value of β_i, the optimization parameters are calculated, cutter is rotated about the X_g axis with these angles, and all the equations from equations 7 to 11 are calculated. If equation 11 provides the spiral angle equal to the given spiral angle within the specified tolerance, the algorithm saves the value of β_r as the final value, otherwise, the parameters are re-calculated, and the iterations are performed, until the defined criteria is reached.

4 MACHINE SETTINGS

The machine settings for the face milling of hypoid gears are calculated in the machine coordinate system $\mathbf{O}_m$. These machine settings parameters, with the cutter and gear coordinate systems are shown in the Figure 9.

Consider a unit vector $\vec{\mathbf{p}}_w$ along the point width of the cutter. A point on this vector is given by $\mathbf{P}_w^b = [0 \quad 0 \quad 1]^T$. Coordinates of a point along the unit normal n_p is given by $\mathbf{N}_p^b = [0 \quad 1 \quad 0]^T$. Coordinates of another point along the gear rotation axis in the coordinate system is presented as $\mathbf{X}_p^2 = [1 \quad 0 \quad 0]^T$.

There are three displacements and two angular machine settings are to be calculated as shown in the Figure 9.

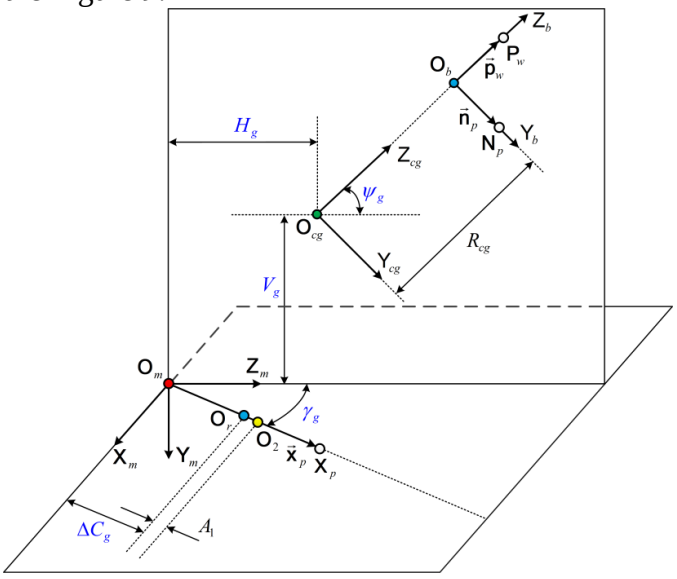

Figure 9. Machine settings for the face milling of hypoid gear

Transforming the coordinates of all origins and mentioned vectors in the pitch cone coordinate system $\mathbf{O}_2$.

$$\mathbf{O}_b^2 = \mathbf{M}_{2,g}.\mathbf{M}_{g,b}.[0 \quad 0 \quad 0 \quad 1]^T \quad (12)$$

$$\mathbf{O}_r^2 = \mathbf{M}_{2,r}.[0 \quad 0 \quad 0 \quad 1]^T \quad (13)$$

$$\mathbf{O}_{cg}^2 = \mathbf{M}_{2,cg}.[0 \quad 0 \quad 0 \quad 1]^T \quad (14)$$

$$\mathbf{P}_w^2 = \mathbf{M}_{2,cg}.\mathbf{P}_w^b \quad (15)$$

$$\mathbf{N}_p^2 = \mathbf{M}_{2,cg}.\mathbf{N}_p^b \quad (16)$$

Origin of the machine coordinate system $\mathbf{O}_m$ is defined as the machine centre, and shown in the Figure 9. It is located at the intersection of the vector along gear rotation axis $\vec{\mathbf{x}}_p$ and the plane formed by the vectors $\vec{\mathbf{p}}_w$ and $\vec{\mathbf{n}}_p$, which is called machine plane. Therefore, the equation of the gear rotation axis and the $\mathsf{Y}_b\mathsf{Z}_b$ plane is given by,

$$\mathsf{L}(t) = (1-t).\mathbf{O}_r^2 + t.\mathbf{X}_p^2 \quad (17)$$

$$\mathsf{P}(u,v) = \mathbf{O}_b^2 + u.\left(\mathbf{P}_w^2 - \mathbf{O}_b^2\right) + v.\left(-\mathbf{N}_p^2 - \mathbf{O}_b^2\right) \quad (18)$$

Where t is the parameter of the line $\mathsf{L}(t)$ along the gear rotation axis, and the parameters u and v belongs to the machine plane. Point of intersection between the line $\mathsf{L}(t)$ and the plane $\mathsf{P}(u,v)$ is evaluated by the relation;

$$\mathsf{L}(t_m) = \mathsf{P}(u_m, v_m) \tag{19}$$

It provides the parameters as the solution, for the machine centre. Parameter t_m represents the distance between the apex of the root cone $\mathbf{O}_r$ and the machine centre $\mathbf{O}_m$, which is called withdraw from the machine plane, and denoted by ΔC_g, Therefore, mathematically the it is calculated by;

$$\Delta C_g = \sqrt{\left(\mathsf{L}_x(t_m)\right)^2 + \left(\mathsf{L}_y(t_m)\right)^2 + \left(\mathsf{L}_z(t_m)\right)^2} \tag{20}$$

Therefore, the machine centre $\mathbf{O}_m$ in the coordinate system $\mathbf{O}_r$ is represented by $\mathbf{O}_m^r = \begin{bmatrix}\Delta C_g & 0 & 0\end{bmatrix}^T$.

The displacement ΔC_g defines the location of the root cone apex in machine reference system, which cannot be located in the gear blank. Therefore, location of the face cone apex $\mathbf{O}_f$ is calculated in the machine coordinate system by the displacement ΔX_g [13], which is mathematically given by;

$$\Delta X_g = \Delta C_g + d_k + A_1 \tag{21}$$

Where d_k be the distance between the pitch cone apex and the face cone apex. Direction of the X_m axis is defined by a vector x_m, which is perpendicular to the machine plane. The normal to the plane formed by the vectors x_m and x_p specifies the direction of the Y_m axis, which is represented by the vector y_m, whereas Z_m axis is perpendicular to the $\mathsf{X}_m\mathsf{Y}_m$ plane. Direction vectors of the machine coordinate system are given by;

$$\vec{\mathbf{X}}_m^p = x_m + \mathbf{O}_m^r = \frac{\vec{\mathbf{n}}_p \times \vec{\mathbf{p}}_w^p}{\left|\vec{\mathbf{n}}_p \times \vec{\mathbf{p}}_w^p\right|} + \mathbf{O}_m^r \tag{22}$$

$$\vec{\mathbf{Y}}_m^p = y_m + \mathbf{O}_m^r = \frac{\vec{\mathbf{x}}_p \times \vec{\mathbf{x}}_m^p}{\left|\vec{\mathbf{x}}_p \times \vec{\mathbf{x}}_m^p\right|} + \mathbf{O}_m^r \tag{23}$$

$$\vec{\mathbf{Z}}_m^p = z_m + \mathbf{O}_m^r = \frac{\vec{\mathbf{x}}_m^p \times \vec{\mathbf{y}}_m^p}{\left|\vec{\mathbf{x}}_m^p \times \vec{\mathbf{y}}_m^p\right|} + \mathbf{O}_m^r \tag{24}$$

An angular machine setting, which measures the angle between the machine plane and the gear rotation axis, it is called machine root angle (γ_g). It is mathematically given by;

$$\gamma_g = \cos^{-1}\left(\vec{\mathbf{x}}_p . \vec{\mathbf{z}}_m^p\right) \tag{25}$$

Another angular machine setting is called machine spiral angle (ψ_g), it is the angle between the cutter tilt plane $\mathsf{X}_{cg}\mathsf{Z}_{cg}$ and the Z_m axis, it is given by;

$$\psi_g = \frac{\pi}{2} - \cos^{-1}\left(\vec{\mathbf{y}}_m^p . \vec{\mathbf{p}}_w^p\right) \tag{26}$$

The location of the cutter coordinate system $\mathbf{O}_{cg}$ in machine coordinate system is defined by the displacements H_g and V_g along the Z_m and Y_m axes respectively. Mathematically these machine settings are given by;

$$H_g = \frac{\left|\left(\mathbf{O}_c^p - \mathbf{O}_m^p\right) \times \left(\mathbf{O}_c^p - \mathbf{Z}_m^p\right)\right|}{\left|\mathbf{Z}_m^p - \mathbf{O}_m^p\right|} \tag{27}$$

$$V_g = \pm \frac{\left|\left(\mathbf{O}_c^p - \mathbf{O}_m^p\right) \times \left(\mathbf{O}_c^p - \mathbf{Y}_m^p\right)\right|}{\left|\mathbf{Y}_m^p - \mathbf{O}_m^p\right|} \tag{28}$$

Where, '±' signs are for the machining of left hand or right hand direction of the hypoid gear teeth.

5 RESULTS

Machine settings of a hypoid gear is calculated for the given spiral angle at the mean point of the driving side tooth. The data for the inside and outside gear-cutting blades, cutter radius, and the specification of the tooth geometry are taken as input in this algorithm, which are shown in the tables 1 to 4. Table 1 shows the specifications of the hypoid gear cones and teeth, whereas, tables 2 and 3 contains the data of the blade and the cutter for the case I and case II respectively [14]. To compare the result of the previous [7] and current research, machine setting for the simplified and accurate blade models for the case 1 and case 2, along with the auxiliary angle are shown in the tables 4 and 5. Fig. 10 and table 6 illustrate the deviation between the gear teeth surfaces modelled with the machine settings and cutter head of simplified and accurate blade models. It can be seen that these deviation cause the geometric errors in the gear models not only on the heel and toe but also at the mean points of the teeth surface.

Table 1. Specification of hypoid gear

Parameters	Sym.	Convex side	Concave side
Gear flank angle	$\alpha_g^{(k)}$	23°11′0″	21°49′0″
Gear face angle	Γ_o	81°06′0″	
Gear root angle	Γ_R	75°28′0″	
Gear dedendum angle	δ_G	4°54′0″	
Gear pitch point length	L_P	150.9600 mm	
Root to pitch apex	A_1	1.6885 mm	
Face width	F	43.0000 mm	
Spiral angle at M_i	β_i	31°34′12″	

Table 2. Specifications of blade and cutter head parameters for the case I (without cutter tilt).

Parameters	Previous literature [7]		Proposed research	
	Convex side	Concave side	Convex side	Concave side
Back rake angle ($\alpha_o^{(k)}$)	0	0	20°0′0″	20°0′0″
Side rake angle ($\alpha_f^{(k)}$)	0	0	12°0′0″	12°0′0″
Side relief angle ($\gamma_f^{(k)}$)	0	0	10°0′0″	10°0′0″
Blade angle ($\alpha_b^{(k)}$)	23°11′0″	21°49′0″	19°01′14″	16°37′35″
Av. cutter radius (R_{cg})	152.4 mm		152.4 mm	
Point width (P_w)	2.54 mm		2.54 mm	

Table 3. Blade and the cutter head data for the case II (with cutter tilt).

Parameters	Previous literature [7]		Proposed research	
	Convex side	Concave side	Convex side	Concave side
Back rake angle ($\alpha_o^{(k)}$)	0	0	$20^\circ 0' 0''$	$20^\circ 0' 0''$
Side rake angle ($\alpha_f^{(k)}$)	0	0	$12^\circ 0' 0''$	$12^\circ 0' 0''$
Side relief angle ($\gamma_f^{(k)}$)	0	0	$10^\circ 0' 0''$	$10^\circ 0' 0''$
Blade angle ($\alpha_b^{(k)}$)	$22^\circ 30' 0''$	$22^\circ 30' 0''$	$18^\circ 22' 6''$	$17^\circ 15' 39''$
Av. cutter radius (R_{cg})	152.4 mm		152.4 mm	
Point width (P_w)	2.54 mm		2.54 mm	
Cutter tilt angle	θ_g		$-0^\circ 41' 0''$	
Cutter corrections	a , b		-0.0151 mm, -0.0001 mm	

Table 4. Machine settings of the hypoid gear for case I (without cutter tilt).

Parameter	Previous research [7]		Proposed research	
	Convex side	Concave side	Convex side	Concave side
Root spiral angle (β_r)	$32^\circ 50' 0''$		$32^\circ 50' 0''$	
Machine root angle (γ_g)	$75^\circ 28' 0''$		$75^\circ 28' 0''$	
Machine spiral angle (ψ_g)	$32^\circ 50' 0''$		$32^\circ 50' 0''$	
Machine centre to back correction (ΔX_g)	1.0685 mm		1.0686 mm	
Cutter horizontal setting (H_g)	128.0694 mm		128.0416 mm	
Cutter vertical setting (V_g)	68.3526 mm		68.2009 mm	

Table 5. Machine settings of the hypoid gear for the case II (with cutter tilt).

Parameter	Previous research [7]		Proposed research	
	Convex side	Concave side	Convex side	Concave side
Root spiral angle (β_r)	$32^\circ 50' 0''$		$32^\circ 50' 0''$	
Machine root angle (γ_g)	$75^\circ 49' 0''$		$75^\circ 49' 33''$	
Machine spiral angle (ψ_g)	$30^\circ 34' 0''$		$30^\circ 33' 40''$	
Machine centre to back correction (ΔX_g)	0.0600 mm		0.0619 mm	
Cutter horizontal setting (H_g)	125.1400 mm		125.2552 mm	
Cutter vertical setting (V_g)	73.0300 mm		72.9789 mm	

Table 6. Surface deviations in the gear teeth modelled with the machine settings and cutter head of simplified and accurate blade models.

	Surface Deviation - Case I (µm)		Surface Deviation - Case II (µm)	
	Convex side	Concave side	Convex side	Concave side
a	168.57	147.30	164.61	99.24
b	153.41	153.83	128.72	128.79
c	143.77	152.43	118.60	129.48
d	149.35	149.71	125.12	125.13
e	178.36	173.98	173.44	167.42

It can be seen from Table 6, that the deviation is maximum at the mean points of the two models which are denoted by "e" in table 6. The mean point is crucial for the contact.

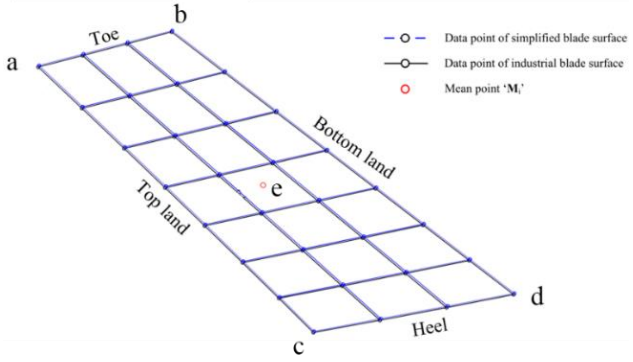

Figure 10. Surface deviations in the gear teeth modelled with the machine settings and cutter head of simplified and accurate blade models

6 CONCLUSION

Results show that the machine settings for the gear teeth modelled with the simplified and the accurate blade model differ, due to reason that the spiral angles at the mean points are different for the same root spiral angle. Machine root angle does not change for in all the examples, since it depends upon the gear cone parameters. It is also observed that the machine settings for the tilted cutter are more sensitive for the rake and relief angles, which also change the machine centre to back setting. The algorithm also covers the cutter tilt corrections, which restrain the cutter to gauge into the root cone, but the corrections cause the change in pitch cone apex for the mean point, which is also overcome in this research.

7 REFERENCES

[1] F.L. Litvin, Y. Gutman, Method of Synthesis and Analysis for Hypoid Gear-Drives of 'Formate' and 'Helixform'" Part 1, *Journal of Mechanical Design*, 103, 83-88; 1981.

[2] F.L. Litvin, Y. Gutman, Method of Synthesis and Analysis for Hypoid Gear-Drives of 'Formate' and 'Helixform'" Part 2, *Journal of Mechanical Design*, 103, 83-88; 1981.

[3] F. L. Litvin, Y. Zhang, M. Lundy and C. Heine, Determination of Settings of a Tilted Head Cutter for Generation of Hypoid and Spiral Bevel Gears, *Journal of Mechanical Design*, 110, 495-500, 1988.

[4] T. J. Krenzer, Computer aided corrective machine settings for manufacturing bevel and hypoid gear sets, *Technical papers : Fall Technical Meeting*, Washington DC, 1984.

[5] C. Gosselin, Corrective machine settings of spiral-bevel and hypoid gears with profile deviations, *World Congress on Gearing and Power Transmission*, Paris, 1999.

[6] C. Gosselin, T. Nonaka, Y. Shiono, A. Kubo and T. Tatsuno, Identification of the Machine Settings of Real Hypoid Gear Tooth Surfaces, *Journal of Mechanical Design*, 120, 429-440, 1998.

[7] C. J. Gosselin and L. Cloutier, The Generating Space for Parabolic Motion Error Spiral Bevel Gears Cut by the Gleason Method, *Journal of Mechanical Design*, 115, 483-489, 1993.

[8] V. Simon, Optimal Machine Tool Setting for Hypoid Gears Improving Load Distribution, *Journal of Mechanical Design*, 123, 577-582, 2001.

[9] V. Simon, Advanced Manufacture of Spiral Bevel Gears on CNC Hypoid Generating Machine, *Journal of Mechanical Design*, 132, 031001-1-8, 2010.

[10] V. Simon, Generation of Hypoid Gears on CNC Hypoid Generator, *Journal of Mechanical Design*, 133, 121003-1-9, 2011.

[11] V. Simon, Machine-Tool Settings to Reduce the Sensitivity of Spiral Bevel Gears to Tooth Errors and Misalignments, *Journal of Mechanical Design*, 130, 082603-1-10, 2008.

[12] I. G. Perez, A. Fuentes and K. Hayasaka, Analytical Determination of Basic Machine-Tool Settings for Generation of Spiral Bevel Gears From Blank Data, *Journal of Mechanical Design*, 132, 101002-1-11, 2010.

[13] S. Xie, A genuine face milling cutter geometric model for spiral bevel and hypoid gears, *Journal of Advanced Manufacturing Technology*, 67(9-12), 2619-2616, 2013.

[14] M. Wasif, Z.C. Chen, Cutter radius and blade angle selection model for the high speed face milling of hypoid gear, *International conference on virtual machining process technology*, Montreal, 2011.

[15] AGMA, Design Manual for Bevel Gears, *ANSI/AGMA standards*, USA, 2005.

IMPLEMENTATION OF WASTE ASSESSMENT MATRIX AND LINE BALANCING FOR PRODUCTIVITY IMPROVEMENT IN A HIGH VARIETY/HIGH VOLUME MANUFACTURING PLANT

Basit Ali[1,*], Sarah Jaweed[2] and Dr. Muhammad Fahad[3]
[1,2]MEM Students, Industrial & Manufacturing Department, NED University of Engineering & Technology, Karachi, Pakistan
[3]Associate Professor, Industrial & Manufacturing Department, NED University of Engineering & Technology, Karachi, Pakistan

[*]Corresponding author. Tel.: +92-331-2096679
E-mail address: basitali_neduet@hotmail.com

Abstract

Principles of lean manufacturing has been known since last two decades, however, its implementation in the local industries is a recent trend. A lot of analysis tools such as 5S, Kaizen, Kanban, flow production and line balancing have commonly been used to improve productivity by organizations across the globe as well as in the local industries. A relatively newer tool, named as waste assessment matrix (developed at Industrial Engineering dept., University of Jordan, Amman) is a technique that defines the interrelationship between different forms of waste in a job shop environment to highlight their relative significance. This study is based on the use of waste assessment matrix for identifying different type of wastes in the packing department of a high variety – high volume manufacturing plant. Other lean tools, such as 5S, Kaizen, flow production and line balancing were then used to analyse and improve the wastes in the plant. The study shows that waste assessment matrix can be equally well applied in a high volume manufacturing plant as can be applied in a job shop. Results show that not only lead time, and workforce were reduced but the availability and performance of the plant were improved.

Keywords: Mass Production; WRM; Online packing; Kaizen; Lean Methodology

1 INTRODUCTION

Wastes are the profits that the company can earn and lean is a revolution that earns that profit [1]. It is not only using tool and changing few step in manufacturing processes, rather it is about complete change of business operation. The background of lean is based in the history of Japanese manufacturing techniques which have now been applied worldwide within many type of industries [2]. Every production process have some different activities. These activities could be easily classified into value added activities (VA) and non-value added activities (NVA). Activities that directly adds value to product or customer is willing to pay for are considered as value added while activities having no impact on product and its value, are termed as non-value added activities [3]. Although, some of the NVAs is considered as necessary for carrying out production but, a large proportion of these NVAs is typically considered as pure waste and could easily be removed to improve the productivity. These are usually referred to as wastes. On a broader scale, waste is divided into three types as follows:

1. Muda (Waste)-Capacity Exceeds Loads
2. Muri (Irrationality)-Loads Exceeds Capacity
3. Mura (Inconsistency)-Both cases may occur

As per Taiichi Ohno, wastes may comprise of motion, waiting time, over production, over processing, defects, transportation and inventory [1]. These wastes add to higher cost, poor quality and less motivation. In order to remove these wastes, a tool named as Lean Manufacturing Methodology is used. By definition, lean manufacturing could be defined as;

"Lean manufacturing is a business model and collection of tactical methods that emphasize eliminating non-value added activities (waste) while delivering quality products on time at least cost with greater efficiency"[4].

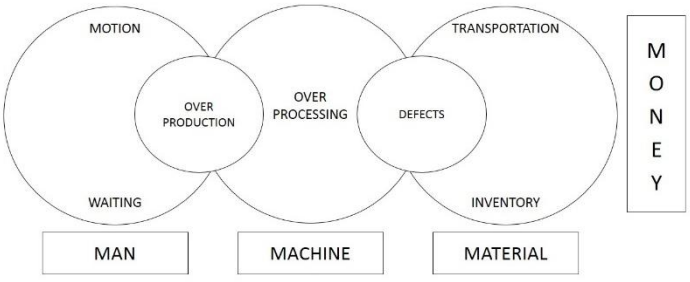

Figure 1. 7 wastes of lean [3]

Lean methodology means to eliminate NVAs or convert them into VAs. It focusses not only on

segments of processes but on the whole process. It includes all the employees and their motivation, hard work and efforts in the development of a lean organization. It is not a work of one man army rather every individual has to include something to it [5]. In today's high competitive market, Pakistan's industrial sector is striving hard in order to achieve the set goals and to achieve that, implementation of lean methodology has been the right way to choose. The common questions that arise are:

1- Why follow lean?
2- What are the basic principles of lean?
3- What are the tools that could be used for executing lean?

Answer to question number one lies in the benefits of utilizing and believing in lean methodology, which are:

- Improved quality
- Less defects
- Reduce inventory
- Improve space utilization
- Easy to manage processes
- Less machine and process breakdowns
- Better efficiency
- Safe work place
- Improve morale of workers
- Improve supply chain
- Better relations from vendors to customer

Similarly, following principles are basics of lean methodology [6]:

- **Specify Value** – Customer requirements.
- **Identify the Value Stream** – All the steps required to fulfil customer requirements.
- **Establish Flow** – Make sure the value flows smoothly (without any disruptions) to the customers.
- **Implement Pull System** – Use a pull system to control inventory/information wherever required and possible.
- **Work to Perfection** – Continuously look for ways to improve the value addition process.

Finally, some of the common tools utilized for implementing lean are [1,5,7]:

- **Value Stream Mapping** – For analysing & streamlining flow of material & information of all the processes
- **Kaizen** – Philosophy of continuous improvement of working practices
- **Just In Time** – Reducing the in process inventory and associated costs
- **Jidoka** – System stops at any un certainty
- **5S** – Methodology for work place organization
- **Kanban** – Visual signal of customer demands
- **Poka Yoke** – Mistake proofing

All the basic principles and tools listed above are targeted towards achieving the benefits of lean mentioned earlier which mainly involved identifying the waste (NVAs) and its subsequent elimination.

2 WASTE ASSESSMENT MODEL

Starting point of any journey is key to the morale of people involved. For improvement if it is started with a big improvement and improvement's impact is as loud as a hammer's noise then it counts in morale and efforts improvement of human resource involved. For this kind of impact, it is very important to find out the major waste that have the highest influence on overall process and if it is improved then whole process will improve. In this regard waste assessment model is used to find out how high the effect of the waste is on system as well as on each other. This assessment model is the most important step to implementation of Lean manufacturing methodology. Ibrahim A. Rawabdeh [3] was the first person who identified the relationship between the different types of wastes by using a concept of WRM (waste relation matrix). The idea of the matrix is to establish a link between all the different types of wastes that occur while performing manufacturing processes. The waste that have strongest direct link with all other wastes is selected as the possible source of non-value adding activities and is subsequently removed/lowered via lean tools to improve the situation. The matrix was used to identify the most important type of waste in a job shop environment [3]. In this project, this approach (WRM) will be implemented in high variety/high volume production environment to find out the waste which should be eliminated from the system.

The waste assessment model was designed on the basis of each type of the seven wastes (Figure 3) and their over lapping area. Then identify the strength of each direct relationship among the seven type of waste and make waste matrix that classifies the strength of relationships using a scale ranging from very weak to very strong.

In second phase, an assessment questionnaire is use to rank a waste by combining the relationship matrix and the result of the assessment questionnaire.

All type of waste are inter-dependent and discussing the relationship among wastes is complex because the relation can appear directly or indirectly.

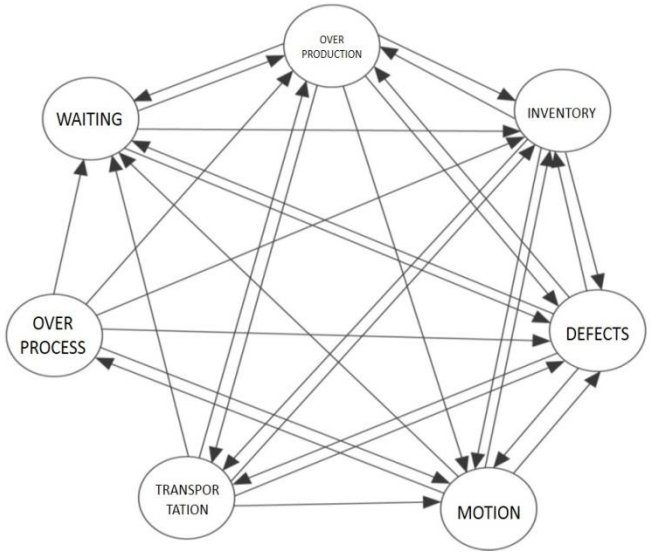

Figure 2. Relation between 7 Wastes [3]

2.1 Explanation of Waste Assessment Model

Inventory

I-O Higher inventory of raw materials can be reason to push the labour for over production in order to get the higher profit for company

I-D Higher inventory of raw material, work in process and finish good will increase the chances to produce defected due to less of concern and unsuitable storing condition

I-M Higher inventory also be the reason to increase the time in each and every process

I-T Excess inventory creates hurdle in the transportation of material

Defects

D-O In order to overcome the defects, over production become necessary

D-I Defects mean they need to reworked, so WIP will be increased in the form of inventory

D-M Defects increase the time of searching, selection and inspection of part

D-T Defects will increase the wasteful transportation activities

D-W As reworks reserve the workstation therefore new parts will be waiting to be processed

Motion

M-I Non- standardize method become reason of WIP

M-D Non-standardize process leads to increase the defects

M-P When process are non-standardize will increase the process waste due to the lack of understanding the available capacity

M-W Due to non-standardize process, time will be consumed searching, selecting the parts so in result part waiting get increase

Transportation

T-O In order to reduce the transportation cost per unit, over production has to be produced

T-I other process can be effected due to insufficient number of material handling equipment (MHE)

T-D Sometime non-suitable MHE be the reason of damage items and defects

T-M When MHE is non-standardize then it leads to motion waste presented by double handling and searching

T-W Insufficient MHE will also lead to waiting to be transported and some of the machine will remain idle [3]

2.2 Waste Assessment Model (WAM)

Waste assessment model starts by first identifying the major forms of waste that occur in the factory/plant in a general perspective. After this, each waste is linked with each other waste to establish link between the wastes. Following six questions are then used in developing the waste assessment matrix for each identified link. Assume 'a' is the source waste and 'b' is the resulting waste, then the questions to be asked are:

1. Does a produce b?
2. What is the type of the relationship between a and b?
3. The effect of b due to a?
4. Eliminating the effect of a on b is achieved by?
5. The effect of b due to a, mainly influences?
6. In which degree does the effect of a and b increases manufacturing lead time?

The answers to these questions are ranked from 0 to 4 and the resulting total is listed in the form of a matrix known as waste relationship matrix (WRM). This WRM is then used to identify the waste (s) which has the most influence on all other wastes and removing this waste could not only reduce the other form of wastes but will also enable a quick improvement in productivity.

3 METHODOLOGY

For the implementation of productivity improvement via WRM, a multinational organization which is considered as global leaders in the manufacturing of safety products was selected. The company is in operation since last thirty years and has various units not only within Pakistan, but across the globe in over forty countries. The organization has five factories in Pakistan and they produce customized as well as high volumes of regular products. This project involved implementation of WAM for productivity improvement in one of the glove manufacturing facility of the organization. After applying WRM,

the waste with highest value was selected for improvement. Value stream mapping (VSM), Line Balancing and 5S techniques were subsequently implemented to improve the system.

4 RESULTS AND DISCUSSION

The facility have strived hard for improvement in packing department through implementing the concept of batch to online (continuous) packing system. Following problems have been faced in the existing system for which this project was initiated; inventory, defects, transportation and motion. The main problem was the cycle time of the packing process (6 sec/pc) which was higher than the takt time (5.33 sec/pc). Total lead time till final finished good (FG) was about 24 hrs to 48 hrs. Not only waiting time was high but this process was also long i.e. have high transportation wastes. The more the good travels, the more the risk of damage (waste of defects). Similarly defects were also highlighted late that causes high loss.

4.1 Waste Assessment Model (WAM)

Waste assessment model was the first step taken in order to check and finalize which waste has to be given high priority in order to start the implementation process of productivity improvement by implementing its lean manufacturing tools. Range distribution of the methodology is as given in the Table 1 [3]:

Table 1. Range Distribution

Range	Type	Relation Symbol
17 to 20	Absolutely necessary	A
13 to 16	Especially important	E
9 to 12	Important	I
5 to 8	Ordinary closeness	O
1 to 4	Unimportant	U

A research was carried out for focusing on relations of all the wastes among each other. In the facility, four major defects were highlighted as discussed earlier i.e. transportation, inventory, motion and defects. Table 2 lists the final results.

Table 2. Relationship of Wastes

Question	1		2		3		4		5		6		Score	Importance
Relation	A	W	A	W	A	W	A	W	A	W	A	W		
T-I	b	2	b	1	b	2	a	2	g	4	b	2	13	E
T-M	a	4	a	2	b	2	b	1	g	4	a	4	17	A
T-D	b	2	c	0	c	0	a	2	g	4	b	2	10	I
I-T	b	2	b	1	a	4	b	1	g	4	b	2	14	E
I-M	a	4	b	1	b	2	c	0	f	2	b	2	11	I
I-D	b	2	c	0	c	0	c	0	d	2	c	0	4	U
M-T	b	2	b	1	c	0	b	1	d	2	a	4	10	I
M-I	c	0	b	1	c	0	a	2	f	2	b	2	7	O
M-D	b	2	b	1	b	2	b	1	d	2	c	0	8	O
D-T	b	2	a	2	b	2	a	2	g	4	b	2	14	E
D-I	b	2	b	1	c	0	b	1	d	2	b	2	8	O
D-M	b	2	c	0	b	2	b	1	f	2	c	0	7	O

A = answer and W = weight of each answer (see [3] for details)

Table 3. Relationship of Wastes

F/T	D	O	W	N	T	I	M	E
D	A	X	X	X	E	O	O	X
O	X	A	X	X	X	X	X	X
W	X	X	A	X	X	X	X	X
N	X	X	X	A	X	X	X	X
T	I	X	X	X	A	E	A	X
I	U	X	X	X	E	A	I	X
M	O	X	X	X	I	O	A	X
E	X	X	X	X	X	X	X	A

After observing the relationship of wastes, next step is to write the relationships by forming a from/to (F/T) matrix as shown in Table 3.

After allotting the numbers to this matrix as defined in the range distribution (Table 1), final total percentage matrix or the *waste relationship matrix* was calculated as shown in the Table 4 below.

From the WRM, it is clear that transportation waste is contributing in generating 23% of the total wastes (Table 4). Similarly, next in the sequence are defects, inventory and motion. Therefore, improvement tools were selected to reduce these wastes to enhance the

Table 4. Relationship of Wastes (%)

F/T	D	O	W	N	T	I	M	E	Score	Percentage
D	10	0	0	0	8	4	4	0	26	17%
O	0	10	0	0	0	0	0	0	10	7%
W	0	0	10	0	0	0	0	0	10	7%
N	0	0	0	10	0	0	0	0	10	7%
T	6	0	0	0	10	8	10	0	34	23%
I	2	0	0	0	8	10	6	0	26	17%
M	4	0	0	0	6	4	10	0	24	16%
E	0	0	0	0	0	0	0	10	10	7%
Score	22	10	10	10	32	26	30	10	150	100%
	15%	7%	7%	7%	21%	17%	20%	7%	100%	
Based On:	A=10	E=8	I=6	O=4	U=2	X=0				

productivity and bring the cycle time within takt time.

4.2 Layout Modification Line Balancing

Waste of transportation is mainly caused by the problems in layout. Current lay out of the facility is shown in Figure 3. Goods were transferred to packing through conveyor. A tray man inspects the gloves and then forward them to inspection. Next step is pad printing, then plastic protector addition, bundle making and then final bundle packing. Lastly, the ready cartons were transferred to pallet.

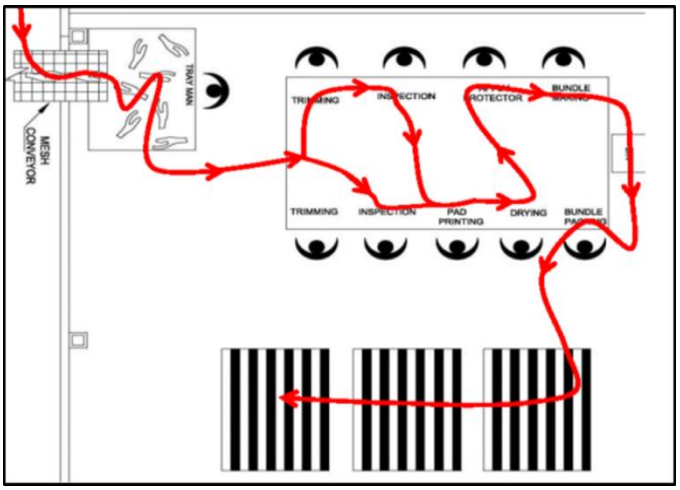

Figure 3. Current (as-is) Layout

Even distribution of task over the work station so that idle time of man and machine can be minimized is said to be line balancing. It is optimized operation technique which has significant industrial importance in lean system [8].

In line balancing bottlenecks and starving problems are tackled and eliminated. An ideal (balanced) line usually follows single piece flow (zero inventory), minimizes waiting and improves quality by ensuring that any defects are caught as soon as they are produced and thus no defects are moved down the line. Thus, it can be noticed that line balancing is the right choice of tool to eliminate the wastes identified by WRM.

Usually the concept of line balancing is applied in assembly line but at the selected facility, it was successfully implemented and executed. This concept of line balancing is somewhat different from traditional implementation but basic concept remains same. The current state of the different stations that were involved in packaging is shown in Figure 4.

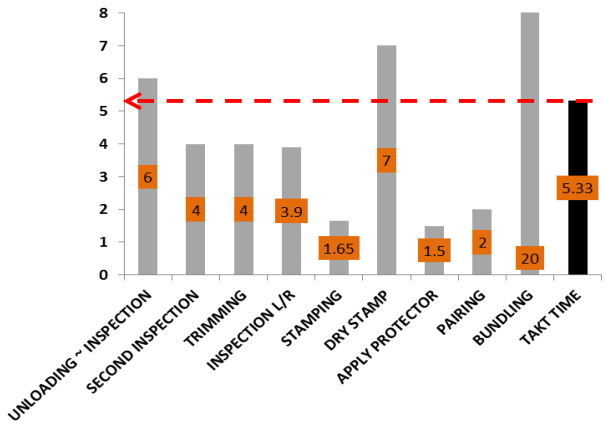

Figure 4. Current (as-is) Load Chart

An improved layout is shown in Figure 5 below. The feasible layout have an e-tone system (conveyor) and an on-line platform tray man, trimmer and pad printing option. While the packing area was converted to two inspectors, plastic sheet cover, pairing, bundling and then pallet. On line platform expansion helped in improving the layout. Similarly, an improved (balanced) line was obtained as a direct consequence of layout changes (Figure 6).

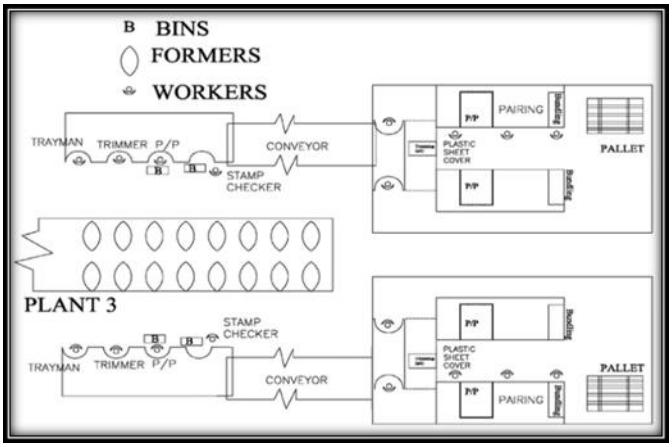

Figure 5. Improved (to-be) Layout

Major wastes that were removed included transport and inventory while motion was also reduced. Transportation and inventory values of current and improved states are compared in Table 5.

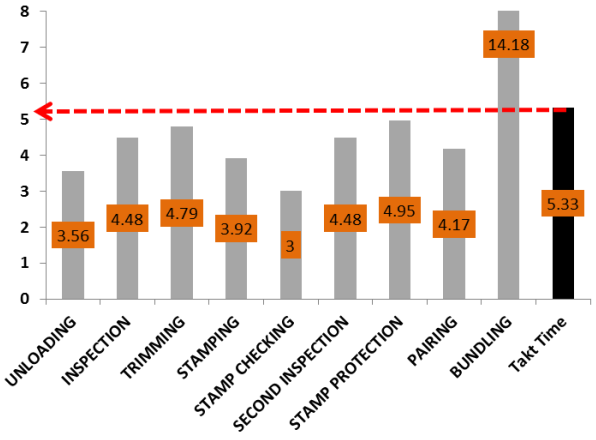

Figure 6. Improved (to-be) Load Chart

Table 5. Transportation& Inventory Comparison

	AS-IS	TO-BE
Glove travelling distance (unloading~carton making)	70 feet	57 feet
Glove travelling time (unloading~carton making)	8 min	2.41 min
Inventory b/w operations	262 DP	12.25 DP
No. Of workers	7	7
No. Of workers (future state)	7	5

Table 6. Red Tag Activity Log

S.No.	ITEM NO.	STATUS	LOCATION	APPROVED BY	COMMENTS
1	Showering Tank 01	Red Tagged	PVC Floor b/w Plant 3 & 4	Production	Cannot be removed as will be utilized in future
2	Showering Tank 02	Red Tagged	PVC Floor b/w Plant 4 & 5	Production	Cannot be removed as will be utilized in future
3	Showering Tank 03	Red Tagged	PVC Floor b/w Plant 3 & 4	Production	Cannot be removed as will be utilized in future
4	Pre Gel 2 Box	Red Tagged	Under Pre Gel 2 Oven Plant 3A	Maintenance	Cannot be removed as it is expensive and req. safe place
5	Liner Rack	Red Tagged	Backside of Plant 3	Production	Will change place in future
6	Spraying Chamber	Red Tagged	At Plant 3 Side B	Production	Cannot be removed as will be utilized in future
7	Insertion Empty Bins	Red Tagged	At Plant 3 Side B	Production	Bins relocated
8	Top Tank	Red Tagged	At Plant 3 Side B (2nd Dip)	Production/Mixing	Has been utilized
9	Liner Shelf	Red Tagged	At Plant 3 Side A	Production	Removed from location
10	Inspection Table	Red Tagged	At Plant 3 Side A	Production	Removed from location
11	Moveable Board	Red Tagged	Front Side of Plant 3	Production	Req. by production for protection against dust

5S

The concept of 5S is constituted on the basis of Kaizen. 5S is used by 5 different Japanese words which are Seiri (Sort), Seiton (Set in order), Seiso (Shine), Seiketsu (Standardize) and Shitsuke (Sustain). These five S focus on effective work place and work procedure and their proper implementation allow for the application of continuous improvement by all the employees within the organization [7].

Sort

Sorting requires the separation of necessary and unnecessary items. Red tagging the unnecessary items is the common step to be taken during sort. The items which are unnecessary for the workplace are marked with red tag and relocated in a review area. After the sorting has been finished, the items tagged red are assessed and then finalized whether to keep on plant or remove from plant and move to drum yard. Results obtained by red tagging are shown in Table 6.

Set in order

All the available equipment of plant was arranged as per the necessities and its use. An example is shown in Figure 7.

Figure 7. Set in Order

Shine

Cleaning and painting of whole plant was done. Marking of floor was performed and better aesthetics were created. Figure 8 shows an example of shine activity being carried out.

Figure 8. Shine

Standardize

Area for putting the right thing in right place was performed and all the equipment were given standard position. Floor marking is evident from Figure 9.

Figure 9. Standardize

Sustain

For sustaining the 5S activities, performance chart was added on visual board and weekly discussion is also set to occur as shown in Figure 10.

Figure 10. Sustain

5 RESULTS

Outcomes of the waste assessment was utilized in the implementation of lean manufacturing concept i.e. line balancing leading to layout change, one piece flow and 5S. These tools lead to valuable decrease in identified wastes of transportation, inventory, motion and defects and thus result in the improvement of produced quantity and decreased lead time. Summary of improvements achieved are listed in Table 8.

Table 8. Summary of Improvement

S.No.	METRIC	AS IS	TARGET	ACHIEVED	QTY. CHANGED	% CHANGED
1	**Value Added (sec) (Unloading to Carton)**	36.00	26.47	34.47	1.53	4%
2	**Total Lead Time (hrs) (Unloading to Carton)**	5.00	0.95	1.00	4.00	80%
3	**Layout**					
a	Glove travelling distance (RFT) (Unloading to Carton)	70.00	55.00	57.00	13.00	19%
b	Glove travelling distance (min) (Unloading to Carton)	8.00	2.00	2.41	5.59	70%
c	Inventory b/w operations (DP)	262.00	10.00	12.25	249.75	95%
d	No. of Workers	7.00	5.00	7.00	-	0%
4	**Production (DP)**	450.00	635.00	600.00	150.00	33%
5	**Inventory WIP (DP)**	682.00	150.00	350.00	332.00	49%
6	**5S Level of Excellence**	1.00	5.00	3.50	2.50	150%

6 CONCLUSIONS

Gut feelings and experience are sometimes not enough in order to bring the change, remove wastes and create improved environment. As per an industry practice, it has been noted that some of the waste cannot be observed or acknowledge as per their intensity by line manager. This research paper proved that waste assessment can be applied in high volume and high variety industry. Also, waste assessment matrix could be used a tool that identifies the exact targets for productivity improvement purposes.

Wastes identified by WRM were subsequently improved by using the tools such as layout change, line balancing and 5S implementation. The results showed real improvements and proved that the wastes as identified by WRM were mainly the causes of disruptions and thus the value was not flowing to the customers. However, by removing these wastes, not only productivity was improved, but the production system was reoriented to ensure the flow of value to the customers in a timely manner which is what required in a lean system. However, this must be kept in mind that these changes could only be sustained only if the continuous improvement route is followed rather than *once in a while* approach.

This model have not only emphasised on a single waste but it has also given the path of continuous improvement i.e. after removal of two or three big waste, it is the time to move to next waste and its removal. There are still some stones un-turned in this methodology of waste assessment model and major one is its implementation in service sector and comparison of results. However, the results in this study suggest in equal relevance in a high variety/high volume production system.

ACKNOWLEDGEMENTS

Authors would like to pay the gratitude to each and every individual involved in the implementation of this project.

REFERENCES

[1] Taiichi Ohno, "The Bible of Toyota Production System", pp. 85/188, Mar 1978

[2] T. Melton, The benefits of lean manufacturing "What Lean Thinking has to Offer the Process Industries", Institution of Chemical Engineers, 2005

[3] I A. Rawabdeh, "A model for the assessment of waste in job shop environments", International Journal of Operation & Production Management, Vol. 25, 2005

[4] Lean manufacturing and the environment, http://www.epa.gov/lean/environment/ (accessed on 12.04.2015)

[5] E R K Mehta, D Mehta, N. K. Mehta, An Exploratory Study on Implementation of Lean Manufacturing Practices (With Special Reference to Automobile Sector Industry), 2012

[6] Manufacturing, http://www.hcltech.com/manufacturing/lean-manufacturing (accessed on 12.04.2015)

[7] T. Karkosazka, J. Honorowicz, "Kaizen philosophy a manner of continuous improvement of processes and products", Journal of achievements in materials and manufacturing engineering, Vol. 35, 2009

[8] N Kumar, D Mahto, "Assembly line balancing: A review of developments and trend in approach to industrial application", Global Journal of researches in engineering and industrial engineering, Vol. 13, pp. 1, 2013.

COMPARISON IN PROFILE AND LEAD VARIATION OF SPUR GEAR DEVELOPED BY CNC WIRE-EDM AND HOBBING

Abdul Rahim*, Aqueel Shah, Salman Nisar
Department of Industrial Manufacturing Engineering and Management, PN Engineering College, National University of Sciences and Technology, PNS Jauhar, Karachi, 75350, Pakistan

*Corresponding author. Tel.: +092(0)300-2536460
E-mail address: a.rahim@modtech-nz.com

Abstract

Hobbing is one of the few conventional methods for gear manufacturing and requires special purpose machine and separate cutters for different gear specifications. This paper reports an alternate method of spur gear manufacturing by CNC wire EDM or commonly known as wire electric discharge machining (WEDM). Comparative study was conducted between hobbing and WEDM by manufacturing gears of same module with two different pressure angles and subsequently gear characteristics viz. gear profile and lead were measured and evaluated. The quality of spur gears manufactured by CNC Wire EDM were found superior than the hobbed gears. On the basis of comparative analysis of spur gear characteristic between WEDM and hobbing, it was concluded that former provides better solution particularly for low production requirement and when special purpose hobbing machines and its cutters are not obtainable.

Keywords: Spur Gear; Hobbing; WEDM; Profile; Base Tangential Line.

1 INTRODUCTION

Gears are among the most important element of a machine because of its function and capability to transmit motion and power. Each industry use different types of gear depending upon its application. Spur gears are the most common types of gears and used to transmit motion between parallel shafts or between a rack and a shaft. Two main conventional methods viz. gear forming and gear generation are used for manufacturing of gears. In gear forming method, cutting tool has identical shape to that of shape of the space between the gears. This method of gear manufacturing can be accomplished by milling and broaching operations. In gear generation method, gear flank is generated as outline of the subsequent position of cutter. This method can be accomplished by hobbing and shaping process respectively [1].

Wire electric discharge machining (WEDM) is a non-conventional machining process and can form intricate geometries with considerable dimensional accuracy which were time consuming and to certain extend impossible. Even mirror finish surface can be achieved depending on cost and time factor. WEDM process is applicable to cut all metals: steel, aluminium, brass, titanium, alloys, super alloys of all types and hard materials [2]. WEDM high accuracy and unattended operation attracts user over conventional EDM process where hours of work and skill is needed to first develop electrodes and subsequent operation of polishing and grinding. WEDM reduced fabrication time by around 37% and processing time 66%. Furthermore its machinability of hard materials makes it useful to develop special purpose tools and cutters. WEDM with its distinct features provides an alternate solution for gear manufacturing especially when special purpose hobbing cutters and machines are not obtainable.

Shape of gear tooth from root to tip of gear tooth is termed as gear profile. Operating or functional portion of profile is that which is in contact during meshing of gear. The measuring probe of gear measuring machine aligns with the test gear at the middle of gear face. Mostly gear measuring machine use the generative principle to create reference profile which is a straight line and it is compare with gear's actual profile which is traced and recorded graphically.

Kapil and Neelesh [3] conducted a comparative study on high-quality miniature gears manufactured by two processes namely hobbing and WEDM. Their study was focused only on manufacturing miniature gears of single module. The miniature gears are categorized as meso-gears and micro-gears. Meso-gear have outside diameter in the range of 1–10 mm and micro-gear has outside diameter less than 1 mm. This study was related to functional

performance and service life of gear depending on surface roughness, material properties, macro & micro-geometry and other surface integrity aspects.
Veera [4] investigated the method of spline manufacturing by milling machine. Spline is similar to gear and are manufactured on hobbing machine. The purpose of spline is to make number of keys on a shaft to stop rotational motion between shaft and attaching flange. The tool is usually developed by CNC wire cut machine and embedded on a wheel which is finally used as cutting tool for spline on milling. Gears can also be manufactured by this method. The drawback of this manufacturing method is that it cannot be used for mass production as single tooth cutter for milling worn out quickly leading to inaccuracy of the resultant product.
Huertas et al. [5] proposed a method of manufacturing a spur tooth gear in Ti_6Al_4V alloy (grade 5) using a wire electrical discharge machine (WEDM). MATLAB program was used to generate geometrical model. WEDM is set to electro-erosion parameters tested for Titanium alloy. The process parameters (power, pause, voltage etc.) were based on the EDM charts. The Taguchi orthogonal array method was chosen to obtain the optimum values for cutting the material. The MATLAB generated interpolation points. This program simplified the task of solving the equations originated by the mathematical model which allowed the wire path to be calculated. WEDM employed in this study provided an alternative solution for machining electrically conductible materials which are difficult to process using conventional machine tools such as milling, turning and boring.
Bergseth et al. [6] investigated the influence of surface roughness on contact condition and subsequently its effect on load transmitted at contact condition and life of gear. Their study was confined to surface measurements of spur gears developed by four different methods. Two pre-hardened gears were machined using honing and grinding respectively while other two gears were machined in the non-hardened condition using hobbing followed by green shaving.
Lin et al. [7] investigated optimization method of manufacturing Spiral Bevel Gear. A mathematical model of an ideal spiral bevel gear-tooth based on the Gleason hypoid gear generator mechanism was proposed. The tooth surface sensitivity matrix to the variations in machine-tool settings and surface variations of a real cut pinion and gear with respect to the theoretical tooth surface was investigated. An optimization procedure for finding corrective machine-tool settings was then proposed to minimize surface variation of real cut pinion and gear-tooth surfaces. The results revealed that surface variation of real cut gear-tooth surfaces with respect to the ideal ones can be reduced to only a few microns. It was found that the proposed method for obtaining corrective machine-tool settings can improve the conventional development process and applied to different manufacturing machines and methods for spiral bevel gear generation.
The aim of this paper is to authenticate spur gear manufacturing by WEDM as an alternate to hobbing process by comparing gear characteristics used in quality control. These quality control characteristics viz. gear profile and lead were measured, analyzed and compared for both processes (i.e. WEDM and hobbing). This study provides an alternate method for local industry and helped build an awareness of the capability of non-conventional technologies.

2 EXPERIMENTATION

Four spur gears of specification mentioned in table 1 were manufactured by both hobbing and WEDM process. Material used for these gears is Alloy Steel 8620 (Nickel-chromium-molybdenum steel). Chemical composition of alloy Steel 8620 is 0.18-0.23C, 0.7-0.9Mn, 0.035P (max), 0.15-0.3Si, 0.0-0.6Cr, 0.4-0.7Ni and 0.15-0.25Mo while tensile strength is 536.4 Mpa [9]. For hobbing, two gear blanks of 51 mm diameter and 20mm in thickness are developed. Similarly two side grinded gear blanks of 80 mm diameter and 20mm in thickness are prepared for WEDM processes.

Table 1. Gear specification table

Gear A	Module = 3, Pressure Angle = 14.5º, Number of teeth Z = 16
Gear B	Module = 3, Pressure Angle = 20º, Number of teeth Z = 16

Dowding & doll v8 gear hobbing machine of England is used which can produce maximum module of 3.5 with maximum face width of 181mm, hob spindle speed 246 rpm, work feed 0.008-0.160 i.p.r, diameter of hob arbor 19mm to 25.4mm, maximum of hob diameter 57mm, maximum hob length 57mm fitted with 2 H.P/1.5 kW motor. High

speed steel (HSS) M2 cutter of module 3 is selected for hobbing process. Hob speed and feed rate of 400 rpm and 0.25 mm per revolution were used based on preliminary experiments.

Chmer CNC Wire EDM Model G32F of Taiwan was used to manufacture gear of module 3. CNC Wire EDM can travel in X, Y axis 360mm x 250 mm and it can hold work piece of 300 Kg (max) having dimension 725x560x215 mm^3 with maximum feed rate of 800 mm/min. Cutting Accuracy of machine is ±15 µm. Brass wire of Vertex Taiwan with 0.25 mm diameter (Brass Zinc ratio of 65/35) equivalent to Alloy No. JIS-H3260 C2700 having tensile strength of 980 N/mm2 was used in WEDM process. Operational parameters of WEDM set to 20V as voltage, 34V as servo voltage, 3ms as pulse-on time, 11ms as pulse-off time and 1.45 mm/min as wire feed rate. These parameters were obtained from operation manual Chmer CNC Wire EDM Model G32F [10]. Gear profile was developed using Solid Works and subsequently imported in MasterCAM software to generate G-Codes for CNC WEDM.

2.1 Gear profile and lead variation measurements

Gear profile and lead variation is measured on David Brown Profile Measuring Machine No. 18. The principle of involute profile measurement is based on a geometric property that a line normal to an involute curve is a tangent to the base circle [11]. Thus an involute is eventually the co-ordinates of heights to a tooth and angles from the base circle. Two base circle discs of sizes 45.11mm & 46.47mm were developed for profile and lead measurement of gear A and gear B respectively as mentioned in table 1. Base circle disc measurement is based on formula:

Base circle diameter = PCD x Cos (Pressure angle)

These discs are grinded on both side. Involute profile variation is observed by this base circle disc that travel on straight edge as shown in figure 1. A small pressure was applied between disc and straight edge which lead them to move simultaneously. Stylus mounted directly above the straight edge traces curve that depicts the variation in involute profile of the gear. Same machine is used for lead variation measurement and mechanism is shown in figure 5. Ideally curve on the graph should be vertical and deflection of the stylus is the measure of imperfection or variation from desired profile.

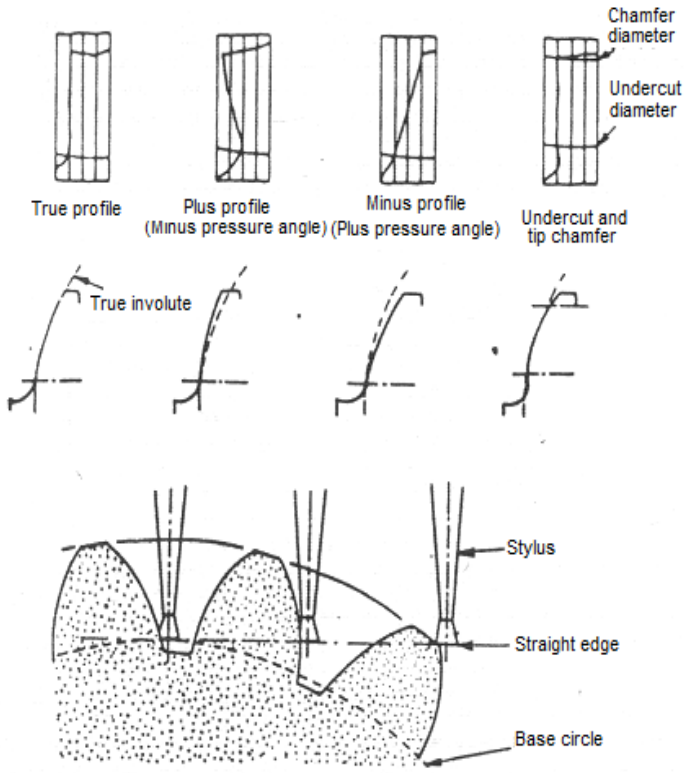

Figure 1. Principle of profile measurement

Following are the graphs of profile deviation traced and recorded from the machine for the Gear A mentioned in table 1. Inspection is done on all four gears two each from WEDM and hobbing. Total four graphs were recorded and in each graph there are four curves showing deviation in profile of four teeth of a gear. Figure 2 and figure 3 show graphs for profile deviation.

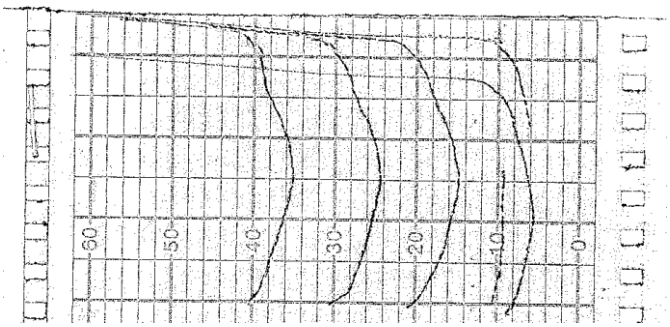

Figure 2. Gear profile of 4 teeth of Gear A manufactured on WEDM.

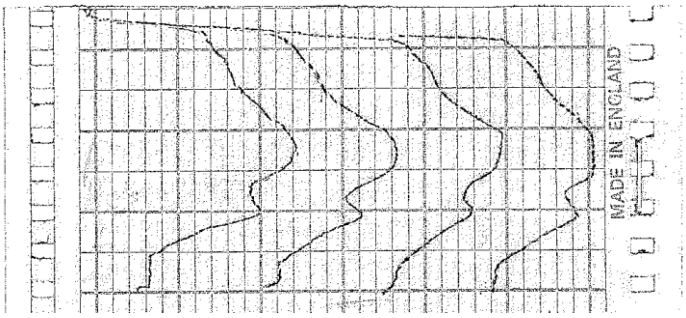

Figure 3. Gear profile of 4 teeth of Gear A manufactured on gear hobbing

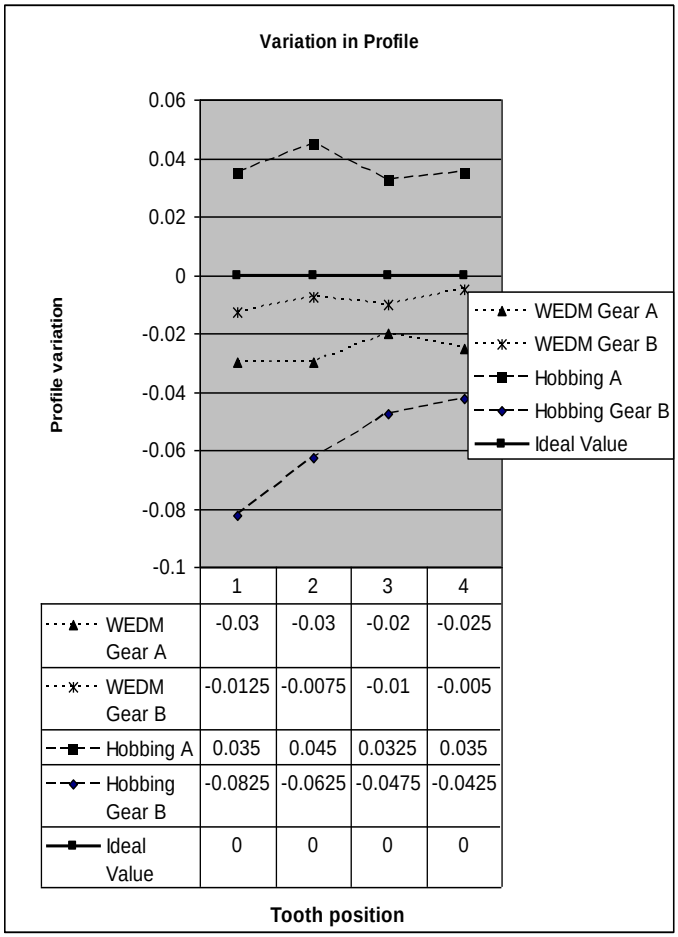

	1	2	3	4
WEDM Gear A	-0.03	-0.03	-0.02	-0.025
WEDM Gear B	-0.0125	-0.0075	-0.01	-0.005
Hobbing A	0.035	0.045	0.0325	0.035
Hobbing Gear B	-0.0825	-0.0625	-0.0475	-0.0425
Ideal Value	0	0	0	0

Figure 4. Gear profile variation graph of Gear A & B manufactured on WEDM and hobbing.

As discussed earlier, in ideal condition the line on graph should be vertical which shows no deviation or zero deviation in gear profile. For calculation purpose, the region of graph taken under consideration is one row below from start of curve and two row up from bottom of curve and a vertical line is drawn from bottom of the curve. If graph goes on left side, it shows that gear is over size. Similarly if graph goes on right side, it shows gear is undersize. One box width of graph represents 0.01mm. On the basis of these graphs, data is tabulated and graph is drawn in figure 4 showing deviation of gear profile in four different gear-teeth located 90° apart with each other mentioned as positions# 1, 2, 3 & 4. Variation is tabulated and depicted in graph for all four gears as shown in figure 4.

As mentioned earlier same machine can measure lead variation by moving stylus in vertical direction along tooth flank. Working principle of lead variation measurement is shown in figure 5.

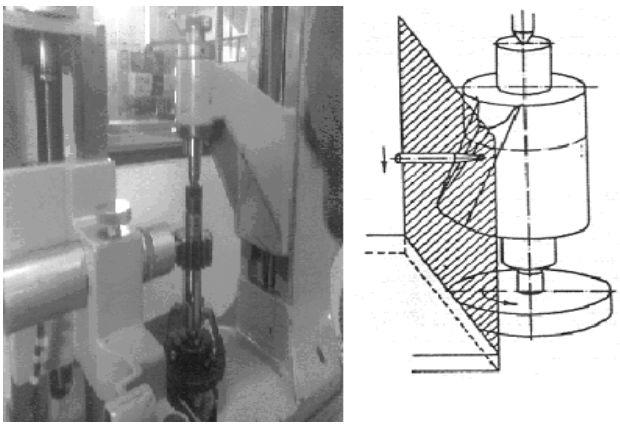

Figure 5. Picture of David Brown Profile on left and its principle for lead measurement on right

Similar procedure mentioned earlier is used for tracing and recording lead deviation curves for all four gears and is shown in figure 6 and figure 7. On the basis of these graphs, tables and graph are drawn in figure 8.

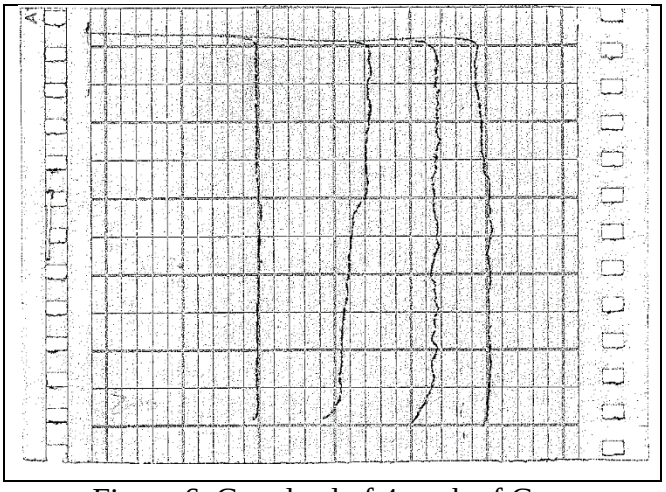

Figure 6. Gear lead of 4 teeth of Gear manufactured on gear WEDM

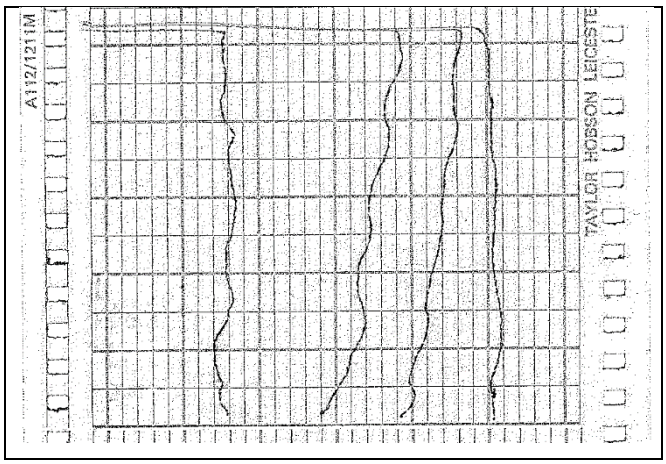

Figure 7. Gear lead of 4 teeth of Gear manufactured on gear hobbing

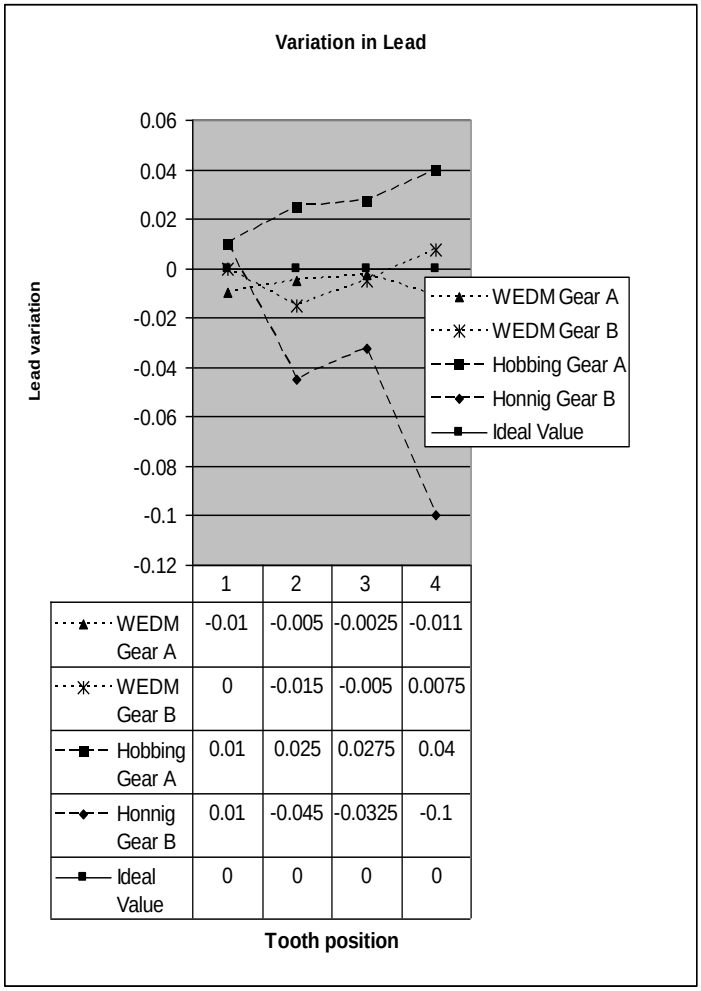

Figure 8. Gear lead variation graph of Gear A & B manufactured on WEDM and hobbing

3. TOOTH PROFILE AND LEAD VARIATION ANALYSIS

Tooth profile and lead variation analysis shown in table 2. Since in ideal condition deviation or error in profile should be zero, therefore, RMSD (Root Mean Square Deviation) values for all four gears are calculated based on observation in above figures 4 & 8.

Table 2. Comparison of RMSD values of two characteristics of gears A & B of module 3 manufactured by WEDM and gear hobbing

Gear Quality Character-istics	Pr. Angle	RMSD of WEDM Gear	RMSD of Hobbing Gear	Difference (%)
Profile Variation (mm)	14.5°	0.027	0.037	27.03
	20°	0.009	0.061	85.25
Lead Variation (mm)	14.5°	0.008	0.028	71.43
	20°	0.009	0.057	84.21

Percentage difference of RMSD in table 2 shows gear profile and lead of all four gears developed by WEDM are more accurate than gears developed by hobbing process.

WEDM process based on the principle of removing material from a part by repeated electrical discharges between brass wire as electrode and blank as work piece. Due to erosive effect of electric discharge from gear blank and brass wire causes removal of material irrespective of blank hardness. Since in WEDM process there is no direct contact between gear blank and wire so there is no mechanical stresses and vibration problem [2] results in less variation in lead. On other hand hobbing machine has two skew spindles, one is fitted with gear blank and other with hob and due to continuous engagement and vibration causes deviation in lead. Table 2 shows that difference in RMSD of both process and confirmed the superiority of CNC Wire EDM (WEDM) process.

WEDM consist of slide fitted with ball screws which are numerically controlled that results in better profile accuracy. Also accuracy mainly depend upon CNC Wire EDM parameters, condition and type of wire used and wire guides. Optimal parameters were set given in Chmer machine's manual. Choice of WEDM wire can be molybdenum or brass. Molybdenum wire is reusable but in this case precision and finish of final product will suffer as wire gets thin due to repetitive use. For the purpose of this study brass wire was selected which is used for one time resulting in

better accuracy and surface finish. On other hand in gear hobbing process a blank is cut into shape of gear progressively by series of cuts with a hob cutter. In hobbing all motions are rotary and both gear blank and hob rotate constantly meeting with each other in a manner such that two gears are mesh with each other and distance between both the axis of gear blank and hob continuously decreases to generate the gear profile on blank. Due to continuous engagement hob cutter results in its wear and ultimately causes variation in profile. Any error in hob results in thick and thin teeth in the blank [11]. Wear in gear-hob effects on accuracy of gear profile and this can be observed and inspected after completion of manufacturing process. The percentage difference of this gear characteristic of both processes mentioned in table 2 also confirms superiority of CNC Wire EDM (WEDM).

4. CONCLUSIONS

This paper presents comparison and analysis of gear characteristics such as gear profile and lead developed by two different processes namely hobbing and CNC wire EDM.

Results show that CNC Wire EDM can manufacture spur gear with more accuracy in respect of profile and lead. Also it shows that we can eliminate additional gear sheaving process which is usually needed to achieve more accuracy.

Hobbing is an special purpose machine and it needs different cutter for each module whereas CNC Wire EDM is general purpose machine.

CNC Wire EDM has an additional advantage of its capability to cut hard materials.

Also hobbing is restricted to only external gears whereas CNC Wire EDM can be used for both internal and external gears. CNC Wire EDM can be a good alternate to hobbing for low production, reverse engineering, prototyping and research work.

The outcomes of this research are useful for engineers to manufacture gears including corrected gears with alternate method of gear manufacturing for low production and research work particularly in case of unavailability of hobbing machine and cutter. However further work is needed to include other quality control gear characteristics. Also research is needed in manufacturing of helical gear.

REFERENCES

[1] Marinov V. (2013). Gear manufacturing. Tharindu Chathuranga. P123- P128.

[2] Moulton D. B. (2012).Wire EDM 'The Fundamentals'. EDM NETWORK Sugar Grove, IL USA.

[3] Kapil Gupta, Neelesh Kumar Jain (2014), Comparative Study of Wire-EDM and Hobbing for Manufacturing High-Quality Miniature Gears, Materials and Manufacturing Processes, Volume 29, Issue 11-12. P 1470-1476

[4] Veera S., Mamidi S., (2012), manufacturing an involute spline cutting tool on Wire EDM using Solid Work and Esprit, California State University, Northridge.

[5] Huertas Talón J. L., Cisneros Ortega J. C., Gómeza C. L., Sanchoa, E. R., Olmosa E. F. (2010), Manufacture of a spur tooth gear in Ti_6Al_4V alloy by electrical discharge, Department of Design and Manufacturing Engineering, University of Zaragoza, Spain. Also published by Department of Industrial and Mechanical Engineering, University of Americas-Puebla, Mexico, Computer-Aided Design, Vol 42, P 221-230.

[6] Bergseth E., Sjoberg S., and Bjorklund S. (2012), Influence of real surfaces topography on the contact area ration in differently manufactured spur gears, Tribology International Elsevier, Vol 56, P 72–80.

[7] Lin C. Y., Tsay C. B., and Fong Z. H. (2001), Computer Aided manufacturing of spiral bevel and hypoid gears by applying optimization techniques-4, Journal of Materials Processing Technology, Vol 114, P 22-35.

[8] Suh S. H., Jih W. S., Hong H. D. and Chung D. H. (2001), Sculptured surface machining of spiral bevel gears with CNC milling-6, International Journal of Machine Tools & Manufacture, 41, 83-3-830.

[9] American Iron and Steel Institute (2014).Steel Works: the online resource for steel. Available at http://www.steel.org/.

[10] Chmer operational manual available at http://www.chmer.com/uploads/product/download/product121.pdf

[11] An overview of gear manufacturing processes. Available at http://drishtikona.files.wordpress.com/2012/08/ch4.pdf

AN EFFICIENT METHOD OF COLLISION DETECTION FOR 5-AXIS CNC MILLING

Aqeel Ahmed[1,*] Liming Wang[2] and Amir Iqbal[1]
[1]Industrial and Manufacturing Engineering Department, NED University of Engineering & Technology, Karachi, Pakistan
[2]Research Centre for Sustainable Manufacturing Shandong University Jinan, China

[*]Aqeel Ahmed. Tel.: (92-21) 99261261-8 Ext. 2463;
E-mail address: sohaibaqi@neduet.edu.pk

Abstract

The shortest cutter length determination without collision for the 5-axis milling machining is a critical task. Short tool length increases the rigidity of the cutting system and chatter stability. In this study a new interference detection method of the complete cutting system with the work in process model as well as with the fixture is developed. The complete cutting system includes spindle (cylinder), tool holder (truncated cone) and cutter (cylinder). All these element of the cutting system form the surface of revolution around the cutter axis. The surfaces of the work-in-process model and the fixture model can be represented as the point cloud data. The KD-tree data structure is employed on the point cloud data. Implementation of this methodology results in efficient searching of possible candidate points for the collision in the system. Other scope of the proposed algorithm is to select the tool holder to minimize the overhang tool length.

Keywords: 5-axis milling; Collision detection; shortest cutter length; K-d tree data structure.

INTRODUCTION

Five degrees of freedom are the minimum required to obtain maximum flexibility in the tool orientation relative to the work-piece. On the other hand these degrees of freedom can increase the possibility of global collision between the moving parts. Global collision means accidental contact of non-active cutting portion of the cutting system (tool, tool holder and spindle) with the other moving parts of the machine such as work piece or fixture or table. The main objective of this work is to determine the shortest possible cutter length for machining the complete part without any global collision. The most important parameter in static tool deflection is the tool slender parameter 'L3/D4' [1,2,3]. Most of the machining simulation software, such as CATIA, can generate the 5-axis machining tool path and different sizes of tool holders can be modelled. Collision checking is performed with the initial stock material and if a collision is found, there are two possibilities to overcome this difficulty. The first is to increase the length of the tool and the second is to change the model of the tool holder. If we fix the tool holder model, an optimal length is needed to avoid collision. All existing algorithms [4,5,6] are capable to detect collision between cutting system and other moving parts i-e work piece and fixture but they did not remove the collision by optimum tool length. In this research a new collision detection method is introduce, which is also capable of given the solution of collision removal with the optimum tool length.

3 METHODOLOGY

For the collision detection, it is necessary to model the possible candidate elements (solid bodies) of the collision for the machining system. Different 5-axis machines configuration gives the different number of possible candidate elements for the collision detection. In most of the 5-axis machining systems possible candidates are complete cutting system, work in process model and the fixture. In this study, possible candidate elements for the collision are divided into two groups. One is the complete cutting system and the other elements are work in process model and fixtures. After the modelling of the possible candidates elements for the collision following steps are used

I. Five axis machining tool paths are generated in the CAM software.
II. At each cutter location, determining the orthogonal range of the spindle and the tool holder in the part coordinate system.

III. From the orthogonal range, determine the possible candidate points of work in process model and fixture by using KD-tree data structure.

IV. By increasing the cutter length (change in the mounting position of the tool), collision can be avoided. Increase and find the optimum (shortest) length of the cutter for the complete machining of the part.

4 MODELLING OF THE SOLID BODIES

4.1 Cutting system modelling:

Due to the axial symmetry nature of the cutting system, the spindle is represented as a cylinder and the tool holder as a truncated cone and the complete cutting system is model as the surface of revolution. Surface of revolution can be represented with two parameters and given as

$$S_n(u \quad \varphi) = R_z(\varphi) \cdot L_n(u) \quad \begin{pmatrix} 0 \le u \le 1 \\ 0 \le \varphi \le 2\pi \end{pmatrix} \quad \text{for n=1,2,3} \qquad (1)$$

$$\text{Where, } R_z(\varphi) = \begin{bmatrix} \cos(\varphi) & -\sin(\varphi) & 0 \\ \sin(\varphi) & \cos(\varphi) & 0 \\ 0 & 0 & 1 \end{bmatrix} \quad 0 \le \varphi \le 2\pi$$

Where 'L' represents the profile of the revolution and 'n' represents the no. of the cutting system elements (cutter, tool holder and the spindle)

4.2 Work in process model:

Different CAM softwares are able to generate tool paths and also capable to store the updated stock after each cutting process. These updated stocks are called in-process work piece models. For an illustration a rough tool path is generated in CATIA and from STL file of the in-process work piece model, a tessellated triangular mesh surface is generated. Demonstration of the work in process model is shown in figure-1 and the tessellated triangular representation of the in-process work piece model is shown in figure-2.

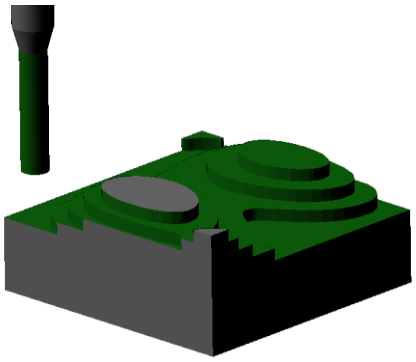

Figure 1. In process work piece model after rough machining operation

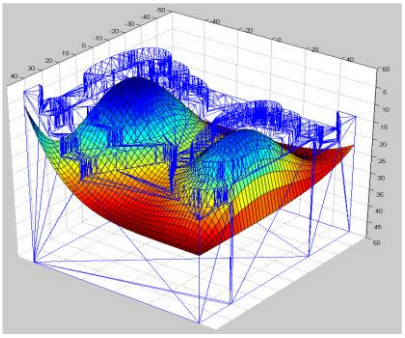

Figure 2. Triangular tessellated representation of in process work piece model

4.3 Point cloud generation:

Randomize points generation with the suitable density (points per unit area) will create point cloud data. In the triangular tessellation representation of the in-process work piece model, point cloud data consist of the vertices of the triangles and randomly generated points on the triangular planes with the suitable density. The method of generating random points on a triangle is well established. For generating the point cloud data of constant density "D" for each triangle, no. of points on each triangle can be calculated as

$$\text{No. of points for a triangle} = \frac{1}{2} \cdot \left| \overline{P_1P_2} \quad X \quad \overline{P_1P_3} \right| \cdot D \qquad (2)$$

Where P_1, P_2 and P_3 are the vertices of a triangle

For the generation of a random point on a triangle, two random numbers r_1 and r_2 at [0, 1] interval are generated and point can be calculated by the following formula as given in the literature [7,8]

$$P = (1-\sqrt{r_1})\cdot \mathrm{P}_1 + \sqrt{r_1}\cdot(1-r_2)\cdot \mathrm{P}_2 + \sqrt{r_1}\cdot r_2 \cdot \mathrm{P}_3 \qquad (3)$$

Example of the point cloud data generation with the density of 0.5 points/mm^2 on the triangular mesh surface is shown in figure-3. No. of points and points on the triangles are calculated by using equations (2) and (3) respectively.

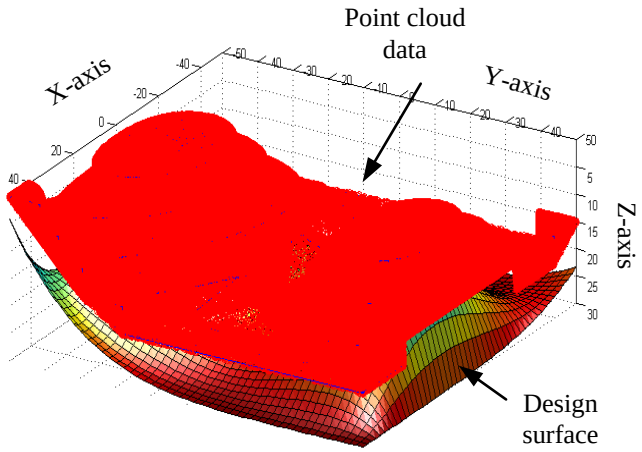

Figure 3. Point cloud generation with the density of 0.5 points/mm^2

5 KD-TREE DATA STRUCTURE APPROACH FOR AN EFFECIENT SEARCHING OF THE COLLISION DETECTION

Kd-tree is a form of data structure from which multiple queries related with the data can be found efficiently. In this research, we are focusing on orthogonal range searching queries i.e report all the points which fall into a rectangular region "R".

First, tool length at any initial mounting position of the tool is considered as the length of the tool and based on this tool length, spindle (cylinder) bottom and top circles in the cutter coordinate system. These circles can be transformed in the part coordinate system by using the transformation matrix from cutter coordinate system to part coordinate system. By taking the projections of the bottom and top circles of the spindle on xy-plane of the part coordinate system, orthogonal range for the spindle can be determined as shown in figure-4

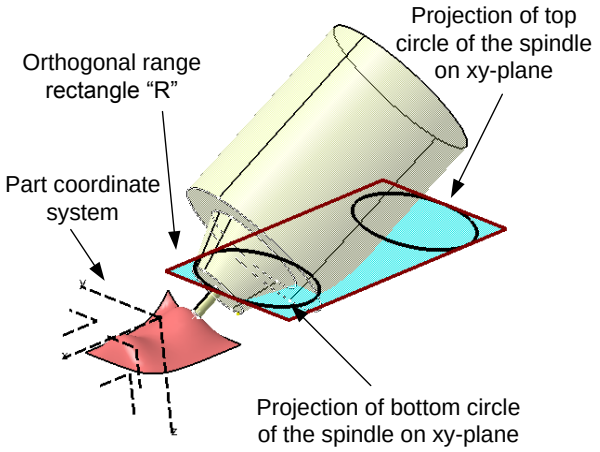

Figure 4. Orthogonal range of spindle at one cutter location (CL) point

For the calculated orthogonal range, possible candidate points for the collision detection can be found with the help of Kd-tree data structure at each cutter location. Following mathematical model is developed for the collision detection with the spindle and removal by optimum tool length

Minimum distance (d)
{Sample point (SP) on work in process model, Tool centre line segment from spindle start point to the pivot point}
Subjected to;
Minimum distance (d) > rs (radius of spindle) (4)

Where, SP ϵ valid point cloud data determined from Kd-tree data structure.

5.1 Steps of algorithm:

Step 1:
Generate the 5-axis machining tool path in CAM software and produce APT file which consist of cutter location points and tool vectors in the part coordinate system.
Step 2:
Determine machine orientation angles from the tool vectors and develop transformation matrix from cutter coordinate system to part coordination T_w^c system for each cutter location.
Step 3:
Calculate the spindle centre line segment in the part coordinate system for each cutter location by using the start point and the end point of the spindle centre

line segment. Following equations can be used to determine spindle centre line segment.

$$\text{line}(u) = (1-u)\cdot P_w^{SS} + (u)\cdot P_w^{SE} \quad \begin{pmatrix} 0 \le u \le 1 \\ \text{line}(u) \in \text{TCLS} \end{pmatrix}$$

$$\begin{bmatrix} P_w^{SS} & P_w^{SE} \end{bmatrix} = T_w^c \cdot \begin{bmatrix} P_C^{SS} & P_C^{SE} \end{bmatrix}$$

$P_C^{SS} = \begin{bmatrix} 0 & 0 & \ell + L_{Th} & 1 \end{bmatrix}^T$ = Spindle start point in the cutter coordinate system

$P_C^{SE} = \begin{bmatrix} 0 & 0 & \ell + L_{Th} + L_S & 1 \end{bmatrix}^T$ = Spindle end point in the cutter coordinate system

Where ℓ = Tool length at initial mounting position.
L_{Th}= Tool holder length
L_S= Spindle length

Step 4:
For each cutter location determine the orthogonal range of the spindle and from the orthogonal range determine possible candidate points of collision by using KD-tree data structure.
Step 5:
Determine the distances between the spindle centre line segment and the possible candidate points of collision calculated in step-4 at each cutter location. If anyone distance is greater than the radius of the spindle there will be collision.
Step 6:
If collision is found use the 1mm increase in length for each loop and determine the collision free tool length for each cutter location.

6 RESULTS AND VERIFICATION OF ALGORITHM IN CATIA:

One five axes machining tool path is generated with 22 CL points. Position and orientation of the tool vectors are shown in above figure-5 and the parameters of the cutting system are given in the table-1

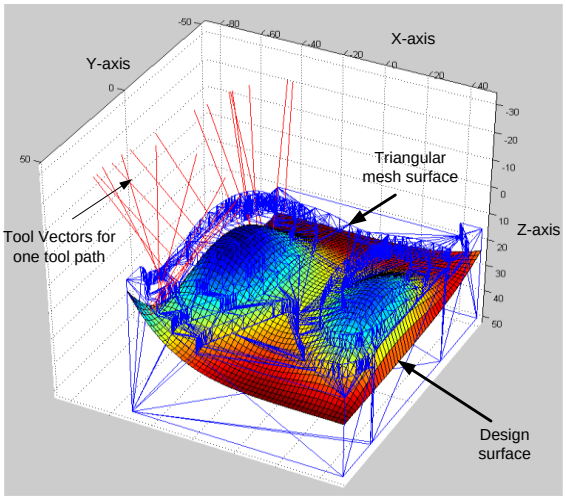

Figure 5. One five axis machining tool path with 22 tool vectors.

Table 1: Parameters of the cutting system

Para-meter	Description	Value
ℓ	Length of the tool at initial mounting position	30mm
r_c	Radius of cutter	5mm
L_{Th}	Tool holder length	50mm
r_i	Bottom radius of tool holder or truncated cone	30mm
r_o	Top radius of tool holder or truncated cone	50mm
L_S	Spindle length	200mm
r_s	Spindle radius	80mm
SP	No. of sample points for Kd-tree structure	610

Based on the above parameters and at each cutter location, no. of points reported from Kd-tree data structure is shown in figure 6 and final results are concluded in the table 2.

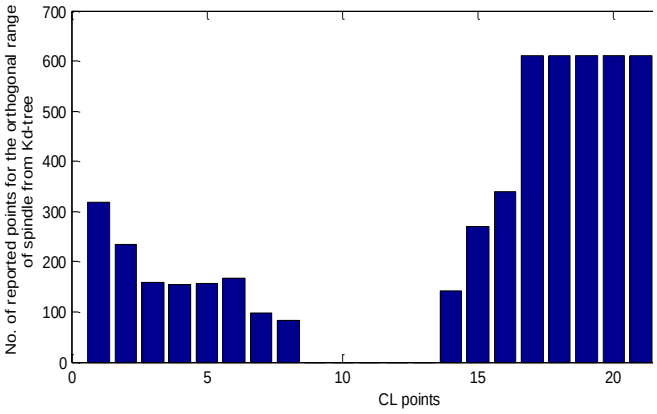

Figure 6. No. of sample points reported by Kd-tree data structure at each cutter location.

Table 2: Incremental length needed at CL 19 & 20 for the avoidance of collision from spindle

Index no. of CL point	19	20	Opt. Length (mm)
For the spindle collision detection, change in length needed at each CL in 'mm'	3.4947	14.710	
Min. length (mm)needed to avoid collision at each CL point	30+3.49 =33.49	30+14.71 =44.71	44.71

CATIA verification at 19th CL point is shown in figure no. 6(a) & (b).

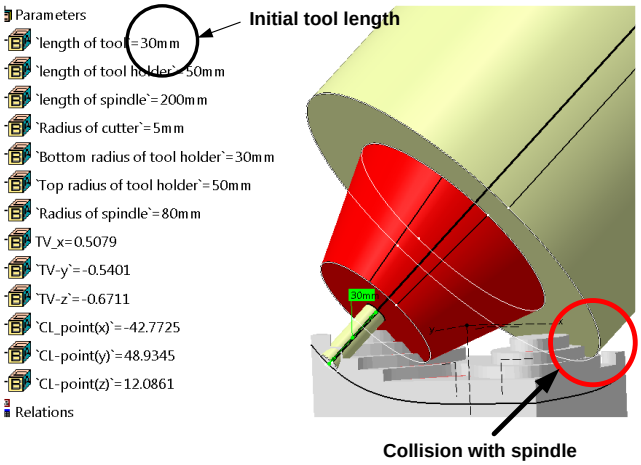

Figure 6(a) -At cutter location 19, with the cutter length of 30mm collision is found with the spindle and tool holder.

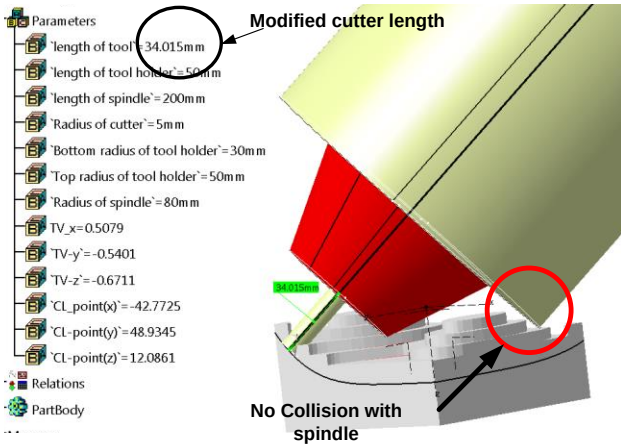

Figure 6(b) -At cutter location 19, with the cutter length of 34mm (determine by algorithm) collision is found with the spindle but collision with tool holder is present.

7 CONCLUSION AND FUTURE WORK:

An efficient algorithm for the collision removal of the spindle by optimum length has been developed for discrete CL points of the five axis machining tool path. This algorithm also has the capability of collision detection and removal of the spindle with the fixture. In the future, algorithm for the collision detection with the tool holder will be required for the collision detection of the complete cutting system.

REFERENCES

[1] Shirase, K.; Altintas, Y.; "Cutting force and dimensional surface error generation in peripheral milling with variable pitch helical end mills"; *In: International Journal of Machine Tools and Manufacture*, vol. 36, pp.567-584; 1996.

[2] Kim, G.M.; Kim, B.H.; Chu, C.N.; "Estimation of cutter deflection and form error in ball-end milling processes"; *In: International Journal of Machine Tools and Manufacture*, vol. 43, pp.917-924; 2003.

[3] L´opez de Lacalle, L.N.; Lamikiz, A.; S´anchez, J.A.; Salgado, M.A; "Effects of tool deflection in the high-speed milling of inclined surfaces"; *In: International Journal of Advanced Manufacturing Technology*, vol. 24, pp.621-631; 2004.

[4] S.Ho, S.Sarma, Y. Adachi, "Real-time interference analysis between a tool and an environment", *Computer-Aided Design* vol. 33, pp. 935-947, 2001.

[5] Oleg Ilushin, Gershon Elber, Dan Halperin, "Precise global collision detection in multi-axis NC-machining", *Computer-Aided Design* vol. 37, pp. 909-920, 2005.

[6] T.D. Tang, Erik L.J. Bohez, Pisut Koomsap, "The sweep plane algorithm for global collision detection with work piece geometry update for five-axis NC machining", *Computer-Aided Design* vol. 39, pp. 1012-1024, 2007.

[7] G. Turk, "Generating random points in triangles" *In: Glassner AS*, editor. *Graphic Gems. Academic Press*, 1990.

[8] O. Robert, F. Thomas, C. Bernard, D. David, "Shape distributions" *ACM transactions on graphics*, vol.21, pp. 807-832, 20

EVALUATION OF MAINTENANCE MANAGEMENT PRACTICES IN AUTOMOTIVE INDUSTRIES OF PAKISTAN

Javeria Younus[1], Dr. Muhammad Fahad[1,*] and Dr. Maqsood A.Khan[1]

[1]Department of Industrial & Manufacturing Engineering, NED University of Engineering & Technology, Karachi, Pakistan

[*]Corresponding author. Tel.: (92-21) 99261261-8 Ext: 2375
E-mail address: mfahad@neduet.edu.pk

Abstract

Increased global competition for manufacturing sector have led many companies towards pursuing ways to gain competitive edge in domains such as service, cost, quality and timely delivery. Role of effective maintenance towards the overall productivity of an organization has received increased attention in the past few years and the role of maintenance has shifted from *necessary evil* to *profit contributor*. The study presents an overview of perspectives and trends of maintenance function in automotive industries of Pakistan. Automotive sector was selected due to its high importance in the economic growth and because it is considered to be a leading industrial domain of Pakistan that steers the growth in large scale manufacturing sector. Performance of different industries were evaluated and compared with each other as well as with that of world class practices. It would bring to light areas which the industries lead and lack and would not only help them to improve their maintenance practices but also bring them up to the global standards.

Keywords: Maintenance management; automotive sector

INTRODUCTION

Maintenance can be defined as "the combination of all technical, administrative and managerial actions during the life cycle of an item intended to retain it in, or restore it to a state in which it can perform the required function" [1] or a combination of functions which are considered necessary to provide a given service. Whereas maintenance management can be defined as management activities that determine the maintenance objectives, priorities, strategies and responsibilities and implement them by using maintenance planning, maintenance control, supervision and several improving methods [2].

Maintenance management is considered to be an important function of any manufacturing firm. If managed effectively it can bring improvement in the performance of any organization. It has been found that maintenance represents from 15 to 40% of the total product cost and improving maintenance is considered to be easier and more likely to occur [3].Therefore in order to make rapid improvement in manufacturing sector maintenance management can play an important role especially for the developing country like Pakistan and has high scope in research. The study presents an overview of trends and perspectives of maintenance function in automotive industries of Pakistan. Automotive sector was selected due to its high importance in the economic growth and due to the reason that it is considered to be a leading industrial domain of Pakistan that steers the growth in large scale manufacturing sector [4]. Performance of different industries were evaluated and compared with each other as well as with that of world class practices to help the industries identify the areas which need improvement and subsequently take measures to improve their performance to the world class standards.

8 METHODOLOGY

The aim of study was to evaluate the performance of the selected industries among themselves and with that of the world class benchmark (WCB) standards. For the purpose, four areas of maintenance management were considered for the study and a questionnaire by Wireman [5] was used to evaluate the performance of the industries. Table 1 shows the maintenance management areas and their WCB values. The questionnaire was being filled by different concerned personnel belonging of the same firm so as to ensure authenticity of data. Then bar charts were used to analyze the collected data and evaluate performance of the selected industries. The performance of industries

individually, and on average were also compared with that of WCB in each section.

Table 1. Maintenance Management activities and world class benchmark values[5]

Sections	WCB
Preventive Maintenance	24.1
Maintenance Work Orders	26.3
Maintenance Inventory & Purchasing	28.4
Asset Care Continuous Improvement	26.9

8.1 Description of Selected industries

8.1.1 Industry 1:

A multinational company (MNC), original equipment manufacturer (OEM), founded twenty six years ago, capacity of 54,000/year and a turnover of Rs. 57,000 millions/year.

8.1.2 Industry 2:

An MNC, OEM, founded twenty two years ago, installed capacity of 150,000/year and a turnover of Rs. 51,000 millions/year.

8.1.3 Industry 3:

An MNC, OEM, founded twenty eight years ago, installed capacity of 750,000/year and a turnover of Rs. 44,000 millions/year.

8.1.4 Industry 4:

A local company, OEM, founded thirteen years ago, installed capacity of 55,000/year and generates a turnover of Rs. 1000 millions/year.

8.1.5 Industry 5:

A local vendor company, founded thirty six years ago, capacity of more than 1,000,000/year and turnover data was unavailable.

9 ANALYSIS

9.1 Preventive Maintenance (PM)

In order to attain world-class performance, most companies are replacing corrective strategies for maintenance with proactive strategies such as preventive and predictive maintenance techniques. Preventive maintenance is often referred to as use/time-based maintenance activities that are executed according to a plan (i.e. planned activities). It is comprised of maintenance activities that are undertaken after a specified period of time or amount of machine use [1,2]. Different researchers have emphasised on the role which preventive maintenance can play in improving maintenance function and have placed it at the foundation of their proposed maintenance frameworks [5,6]. World class manufacturing experts believe that a rigid and disciplined preventive programs helps to produce high quality products. Also, the use of effective preventive maintenance activities can lead a company to achieve a ratio of 4:1 between proactive maintenance and reactive maintenance respectively. This means approximately 80% activities are planned and only 20% activities are corrective which could help to make other maintenance practices and processes to become more effective in terms of planning, execution and control [5].

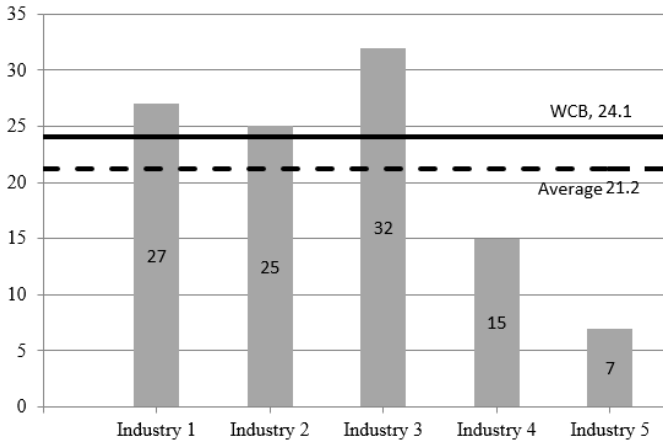

Figure 1. Preventive Maintenance

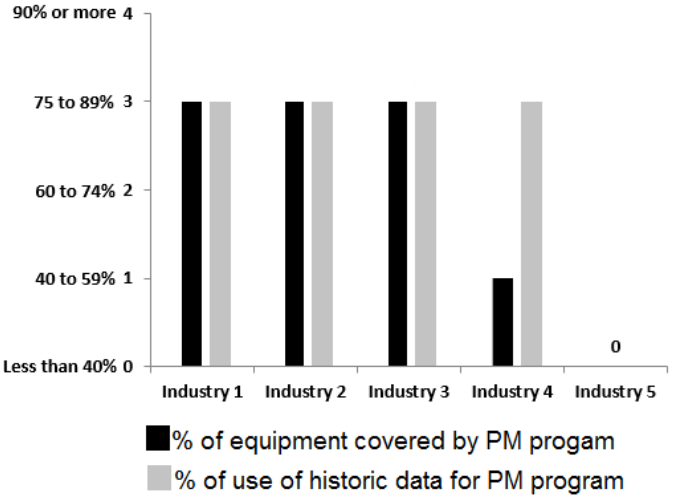

Figure 2. Percentage of critical equipment coverage and use of historic data by preventive maintenance program

Results presented in Figure 1 show that the average performance of the evaluated industries stands below than that of WCB standards. On further evaluation it can be seen that industries which are MNCs, have scored high in the evaluated section whereas the performance of both local industries is well below the evaluated average as well as WCB.

Use of historic data along with the inclusion of critical equipment in PM program are the ingredients that make a PM program [5]. Historical data, if accurate and used properly, could give useful information about the equipment such as mean time between failures, date of last repairs, causes of failure etc. which, in turn, helps to design an effective preventive maintenance plan. Without effective historic records, PM would only become a guess work. From Figure 2, it is clear that industries utilizing historic data perform better than those which do not make use of historic data for their PM program. Industry 4, as indicated by results (Figures 1 and 2), shows exception from the above argument as it showed the same usage of historic data as industries 1, 2 and 3 but its performance in PM was below the average as well as WCB (Figure 1). This could be attributed to the percentage of equipment covered by PM program. Although, it may not be cost effective to include all the equipment in the facility in a preventive maintenance program, however, it seems obvious from the results in Figure 2 that the organizations (i.e. industry 1, 2 and 3) which include a higher percentage of their equipment to be covered by preventive maintenance program perform better. On the other hand, industry 4 and 5 did not cover a high percentage of their equipment under PM program which resulted in their low performance in the context of PM program implementation.

9.2 Maintenance Work Orders (WO)

An essential part of the maintenance control is the work order system which is based on utilizing a document (i.e. WO) which provides necessary information for planning, monitoring and reporting maintenance work. Work order system is a tool to measure and control the maintenance function and is considered to be an important indicator of maintenance performance [9]. Studies show that it is impossible to measure and control maintenance activities if an organization does not have a well implemented work order system [5].

Results in Figure 3 show that, similar to the results of PM domain, the performance of local industries (4 and 5) in the domain of work order system is well below the average performance and the WCB. Work orders if properly managed contain historical data which can not only be used for forecasting equipment failure but also for optimizing maintenance strategy, resource allocation and hence making maintenance function cost effective and more efficient. Figure 4 shows that for Industry 4 and Industry 5, very low percentage of work orders are available for historical data analysis.

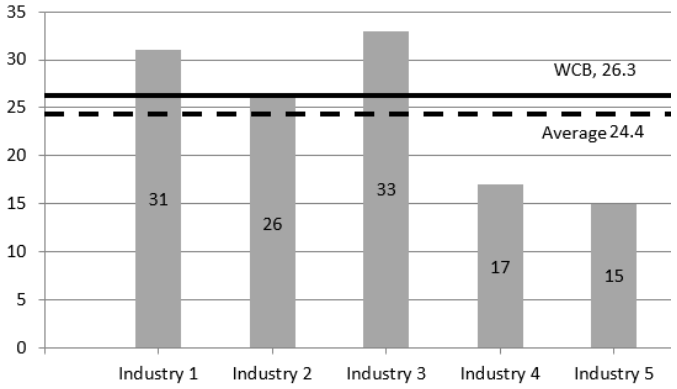

Figure 3. Maintenance Work Order System

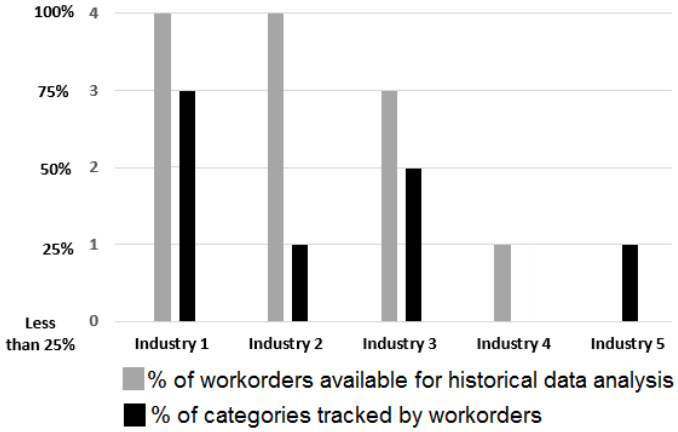

Figure 4. Work orders available for historical data analysis and categories tracked by workorders

One of the reasons could be that the concerned personnel are usually reluctant of filling up the work orders and if filled the data is either not accurate or complete and hence cannot be used for future use which is also evident from 4. Majority of the firms track only 25% or even less of the categories for the future use through work orders. It is important that work order system should not only cover the jobs performed but also the data entered should be relevant, accurate and complete.

9.3 Maintenance Inventory and Purchasing

The timely availability of materials, spare parts and services is a key element of an effective and strong maintenance program. However having too many parts in stock will increase inventory and would result in tie up of capital. The purpose of maintenance inventory and purchasing is to maintain the spare parts and inventory required at

an optimize level. Too low or too high both levels can affect the performance.

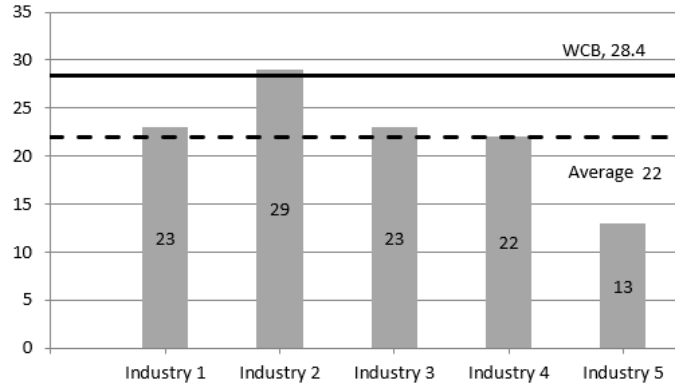

Figure 5. Maintenance Inventory and Purchasing.

Results evaluated in Figure 5 show that the performance of all selected industries, apart from industry 2, is not up to the mark (WCB) in the context of maintenance inventory and purchasing.

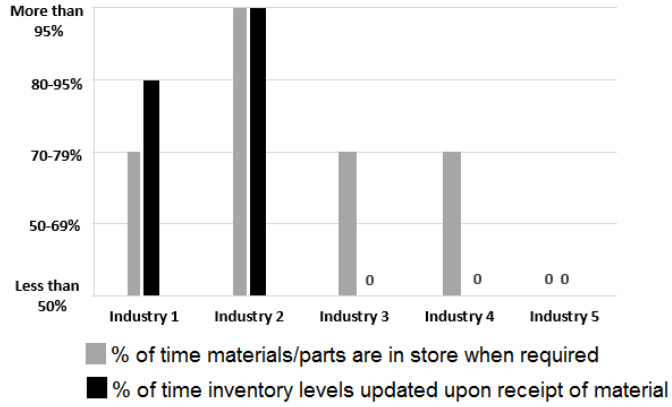

Figure 6. Percent of time materials in store when required

In order to be successful within the highly competitive market it is essential to have spare parts where and when required as it ensures reliable equipment and customer satisfaction [10]. Good inventory control enables the maintenance department to be responsive to the operations group, while increasing the its own personal productivity [5]. Results in Figure 6 show that only Industry 2 has an inventory system that is efficient enough to provide spare parts when required. On the other hand, Industry 5 is not able to get the required spare part for even 50% of the times which is not a good sign and reflects poor practices of the company.
Updating inventory levels on regular basis would convey actual number of inventory items and spare parts present resulting in correct reorder quantities without having unnecessarily high or low inventories. From Figure 6, it also evident that only Industry 2 is able to update its inventory levels (spare parts) on frequent basis. This suggests that regular updating of inventory would result in keeping the right spare parts inventory and thus the operation of maintenance department would be enhanced, which is the case for industry 2.

9.4 Asset Care Continuous Improvement

In all aspects of business, continuous improvement is considered to be an essential element for meeting the challenge of today's turbulent environments [11]. Continual improvement, when considered in reference to asset care is an ongoing evolution that includes constantly looking for the *little things* that can make an organization more competitive[12]. Many authors have included different continuous improvement techniques as a part of their proposed frameworks for asset care and maintenance management [2–5] since it can tremendously increase asset productivity [16].

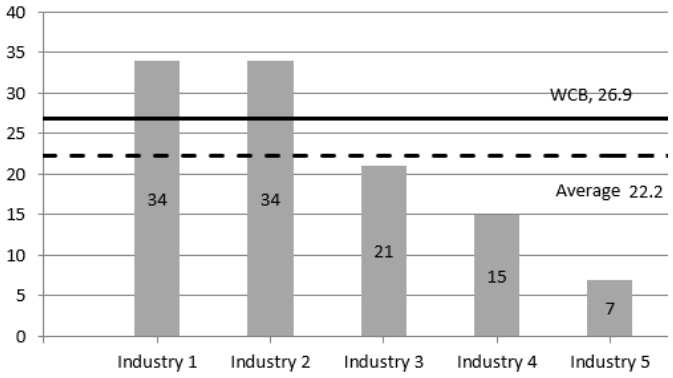

Figure 7. Performance of automotive industries of Pakistan in asset care and continuous improvement.

Results depicted in 7 show that the performance of Industry 1 and 2 have been exceptional whereas the other three industries have performance below WCB in this domain.

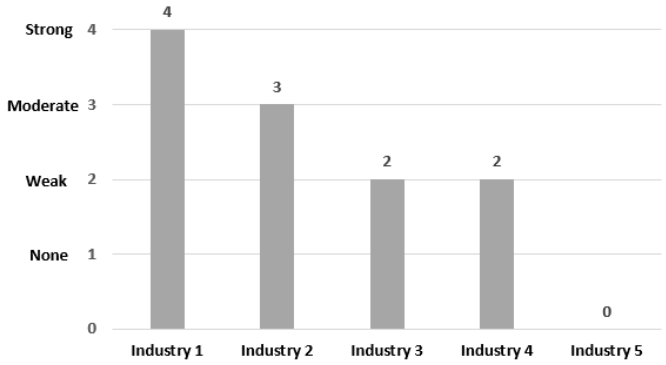

Figure 8. Management support for continuous improvement

Management support can play an important role to enhance continuous improvement efforts for maintenance function [14]. Senior management must not only communicate its support throughout the organization but the message must be repeated over time to encourage continuous improvement. Similarly, performance audits should be conducted to ensure that optimization is achieved and show management concern [16]. Results in Figure 8 show that both the industries 1 and 2 have moderate to high support of management in relation to continuous improvement efforts. Whereas the same for industries 3, 4 and 5 is weak to none. Thus, it is clear that in order to have a world class performance, management support is an important element.

Researchers believe that utilization of emerging techniques and technologies such as Total Productive Maintenance (TPM) and Reliability Centered Maintenance (RCM) can have higher impact on the maintenance practices and its outcomes [14]. Reliability engineering is comparatively a new philosophy in maintenance domain for industries of a developing country like Pakistan. When evaluated in reference to continuous improvement effort it was found that none of the evaluated organizations have positive attitude towards it (i.e. no industry showed any response to using reliability engineering for improvement of maintenance activities). This could definitely be an important reason behind the average performance of industries being below te WCB in this domain.

10 CONCLUSION

Maintenance is considered to be a critical support activity for any manufacturing industry. For a developing country like Pakistan the role maintenance can play for the development and improvement of industries cannot be denied. The study conducted shows that the average performance of the Industries, in the evaluated sections is below the WCB. Moreover on further evaluation this can be noted that multinational industries and the industries which are in business for longer time have scored and showed comparatively better performance. Therefore the newly emerging and the local industries can target those industries as their benchmark to improve their performances. Results also reflect that the industries have not scored well in the section of continuous improvement and do not show positive attitude towards the newly emerging techniques. Industries should continuously evaluate and improve their present practices and also welcome new techniques since it would help them to improve their current performance and bring their standards to international level.

REFERENCES

[1] British Standards Institution, *Glossary of terms used in terotechnology*. London: BSI, 1993.

[2] A. C. Marquez and J. N. D. Gupta, "Contemporary maintenance management: process,framework and supporting pillars," *Int. J. Manag. Sci.*, vol. 34, pp. 313–326, 2006.

[3] T. Wireman, "How to calculate return on investment for maintenance improvement projects," 2007. [Online]. Available: www.vestapartners.com.

[4] Minister for Industries, "Auto Industry Development Programme." [Online]. Available: http://www.pama.org.pk/images/stories/pdf/AIDP/AIDP.pdf.

[5] T. Wireman, *Benchmarking best practices in maintenance management*, 2nd ed., vol. 34. New York: Industrial Press Inc, 2004.

[6] C. W. Gits, "Design of maintenance concepts," *Int. J. Prod. Econ.*, vol. 24, no. 3, pp. 217–226.

[7] F. Herbaty, *Handbook of maintenance management: cost-effective practices*, 2nd ed. Park Ridge, N.J., U.S.A: Noyes Publications, 1990.

[8] R. Smith, "Benchmarks maintenance organization effectiveness," *reliabilityweb*, Apr-2003. [Online]. Available: http://www.reliabilityweb.com/excerpts/excerpts/Maintenance_Benchmarks.pdf.

[9] *Handbook of maintenance management and engineering*. Dordrecht ; New York: Springer, 2009.

[10] A. BÖRJESSON and A. SVENSSON, "Critical equipment classification and cost reduction within professional maintenance," Master of Science Thesis in Production Engineering, CHALMERS UNIVERSITY OF TECHNOLOGY, Sweden, 2011.

[11] J. Bessant and S. Caffyn, "High-involvement innovation through continuous improvement," *Int. J. Technol. Manag.*, vol. 14, no. 1, p. 7, 1997.

[12] M. C. Eti, S. O. T. Ogaji, and S. D. Probert, "Reducing the cost of preventive maintenance (PM) through adopting a proactive reliability-focused culture," *Appl. Energy*, vol. 83, no. 11, pp. 1235–1248, Nov. 2006.

[13] J. D. Campbell, *Uptime: strategies for excellence in maintenance management*, 2nd ed., New ed. New York: Productivity Press, 2006.

[14] A. Crespo Márquez, *The maintenance management framework: models and methods for complex systems maintenance*. London: Springer, 2007.

[15] P. Jonsson, "The status of maintenance management in Swedish manufacturing firms," *J. Qual. Maint. Eng.*, vol. 3, no. 4, pp. 233–258, 1997.

[16] J. D. Campbell, Jardine, and J. McGlynn, *Asset management excellence optimizing equipment life-cycle decisions*. Boca Raton, FL: CRC Press, 2011.

AN APPLICATION OF SUB-STRUCTURING TECHNIQUE FOR A LARGE BODY DYNAMIC ANALYSIS

Nadeem Shafi Khan* and Huda Zahid
National University of Sciences and Technology, Islamabad, Pakistan

*Corresponding author: Nadeem@gatech.edu

ABSTRACT

Finite element models of complex structures involve a very large number of degrees of freedom (DOF) and this entails substantial computational efforts and simultaneous dealings with both linear and nonlinear parts in geometry. To address these problems, we opt for sub-structuring technique or model reduction method. This technique involves division of complete assembly into several components and would predict the behavior (dynamic or static) of the complete assembly by assimilating characteristic behavior of its components. With the help of this technique, there is ease in analyzing the model in parts where each part is a super-element. In this research, we consider a flying vehicle and would apply the sub-structuring technique for its static, model, harmonic and transient dynamic analysis. The vehicle geometry is divided into requisite number of super-elements to reduce the model. The 'Top down sub-structuring' procedure has been opted in which notion of super- elements as being large pieces of a complete structure is taken, has been opted. It has been shown that our static and transient nonlinear analysis's problem size and CPU-resource requirements is diminished and structural analysis is straightforwardly carried out. The technique has been applied on two different types of wings and for each type of analysis, the comparison is carried out for the Complete method and Sub-Structuring method.

INTRODUCTION

Finite element models of classic modern structures can involve a very large number of degrees of freedom (DOF) and this implies considerable computational effort. Significant research efforts have been focused toward model reduction. Sub-structuring, therefore is a technique that involve partitioning of the entire structure into several sub-structures or components [1]. The essential idea is of deriving the behavior of the entire assembly from its constituents to reduce time consumption and computational efforts. Hence, in an optimization setting, re-computations need to be done only for those sub-structure involving modifications.

The inspiration for carrying out analysis of complex structures such that some form of structural partitioning would be possible for direct model updating [2], could be either because of different methods being used on different structural components or because of the limitations imposed by the capacity of the digital computers .Thus, such necessities generated the idea for implementation of sub-structuring technique. [3]

Sub-structuring is a course of action that condenses a group of finite elements into one element represented as a matrix. The single-matrix element is called a super-element or a sub-structure [4] which could be used in an analysis as we would any other element type. In this way, the matrix for the whole structure is reduced and calculations could be carried out in ease.

For structural systems that have a large number of DOF or have components designed by separate groups of organizations, the method of sub-structuring has proven to be an accurate, efficient, and economical method of analysis[3]. The primary merit of sub-structuring is that the number of DOF in the total structure is far less than in direct use of the finite element method.

Sub-structuring is a very popular method of model reduction for any structural dynamics problems. It is very useful in a design situation; for example, different teams of researchers design different components in an aircraft or nuclear reactor structure. Any design changes affect only the particular component concerned. Through sub-structuring, nonlinear analysis could be handled well. In a nonlinear analysis, we can sub-structure the linear portion of the model so that the element

matrices for that portion need not be recalculated at every equilibrium iteration [5]. Any kind of model updating or modifications of a specific part is highly supported by this technique as calculations for that specific part would only be carried out. Less memory consumption is possible with sub-structuring. Reduction in consumption of time by reduction of matrix of elements results due to portioning of the structure.

A super-element is a grouping of finite elements that, upon assembly, maybe regarded as an individual element for computational purposes [6-8]. These purposes may be driven by modeling or processing needs. In other words, complex assemblies of elements that result on breaking up a structure into distinguishable portions are called a super-element or a sub-structure. Each super-element can be analyzed individually, hence saving analysis time.

18 MATHEMATICAL REPRESENTATION

Consider the wing as a sub-structure (super-element) as shown in Figure 1.

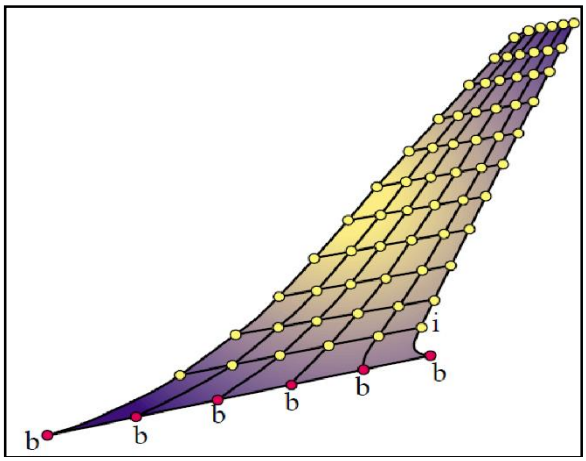

Figure 1. Super-element or sub-structure with internal and boundary nodes identified.

The DOF related to super-element are of two types. Internal Freedoms are not connected to the freedoms of another super-element. Nodes whose freedoms are internal are called internal nodes [9]. Master degree of Freedoms (MDOFs) is connected to at least another super-element [10]. They usually reside at boundary nodes placed on the periphery of the super-element, also called as boundary nodes.

The nodes where the super-element attaches to the main body or in non-technical terms to the non super-element body are called as Interface Nodes. Interface nodes are also called as Master Nodes. At master nodes, the degree of freedom, defined, therefore is called as Master Degree Of Freedom. Master DOF is also defined on the nodes where the force is applied on the sub-structure. Master DOF is of great importance as it acts as the boundary condition in calculation of results for the complete structure.

The objective is to get rid of all displacement degrees of freedom associated with internal freedoms. This elimination process is called static condensation, or simply condensation. [11-14]

Let F be the exterior forces, K the stiffness matrix, and U the displacement vector (see Figure 2). Then these quantities satisfy the system of equations

$$\mathbf{KU = F} \qquad \textbf{(1)}$$

Now dividing U into unknowns U_i of the interior of each sub-structure, and the unknowns U_b of the boundaries between sub-structure.

Partition $\begin{bmatrix} \mathbf{K}_{bb} & \mathbf{K}_{bi} \\ \mathbf{K}_{ib} & \mathbf{K}_{ii} \end{bmatrix} \begin{bmatrix} \mathbf{u}_b \\ \mathbf{u}_i \end{bmatrix} = \begin{bmatrix} \mathbf{f}_b \\ \mathbf{f}_i \end{bmatrix}$

Solve for interior displacements from 2nd matrix equation

$$\mathbf{u}_i = \mathbf{K}_{ii}^{-1}(\mathbf{f}_i - \mathbf{K}_{ib}\mathbf{u}_b)$$

replace into first matrix equation

$$\tilde{\mathbf{K}}_{bb}\mathbf{u}_b = \tilde{\mathbf{f}}_b$$ *Condensed stiffness equations*

where

$$\tilde{\mathbf{K}}_{bb} = \mathbf{K}_{bb} - \mathbf{K}_{bi}\mathbf{K}_{ii}^{-1}\mathbf{K}_{ib}$$

$$\tilde{\mathbf{f}}_b = \mathbf{f}_b - \mathbf{K}_{bi}\mathbf{K}_{ii}^{-1}\mathbf{f}_i$$

Figure 2. Static condensation explained.

From this point onward, the condensed super-element may be viewed, from the standpoint of further operations, as an individual element whose element stiffness matrix and nodal force vector are K_{bb} and $\widetilde{fb}$ respectively.

Considering Fig 3, treating the displacements as unknowns, the complete structure is initially partitioned into a number of sub-structures, whose boundaries could be specified arbitrarily. In the first step of the analysis, each sub-structure displacements under the external forces acting on its interior are obtained with all the generalized displacements on common boundaries completely arrested. Subsequently all the boundaries are simultaneously relaxed and the sub-structure boundary displacements are calculated. The total

displacements of the structure are then obtained as the superposition of these displacements.

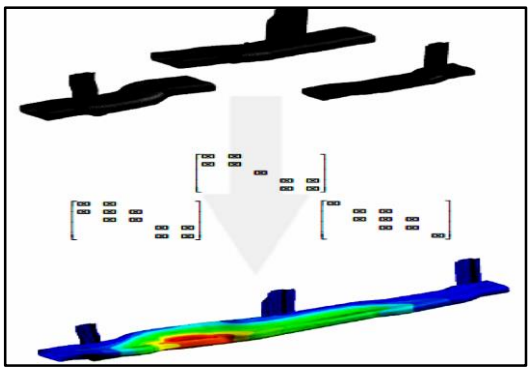

Figure 3..Model reduction

19 SUB-STRUCTURING PROCEDURAL VIEW

Three discrete steps are used for completion of sub-structuring technique.

19.1 Generation Pass

Sub-structures or super-elements are generated during this step. It involves selection of master degree of freedom, which is located along the border between the super-element and the main structure [15]. At the end of this step, matrices equivalent to each super-element are written to separate files (see Fig 4) and super-element matrix is generated to use in further steps. Master DOF is defined at the nodes of the super-element at which it is made in contact with the main body. This is basically the degree of freedom in which the major motion of the body is to be occurred. The master degree of freedom is fixed to the super-element and rotates with it if it's rotated.

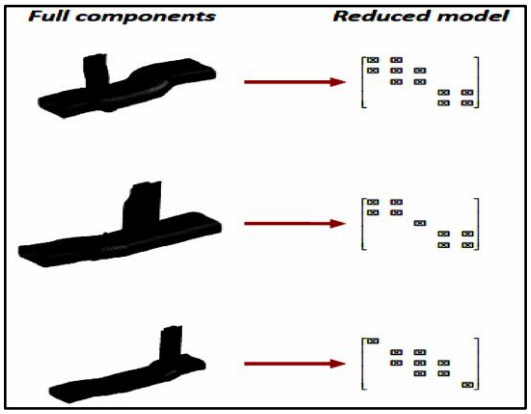

Figure 4. Generation pass

19.2 Use Pass

In this phase, main structure is generated. Also the super-element is brought in the main structure [16-17]. At the end of this step, the solution for the main structure is obtained, which includes the solution for the master degree of freedom of each super-element. From matrix point of view, an assembly matrix is generated as shown in Figure 5.

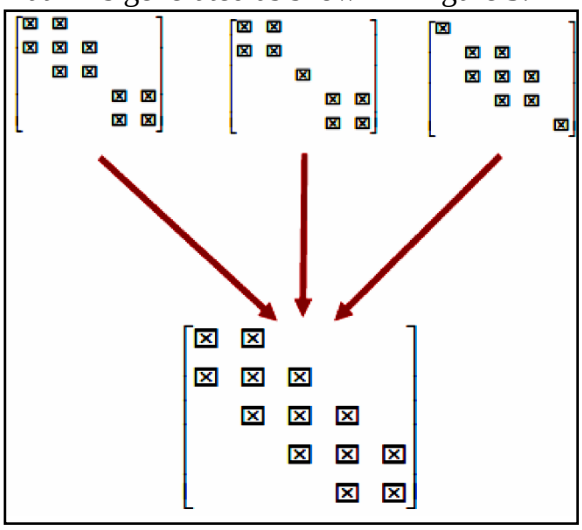

Figure 5. Use pass

19.3 Expansion Pass

During this step, complete solution for super-elements is obtained by expanding the solution of master degree of freedom from the use pass [18]. Figure 6 shows the final result of the entire process.

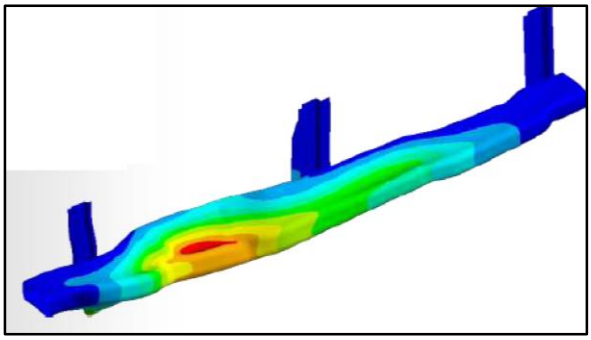

Figure 6. Final result after the use pass

20 TYPES OF APPROACHES

Three types of sub-structuring approaches can be found in literature. [19]

20.1 Bottom up Sub-Structuring

This category approach is usually used in solution of large models which are divided into number of super-element so they could fit in computer[19]. In

the first step, each super-element is generated individually through generation pass. Use pass will carry out the assembly of all super-elements. Complete solution for non-super element types and reduced solution for super-element is obtained and then in later stages, the solution for entire model including each super-element and other elements is expanded.

20.2 Top down Sub-Structuring

This technique is helpful for relatively smaller models and especially for the isolated component analysis[19]. Basically, in the first step, the entire model is built. In generation pass, the portion to be represented by super- element is selected and super- element is created by applying desired loads. In Use pass, the full model is restored and only non super- element geometry is selected, loads are applied and solved. In last step, the expansion pass, the entire model is restored and each super-element is expanded separately, allowing the solution for each super-element to be reviewed separately and overall solution analysis of assembled super-elements to be obtained in post processing.

In this method the super- elements are not assembled together in use pass. They are just specified in entire model in first step. Loads are applied to them and non-super elements (also specified in the model). We just have to set all active DOFs as master DOF as the portion for super-element is selected within the model, so that in final step, the super- elements can easily be identified out of entire model and an analysis can be reviewed over them.

In a bottom up technique one thinks of super-elements as built from simpler elements. In a top-down technique, super- elements may be thought as being large pieces of a complete structure.

20.3 Nested Sub-Structuring

In this technique we usually deal with the models containing super-element with in the super-element [19]. The solution for the parent super-element is obtained first and then for the super-element inside. For the project work out, top down sub-structuring technique is used as we aim to handle a smaller, isolated and already build component. Also, in this paper, Complete method refers to the normal method of analysis i.e. Without Sub-Structuring.

21 RECTANGULAR WING ANALYSIS

Initially a rectangular wing was modeled and analyses were carried out using complete method. Later, the implementation of sub-structuring technique was conducted over it.

21.1 Static Analysis

Code for static analysis of the rectangular wing for complete method and sub-structuring method is shown in Figure 7.

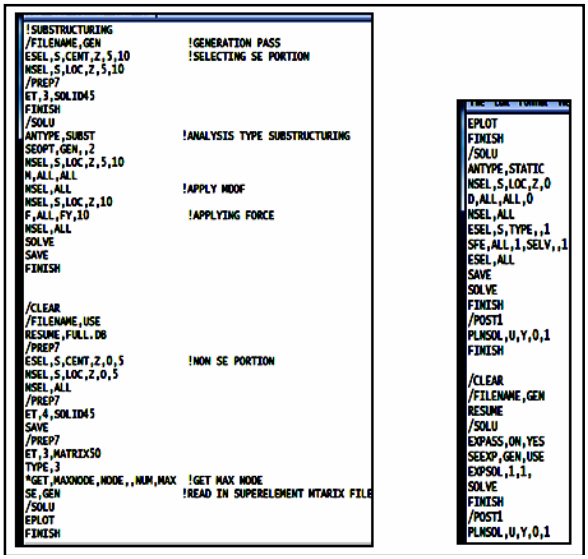

Figure 7. static analysis with sub-structuring method

21.2 Modal analysis

Modal analysis of the rectangular wing was carried out with the intention to compare the results with that obtained after the implementation of the technique. Figure 8 shows the code for modal analysis, Figure 9 depicts the result of the complete method and Figure 10 shows the results of Sub-structuring method. Finally, the comparison of the results is depicted in Table 1.

```
/FILENAME,FULL
/PREP7
ET,1,PLANE42
ET,2,SOLID45
MP,EX,1,38E3
MP,PRXY,1,.3
MP,DENS,1,1.033E-3
K,1
K,2,2
K,3,2.3,.2
K,4,1.9,.45
K,5,1,.25
LSTR,1,2
LSTR,5,1
BSPLIN,2,3,4,5,,,-1,,,-1,-1,-.25
AL,1,3,2
ESIZE,.25
AMESH,1
ESIZE,,10
TYPE,2,
VEXT,ALL,,,,,10
/VIEW,,1,1,1
/ANG,1
/REP
EPLOT
FINISH
/SOLU
ANTYPE,MODAL
MODOPT,LANB,10
ESEL,U,TYPE,,1
NSEL,S,LOC,Z,0
D,ALL,ALL
NSEL,ALL
MXPAND,10
SOLVE
FINISH
```

```
/FILENAME,GEN
/PREP7
ET,2,SOLID45
ESEL,CENT,Z,5,10
MSLE
/SOLU
ANTYPE,SUBSTR
NSEL,S,LOC,Z,5
M,ALL,ALL
NSEL,ALL
SOLVE
SAVE
FINISH
/CLEAR,NOSTART
/FILENAME,USE
ESEL,CENT,Z,0,5
MSLE
ET,3,SOLID45
ESEL,U,TYPE,,1
NSEL,S,LOC,Z,0
D,ALL,ALL
NSEL,ALL
ET,2,MATRIX50
TYPE,3
SE,GEN
SFE,1,SLVE,,,1
SAVE
ANTYPE,MODAL
MODOPT,LANB,10
MXPAND,10
SOLVE
FINISH

/CLEAR,NOSTART
/FILENAME,GEN
RESUME
/SOLU
EXPASS,ON,YES
SEEXP,GEN,USE
EXPSOL,1,1,
SOLVE
FINISH
/POST1
PLNSOL,U,Y,0,1
/POST1
SET,LIST,2
SET,FIRST
*GET,FREQ1,ACTIVE,0,SET,FREQ
PLDISP,0
ANMODE,10,.7E-1
SAVE
```

Figure 8. Code for modal analysis for rectangular wing (left) Complete Method (right) Sub-structuring Method

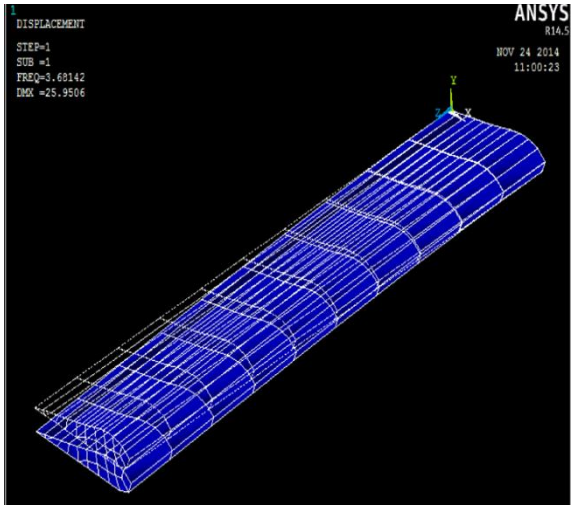

Figure 9. Deformation results for first mode shape of the rectangular model as per Complete method.

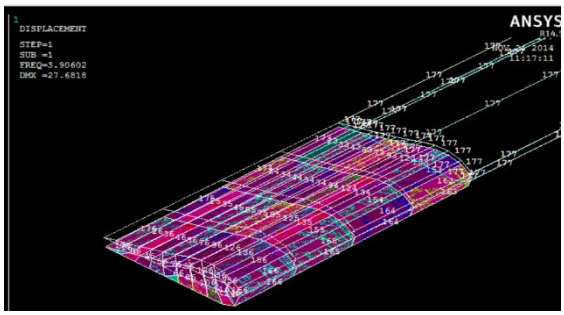

Figure 10. Deformation results for first mode shape of the rectangular model as per Sub-Structuring method.

Table 1. Comparison of results for modal analysis of rectangular wing

PARAMETERS	COMPLETE METHOD	SUB-STRUCTURING METHOD
FREQUENCY OF 1ST MODE	3.6812	3.906
DEFLECTION IN Y DIRECTION	25.9506 mm	27.661 mm

21.3 Mode Superposition Harmonic Analysis

Mode superposition method is a method of using the natural frequencies and mode shapes from the modal analysis (ANTYPE, MODAL) to describe the dynamic behavior of a structure to transient or steady harmonic excitations. Code for harmonic analysis of rectangular wing using Complete method and Sub-structuring method are shown as Figure 11 and Figure 12 respectively. This is followed by Table 2 which compares the results for the two methods.

```
/CLEAR,NOSTART
/FILENAME,FULL
/PREP7
ET,1,PLANE42          ! ELEMENT TYPE
ET,2,SOLID45
MP,EX,1,38E3          ! MATERIAL PROPERTIES
MP,PRXY,1,.3
MP,DENS,1,1.033E-3
K,1                   ! DEFINING KEYPOINTS
K,2,2
K,3,2.3,.2
K,4,1.9,.45
K,5,1,.25
LSTR,1,2              ! STRAIGHT LINE
LSTR,5,1
BSPLIN,2,3,4,5,,,-1,,,-1,-.25! SPLINE FORMATION
AL,1,3,2              ! AREA LINES
ESIZE,.25             ! MESH SIZE
AMESH,1
ESIZE,,10             ! ELEMENT DIVISION SIZE
TYPE,2
VEXT,ALL,,,,,10       ! EXTRUDE VOLUME
/VIEW,,1,1,1
/ANG,1
/REP
EPLOT
FINISH
SAVE
```

```
/CLEAR,NOSTART
/FILENAME,FULL
SAVE
/SOLU
ANTYPE,MODAL                ! ANALYSIS TYPE
MODOPT,LANB,10,1            ! TYPE OF METHOD,NO OF MODES,STARING FREQ
NSEL,S,LOC,Z,0
D,ALL,ALL                   ! CONSTRAINTS DEFINED
NSEL,ALL
MXPAND,10,,,YES
DMPR,.02                    ! DAMPING RATIO
NSEL,S,LOC,Z,5
SAVE
SOLVE
FINISH
/SOLU
ANTYPE,HARMIC               ! ANALYSIS TYPE
HROPT,MSUP,10,,1,YES,0      ! MODE SUPERPOSITION HARMONIC ANALYSIS
HROUT,0,ALL
SBC,,0                      ! RAMP LOADING
NSEL,S,LOC,Z,5
F,ALL,FY,1200               ! FORCE APPLICATION
NSEL,ALL
HARFRQ,0,500                ! FREQUENCY RANGE
NSUBST,500                  ! SUBSETS
OUTRES,ALL,ALL
OUTRES,NSOL,ALL
SOLVE
SAVE
FINISH
/SOLU                       ! EXPANSION PASS
EXPASS,ON
NUMEXP,ALL,ALL              ! NO OF SOLU TO EXPAND
SOLVE
FINISH
/POST26
/FILE,,RFRQ
NSOL,2,37,U,Y,DISPLACEMENT  ! DISPLACEMENT CONTOUR
NSOL,3,38,U,Y,DISPLACEMENT
PLVAR,2,3                   ! PLOTTING GRAPH
/GLAB,Y,DISPLACEMENTS
/GRID,1
/PLVAR,2,3
/SHOW,CLOSE
SAVE
```

Figure 11. Code for harmonic analysis of rectangular wing using Complete method

```
/CLEAR,NOSTART
/FILENAME,SUBS
/PREP7
/SOLU
ANTYPE,MODAL                !MODAL ANALYSIS*
MODOPT,LANB,10              !CONSTRAINT
D,ALL,ALL
NSEL,ALL
MXPAND,10,,,YES
FINISH
/CLEAR,NOSTART              !SUBSTRUCTURING
/FILENAME,GEN               !SELECTING SE PORTION
/PREP7
ET,2,SOLID45                !ELEMENT TYPE
/SOLU
ANTYPE,SUBSTR               !ANALYSIS TYPE SUBSTRUCTURING
NSEL,S,LOC,Z,5,10
M,ALL,ALL                   !APPLY MSUP
NSEL,ALL                    !APPLYING FORCE
SOLVE
FINISH
/CLEAR,NOSTART              !USE PASS
/FILENAME,SUBS              ! RESUME FULL MODEL
RESUME,FULL,SE
/SOLU                       ! ANALYSIS TYPE
ANTYPE,MODAL                ! TYPE OF METHOD,NO OF MODES,STARING FREQ
MODOPT,LANB,10              ! NO OF MODES TO EXPAND AND CALC ELEMENT RESULTS
EXPASS,ON
SEEXP,GEN,USE
EXPSOL,1,1,
SOLVE
FINISH
/PREP7
ET,3,MATRIX50
TYPE,3
*GET,MAXNODE,NODE,,NUM,MAX  !GET MAX NODE
SE,GEN                      !READ IN SUPERELEMENT MTARIX FILE
ESEL,S,LOC,Z,0,5
NSLE,S,ALL
D,ALL,ALL
EPLOT
SAVE
FINISH
/SOLU
ANTYPE,HARMIC               ! ANALYSIS TYPE
HROPT,MSUP,10,1,YES,0       ! MODE SUPERPOSITION HARMONIC ANALYSIS
HROUT,0,ALL
DSCALE,ALL,1.0              !APPLYING CONSTRAINTS TO MAIN BODY
SFE,ALL,1,SELV,0,1          !APPLYING SE LOAD VECTOR
HARFRQ,0,500
NSUBST,500                  ! RAMP LOADING
OUTRES,ALL,ALL
OUTRES,NSOL,ALL
SAVE
SOLVE
/SOLU                       ! EXPANSION PASS
EXPASS,ON                   ! NO OF SOLU TO EXPAND
NUMEXP,ALL                  ! SAVE RESULTS FOR EVERY SUBSTEP
OUTRES,ESOL,ALL             ! READ RESULTS FILE
OUTRES,NSOL,ALL
SOLVE
FINISH
/POST26
/FILE,,RFRQ
NSOL,2,37,U,Y,DISPLACEMENT
NSOL,3,38,U,Y,DISPLACEMENT
/GRID,1
/GLAB,Y,DISPLACEMENTS
/SHOW,JPEG
```

Figure 12. Code for harmonic analysis of rectangular wing using Sub-Structuring method

Table 2. comparison of results for harmonic analysis of the rectangular wing.

PARAMETERS	COMPLETE METHOD	SUB-STRUCTURING METHOD
FREQ	500 Hz	500 Hz
DEFLECTION	2.8768mm	2.84102mm
STRESSES	29.1N/mm²	29.1N/mm²

During the conduction of modal analysis over the model wing the research over the modal analysis revealed that there are six different mode extraction methods option available in ANSYS Parametric Design Language (APDL). The main concern was the selection of accurate and satisfactory method for the modal analysis. Research was carried out on different mode extraction methods. Out of the available methods, Block-Lanczos method was selected as it uses sparse equation solver method and is comparatively easy to use. As per the requirement of the project, the sub-structuring technique is used for accurate results at lower frequency range and lower number of modes.

21.4 Transient analysis

During literature review and research, three types of transient analysis were found to be available in APDL. The Complete Method can cater to all types of non-linearities but as expected, is very CPU intensive as complete system matrices are being utilized. The Reduced Method instead is basically concerned with Master Degrees Of Freedom (MDOFs). The method is rapid but unable to cater for any non-linearities. The Mode Superposition Method is based upon the concept that the overall system response is the sum of factored mode shapes.

For our case, we started with the transient analysis using full method. With sub-structuring, it was revealed that sub-structuring is not supported by transient full method. Hence, mode superposition based approach was adopted. APDL code for transient analysis using Complete method is shown in Figure 13 while graphical result output of the same is shown in Figure 14.

```
                                !MODELING OF THE WING
/CLEAR,NOSTART                  !FILENAME
/FILENAME,FULL                  !PREPROCESSOR
/PREP7                          !OBTAINING THE MODAL SOLUTION
SAVE
/SOLU
ANTYPE,MODAL                    !ANALYSIS TYPE
MODOPT,LANB,10,1                 !BLOCK LANCZOS METHOD
ESEL,U,TYPE,,1                  !ELEMENT SELECTION
NSEL,S,LOC,Z,0
D,ALL,ALL                       !CONSTRAINTS
NSEL,ALL,
MXPAND,10,,,YES                  !MODES EXPANDING
DMPRT,,,02
OUTRES,ALL,ALL
SOLVE
SAVE
FINISH
/POST1
SET,FIRST
FINISH
                                !OBTAINING MODE SUPERPOSITION TRANSIENT SOLUTION
/SOLU
ANTYPE,TRANSIENT                ! ANALYSIS TYPE
NLGEOM,1
TRNOPT,MSUP,10,,1,YES,0         ! MODE SUPERPOSITION TRANSIENT ANALYSIS
NSEL,S,LOC,Z,10
F,ALL,FY,2200
TIME,1
DELTIME,.005                    ! TIME INCRESAMENT
KBC,0                           ! RAMP LOADING
LSWRITE,1
FDELE,ALL,FY                    ! APPLY LOAD
DELTIME,.005                    ! TIME INCRESAMENT
TIME,2
LSWRITE,2
OUTRES,ALL,ALL
LSSOLVE,1,2,1
SAVE
FINISH
                                !EXPANDING THE MODE SUPERPOSITION SOLUTION
/SOLU
EXPASS,ON
NUMEXP,ALL                      ! NO OF SOLU TO EXPAND
OUTRES,ALL,ALL                  ! SAVE RESULTS FOR EVERY SUBSTEP
OUTRES,ESOL,ALL                 ! READ RESULTS FILE
OUTRES,NSOL,ALL
SOLVE
FINISH
/POST26                             ! REVIEW RESULTS OF MSUP
FILE,,RDSP                          ! RESULT FILE
SAVE
FINISH
/POST1
SET,LAST,ALL,,                  ! READ RESULTS OF DESIRED SET
/POST26
NSOL,2,27,U,Y, DISPLACEMENT
NSOL,3,28,U,Y, DISPLACEMENT
/SHOW,JPEG
PLVAR,2,3
/SHOW,CLOSE
```

Figure 13. Code for transient analysis of rectangular wing using Complete Method.

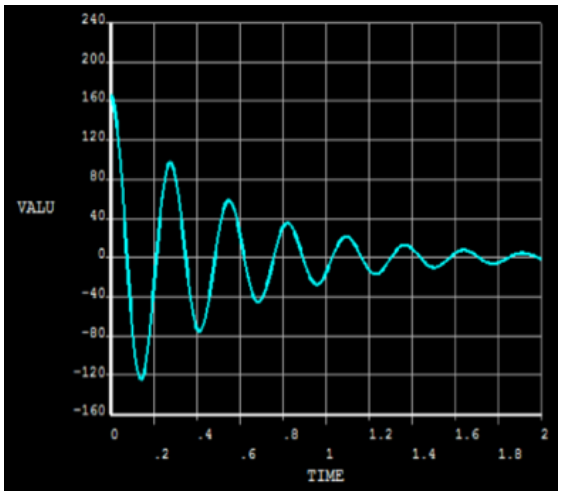

Figure 14. Displacement response for transient analysis of rectangular wing using Complete Method.

Code for the same scenario using sub-structuring method is shown in Figure 15 while the comparison of results for the transient dynamic analysis of the rectangular wing is shown in Table 3.

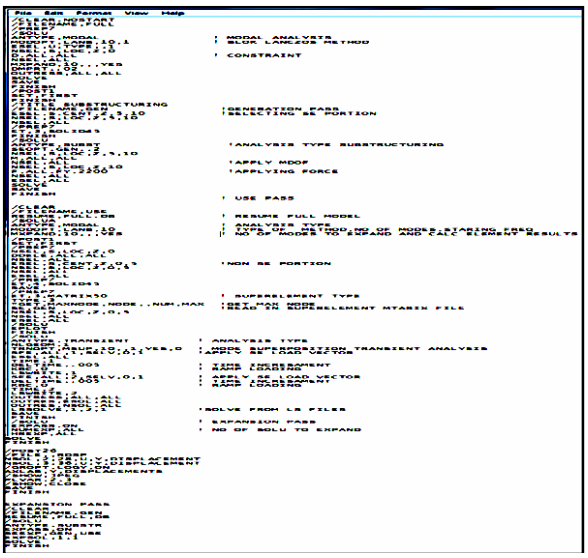

Figure 15. Code for transient analysis of rectangular wing using sub-structuring method

Table 3. Comparison of results for transient dynamic analysis of rectangular wing

PARAMETERS	COMPLETE METHOD	SUB-STRUCTURING METHOD
TIME STEP	.005	.005
DEFLECTION	165.301mm	164.64mm

22 CROPPED DELTA WING ANALYSIS

The Cropped Delta wing was imported to the software. Initially various problems were faced related to the import of wing to the APDL. There are options available respective to the preferences accepted while the installation of the software. The basic format is to import the file in the IGES format.

The file was imported to the software with the assurance that no warning or error is shown while importing the file. In the present case, the file was imported via CATIA V5 option. Initially according to the code mentioned previously harmonic mode superposition analysis was carried out on the wing with and without sub-structuring technique. The results were analyzed.

Analysis pre requisites were defined as explained here. The damping effects were included in the result. Distributed loads were applied only on the tip portion rather than the whole wing. Frequency range was kept to be in between 1-1000 Hz. 200 modes were extracted and expanded. 1000 subsets were specified.

22.1 Modal Analysis

Initially, a modal analysis was carried out on the wing and different mode shapes and nodal solution were obtained. Figure 16 shows the result of modal analysis for the cropped delta wing.

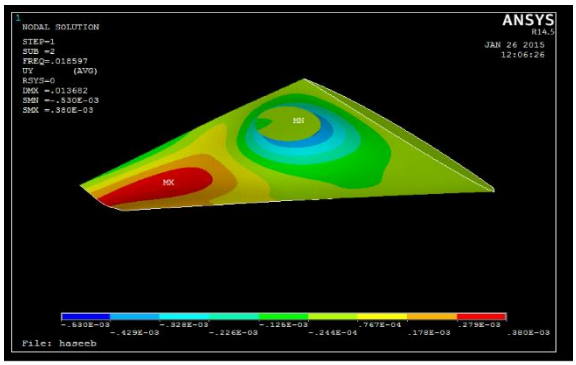

Figure 16. Result for modal analysis of cropped delta wing.

22.2 Transient Dynamic Analysis

With the effects of damping and nodal forces, the transient mode superposition analysis of the wing was carried out in ANSYS with two load steps ending in 2 sec and damping effect with ratio 0.08. Graphical display of the results for transient dynamic analysis of cropped delta wing using Complete Method is shown in Figure 17 while the nodal solution for the same case is shown in Figure 18. Sub-structuring results are displayed as Figure 19 while the comparison of the results is depicted in Table 4.

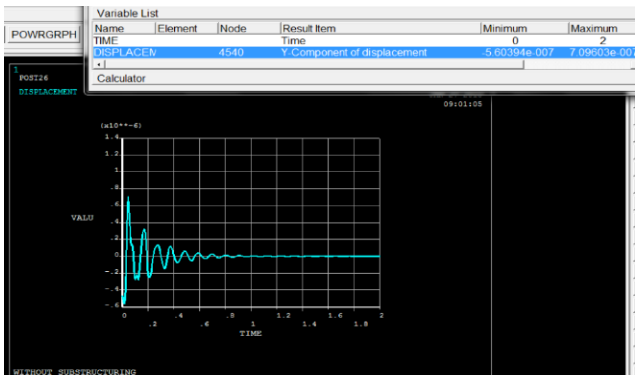

Figure 17. Graphical display of displacement response for transient dynamic analysis of cropped delta wing using Complete method

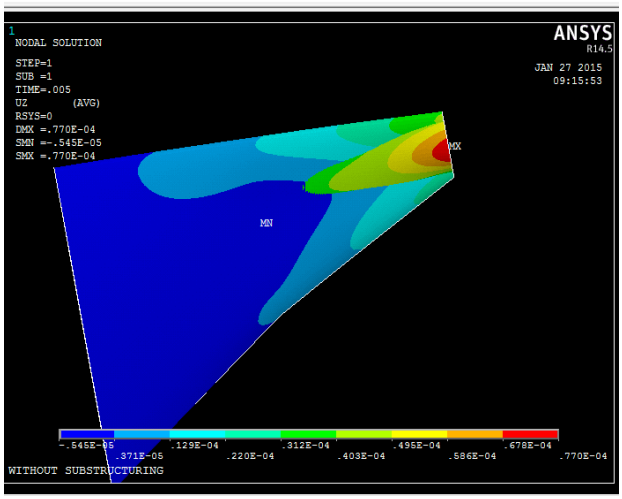

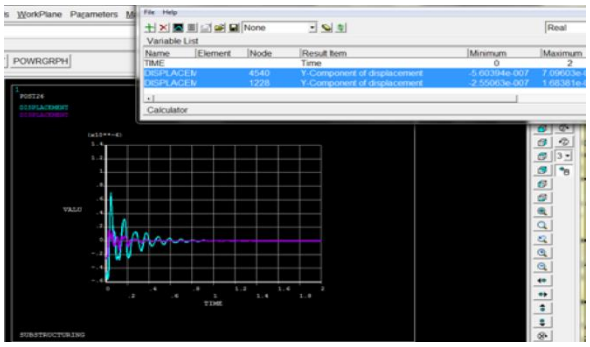

Figure 19. Graphical display of displacement response for transient dynamic analysis of cropped delta wing using Sub-structuring method

Table 4. Comparison of results for transient dynamic analysis of cropped delta wing

PARAMETERS	SUB-STRUCTURING METHOD	COMPLETE METHOD
TIME STEP	0.005	0.005
DISPLACEMENT	0.70 mm	0.703 mm
STRESSES	422.5N/mm²	422.5N/mm²
CPU TIME	569.154	1425.568
FILE SIZE	10226.188 Mb	18399.562 Mb

7.

23 CONCLUSION

The comparison of the results shows the accuracy of technique. It was discovered that the technique accuracy is supported on the lower frequency modes. On higher frequency modes, the result accuracy might not be up to the mark and also the APDL software has its own limitations. It might not support very high number of nodes for the results calculations or the solution for higher frequency and higher number of modes might ask for large memory allocation which might not be held with computer at hand.

The biggest advantage of the technique is the direct model updating. In the present era, when complex assemblies made by different sections in different organizations or by different industries, need to be analyzed separately or modified separately, this technique helps in saving time as the stiffness matrix of the unmodified portion is already saved. For modified portion, only its stiffness matrix has to be regenerated. This helps in less time consumption and memory allocation. This technique could prove very efficient and helpful and mechanical and aviation industry where every new day modifications and up gradation of the products is being carried out.

Figure 18. Nodal solution for transient dynamic analysis of the cropped delta wing using Complete method.

REFERENCES

[1]. Przemieniecki, Janusz S. "Matrix structural analysis of sub-structures." *AIAA Journal* 1, no. 1 (1963): 138-147.

[2]. Friswell, Michael, and John E. Mottershead. *Finite element model updating in structural dynamics*, Vol. 38, Springer Science & Business Media, 1995.

[3]. Lee, Sung-Kyung, Eun Churn Park, Kyung-Won Min, and Ji-Hun Park. "Real-time sub-structuring technique for the shaking table test of upper sub-structures" *Engineering structures* 29, no. 9 (2007): 2219-2232.

[4]. Massi, Francesco, Laurent Baillet, and Antonio Culla. "Structural modifications for squeal noise reduction: numerical and experimental validation." *International Journal of Vehicle Design* 51, no. 1 (2009): 168-189.

[5]. Bathe, Klaus-Jürgen, Ekkehard Ramm, and Edward L. Wilson. "Finite element formulations for large deformation dynamic analysis" *International Journal for Numerical Methods in Engineering* 9, no. 2 (1975): 353-386.

[6]. Mukunda, G. R., Elisa D. Sotelino, and Shang-Hsien Hsieh. "Distributed finite element computations using object-oriented techniques" *Engineering with Computers* 14, no. 1 (1998): 59-72.

[7]. Smith, I. M. "A general purpose system for finite element analyses in parallel" *Engineering Computations* 17, no. 1 (2000): 75-91.

[8]. Shebini, Nader O. "Automated design of structures using a finite element database." U.S. Patent 4,858,146, issued August 15, 1989.

[9]. Park, K. C., and Carlos A. Felippa. "A variational principle for the formulation of partitioned structural systems" *International Journal for Numerical Methods in* Engineering 47, no. 1-3 (2000): 395-418.

[10]. Ianakiev, Anton. "Modelling of complex structures using super-elements" International Journal of Design Engineering 1, no. 4 (2008): 396-411.

[11]. Paz, Mario. "Dynamic condensation" *AIAA journal* 22, no. 5 (1984): 724-727.

[12]. Paz, Mario. "Modified dynamic condensation method" *Journal of Structural Engineering* 115, no. 1 (1989): 234-238.

[13]. Irons, Bruce. "Structural eigenvalue problems-elimination of unwanted variables" AIAA journal 3, no. 5 (1965): 961-962.

[14]. Paz, Mario. "Practical reduction of structural eigen problems" Journal of Structural Engineering 109, no. 11 (1983): 2591-2599.

[15]. Rodgers, Bryan, Jeff Punch, and John Jarvis. "Finite element modelling of a BGA package subjected to thermal and power cycling." in Thermal and Thermo mechanical Phenomena in Electronic Systems, 2002, ITHERM 2002, The Eighth Intersociety Conference on, pp. 993-1000, IEEE, 2002.

[16]. Law, S. S., Tommy HT Chan, and D. Wu. "Efficient numerical model for the damage detection of large scale structure" Engineering Structures 23, no. 5 (2001): 436-451.

[17]. Carey, Graham F. "Parallelism in finite element modelling." Communications in applied numerical methods 2, no. 3 (1986): 281-287.

[18]. Madenci, Erdogan, and Ibrahim Guven. The finite element method and applications in engineering using ANSYS® Springer Science & Business Media, 2007.

[19]. Ansys, Inc. "ANSYS advanced analysis techniques guide." Ansys Help (2007).

ERGONOMIC ANALYSIS OF A HUMAN BODY IN A RESTRICTED SPACE ENVIRONMENT

Nadeem Shafi Khan* and Faria Mazhar
CAE, National University of Sciences and Technology, Islamabad, Pakistan

*Corresponding author: Nadeem@gatech.edu

Abstract

Proper assessment of human reach posture is one of the essential functions for ergonomic workspace design in any CAD system with a built- in human model. Human mannequins will be analyzed in different positions for example sitting, arms extending etc. This study will help to manage space for a human body in a cockpit. For Instruments which are mostly used in the cockpit; their positions can be relocated to minimize the stressed areas. Most stressing situations and places too can be identified e.g. it can be found out which sitting position will cause less stress on neck and collar, in which posture handling the throttle will cause less stress on hands, arms or joints, how the human body will respond to side or center location of control stick etc. and so it will help to diminish the fatigue factor for operator. Results inferred from this analysis can be pragmatically applied to real time postures and situations and their effectiveness will be determined. This study will assist to find out most comfortable postures and positions for the operators in the cockpit analyzing all conceivable maximum angles of sitting and using the instruments for the human body so the cockpit can be remodeled to ease the operator. Moreover, the results can additionally be used to remodel different vehicles for the drivers in day to day life.

INTRODUCTION

Ergonomic analysis is a multidisciplinary field which incorporates contributions from psychology, engineering, physiology and anthropometry. In essence it is the study of designing devices and equipment that best suits the human body and its cognitive abilities.

This project focuses on the man-machine-environment system for the cockpit of General Training Aircraft (GTA) which fulfills the requirements of ergonomic design and evaluation, on the basis of corresponding evaluation system established.

Ergonomic analysis is the main factor while designing a work space and especially a cockpit. In recent few years most of the cockpits have been developed with great emphasis on ergonomics. The aim of this project is to analyze behaviors of human body under various conditions in modern aircraft cockpit.

11 LITERATURE REVIEW

The word "ergonomics" comes from two Greek words "ergono" meaning "work" and "nomos" meaning" laws[1]. It basically means efficiency of people in their working environments.

Nowadays ergonomics is taken as the science of "designing the job to fit in the worker" not forcing the worker to fit the job or the workplace. It covers all aspects of job like the stresses on the joints, stresses in a specific posture, factors increasing the fatigue, repetitive movements affecting the worker/pilot and awkward positions etc.

Ergonomics is the scientific discipline concerned with the understanding of interactions among humans and other elements of a system, and the profession that applies theory, principles, data and methods to design in order to optimize human well-being and overall system performance[2,3].

There are various tools and techniques which are used for the ergonomic assessment e.g. mantra, RULA, HAL-TLV, LUBA, OCRA, SNOOK tables and the NIOSH lifting equations[4]. For this specific project RULA analysis was chosen which exists in CATIA software under the ergonomic analysis workbench. RULA stands for **Rapid Upper Limb Assessment**. It examines all the risk factors like the number of movements, muscle work, working posture etc.

All these factors combine to provide a final score that ranges from 1 to 7 as shown in table-1 below:-

Table 1. RULA colors and associated scores

Color	Score
Green	1 & 2
Yellow	3 & 4
Orange	5 &6
Red	7

The details of RULA assessment procedure and the score calculation is shown in Figure 1 through a sample analysis. As can be seen, this consists of two individual analysis; Arm and Wrist Analysis and Neck, Trunk and Leg analysis. Arm and Wrist Analysis consists of eight steps which are 1) Locate Upper Arm position, 2) Locate Lower Arm position, 3) Locate Wrist position, 4) Calculate Wrist Twist, 5) Look up Posture Score in Table A, 6) Add Muscle use score, 7) Add Force/Load Score and 8) Find Row in Table C. Neck , Trunk and Leg Analysis consist of seven further steps which are 9) Locate Neck Position, 10) Locate Trunk Position, 11) Calculate Legs Score, 12) Look up Posture score in Table B, 13) Add Muscle Use Score, 14) Add Force/ Load Score and 15) Find Column in Table C. The intersection of row and column identified gives the RULA score.

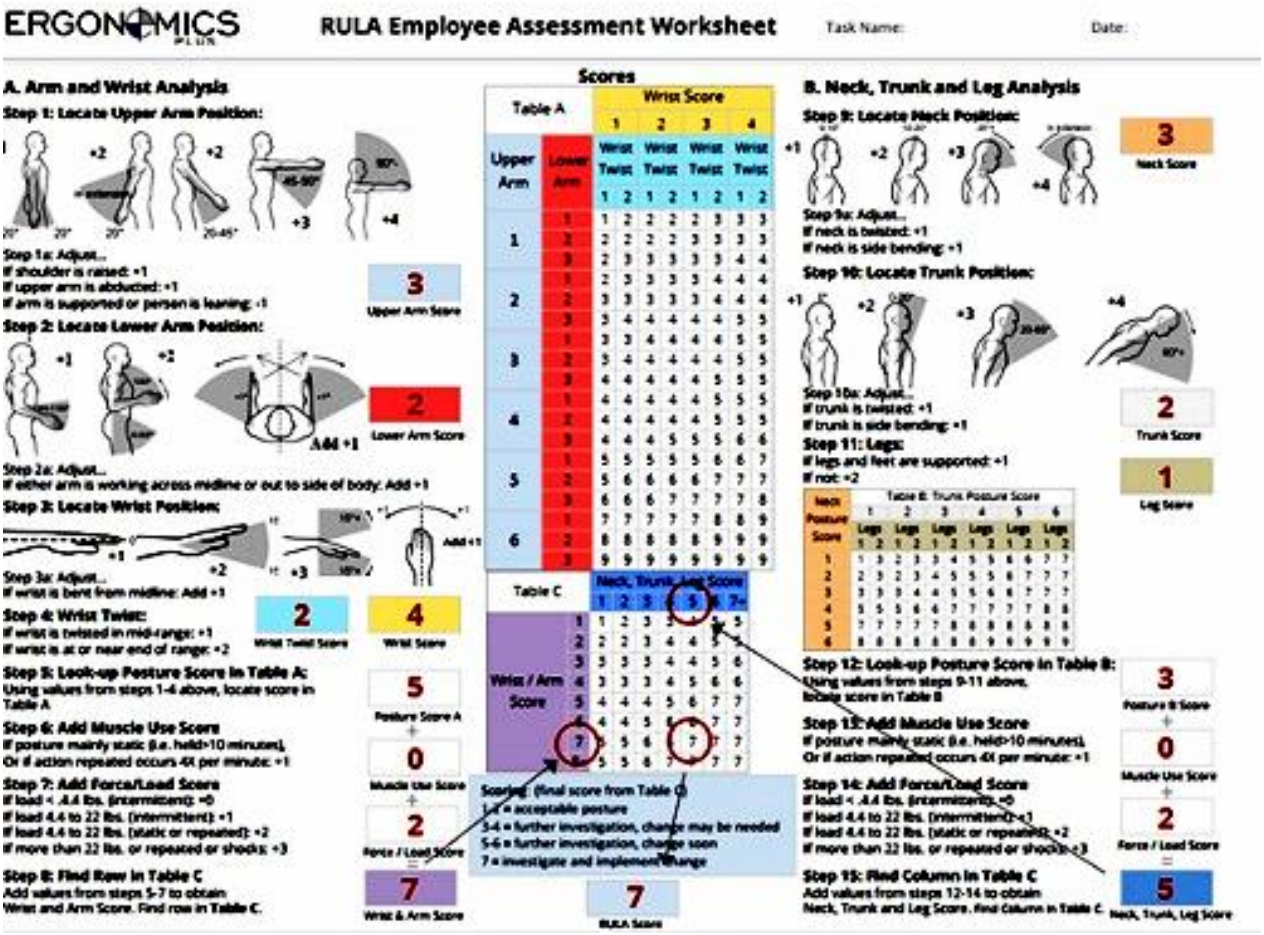

Figure 1. RULA Assessment; Step wise procedure and scores interpretation

RULA analysis helps in determining the stressed position and gives ways to solve those problems. The development of RULA occurred in three phases. The first was the development of the method for recording the working posture, the second was the development of the scoring system, and the third was the development of the scale of action levels which provide a guide to the level of risk and need for action to conduct more detailed assessments[5].

Ergonomic analysis is quite a new field in the engineering but is very important because whenever a job is done, human body may be stressed out by an awkward position, extreme

temperature or repeated movements which effect the musculoskeletal system[6]. Musculoskeletal disorders affect the body muscles, joints, ligaments and nerves. The ergonomic analysis helps to find out the most comfortable postures and help to find if the redesigning of the workplace is needed or change of posture is a better option.

12 SELECTION OF THE ANALYSIS TYPE

The software selected for the ergonomic analysis was CATIA. CATIA software has two modules under ergonomic analysis and design named as Activity analysis and Posture analysis

Activity analysis has got further options for different types of analysis which includes RULA, Push/Pull analysis, Biomechanics single action analysis, Carry analysis and Lift/Lower analysis

Out of all, RULA analysis was chosen because it has the capability to monitor the whole activity. Push/Pull, Carry analysis, Lift/lower analysis were ruled out because there are no such movements involved in a cockpit where a pilot has got to lift up an object or carry any kind of weight.

13 SET UP FOR ERGONOMIC TRAINER AIRCRAFT (GTA)

A CAD model of GTA was downloaded from the internet to carry out its ergonomic analysis. GTA is a two seater plane. However, only the front cockpit has been analysed. The aircraft was analyzed with a bar inserted as dummy control stick at two different positions i.e. center stick and side stick. It was subjected to perform a pitch up, pitch down, right roll and left roll and the score for each position was calculated. Overall methodology followed in this paper is shown in Figure 2.

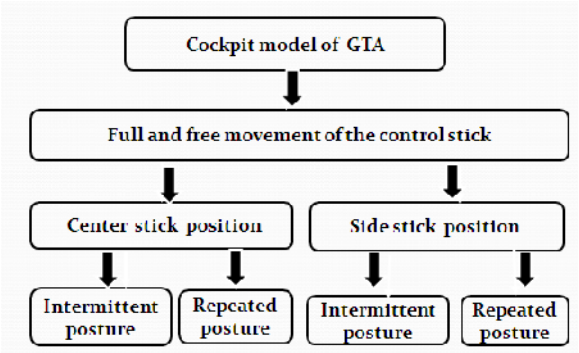

Figure 2. Overall methodology followed

14 ERGONOMIC EVALUATION OF

Firstly for the sample analysis and to find a way to optimize the control stick, a rough analysis with all its calculations was done on GTA aircraft cockpit. For both the positions, cockpit controls tick was analyzed for a full and free movement which included following motions.

- Maximum forward deflection
- Maximum backward deflection
- Left side deflection and
- Right side deflection.

The control stick movements at which ergonomic analysis was carried out are shown in Figure 3.

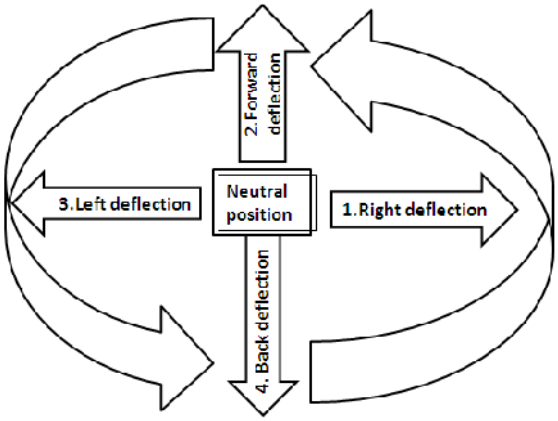

Figure 3. Full and Free Movement of the control stick

Values for all these movements were assumed as shown in Table 2.

Table 2. Maximum assumed values for control Stick deflections of GTA

Position of the control stick	Deflection
Forward deflection	2 in
Backward deflection	3.5 in
Left side deflection	3 in
Right side deflection	3 in

RULA analysis has the capability to monitor the whole activity and keep a look on each part of the body. Whenever a control or the posture for that control is analyzed it can be analyzed under two options

- Intermittent
- Repeated

Intermittent means that the frequency of repeating that movement is less than 4 times per minute while repeated movement means that frequency exceeds the described number. So each posture was analyzed for both the options to see what would be the effect on muscles for repeated and intermittent postures.

14.1 Intermittent Posture consideration in ergonomic evaluation of center stick position of GTA

Firstly, the control stick is at its neutral position (which is perfect vertical) and once evaluated, the RULA score for the posture is green which says that the posture is acceptable as shown in Figure 4.

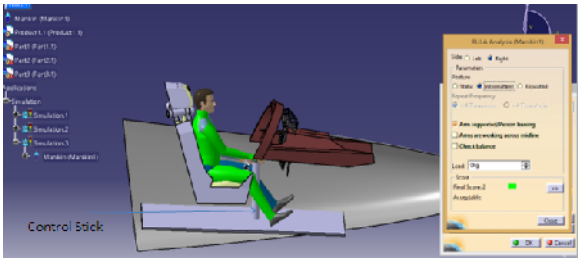

Figure 4. Neutral position of the control stick(labeled) for intermittent posture when the full and free movement starts

After this, the control stick is subjected to move to its right side to its maximum deflection as shown in Figure 5.

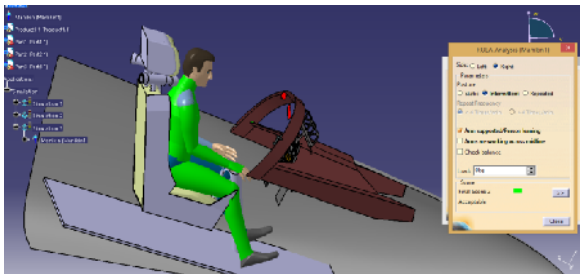

Figure 5. Right Side Deflection of the control stick keeps the posture safe

When the control stick is moved towards it right side again the posture is green with the score of 2 revealing that the operator is comfortable with this posture and that the joints deflections are within their limits. Next the control stick is moved forward as shown in Figure 6.

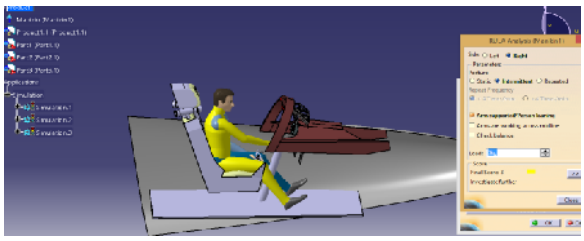

Figure 6. Forward Deflection of the control stick gave RULA score of 3.

For this movement, the RULA score is 3 indicated by a yellow color. Yellow color indicates that the posture needs to be investigated further. Also from Figure 6, it can be seen that spine, arm and forearm are all indicated by a yellow color which means that if this posture is needed to be investigated further, then all the parts are to be examined.

After that left deflection to the left side is given to the stick as shown in Figure 7.

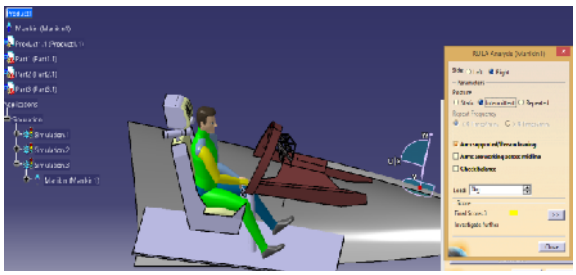

Figure 7. Left Side Deflection of the control stick gave a yellow color for the posture

For this posture, the RULA score of 3 is denoted by a yellow color. Finally, a backwards full deflection is given to the stick and score came out as shown in Figure 8.

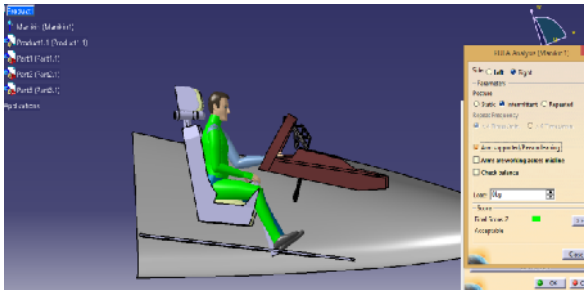

Figure 8. Back Deflection of control stick keeps the posture safe

This posture has a RULA score of 2 as indicated by green color.

Results for full and free movement of the control in intermittent posture can be summarized as shown in Table 3.

Table 3. Summary of the final RULA scores for the intermittent posture of the center stick

Position	RULA Score	Color
Neutral position	2	
Right deflection	2	
Forward deflection	3	
Left deflection	3	
Back deflection	2	

14.2 Repeated Posture consideration in ergonomic evaluation of center stick position of GTA

Repeated posture is that posture whose frequency of the movement is greater than 4 times per minute. Again, the stick's full and free movement is analyzed for repeated posture. When the stick is at its neutral position, posture is as shown in Figure 9.

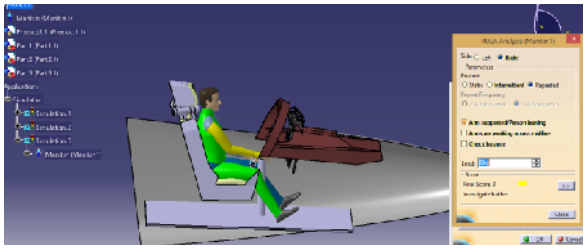

Figure 9. Neutral Position of the Control Stick for repeated posture gives a yellow color for final RULA score

For the repeated posture neutral position had a RULA score of 3 whereas it was a green color with a RULA score of 2 for intermittent posture. So it is very obvious that for the same posture, score can be different depending upon the frequency of the movement. Later, the stick was given left side deflection and the angles of all joints of arms and forearms were accordingly changed so as to reach the control stick as shown in Figure 10.

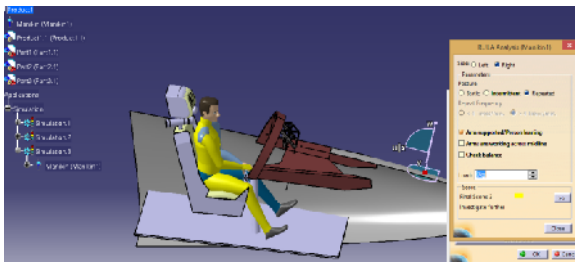

Figure 10. Left Side deflection of the center stick gives a RULA score of 3

For the left side of control stick pilot had a yellow score. From the left side control stick was assumed to travel to forward maximum position as shown in Figure 11.

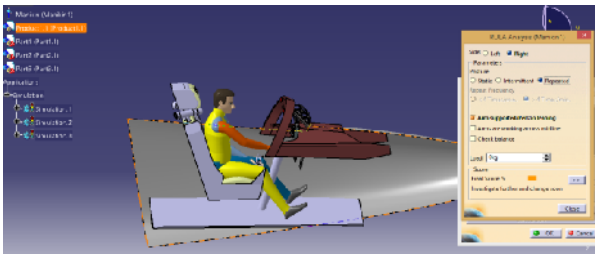

Figure 11. Forward Deflection of the stick gives RULA score 5

Forward position revealed a RULA score of 5 indicated by an orange color as shown in Figure 11. If this posture is to be analyzed further, main focus has to be the arm as it bears an orange color. With little changes in degree of freedom of arm or forearm, it is possible to bring the arm to a safe posture but this is not the concern. Our concern is to find that for a specific location of control when a pilot reaches out to that control what kind of movements are involved in that and for each movement what the score is so that we can conclude if that position of the control is desirable or not. Furthermore, nowadays, ergonomics is more focused upon fitting the workplace for the human not the human for the workplaces. Moving on, control stick was moved to right side with maximum allowable deflection as shown in Figure 12.

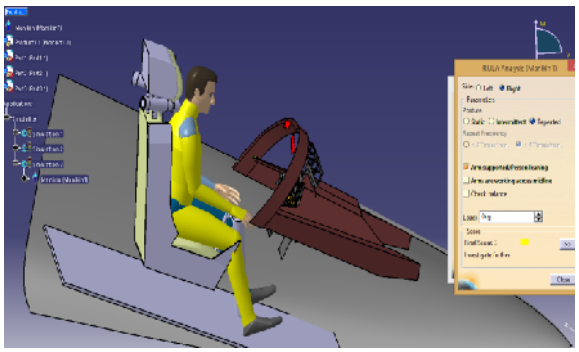

Figure 12. Right Side Deflection of control stick needs further investigation

Right position of the control stick resulted in a yellow color with a RULA score of 3 for the operator. Form the right side position, it was moved to back side so as to complete full and free movement of the control stick as shown in Figure

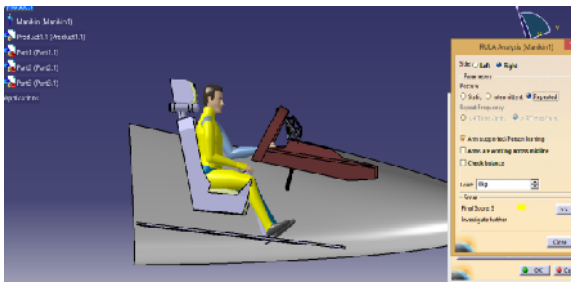

Figure 13. Back Deflection of the control stick gives yellow color

RULA score for the back deflection was 3 as evident by a yellow color.
Results for the repeated posture can be summarized as shown in Table 4.

Table 4. Summary of the RULA scores of the center stick position for repeated posture

Position of the control stick	RULA score	Color
Neutral position	3	
Left deflection	3	
Forward deflection	5	
Right deflection	3	
Back deflection	3	

15 ERGONOMIC EVALUATION OF SIDE STICK POSITION

After completing the ergonomic evaluation of the control stick in center position, it was time to evaluate the side stick control position from ergonomic point of view as already shown in Figure 2.

15.1 Intermittent Posture consideration in ergonomic evaluation of side stick position of GTA

Firstly the control stick was analyzed at its neutral position as shown in Figure 14.

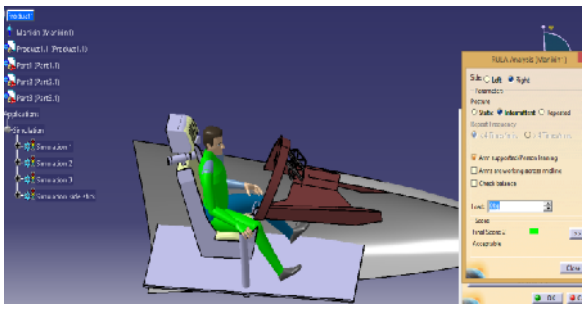

Figure 14. Neutral Position of the control Stick for intermittent posture

Neutral position in this posture is acceptable as it is shown by green color. After this, control stick was deflected to its left side to its maximum allowable value as shown in Figure 15.

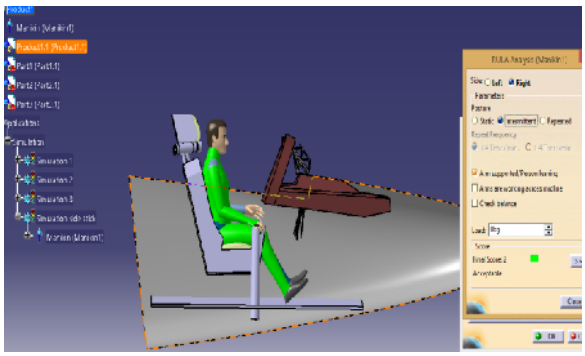

Figure 15. Left Side Deflection of the control stick kept the posture safe

For the left side deflection of the control stick, posture had a green color with a RULA score of 2. After this the stick was given forward deflection and the posture was analyzed as shown in Figure 16.

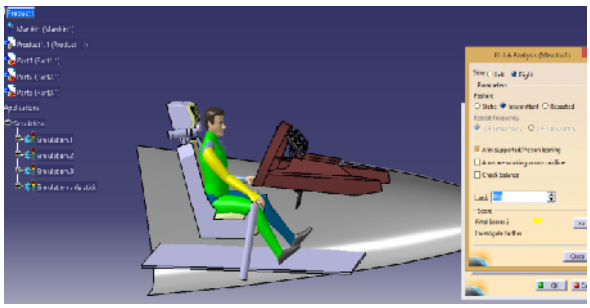

Figure 16. Forward Deflection of the control stick returned a RULA score of 3

For the forward deflection posture was yellow with more focus on the right arm which is shown in yellow color in Figure 17. The stick was then moved to its right side.

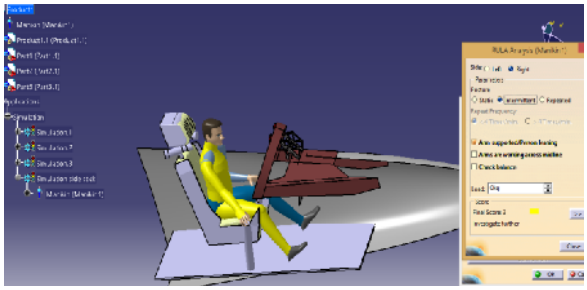

Figure 17. Right Side Deflection of the control stick gives a yellow color

The above posture had a RULA score of 3 with a yellow color as shown in Figure 17. Finally, the stick is moved backwards to complete the full and free movement of the stick as shown in Figure 18.

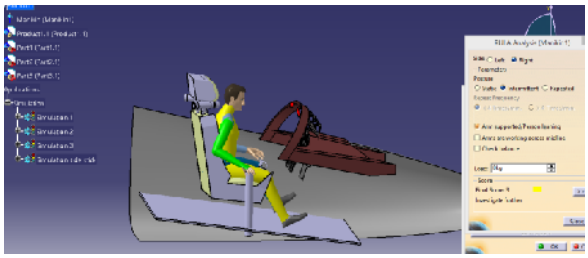

Figure 18. Forward Deflection of the control stick with a RULA score of 3

For the back deflection, result came out to be 3 with a yellow color as shown in Figure 18.
The results for the intermittent posture with a side stick can be summarized as shown in Table 5.

Table 5. Summary of final RULA scores of the intermittent posture of side stick

Position of the control stick	RULA score	color
Neutral position	2	
Left deflection	2	
Forward deflection	3	
Right deflection	3	
Back deflection	3	

15.2 Repeated Posture consideration in ergonomic evaluation of side stick position of GTA

Same full and free movement, for the repeated posture for same angles and deflections of joints and body parts, was analyzed and the scores were recorded. RULA score for the neutral position is 3 with a color of yellow as shown in Figure 19.

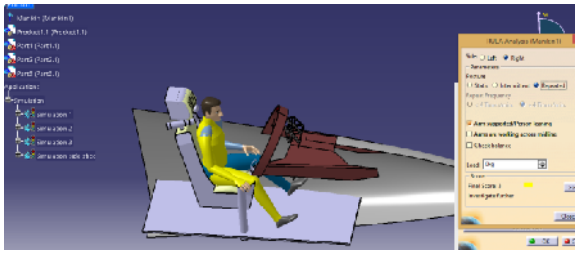

Figure 19. Neutral Position of the control stick for Repeated Posture with a yellow color

It is important to highlight that for the same deflection of control stick to its right and same angles of the arm for the intermittent posture, RULA score was 2 with a green color as already shown in Figure 15.
The RULA score for the left deflection of the stick came out to be yellow as shown in Figure 20.

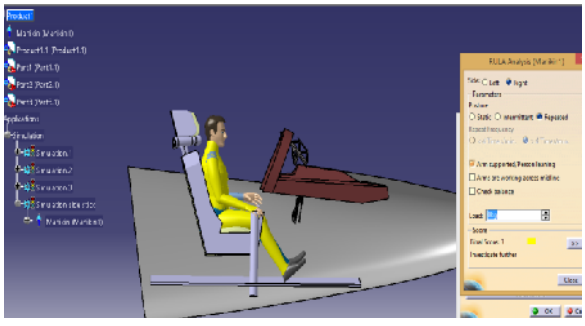

Figure 20. Left Side Deflection of the side stick gave yellow color with a RULA score of 3

For the forward deflection too, the RULA score was 3 as shown in Figure 21.

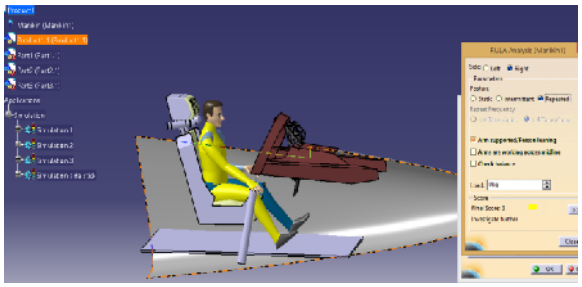

Figure 21. Forward Deflection of the side stick gave a RULA score of 3

For the right side deflection the RULA score came out to be 5 with the arm being the most stressed area as shown in Figure 22.

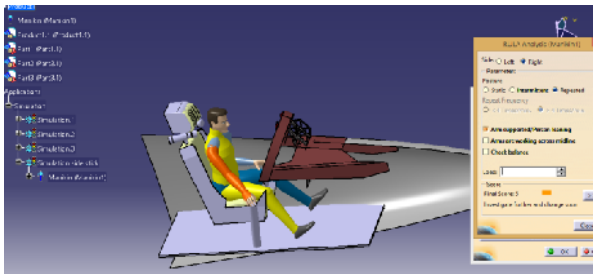

Figure 22. Right Side Deflection of the side stick with a RULA score of 5

After that the control stick was moved backwards to calculate the RULA score for the back deflection as shown in Figure 23.

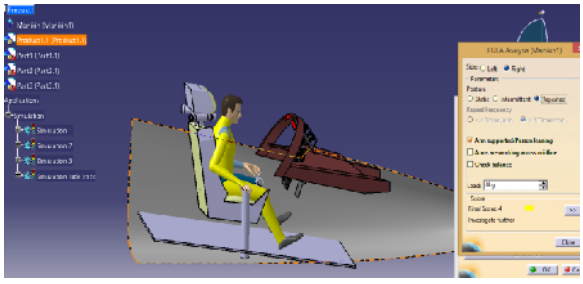

Figure 23. Back Deflection of the side stick with a yellow color

With the back deflection, given operator had a RULA score of 3 indicated by yellow color.
The results for the repeated posture can be summarized in next table 6.

Table 6. Summary of the final RULA score of side stick for the repeated posture

Position of the control stick	RULA score	color
Neutral position	3	
Left deflection	3	
Forward deflection	3	
Right deflection	5	
Back deflection	3	

16 COMPARISON OF RESULTS

Finally the results were compared to find out which position is better as shown in Tables 7 and 8.

Table 7. Comparison of RULA scores for intermittent posture for both positions of control stick

INTERMITTENT				
	CENTER STICK		SIDE STICK	
	Score	Color	Score	Color
Neutral position	2		2	
Left deflection	2		2	
Forward deflection	3		3	
Right deflection	3		3	
Back deflection	2		3	

Table 8. Comparison of RULA scores for repeated posture for both positions of control stick

Repeated Posture				
	Center stick		Side stick	
	Score	Color	Score	Color
Neutral position	3		3	
Left deflection	3		3	
Forward deflection	5		3	
Right deflection	3		5	
Back deflection	3		3	

17 CONCLUSION

From the above results, it can be concluded that when the posture is intermittent, it is better to keep the control stick at center position as the center

position has 3 green RULA scores and two yellow RULA scores while for the same full and free movement side stick has two green RULA scores and three yellow RULA scores which makes the center stick position less comfortable as compared to side stick.

For the repeated posture, score is same i.e. 4 yellow RULA scores and one orange RULA scores so the stick needs to be analyzed for further few movements or maneuvers so that a wider picture is obtained to conclude the result.

REFERENCES

[1] Salvendy, G., Handbook of human factors and ergonomics. 2012. 16.

[2]. Sanders, M.S.M., Ernest J, Human factors in engineering and design.

[3]. Posner, R.A., Economic analysis of law.

[4]. Vignais, N.M., Markus Bleser, Gabriele Mura, Katharina Gorecky, Dominic Marin, Frédéric, Innovative system for real-time ergonomic feedback in industrial manufacturing. Applied ergonomics, 2103. 44(4): p. 566-574.

[5]. McAtamney, L.N.C., E, RULA: a survey method for the investigation of work-related upper limb disorders. Applied ergonomics, 1993. 24(2): p. 91-99.

[6]. Porter, J.C., Keith Freer, MT Bonney, Maurice C, Automotive Ergonomics. Chapter 3. Computer-Aided Ergonomics Design Of Automobiles. Publication of: Taylor And Francis Ltd, 1993.

[7]. McAtamney, L. and E. Nigel Corlett, *RULA: a survey method for the investigation of work-related upper limb disorders.* Applied Ergonomics, 1993. **24**(2): p. 91-99.

NUMERICAL STUDY OF TENSILE TESTING OF THIN POLYDIMETHYLSILOXANE (PDMS) SAMPLE

Syed Murtuza Mehdi[*] Maaz Akhtar[*] Soo Wan Kim[**] and Muhammad Muzamil[*]
[*]Department of Mechanical Engineering, NED University of Engineering and Technology, Karachi, Pakistan.
[**]Department of Mechatronics Engineering, Jeju National University, Jeju, South Korea.

[*]Corresponding author. Fax: 92-21-99261255
E-mail address: drmurtuza@neduet.edu.pk (Syed Murtuza Mehdi)

ABSTRACT

Polydimethylsiloxane (PDMS) being biocompatible and thermally stable silicone polymer has been widely used as a stretchable substrate for stretchable electronics, biomedical implants, lab-on-a-chip and microelectromechanical systems (MEMS). In this paper we have numerically studied the effect of linear and quadratic basis functions and incompressibility option during a tension test. The main goal of the study is to identify the most optimum combination of the finite element basis function and the incompressibility option that can offer the best comparison with the experimental linear stress-strain curve for PDMS.

Keywords: Polydimethylsiloxane, Tensile test, Stretchable substrate, Stretchable electronics, Basis functions, Incompressibility option1

1 INTRODUCTION

Polydimethylsiloxane (PDMS) is a biocompatible polymer that can be used in variety of applications such as microelectromechanical systems (MEMS), stretchable electronics and biomedical sensors [1-5]. PDMS can be used as a flexible and stretchable substrate for deposition of thin films of different materials that can function as a sensing layer or as a conductor for various thin film devices [6-8]. Also rough PDMS has been widely used as a substrate material for the fabrication of stretchable conductors [9-11]. PDMS can also be used as a biomedical implant (external or internal) which can carry a thin film of sensing material on it [5, 12]. For better product development, increasing popularity of PDMS and commercialization of stretchable electronics it is unavoidable to carry out research at different levels in understanding and simplifying the behaviors of this polymer when subjected to mechanical loads such as stretching or tension.

Therefore, in this paper we have used finite element based software Comsol Multiphysics to mimic a tensile test performed on a PDMS test sample. The main goal of this study is to identify the best combination of numerical parameters such as the basis functions and the effect of incompressibility option which can offer the best comparison with the experiments and theory.

2 NUMERICAL DETAILS

Figure 1 elaborates the geometry and grid used for the numerical simulations.

The dimension of the test sample is 10x5x1mm. The material model considered in this study was linear-elastic and isotropic. As the boundary

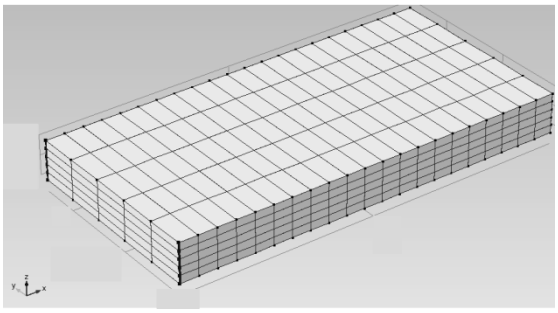

Figure 1. Geometry and grid used for numerical simulations

conditions one end was rigidly fixed while the other end was subjected to axial displacement which corresponds to axial strain in steps of 0.05 till 0.3. All other surfaces were kept free. The tensile test conditions and all material properties were taken from Johnston *et al*. [13]. Since, the geometry is simple with no curvatures therefore quadrilaterals (hexahedrons) elements were preferred for all simulations, as shown in Figure 2.

It can be noticed from Fig. 2 that the human skin can be stretched approximately up to 30% axial strain without any irreversible effects therefore; in this work the applied axial strain was limited to 30% only. It is well known that under such circumstances the PDMS behaves linearly and obeys Hooke's law ($\sigma = E\varepsilon$) where σ is the normal stress, E is the Young's modulus and ϵ is the applied axial strain [13]. The computed normal stress at each strain was then compared to the theoretical stress (Hooke's law) and with the experiments of Johnston *et al*. [13] within the linear $\sigma - \varepsilon$ region.

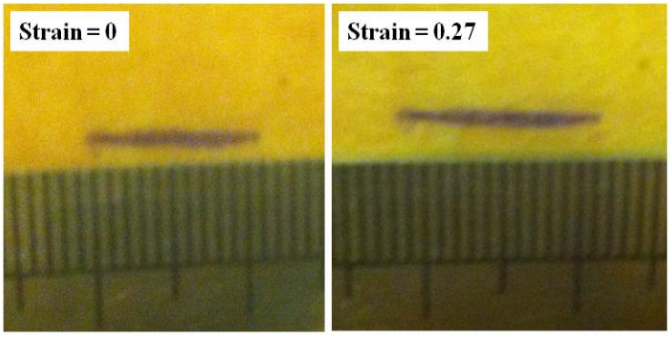

Figure 2. Real time photographs depicting the stretchability of human skin (forearm). It can be noticed in the right photograph that the skin has been stretched up to 27%.

In the regime of this paper we have investigated the effect of finite element basis functions (linear and quadratic) and the effect of incompressibility option on the computed stress. The incompressibility option within Comsol environment is valid for materials having Poisson ratio of 0.5 such as the PDMS [14]. Table 1 shows the simulation test cases studied in this paper.

Table 1 Simulation cases studied

Case No.	Basis Function	Incompressibility option
1	Linear	on
2	Linear	off
3	Quadratic	on
4	Quadratic	off

3 RESULTS AND DISCUSSION

Figure 3 depicts the effect of using linear finite elements with the incompressibility option on (Case 1) on a grid size of 21x5x5.

Further, it was observed that no improvement in the value of the computed stress takes place when the number of element along the width and thickness direction was increased by a factor of 4. This means that the numerical tensile test of PDMS sample remain unaffected of the grid size along the lateral dimensions. The results of Figure 3 then suggest that the computed stress varies with a maximum of 11.5% error with the experiments and with 8.2% error with the theoretical stress (Hooke's law). On the other hand, when the incompressibility option was turned off with linear basis elements (Case 2) the error with the experiments reduces to 10% and reaches 6.8% maximum with the theoretical stress. This is shown in Figure 4.

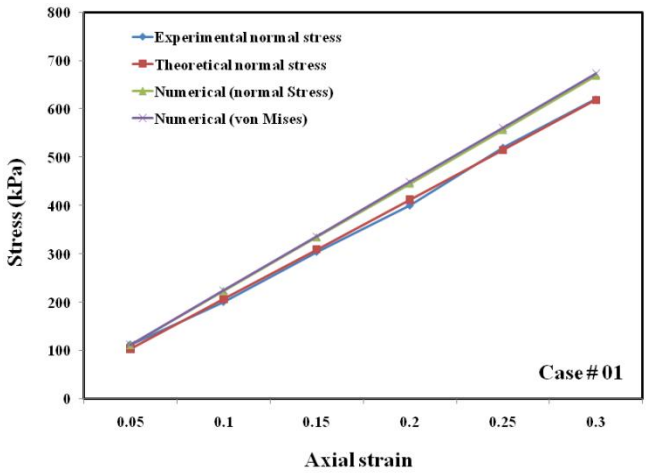

Figure 3. Comparison of computed stress with experiments and theory for simulation case 1

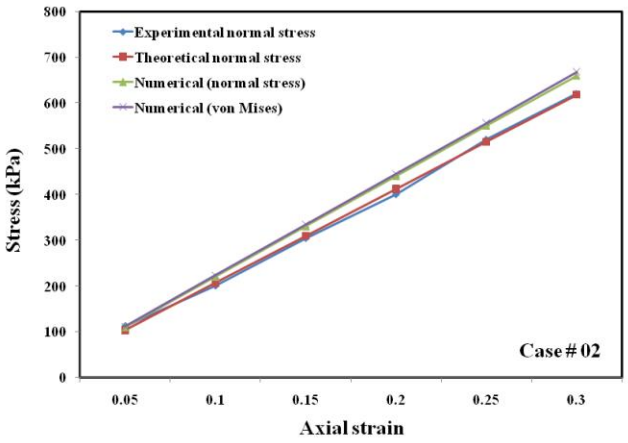

Figure 4. Comparison of computed stress with experiments and theory for simulation case 2

Finally when quadratic basis function was used with the incompressibility option on (Case 3) the maximum error with the experiments was 6% and with that of theoretical stress was 2.9%. No further reduction in the error was observed when the simulations were repeated using quadratic basis function and the incompressibility option off (case 4). These results are shown in Figure 5 and Figure 6 respectively.

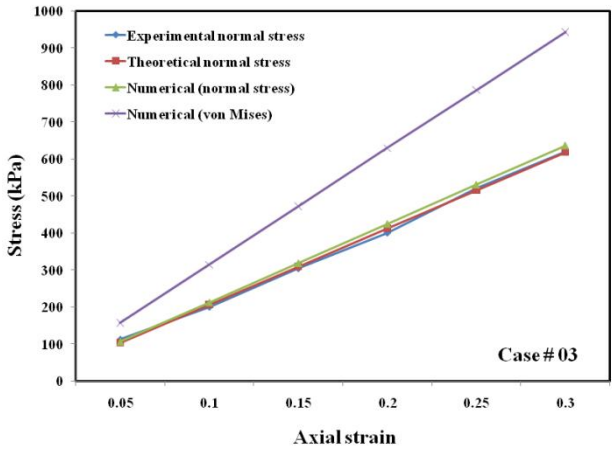

Figure 5. Comparison of computed stress with experiments and theory for simulation case 3

It can also be noticed that for these cases no match between the von Mises stress and the

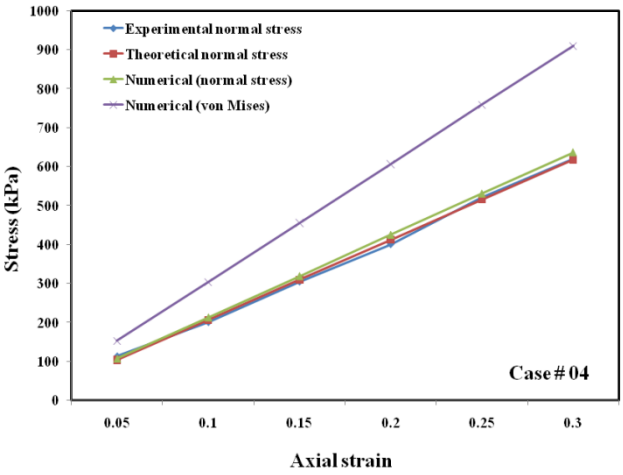

Figure. 6 Comparison of computed stress with experiments and theory for simulation case 4

experimental/theoretical stress exist. It was found out that without using the option of incompressibility the error between the computed and experimental/theoretical stress tends to reduce therefore, the errors were recalculated for the linear and quadratic basis functions with the incompressibility option turned off on a refined grid size of 30x5x5. This time the maximum error for the linear basis function reduces to 8.5% as compared to the experiments and 5.3% as compared to the theoretical stress, while for the quadratic basis function it was 6% with the experiments and 2.9% with the theoretical stress. As indicated earlier that only the number of element in the axial direction were increased and it was found out that for each basis function an optimized grid in the axial direction tends to reduce the error. However, this effect was higher for the linear basis function as compared to the quadratic basis function.

4 CONCLUSIONS AND FUTURE WORK

In summary following conclusive points can be drawn from the study:

Within the linear material model regime (Hooke's law) the results for the tensile test of PDMS can be well compared with the experiments and theory with less than 5% and 3% error respectively.

The incompressibility option when used in combination with the linear basis function tends to increase the error between the computed stress and the experimental/theoretical stress while its effect with the quadratic basis function was found to remain negligible.

Both the linear and quadratic basis functions can be effectively used for conducting virtual tensile test for the PDMS within the Hooke's law regime.

An optimized grid size must be chosen for each basis function in order to compare the results.

For the geometry, boundary conditions, material model and the basis functions considered in this study the number of elements along the lateral dimensions seems to remain ineffective for the results and therefore, only the grid size in the longitudinal direction is to be optimized.

Unlike the quadratic basis function when linear basis function is used the maximum von Mises stress also matches with the experimental and theoretical stress.

In general the quadratic basis function tends to minimize the error between the computed stress and the experimental/theoretical stress.

In future numerical simulations and experiments regarding tensile test of PDMS samples having micro roughness features will be investigated with and without a thin metallic layer on it.

ACKNOWLEDGMENT

The authors would like to thank the NED University of Engineering and Technology, Karachi, Pakistan and Jeju National University South Korea for providing support to carry out this study.

REFERENCES

[1] F. Schneider, J. Draheim, R. Kamberger, & U. Wallrabe, Process and Material Properties of Polydimethylsiloxane (PDMS) for Optical MEMS. *Sensors and Actuators A*: Physical, 151(2), 95-99, 2009.

[2] X. M. Jing, D. Chen, C. Huang, et al., Elastic MEMS Probe Card BASED on the PDMS

substrate, Journal of Micromechanics and Microengineering, 20(2), 2010.
[3] S. M. Mehdi, H. W. Dang, C. N. Kang, & K. H. Choi, Resistive behaviour of silver nanoparticle films on ultra-low modulus polydimethylsiloxane with trench type roughness, *Journal of Physics D: Applied Physics*, *48*(1), 015303, 2015.
[4] D. S. Gray, J. Tien, and C.S. Chen, High-Conductivity Elastomeric Electronics, *Advanced Material*, Vol. 16, No. 5, pp. 393-397, 2004.
[5] N. T. Boker. Prototyping of a Stretchable Microelectrode Array for Cardiotoxicity Drug Screening, Master Thesis. *Delft University of Technology ,*2009.
[6] S. Xu, Y. Zhang, J. Cho, J. Lee, X. Huang, L. Jia, & J. A. Rogers, Stretchable batteries with self-similar serpentine interconnects and integrated wireless recharging systems, *Nature communications*, *4*, 1543. 2013.
[7] P. Gutruf, C. M. Shah, S. Walia, H. Nili, A. S. Zoolfakar, C. Karnutsch, & M. Bhaskaran, Transparent functional oxide stretchable electronics: micro-tectonics enabled high strain electrodes, *NPG Asia Materials*, *5*(9), e62, 2013.
[8] M. S. White, M. Kaltenbrunner, E. D. Głowacki, K. Gutnichenko, G. Kettlgruber, I. Graz, & N. S. Sariciftci, Ultrathin, Highly Flexible and Stretchable PLEDs. *Nature Photonics*, *7*(10), 811-816, 2013.
[9] N. Lambricht, T. Pardoen and S. Yunus. Giant Stretchability of Thin Gold Films on Rough Elastomeric Substrates. *Acta Materialia,* vol. 61, 2013.
[10] C. W. Park, S. W. Jung, S. C. Lim, J. Y. Oh, B. S. Na, S. S. Lee, & J. B. Koo, Fabrication of well-controlled wavy metal interconnect structures on stress-free elastomeric substrates. *Microelectronic Engineering*, *113*, 55-60, 2014.
[11] S. M. Mehdi, J. Jo, Y. H. Doh, H. W. Dang, & K. H. Choi, Stretchable and flexible resistive behavior of poly (3, 4-ethylenedioxythiophene): Poly (styrenesulfonate) thin film on ultra-low modulus polydimethylsiloxane with trench-type roughness. *Journal of Polymer Science Part B: Polymer Physics*, *53*(3), 226-233, 2015.
[12] D. H. Kim, N. Lu, R. Ma, Y.S. Kim, R. H. Kim, S. Wang, and J. A. Rogers, Epidermal Electronics, *Science*, 333(6044), 838-843, 2011.
[13] I. D. Johnston, D. K. McCluskey, C. K. L. Tan, and M. C. Tracey, Mechanical characterization of bulk Sylgard 184 for microfluidics and microengineering. *Journal of Micromechanics and Microengineering*, *24*(3), 035017, 2014.
[14] Comsol Multiphysics v 4.2 Structural Mechanics Module User's Guide.

NUMERICAL INVESTIGATION OF THERMAL PERFORMANCE OF SOLAR AIR HEATER WITH RIB-ROUGHENED CHANNELS

M. Shakaib[1,*], IslahUddin[1], I. Ahmed[2]
[1]Mechanical Engineering Department, NED University of Engineering & Technology, Karachi, Pakistan
[2]Faculty of Engineering Technology, University Malaysia Pahang, Kuantan, Malaysia

[*]Corresponding author. Tel.: 021-99261261 Ext. 2334
E-mail address: mshakaib@neduet.edu.pk

Abstract

Two dimensional CFD modelling reveal velocity and temperature profiles in rib-filled channels of solar air heaters. The pitch and height of ribs used for creating artificial roughness change the pattern of local heat transfer coefficients. When absorber plate is placed opposite to the rough surface, higher heat transfer is observed when compared to smooth channel. Heat transfer reduces if ribs are touching the absorber plate. A comparison with experimental results shows fair agreement.

Keywords: CFD; air heater; heat transfer coefficient

1 INTRODUCTION

Solar air heaters are widely used for numerous heating applications due to its simplicity, less maintenance requirement and low cost. This device typically includes a channel / duct along with a solar absorber plate on one side. The temperature of air flowing through the duct increases due to heated absorber plate. A limitation of air heater, however, is that the heat transfer rates are quite low. A method for thermal enhancement is to create artificial roughness such as repeated wires or ribs in the rectangular channel. Several studies have been done to investigate the effect of artificial roughness on the heat transfer performance. Yadav and Bhagoria [1] studied the effect of artificial roughness using CFD approach by considering circular transverse wires. Relative pitch of about 10 and relative roughness of approximately 0.04 was found to result in maximum thermal enhancement. In another work [2] the same authors tested the effect of triangular-shaped ribs and reported optimal values of pitch and roughness height. The experimental study of Promvonge and Thianpong [3] indicated that use of rib turbulators of e/H= 0.3 though causes a very high-pressure drop increase, particularly for the in-line rib arrangement but also provides considerable heat transfer augmentations. Kumar [4] showed that heat transfer and pressure drop was higher in multi v-shaped ribs with gap than in other shapes v-shaped ribs and multi v-shaped ribs. Eiamsa-ard and Promvonge [5] experimentally investigated the flow and thermal behaviour in a channel with combined rib-grooved surface. The research showed that triangular-rib with triangular-groove had best thermal enhancement index. Chaube et al. [6] found that the peak in local heat transfer coefficient occurs at the point of reattachment of the separated flow. Prasad and Sah [7] showed that thermal performance of solar air heater increased due to booster mirror and rough channel surface. Tanda [8, 9] examined the effect of continuous and broken ribs experimentally using liquid crystal thermography. Transverse broken ribs with p=e/4 and 13.3 had the best performance. In this paper we study the effect of pitch and height of square shaped rib on heat transfer coefficient. The effect of placement of ribs is also determined at various Reynolds number.

2 MODELLING PROCEDURE

A geometry of two dimensional rectangular duct with square-shaped multiple obstructions was created and meshed in Gambit as shown in Figs. 1 and 2. The height and length of channel were 20 mm and 280 mm respectively. Three different geometries were considered:
Roughness / rib height (h_r) = 2 mm, pitch / inter-rib spacing (s) = 40 mm]\

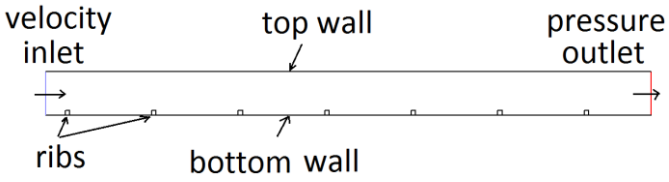

Figure 1. Computational domain

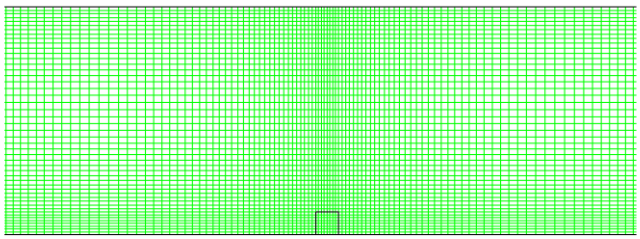

Figure 2. Mesh of the geometry

Roughness / rib height (h_r) = 2 mm, pitch / inter-rib spacing (s) = 20 mm
Roughness / rib height (h_r) = 3 mm, pitch / inter-rib spacing (s) = 40 mm
The ribs were either in contact / adjacent to the heated wall (absorber plate) or opposite to the heated wall. The boundary conditions were velocity inlet and pressure outlet at two vertical faces. Heat flux was 500 W/m^2 at:

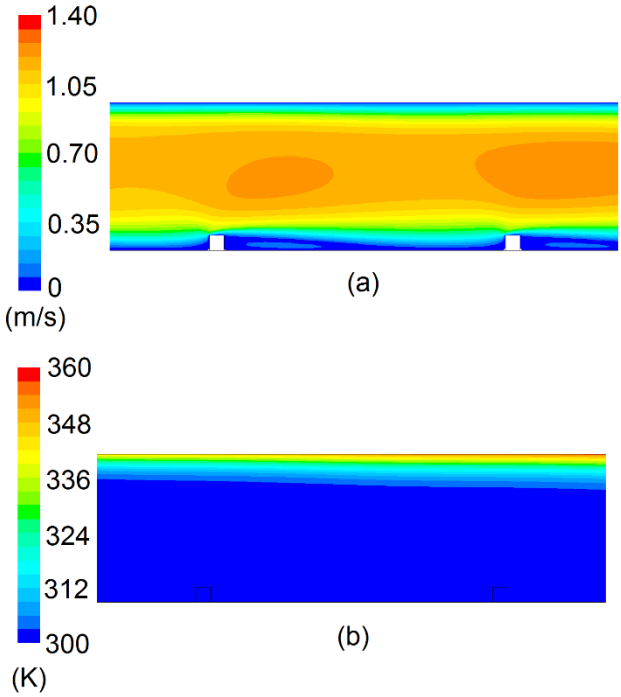

Figure 3. Flow and temperature profiles (h_r = 3 mm, s = 40 mm, top heated wall, Re = 2500)
Top face when ribs / artificial roughness is assumed opposite to absorber plate
Bottom face when ribs / artificial roughness is assumed touching the absorber plate
Reynolds number Re varied from 1000-2500. Fluid was air with density of 1.23 kg/^{3}, viscosity 1.79 × 10^{-5} kg/m·s and thermal conductivity 0.024 W/m·K, Ribs were of wood with density 150 kg/m^3 and thermal conductivity 0.048 W/m·K. The computational domain had 25,000 cells which were found to yield grid independent results. A comparison of heat transfer coefficient using 50,000 cells for the geometry containing roughness of 3 mm height at a Reynolds number of 2500 showed difference less than 0.5%. The governing equations were continuity, momentum and energy which were solved using finite volume code ANSYS FLUENT 12. Second order upwind scheme was used to discretize the governing equations. One equation Spalart Allmaras turbulence model was used for Reynolds number greater than 2000.

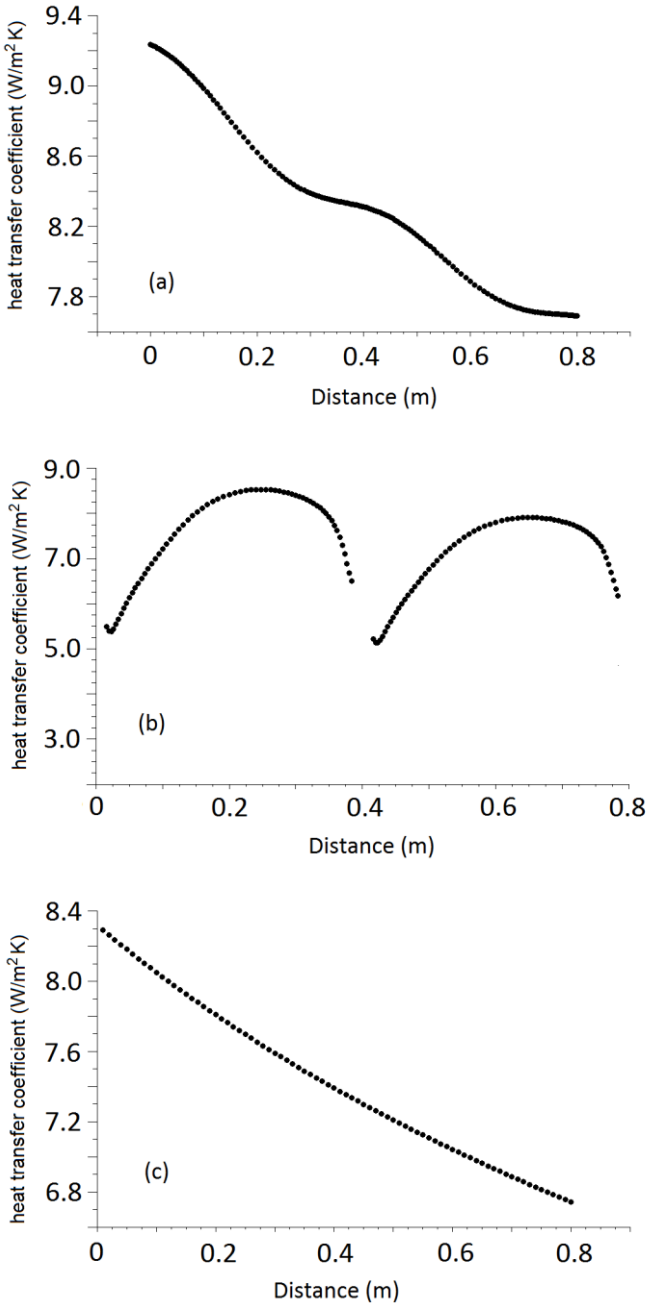

Figure 4. Heat transfer coefficient Re = 2500 (a) h_r = 3 mm, s = 40 mm, top heated wall (b) h_r = 3 mm, s = 40 mm, bottom heated wall (c) smooth wall

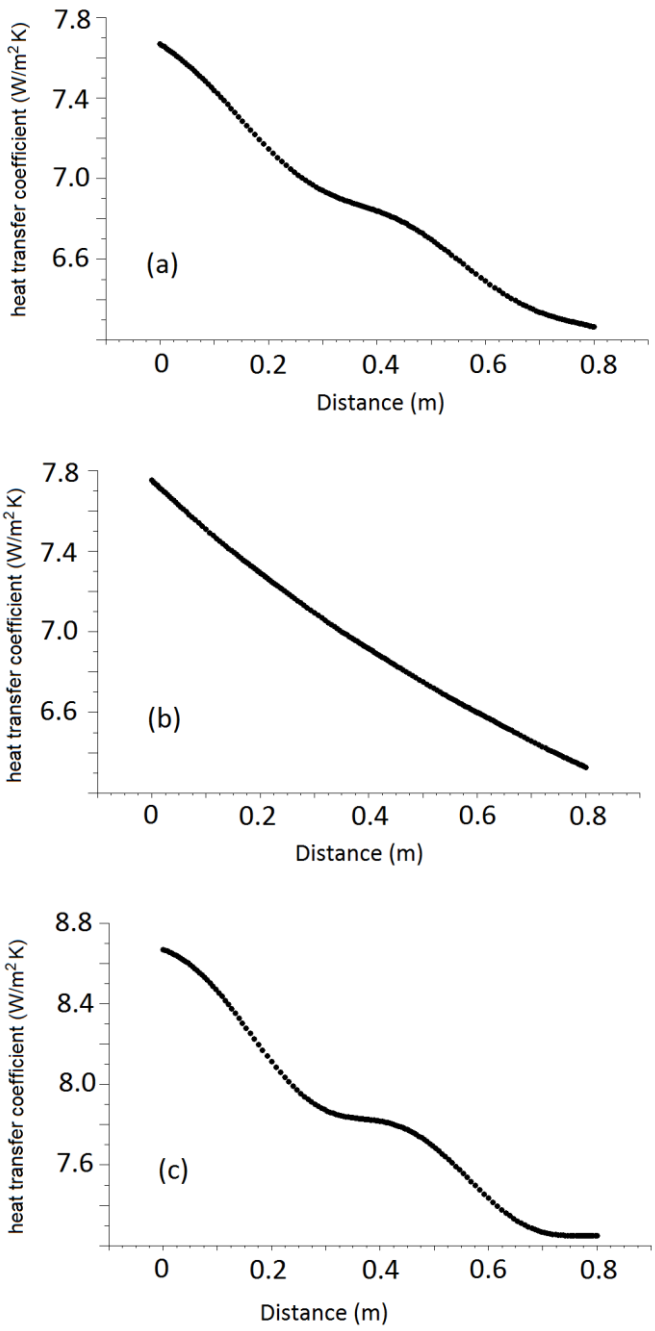

Figure 5. Heat transfer coefficient Re = 2000, top heated wall (a) h_r = 2 mm, s = 40 mm (b) h_r = 2 mm, s = 20 mml (c) h_r = 3 mm, s = 40 mm

3 RESULTS AND DISCUSSION

The velocity and temperature contours are shown in a channel with roughness rib of 3 mm and pitch of 20 mm at a Reynolds number of 2500. Rough surface is opposite to the heated surface. Due to obstructions / ribs velocity increases in the top portion and a low velocity region is created in the bottom region. Temperature values increase in the top zone due to applied heat flux. Similar patterns are seen for other geometries except the higher temperature values are observed in the bottom portion for the case when ribs were touching the heated wall (absorber plate). Variation of heat transfer coefficient is shown between three ribs (at reference positions of '0', 0.4 and 0.8 m) in Fig. 4. Heat transfer coefficient continuously decreases (Fig. 4a) in the flow direction when absorber plate coefficients (Fig. 6b). The average heat transfer coefficients are also calculated. When absorber plate is considered on the top wall, maximum heat transfer is achieved when rib height is 3 mm and pitch is 40 mm as shown in Fig. 7. The other rough channels (with rib heights of 2 mm) are almost same as smooth channel in terms of thermal

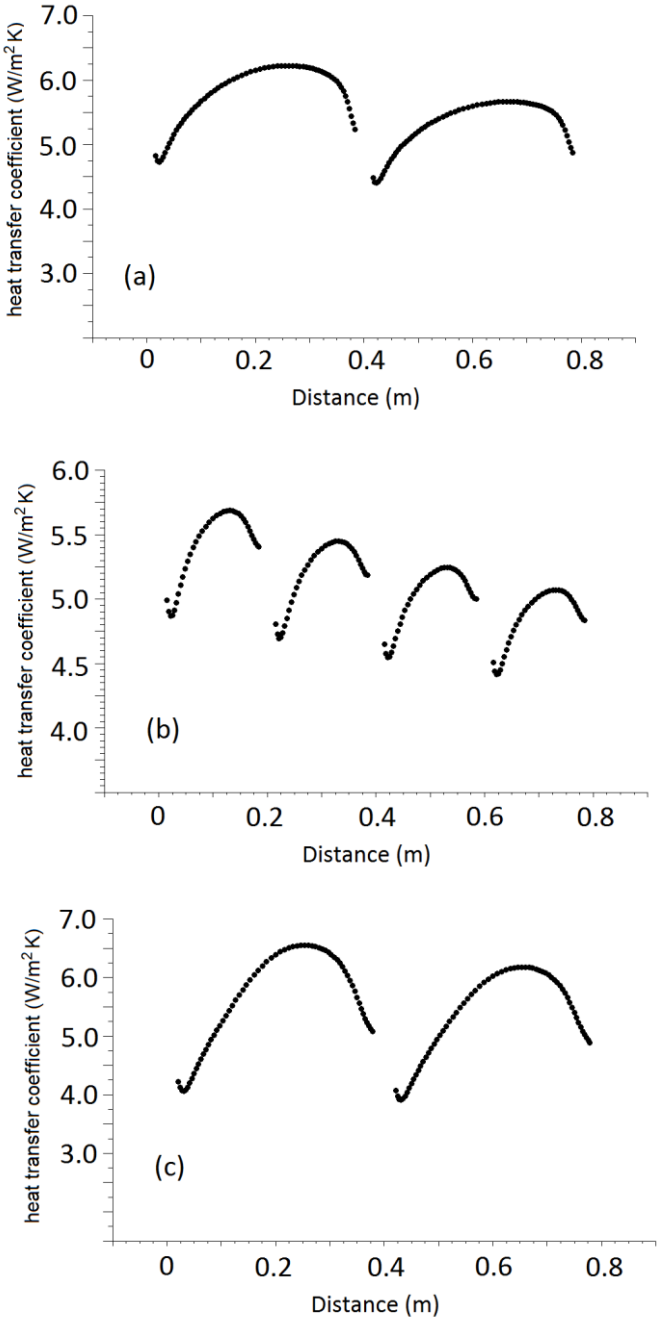

Figure 6. Heat transfer coefficient Re = 2000, bottom heated wall (a) h_r = 2 mm, s = 40 mm (b) h_r = 2 mm, s = 20 mml (c) h_r = 3 mm, s = 40 mm

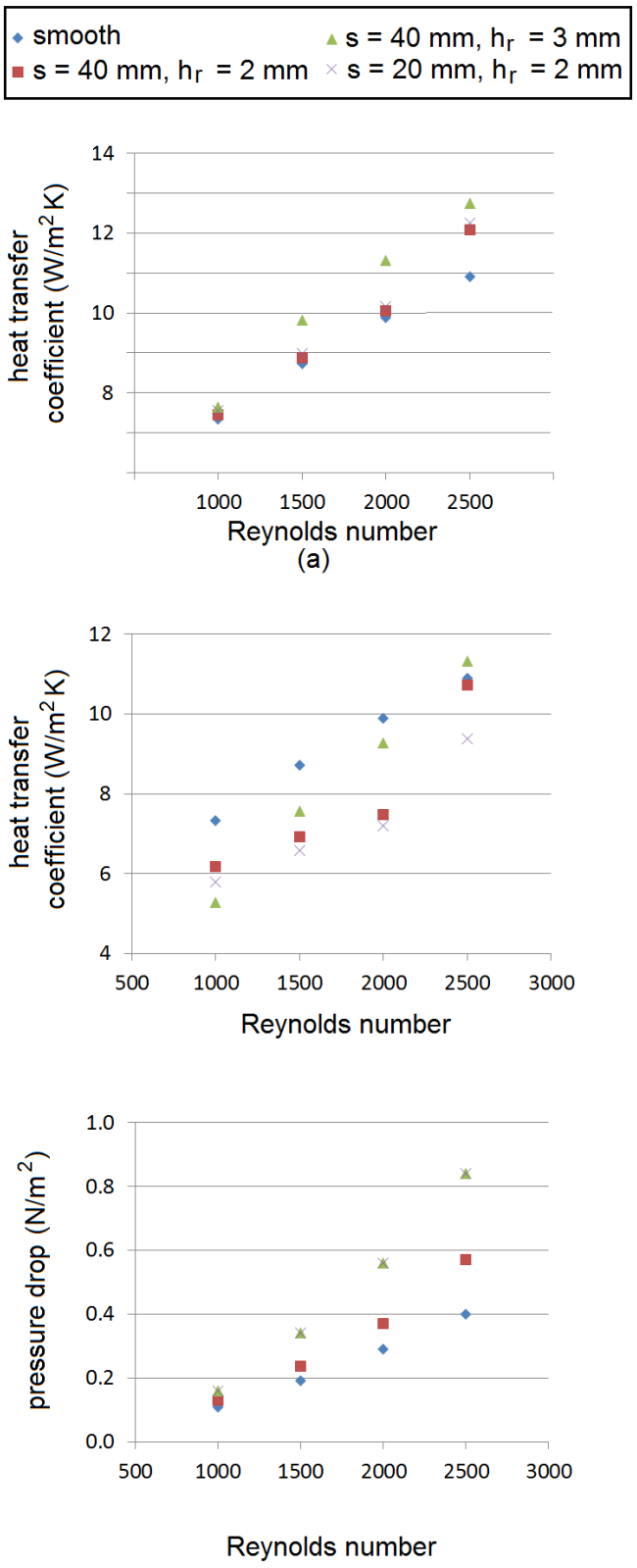

Figure 7. Average heat transfer coefficient (a) top heated wall (b) bottom heated wall and (c) pressure drop

performance as the heat transfer rates are approximately equal particularly at low Reynolds number (1000–2000). When absorber plate contacts the rough surface, the average heat transfer coefficient values in rough channels are lower than in smooth channel. The previous studies [1,2] which were conducted at higher Reynolds number showed better heat transfer performance of rough channels (in comparison to smooth channel) even though the absorber was touching the rough surface. The present work thus shows that rough surface is not always suitable for enhancing the heat transfer. Pressure drop is another important factor and its lower value is desirable. A comparison shows that the geometry which results in higher heat transfer also has higher pressure drop. To validate the findings of the present research work, Nusselt number is determined and compared with the experimentally determined Nusselt number in the paper of Tanda [8,9]. The difference was about 25% showing satisfactory agreement of the numerical results with experiments.

4 CONCLUSIONS

CFD simulations are carried out to study hydrodynamic and heat transfer in rib-roughened channels of air solar heater. The simulations reveal that use of rough channel can improve the thermal performance of the device. Ribs of 3 mm and 40 mm pitch had higher heat transfer coefficients at different Reynolds number. Further work is expected to indicate more suitable rib geometry / configurations which not only increase the thermal efficiency but also has lower pressure drops.

ACKNOWLEDGEMENTS

The authors acknowledge the support provided by the NED University of Engineering and Technology, Karachi.

REFERENCES

[1] A.S. Yadav, J.L. Bhagoria, A CFD (computational fluid dynamics) based heat transfer and fluid flow analysis of a solar air heater provided with circular transverse wire rib roughness on the absorber plate. *Energy*, 55, 1127–1142, 2013.

[2] A.S. Yadav, J.L. Bhagoria, A CFD based thermo-hydraulic performance analysis of an artificially roughened solar air heater having equilateral triangular sectioned rib roughness on the absorber plate, *International Journal of Heat and Mass Transfer*, 70, 1016–1039, 2014.

[3] P. Promvonge, C. Thianpong, Thermal performance assessment of turbulent channel flows over different shaped ribs, *International Communications in Heat and Mass Transfer*, 35, 1327–133, 2008.
[4] A. Kumar, Analysis of heat transfer and fluid flow in different shaped roughness elements on the absorber plate solar air heater duct, *Energy Procedia* 57, 2102 – 2111, 2014.
[5] E. Smith, P. Promvonge, Thermal characteristics of turbulent rib-grooved channel flows, *International Communications in Heat and Mass Transfer*, 36 705–711, 2009.
[6] A. Chaube, P.K. Sahoo, S.C. Solanki, Analysis of heat transfer augmentation and flow characteristics due to rib roughness over absorber plate of a solar air heater, *Renewable Energy* 31, 317–331, 2006.
[7] B. N. Prasad, G.N Sah, Plate temperature and heat transfer characteristics of artificially roughened solar air heater, *Energy Procedia*, 62, 256–269, 2014.
[8] G. Tanda, Heat transfer in rectangular channels with transverse and V-shaped broken ribs, *International Journal of Heat and Mass Transfer*, 47, 229–243, 2004.
[9] G. Tanda, Performance of solar air heater ducts with different types of ribs on the absorber plate, *Energy*, 36, 6651–6660, 2011.

HORIZONTAL AXIS WIND TURBINE BLADE MANUFACTURING THROUGH VARTM (VACUUM ASSISTED RESIN TRANSFER MOLDING)

Muhammad Muzamil*, Daniyal Rizwan, Hassan Mehboob, Umair Mohiuddin and Sadiqeen Noor

Mechanical Engineering Department, NED University of Engineering & Technology, Karachi, Pakistan

*Corresponding author. Tel.: +92-345-3153461
E-mail address: muzamil@neduet.edu.pk

ABSTRACT

The use of composite materials have been growing recently for structural application due to some novel properties over metals. The use of Vacuum assisted Resin Transfer Molding (VRTM) is become popular technique for the manufacturing of small and medium wind turbine blades. This process has great advantages over the conventional method (Hand Layup Method) like increase structural reliability, lower the blade weight, consistent fiber volume or orientations and mechanical strength. The presented work is to develop the setup of VRTM process through which the two halves of wind turbine blade can be manufactured separately, then assembled together to form the complete structure. The selected airfoil shape was NREL S822 with 1.2 meters in blade length. The blade is made from three layers of S-glass woven roving cloth as fiber and unsaturated Polyester as resin. In VRTM, the resin in force to draw through the whole length and width of the mold by applying pressure which was controlled through the vacuum pump attached with the portable setup. A number of blades have been fabricated to illustrate the feasibility and the application of this manufacturing method. This portable setup of VRTM has numerous cost advantages over traditional methods due to lower tooling costs, potential for room temperature processing and scalability for large structures.

Keywords: VRTM, Manufacturing, Wind Turbine Blade, Vacuum Pump.

1 INTRODUCTION

The blades of the wind turbine blades are supposed to continuously rotate under the cyclic action of wind and gravity of the structure. The life of the blades are generally designed for 15 to 20 years with the primarily required of high stiffness, low weight and high fatigue life. Several materials are available in nature and synthetically been manufactured including metals, plastics, wood, fibers and resins.

Aluminum blades are appeared first when the domestic wind power industry exploded. It offers many advantages like highly precision in dimension, improved strength and rigidity, better shear strength, not affected by UV light, recyclable and good weather stability but they are relatively heavy and costly. Wood is another readily available and inexpensive material but it requires a good shaping skills. In addition it is extremely susceptible to weather, soaking of moisture making it brittle in the sun, even it is not resilient under lateral stresses, and heavy wind can snap it without any difficulty. PVC (Polyvinyl Chloride) is another do-it-yourself choice available of turbine builders. The advantage of this material is to consume less time in shaping, good synthetic appeal and far more temperature and humidity resilient than wood, but when exposed to sunlight forms tiny hairline crack on the surface. It is noticed that PVC materials are used where don't see much and direct expose to sunlight which is common when to place wind turbine for long period of time in most Asian countries.

Nowadays the most common method for producing wind turbine blades is using fiber impregnated with resin due to it narratives properties like lightweight, high tensile strength, fatigue strength and low cost. There are a group of fibers that have become commercially available like Carbon Fiber, Kevlar and Fiber Glass that offers superior strength and stiffness when compared to high performance metal. Even different resins are also available like Polyester based, vinylester, Phenolic and epoxy based resins. Based on the easily availability of materials, the selected combination is S- Glass Fiber Woven Roving Polyester based resin upon their better properties at higher temperature, stiffness, strength and toughness.

The next step is to select the manufacturing process that reduces the number of joined in composites through structural bonding and mechanical fastening with uniform mechanical properties

along the surface. The VRTM (Vacuum assisted resin transfer molding) portable setup has been developed to fulfil the above stated output. VARTM is an advanced fabricating process for composite materials, performed by infusing liquid resin, which is sucked up by utilizing the differential pressure between the atmosphere and a vacuum, into laminated or woven fabric. To make the system cost effective, a portable setup of VRTM has been developed, to demonstrate, check the feasibility of the process and results, using home available vacuum cleaner suction pump. The blade is manufactured in two different halves through the profile of upper and lower shaped female molds which joined together through industrial glue.

The composite properties were studied via fabrication hand lay-up and VARI techniques using different layers and fiber orientation by Wisojodharmo and Roseno, concluded VRTM have better properties. [2]

Kong et al. [3] investigated the mechanical properties flax/vinyl ester natural fiber composite for eco-friendly structure using Vacuum Assisted Resin Transfer Molding (VARTM) manufacturing method. Through the structural testing, it is confirmed that the designed structure tank is acceptable for structural safety and stability using VRTM.

The application of VRTM process in composite manufacturing is presented by Brouwer et al [4] for large industrial application. With the support of two examples, they presented the successful development of large structure, i.e. 20m Rotor Blade and 16m long Hull for a Sailing Yacht.

Dong [5] developed a process model for the vacuum assisted resin transfer molding simulation by the response surface method. The factors like permeability, porosity and thickness of the fiber preform were studied on RTM mold filling time as response output. The significant process variables were identified and a quadratic regression equation developed to find the mold filling time.

2 EXPERIMENTAL WORKS

The materials employed in the fabrication of wind turbine blades are: Fiber glass WR 400, unsaturated Polyester resin, polystyrene block, gel coat, vacuum pump, and plastic sheets for vacuum bagging.

NREL S823 (un-symmetric airfoil) was chosen as an airfoil shape because for 1kw turbine it is recommended to use this shape which generates lift at low wind speed. The shape of blade to be generated is known in the form of chord and twist distribution, for convenience took ten values or section points along the 1.2m blade length. These 10 cross sectional airfoil templates is generated on software and paste on soft ply wood as shown in Figure 1

These 10 templates of airfoil are placed on both the edges of Styrofoam (Polystyrene) block. Hot wire cutter is used to turn Polystyrene blocks into 10 components of female molds. The hot wire cutter moved slightly along the interface of a soft wood ply template, as long as the wire moves, polystyrene block gets the shape of desired profile molds. Furthermore the 10 Pieces of Polystyrene blocks were glued together to form a mold as shown in Figure 2. and plastic sheet was laid on the halves of mold to protect it from resin.

The surface of the blade is made from three layers of S-glass fiber with a layer orientation of 0/+45/0 sequence. These layers of fibers were wetted by small amount of Polyester resin with the help of rollers and then placed on wax coated female mold. A piece gauze wire is also placed on the mold to control the flowing pattern of the resin. This system of mold was inserted into the plastic sheet and sealed for vacuum bagging purpose as shown in Figure 3. The vacuum bag was contained ports for resin injection and for suction.

The representation of the whole portable system is shown in Figure 4 and 5, in which a single inlet for resin but seven injection points for uniform distribution of resin were also presented inside the vacuum. The vacuum suction points were also presented at different locations which are connected to the vacuum pump. This Vacuum pump creates a suction of negative pressure. A Catch pot is connected between the suction line and the vacuum pump in order to prevent the pump from extra resin to enter in it. Now the process is carried out with this arranged portable setup when the matt is completely impregnated, removes the blade and allowed it to cure at the room temperature.

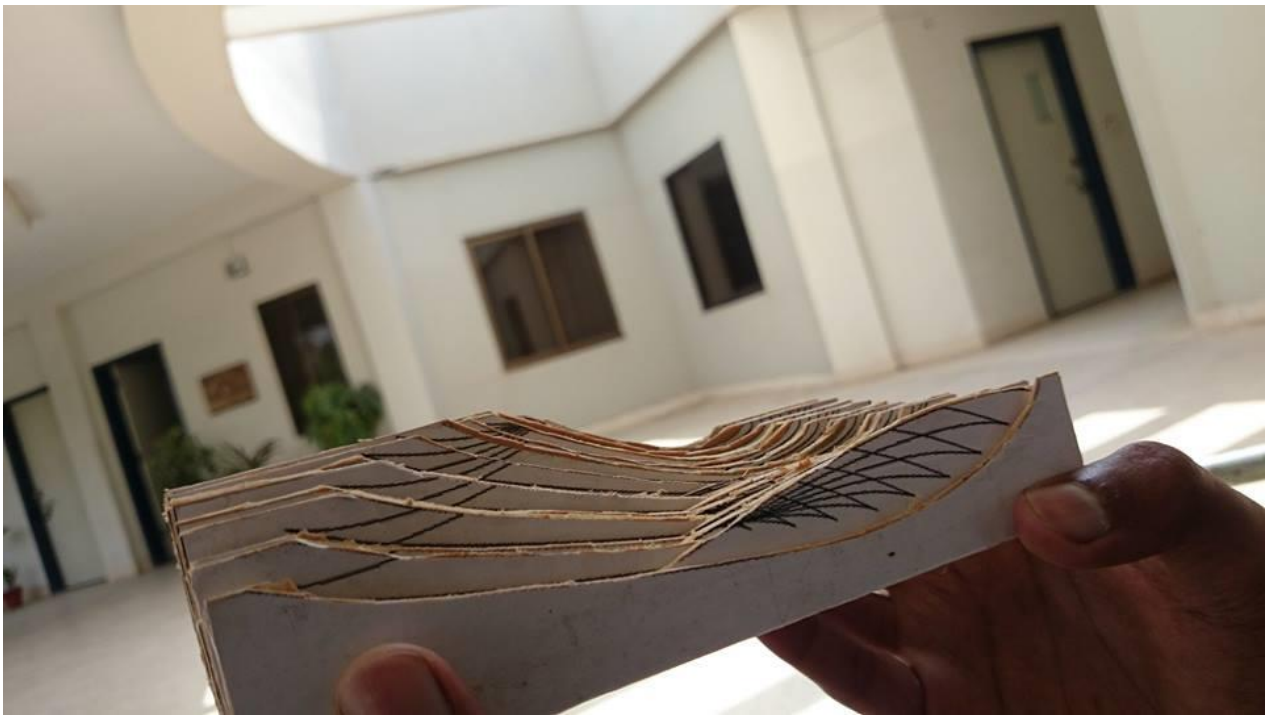

Figure 1. 10 Cross Sectional Airfoil Templates

Figure 2. Polystyrene blocks were glued together to form a mold

.

Figure 3

Figure 4. Portable VRTM setup with Vacuum Pump

Figure 6. Portable System with Resin Inlet and Suction Points

Figure 5. Fabricated Wind Turbine Blade

3 RESULTS

The completely fabricated and joined Horizontal axis wind turbine blade is shown in figure 6 and figure 7. The vacuum pressure is applied on a weave pattern of fiber glass, which completely impregnated the matt in 10s minutes. Trial-error method and adjustment of making blade reveals various perceptions for pre and post processing phases. Blade trimming from sharp edges of fibers and extra resin deposited on outside surfaces is an important finishing process. The dust from cutting fiber glass during grinding is toxic. A dust mask must be worn during this operation - ensure others around the blade do not inhale the dust. To improve the surface finish of the blade a layers of primer coating is applied on the entire surface.

applications. A number of blades have been fabricated to illustrate the feasibility and the application of this manufacturing method. In future this process can be repeated with different high viscosity resin by increasing the suction pressure and study their effect on the strength of composite structure. The distribution of resin through different flow pattern are also in planned to reduce the process time.

4 CONCLUSION

A portable Vacuum-Assisted Resin Transfer Molding (VARTM) process has been successfully developed through which structural composite components can be manufactured. It is a clean and closed mold technique that allows for manufacturing of complex composite structures. VARTM has proven to be a cost-effective method for wind turbine blades and also for other newly

ACKNOWLEDGEMENTS

The authors acknowledged the cooperation of Carpentry Shop of Mechanical Engineering Dept. NEDUET in carrying out the Process testing and the real experiments.

Figure 7. Fabricated Wind Turbine

REFERENCES

[1] M. S. Koefoed, *Modeling and Simulation of the VARTM Process for Wind Turbine Blades*, (Thesis) Institute of Mechanical Engineering Aalborg University, Denmark, 2003.

[2] L. A. Wisojodharmo, & S. Roseno, The Use of Vacuum Assisted Resin Infusion Process on the Manufacturing of Wind Blade Composites, *Journal of Materials Science and Engineering*, *2*(1), 74-78, 2012.

[3] C. Kong, H. Park & J. Lee, Study on structural design and analysis of flax natural fiber composite tank manufactured by vacuum assisted resin transfer molding, *Materials Letters*, *130*, 21-25, 2014.

[4] W. D. Brouwer & M. Labordus, Vacuum Injection Moulding for Large Structural Applications, *Composites*, 34, 551–558, 2003.

[5] C. J. Dong, Development of a process model for the vacuum assisted resin transfer molding simulation by the response surface method, *Composites Part A: Applied Science and Manufacturing*, 37(9), 1316-1324, 2006.

[6] J. Merotte, P. Simacek, & S. G. Advani, Resin flow analysis with fiber preform deformation in through thickness direction during Compression Resin Transfer Molding, *Composites Part A: Applied Science and Manufacturing*, *41*(7), 881-887, 2010.[7] S. Laurenzi, A. Casini, & D. Pocci, Design and fabrication of a helicopter unitized structure using resin transfer moulding. *Composites Part A: Applied Science and Manufacturing*, *67*, 221-232, 2014.

[8] G. W. Lee, N. J. Lee, J. Jang, K. J. Lee, & J. D. Nam, Effect of surface modification on the resin transfer moulding (RTM) of glass fibre/unsaturated polyester composites, *Composite science and technology*, 62(1), 9-16, 2002.

[9] D. Bender, J. Schuster, & D. Heider, Flow rate control during vacuum-assisted resin transfer molding (VARTM) processing, *Composites Science and Technology*, 66(13), 2265-2271, 2006.

[10] Jon Dana Skramstad, Evaluation of hand lay-up and resin transfer molding in Composite wind turbineblade manufacturing, (Thesis) Montana State University-Bozeman, Bozeman, Montana, 1999.

MHD VISCOUS FLUID FLOWS WHEN VORTICITY DISTRIBUTION PERTURBED BY UNIFORM AND EXPONENTIAL STREAMS

MUHAMMAD JAMIL[1] AFAQUE AHMED[2]
Department of mathematics, NED University of Engineering & Technology Karachi-75270, Pakistan

*Corresponding author. Tel: +92 3337168622 Fax: (92-21) 99261255
Email address: afaq_bhutto@yahoo.com

ABSTRACT

Some exact solutions of equations of motion of a finitely conducting incompressible fluid of variable viscosity with heat transform in the presence of transvers magnetic field are determined. These solutions consist of flows for which the vorticity distribution is proportional to the stream function perturbed by uniform and exponential streams. Defining a transformation variable, we are able to linearize the governing equation in to simple ordinary differential equations and some exact solutions are obtained.

Key words: Viscous fluid, incompressible, variable viscosity, magnetohydrodynamics(MHD), vorticity distribution, exact solutions.

1 INTRODUCTION

Nonlinear Navier-Stokes equations to describe fluid motion are fundamental equations in fluid mechanics, which were first introduced by Navier in 1821 and developed by Stokes in 1845. However, up to now, the problem of uniqueness of solutions for Navier-Stokes equations has not yet been solved, and general analytical methods for the solutions are absent. At present, numerical solutions to fluid mechanics problems are very attractive due to wide availability of computer programs. But these numerical solutions are insignificant if they cannot be compared with either analytical solutions or experimental result. Exact solutions are important not only because
They are solution of some fundamental flows, but also because they serve as accuracy standards for approximate methods, whether numerical, asymptotic or experimental. Wang [1] has given an excellent review of these solutions of the Navier-Stokes Equation. These known solutions of viscous incompressible Newtonian fluid may be classified generally into three types.
(a): Flows for which the non-linear inertial terms in the linear momentum equations vanish identically. Parallel flows and flow with uniform suction are examples of these flows.(b): Similarity properties of the flows such that the flow equations reduce to a set of ordinary differential equations. Stagnation point flow is an example of such flow.(c): Flow for which the vorticity function or stream function is chosen so that the governing equations in terms of the stream function reduce to a linear equation.
Taylor [2] considering the vorticity distribution directly proportional to the stream function $\nabla^2\psi = \mathrm{K}\psi$, showed that the non-linearities are self-canceling and obtained an exact solution which represent the decay of the double array of vortices. Kampe-De-Feriet [3] generalized the Taylor's idea by taking the vorticity of the form $\nabla^2\psi = \mathrm{f}(\psi)$.
Kovasznay [4] extended Taylor's idea by taking the vorticity to be proportional to the stream function perturbed by a uniform stream of the for $\nabla^2\psi = \mathrm{y} + (\mathrm{K}^2 - 4\pi^2)\psi$. Kovaszany was able to linearize the Navier-Stokes equation and determine an exact solution for steady flow, which resembles that the downstream of a two-dimensional gird. Wang [5] was able to linearize the Navier-Stokes equations and showed that the result established. Taylor and Kovasznay could be obtained from his finding as special cases by taking the vorticity $\nabla^2\psi = \mathrm{Cy} + \mathrm{A}\psi$. Lin and Tobak [6], Hui [7] and Naeem and Jamil [8] obtained more results by studying similar flows, taking $\nabla^2\psi = \mathrm{K}(\psi - \mathrm{Rz})$, $\nabla^2\psi = \mathrm{K}(\psi - \mathrm{Ry})$ and $\nabla^2\psi = \mathrm{K}(\psi - \mathrm{Ry})$.By assuming certain form of vorticity distribution or stream function, solution for Newtonian and non-Newtonian fluids are obtained in [9 - 27]. In this paper we present some exact solutions to the equation governing the steady plane flows of an incompressible fluid with variable viscosity and heat transfer for which the vorticity distribution is proportional to the stream function perturbed by a uniform and exponential stream of the form $\nabla^2\psi = K\left[\psi - U_1(ax + by) - U_1 e^{(ax+by)}\right]$. We point out that the exact solutions obtained by taking this form of vorticity to the best of our knowledge is yet not consider either in Newtonian or non-Newtonian flows.

2 BASIC GOVERNING EQUATIONS

The basic governing equation is same, therefore we employ the equation from [18]

$$J_x = -\psi_x\omega + \frac{1}{Re}\left[\mu\left(\psi_{yy} - \psi_{xx}\right)\right]_y \quad (1)$$

$$J_y = -\psi_y\omega + \frac{1}{Re}\left[\mu\left(\psi_{yy} - \psi_{xx}\right)\right]_x - \frac{4}{Re}\left[\mu\psi_{xy}\right]_y \quad (2)$$

$$\psi_y H_x - \psi_x H_y = \frac{1}{R_\sigma}\left[H_{xx} + H_{yy}\right] \quad (3)$$

$$\psi_y T_x - \psi_x T_y = \frac{1}{RePr}\left[T_{xx} + T_{yy}\right] + \frac{Ec}{Re}\mu\left[4\left(\psi_{xy}\right)^2 + \left(\psi_{yy} - \psi_{xx}\right)^2\right] + \frac{R_H Ec}{R_\sigma}\left[H_x^2 + H_y^2\right] \quad (4)$$

where the vorticity function ω and the generalized energy function J are defined by

$$\omega = -\left(\psi_{xx} + \psi_{yy}\right) \quad (5)$$

$$J = p + R_H\frac{H^2}{2} + \frac{1}{2}\left[\psi_x^2 + \psi_y^2\right] - \frac{2\mu\psi_{xy}}{Re} \quad (6)$$

Once a solution of system of equations (1–4) is determined, the pressure p is obtained from equation (6) since we are interested in the solution of the system of equations (1–4) when the vorticity distribution is proportional to the stream function, perturbed by a uniform and exponential stream. Therefore we set

$$\psi_{xx} + \psi_{yy} = K[\psi - U_1(ax + by) - U_2 e^{(ax+by)}] \quad (7)$$

where K, a, $b \neq 0$, $a \neq b$ and U are real constants. Using perturbed stream function

$$\Psi = \psi - U_1(ax + by) - U_2 e^{(ax+by)} \quad (8)$$

and employing equation (7), the equation (5) becomes

$$\omega = -K\Psi \quad (9)$$

Equation (1) and (2), utilizing equation (8) and (9) becomes

$$J_x = \left[\frac{K\Psi^2}{2}\right]_x + aK\Psi\left[U_1(ax + by) + U_2 e^{(ax+by)}\right] + M_y \quad (10)$$

$$J_y = \left[\frac{K\Psi^2}{2}\right]_y + bK\Psi\left[U_1(ax + by) + U_2 e^{(ax+by)}\right] - \frac{4}{Re}\left[\mu\left\{\Psi_{xy} + ab\left(U_1(ax + by) + U_2 e^{(ax+by)}\right)\right\}\right]_y + M_x$$

where

$$M = \frac{1}{Re}\left[\mu\left\{\Psi_{yy} - \Psi_{xx} + (b^2 - a^2)\right\}\left(U_1(ax + by)\right) + U_2 e^{(ax+by)}\right)\right] \quad (11)$$

equation (10) and (11), on using the integrability condition $J_{xy} = J_{yx}$ provide

$$M_{xx} - M_{yy} + k\left(b\Psi_x - a\Psi_y\right)\left[U_1(ax + by) + U_2 e^{(ax+by)}\right] - \frac{4}{Re}\left[\mu\left\{\Psi_{xy} + ab(U_1(ax + by) + U_2 e^{(ax+by)})\right\}\right]_{yx} = 0 \quad (12)$$

Equation (12) is the equation that must be satisfied by the function Ψ and the viscosity μ for the motion of a finitely conducting incompressible fluid of variable viscosity with heat transfer to the presence of transverse magnetic field in which the vorticity distribution is proportional to the stream function perturbed by a uniform and exponential stream. Equation (3) and (4), employing equation (5), becomes

$$\left[\Psi_y + b(U_1(ax + by) + U_2 e^{(ax+by)})\right]H_x - \left[\Psi_x + a(U_1 (ax + by) + U_2 e^{(ax+by)})\right] H_y = \frac{1}{R\sigma}\left[H_{xx} + H_{yy}\right] \quad (13)$$

$$\left[\Psi_y + b\left\{U_1(ax + by) + U_2 e^{(ax+by)}\right\}\right]T_x - \left[\Psi_x + a\left\{U_1(ax + by) + U_2 e^{(ax+by)}\right\}\right]T_y = \frac{1}{RePr}\left[T_{xx} + T_{yy}\right] + \frac{Ec\mu}{Re}\left[4\left\{\Psi_{xy} + a\,b(U_1(ax + by) + U_2 e^{(ax+by)})\right\}^2 \left\{\Psi_{yy} - \Psi_{xx} + \left(b^2 - a^2\right)(U_1(ax + by)) + U_2 e^{(ax+by)})\right\}^2\right] + \frac{EcR_H}{R\sigma}\left[H_x^2 + H_y^2\right] \quad (14)$$

equation (7) employing, equation (8) becomes

$$\Psi_{xx} + \Psi_{yy} - K\Psi = -(a^2 + b^2)[U_1(ax + by) + U_2 e^{(ax+by)}] \quad (15)$$

Introducing the transformation variable as

$$\xi = ax + by \quad (16)$$

transforming the equations (12 –15), into new independent variable ξ, we get

$$\Psi_{\xi\xi} - \Lambda\Psi = -U_1\xi - U_2 e^{\xi} \quad (17)$$

where

$$\Lambda = \frac{k}{(a^2 + b^2)},$$

and

$$(\mu\Psi)_{\xi\xi} = 0 \quad (18)$$

$$H_{\xi\xi} = 0 \quad (19)$$

$$T_{\xi\xi} + PrEc\mu\Psi^2\Lambda^2(a^2 + b^2) + \frac{EcR_H RePr}{R_\sigma}H_\xi^2 = 0 \quad (20)$$

3 EXACT SOLUTIONS

In this section we present some exact solutions of the system of equations (17–20), as follows we consider the following three cases

Case I: $\Lambda = -n^2$, n > 0,

Case II: $\Lambda = m^2$, m> 0,

Case III: $\Lambda = 0$.

Case – I:

For this case the solution of equation (17) in the physical plane is given by

$$\Psi = A_{11}sin(n(ax + by) + A_{12}) - \frac{U_1(ax + by)}{n^2} - \frac{U_2 e^{(ax + by)}}{n^2+1} \quad (21)$$

equation (18) utilizing (21) gives

$$\mu = \frac{A_{13}(ax+by)+A_{14}}{A_{11}sin(n(ax+by)+A_{12})-\frac{U_1\,(ax+by)}{n^2}-\frac{U_2\,e^{(ax+by)}}{n^2+1}}. \quad (22)$$

The solution of equation (19) is

$$H = A_{15}(ax + by) + A_{16} \quad (23)$$

equation (20), using equations (22) and (23), becomes

$$T_{\xi\xi} + EcPr\Lambda^2(a^2+b^2)(A_{13}\xi + A_{14})\Psi + \frac{R_H EcPrReH_\xi^2}{R_\sigma} = 0 \quad (24)$$

The solution of (24) is

$$T = \frac{Ec\,Pr\Lambda^2(a^2+b^2)}{12n^3(n^2+1)}\,[A_{13}\{12A_{31}(n^2+1)\{n\,(ax+by)\,sin(n(ax+by)+A_{12}) - 2cos(n(ax+by)+A_{12})\} + n\{(n^2+1)U_1(ax+by)^4 - 12n^2U_2e^{(ax+by)}\}\}(ax+by-2)\}\} + 2nA_{14}\{A_{11}(n^2+1)\big(6sin(n(ax+by)\big) + (ax+by)^3) - 6n^2U_2e^{(ax+by)}\}] - \frac{Ec\,R_H\,Pr\,Re\,A_{15}^2}{2R_\sigma}(ax+by)^2 + A_{17}(ax+by) + A_{18}. \quad (25)$$

The stream function Ψ for this case is given by

$$\psi = A_{11}sin(n(ax+by)+A_{12}) - \frac{n^2+1}{n^2}\,U_1(ax+by) - \frac{2+n^2}{n^2+1}U_2\mathrm{e}^{\mathrm{ax+by}} \quad (26)$$

It represent a sine stream $sin(n(ax+by)+A_{12})$ in the positive x-direction plus a perturbation that is not periodic in x and y. The component of velocity distribution equations (5) and (10) and pressure from equation (10), are given by

$$u = A_{11}n\,b\,cos(n(ax+by)+A_{12}) - \frac{n^2+1}{n^2}\,b\,U_1 - \frac{2+n^2}{n^2+1}\,b\,U_2e^{(ax+by)} \quad (27)$$

$$v = -A_{11}\,a\,n\,cos\{n(ax+by)+A_{12}\} + \frac{a(n^2-1)}{n^2}U_1 + \frac{a\,(2+n^2)}{n^2+1}U_2e^{(ax+by)}, \quad (28)$$

$$p = \frac{K}{2n^4(n^2+1)^2}\,[A_{11}\{n(1+n^2)^2\{n^3A_{11}sin(n(ax+by)+A_{12}) - 2U_1\{n(ax+by)sin(n(ax+by)+A_{12}) + cos(n(ax+by)+A_{12})\}\} - 2n\{n^4U_2\{nsin(n(ax+by)+A_{12}) + cos(n(ax+by)+A_{12})\} - U_1(1+n^2)^3 cos(n(ax+by)+A_{12}) - n^3(2+n^2)U_2e^{(ax+by)}\{U_1(1+n^2)(ax+by)^2 + 2n^2U_2e^{(ax+by)}\} + n^2(1+n^2)(2+n^2)U_2e^{(ax+by)}\{2U_1\big((ax+by)-1\big) + n^2e^{(ax+by)}\}]$$

$$-\frac{(a^2+b^2)}{2aR_e(1+n^2)}\,[2b\mu\{A_{11}n^2(1+n^2)sin(n(ax+by)+A_{12}) + (2+n^2)U_2e^{(ax+by)}\} - 2aR_en^4(1+n^2)^3\{A_{11}n^3(1+n^2)cos(n(ax+by)-A_{12}) - (n^2+1)^2U_1 - (2+n^2)n^2U_2e^{(ax+by)}\}^2 - R_H\frac{H^2}{2} + A_{19}. \quad (29)$$

where $A_{11}A_{12}A_{13}$ ... A_{19} is a real constant.

Case - II

For this case

$$\Psi = B_{11}e^{m(ax+by)} + B_{12}e^{-m(ax+by)} + \frac{U_1(ax+by)}{m^2} - \frac{U_2\,e^{(ax+by)}}{1-m^2}, \quad (30)$$

$$\mu = \frac{B_{13}(ax+by)+B_{14}}{B_{11}e^{m(ax+by)}+B_{12}e^{-m(ax+by)}+\frac{U_1(ax+by)}{m^2}-\frac{U_2\,e^{(ax+by)}}{1-m^2}} \quad (31)$$

$$H = B_{15}(ax + by) + B_{16}, \quad (32)$$

$$T = \frac{EcPr\Lambda^2(a^2+b^2)}{12m^3(1-m^2)}\,[B_{13}\{12(1-m^2)\{B_{11}e^{m(ax+by)}(2-m(ax+by)) - B_{12}e^{-m(ax+by)}(m\,(ax+by)+2) - m(1-m^2)U_1(ax+by)^4 - 12mU_2\big(e^{m(ax+by)}(m(ax+by)-1) - m^2e^{m(ax+by)}\big)\} - 2B_{14}m(1-m^2)\{6B_{11}e^{m(ax+by)} + 6B_{12}e^{-m(ax+by)} + U_1(ax+by)^3 - 6n^2U_2e^{m(ax+by)}\}] - \frac{R_HEcPrReB_{15}^2}{2R_\sigma}(ax+by)^2 + B_{37}(ax+by) + B_{18}, \quad (33)$$

for this case stream function,

$$\psi = B_{11}e^{m(ax+by)} + B_{12}e^{-m(ax+by)} + \frac{1-m^2}{m^2}U_1(ax+by) - \frac{2-m^2}{1-m^2}U_2e^{(ax+by)}. \quad (34)$$

It represent a hyperbolic (sine or cosine) stream $B_{11}e^{m(ax+by)} + B_{12}e^{-m(ax+by)}$ in the positive *x*-direction plus a perturbation that is not periodic in *x* and *y*. The component of velocity distribution and pressure, in this case are given by32570048

$$u = mbB_{11}e^{m(ax+by)} - mbB_{12}e^{-m(ax+by)} + \frac{U_1b(1-m^2)}{m^2} - \frac{2-m^2}{1-m^2}U_2be^{(ax+by)} \quad (35),$$

$$v = -maB_{11}e^{m(ax+by)} + maB_{12}e^{-m(ax+by)} - \frac{aU_1(1-m^2)}{m^2} + \frac{2-m^2}{1-m^2}U_2ae^{(ax+by)}, \quad (36)$$

$$p = \frac{K}{2m^4(1-m)^2}[nB_{11}\{(1 - m^2)^2 e^{m(ax+by)}\{m^3 B_{11} e^{m(ax+by)} + 2U_1(m(ax+by)-1)\} + 2m^5 B_{11} U_2^2 e^{(m+1)(ax+by)}\} + m(1 - m^2)B_{12}\{(1 - m^2)e^{-m(ax+by)}\{m^3 B_{12} e^{-m(ax+by)} + 2U_1(m(ax + by) - 1)\} - 2m^3 U_1 e^{(ax+by)(1-m)}\} + (1 - m^2)\{U_1(1-m^2)(m^2+1)\{2(B_{11}e^{m(ax+by)} - B_{12}e^{-m(ax+by)}) + (ax+by)^2\} + 2m^2 U_1 U_2 e^{(ax+by)}(m^2(ax+by) + 1) + m^5 U_2 e^{2(ax+by)}] + \frac{b}{a\,Re}[\mu(b^2-a^2)\{m^2 B_{11} e^{m(ax+by)} + m^2 B_{12} e^{-m(ax+by)} - \frac{U_2}{1-m^2} e^{(ax+by)}\}] - R_H \frac{H^2}{2} - \left[\left\{\frac{(a^2+b^2)}{2} + 2\frac{\mu ab}{Re}\right\}\{mB_{11}e^{m(ax+by)} - mB_{12}e^{-m(ax+by)} - \frac{U_1}{m^2} - \frac{U_2}{1-m^2}e^{(ax+by)}\}^2\right] + B_{19}, \quad (37)$$

where $B_{11}B_{12}B_{13} \ldots B_{19}$ is a real constant.

Case-III

For this case we have

$$\Psi = -\frac{U_1(ax+by)^3}{6} - U_2 e^{(ax+by)} + C_{11}(ax+by) + C_{32} \quad (38)$$

$$\mu = \frac{C_{13}(ax+by)+C_{14}}{\frac{-U_1(ax+by)^3}{6} - U_2 e^{(ax+by)} + C_{11}(ax+by) + C_{12}}, \quad (39)$$

$$H = C_{15}(ax+by) + C_{16}, \quad (40)$$

$$T = \frac{EcPr\Lambda^2(a^2+b^2)}{180}[C_{13}\{180U_2 e^{(ax+by)}(2 - (ax+by)) + (ax+by)^3(U_1(ax+by)^3) - 15(C_{11}(ax+by) + 2C_{12})\} + C_{14}\{(ax + by)^2\left(\frac{3}{2}U_1(ax+by)^3 - 30(C_{11}(ax + by) + 3C_{12}) - 180U_2 e^{(ax+by)}\right)\}] - \frac{R_H EcPrRe\, H_{15}^2}{2R\sigma}(ax+by)^2 + (ax+by)C_{37} + C_{38}, \quad (41)$$

$$\psi = -\frac{U_1(ax+by)}{6}\{(ax+by)^2 + 6\} - 2U_2 e^{(ax+by)} + C_{11}(ax+by) + C_{12} \quad (42)$$

$$u = -\frac{U_1 b}{2}\{(ax+by)^2 + 2\} - 2bU_2 e^{(ax+by)} + bC_{11} \quad (43)$$

$$v = \frac{aU_1}{2}\{(ax+by)^2 + 2\} + 2aU_2 e^{(ax+by)} - aC_{11} \quad (44)$$

$$p = K\left[U_1^2(ax+by)^2 - \frac{U_1U_2}{2}\{(ax + by)^2 e^{(ax+by)} - 2e^{(ax+by)}((ax+by)+1)\} - \frac{C_{11}U_1}{8}(ax+by)^4 - \frac{C_{12}U_1(ax+by)^3}{6} - \frac{(U_1+C_{11}+C_{12})U_1}{24}(ax+by)^4 + U_2(U_1 + C_{31} + C_{32})e^{(ax+by)} + \frac{C_1(U_1+C_{11}+C_{12})(ax+by)^2}{2} + C_2(U_1 + C_{11} + C_{12})(ax+by) + \left[\frac{b\mu(b^2-a^2)}{aRe} - \frac{2\,\mu\,a\,b}{Re}\right]\left[\frac{U_1}{2}(ax+by)^2 + U_1 + C_{11}\right]^2 - R_H\frac{H^2}{2} + \frac{U_1}{2}(a^2-b^2)(ax+by) + C_{19}, \quad (45)$$

where $C_{11}, C_{12}, C_{13} \ldots C_{39}$ are real constant. $\Lambda = 0$ corresponds to an irrotational flow and it is the following uniform flow.

4 NUMERICAL RESULTS AND DISCUSSION

In order to have a discussion about some suitable physical aspects of the obtained results, many graphs are sketched in the present section. Attention has been focused on analyzing the difference between the profiles of the velocity field components $u(x,y)$ and $v(x,y)$ of steady plane flows of an incompressible fluid with variable viscosity and heat transfer moving on a plane. We infer these results with respect to the variations of emerging parameters of interest. The velocity components $u(x,y)$ and $v(x,y)$ that have been considered here is only for Case-I ($\Lambda = 1$) and Case-II ($\Lambda = 1$). The diagrams of the velocity components $u(x,y)$ and $v(x,y)$ have been presented against x and y for different values of emerging parameters of interest a, b, n, m and U_1 and U_2. For the sake of convenience, all graphs are sketched by using, $A_{11} = 0.1$, $A_{12} = 2, B_{11} = 0.002, B_{12} = 0.003, a = 2, b = 3, n = 2, m = 2$, $U_1 = 0.1$, $U_2 = 0.1$ and using Mathcad as a computational software. The figure 1 to figure 10 is for case-I and figure 11 to figure 20 are for case-II. All figure 1 (a) to figure 20 (a), for the velocity components $u(x,y)$ and $v(x,y)$ are considered as function of "x" only and "y" treat as constant and it is "$y = 2$". All figure 1 (b) to figure 20 (b), when the velocity components are considered as function of "y" only and "x" treat as constant and it is "$x = 1$".

For Case-I: figure 1, 2, 3 and 4, show the graphs of the velocity components at four different values

of the parameter "*a*" and "*b*". It is notice that, the velocity components have opposite behavior for varied values of "*a"* and "*b"*. For instance, the first velocity component is decreasing and second component of velocity is increasing functions respectively of the parameter "*a*" and "*b"*. It is also observed in all graphs that the first velocity component have greater values (in absolute value) in comparison with second component of velocity. figure 5 and 6 give graphical demonstration for the influence of parameter "*n*" on the two components of velocity. It is observe that the component of velocity $u(x,y)$ is increasing function of "*n*". However the component $v(x,y)$ decreases with respect to the parameter "*n*". figures. 7, 8, 9 and 10 show the variation of U_1 and U_2 on the two component of velocity field. Qualitatively the effects of these parameters on the profile of the velocity components are similar. For instant the velocity component $u(x,y)$ decays with regard to the parameters U_1 and U_2 and the seconed component velocity field $v(x,y)$ have quite opposite behavior with respect these parameters with comparison to $u(x,y)$.

For Case-II: Figures 11, 12, 13 and 14 are made to discuss the variation of the parameter "*a*" and "*b*" on the two component velocity profile it is notice that the effect of these parameter on the two component velocity profiles are quite reverse. For example the first component of velocity $u(x,y)$ increased and second component of velocity $v(x,y)$ decreased with respect to these parameters. To see the effect of the parameter "*m*" on the velocity profile Figures 15 and 16 are constructed. From these figures it is clear that the first component of velocity field $u(x,y)$ decays and second component of velocity field $v(x,y)$ grows exponentialy with increasing values of "*m*". In order to the discuss the impact of the parameter U_1 on the two component of the velocity field, Figures 17, 18 are prepared. It is observe that both component of velocity field are decreasing with regard to U_1. Finally for comparison the two components of velocity field for different values of U_2 are combined presented in figure 19 and 20. From these figures it is obvious the component $u(x,y)$ goes down and the component $v(x,y)$ goes up respectively as the values U_2 increased. The units of the material constants in all figures are SI units.

5 CONCLUDING REMARKS

The aim of this paper is to the study the steady motion of a finitely conducting incompressible fluid of variable viscosity in the presences of a magnetic field and heat transfer over an infinite plane. The general solutions are determined involved of flows for which the vorticity distribution is proportional to the stream function perturbed by a uniform and exponential streams of the form $\square^2\psi = K[\psi - U_1(ax + by) - U_2 e^{(ax+by)}]$. Lastly the effects of numerous parameters of concentration on the velocity components are outlined and discussed.

REFERENCES

[1] C. Y. Wang, On a class of exact solutions of the Navier-Stokes equations, J. of Appl. Mech., 33 (1966) 696-698.

[2] G. I. Taylor, On the decay of vortices in a viscous fluid, Phil.Mag.46 (1923) 671-674.

[3] K. D. J. Feriet, Sur quelques cas d'integration des equations du movement pland'un fluid visqueux incopmpressible, Proc. Int. Congr. Appl. Mech., 3 rd. Stockholm 1 (1930) 334-338.

[4] L. I. G Kovaszany, Laminar flow behind a two dimensional grid, Proc Cambridge Phill, Soc. 44 (1948) 58-62.

[5] C. Y. Wang, Exact solutions of the Navier-Stokes equations the generalized Beltrami flows, review and extension, Acta Mech., 81 (1990) 69-74.

[6] S. P. Lin, M. Tobak, Reversed flow above a plate with suction, AIAAJ, 24 (1986) 334-335.

[7] W. H. Hui, Exact solutions of the unsteady two-dimensional Navier-Stokes equations, Journal of Applied Mathematics and Physics, 38 (1987) 689-702.

[8] R. K. Naeem, M.Jamil, On plane steady flows of an incompressible fluid with variable viscosity, Int. J. of Appl. Math. and Mech, 2 (2006) 1-19.

[9] A. M. Benharbit , A. M. Siddiqui, Certain solutions of the equations of the planar motion of a second grade fluid for steady and unsteady cases, Acta Mech., 94(1991) 85-96.

[10] F. Labropulu, Exact solutions of non-Newtonian fluid flows with prescribed vorticity, Acta Mech., 141 (2000) 11-20.

[11] F. Labropulu, Generalized Beltrami flows and other closed-form solutions of an unsteady viscolastic
fluid, Interanat. J. Math. and Math. Sci, 30 (2001) 271-282.

[12] M. R. Mohyuddin, T. Hayat, F. M. Mohamed, S. Asgher, A. M. Siddiqui, On Solutions
for non-linear differential equations arising in Newtonian and non-Newtonian fluids, Non-Linear Dynamics, 35 (2004) 237-262.

[13] P. F. Nemenyi, Recent development in inverse and semi-inverse method in the mechanics of continua, Adv. Appl. Mech., 11 (1951) 123-151.

[14] E. O. Oku-Ukpong, O. P. Chandna, Some reversed and non-reversed flows of a second grade fluid, Mech. Res. Comm., 20 (1993) 73-82.

[15] K. R. Rajagopal, On the decay of vortices in a second grade fluid. Mechanica, 9 (1980) 185-188.

[16] K. R. Rajagopal, A. S. Gupta, On class of exact solutions to the equations of motion of a second grade fluid, Int. J. Eng. Sci., 19 (1981) 1009-1014.

[17] D. Riabouchinsky, Some considerations regarding plane irrotational motion of a liquid.

[18] M. Jamil, N. A. Khan, Some exact solutions of equations of motion of a finitely conducting incompressible fluid of variable viscosity in the presence of transverse magnetic field by transformation method, ARPN J of Engg & App Math, 1 (2006) 5-25.

EFFECT OF HEAT TREATMENT ON THE CORROSION RATE OF AISI 1045 STEEL, WHEN SUBJECTED TO VARIOUS ENVIRONMENTS

M.Rizwan[1], M.Ali[2], M.Samiuddin[3]

[1,2,3] Metallurgical Engineering Department, NED University of Engineering & Technology, Karachi, Pakistan

[*]Corresponding author. Tel: +923333657963
Email address: materialist.riz@gmail.com

ABSTRACT

Carbon steels are by far the most economical and one of the most used materials throughout the world. In this work the usability of AISI 1045 steel has been studied in various practical environments. The corrosion behavior of AISI 1045 steel has been observed having been heat treated and subjected to various environments. Several samples in Annealed, Normalized and quenched state were subjected to LPR (Linear Polarization Resistance) testing to determine Corrosion rate of each sample in different environments by Potentiostat using Dr.Bob's Cell. LPR test results revealed the corrosion behavior of each sample in particular environments. Results of this experiment can be very helpful to decide that, in which environments AISI 1045 steel can be used and which heat treated conditions suits that particular environment.

Keywords: AISI 1045, LPR, Potentiostat.

1 INTRODUCTION

The corrosion of metals is the primary concern to the engineers in desalination, petrochemical and power plants. Like other natural disasters such as floods or severe earthquakes, corrosion can be very disastrous for everything from vehicles, home appliances, and water and wastewater systems to pipelines, bridges, and public buildings.

The dependence of Microstructure on Corrosion behavior of Carbon steels is widely recognized. Many contradictory results are present in literature due to the fact that the involved mechanisms are quite complex [1].

AISI 1045 is a medium carbon steel which is quite common material for general Engineering applications requiring strength and wear resistance, Such as; Gears, Ratchets, Bolts and Axles

Corrosion behavior of metals depends largely on the phases present in the alloy. Heat treatment may be utilized to produce several phases and their combinations in a steel sample. In this work the corrosion behavior of AISI 1045 steel has been studied for annealed, normalized and hardened samples.

The corrosion behavior of any metal depends on the environment conditions to which it is exposed [2]. One of the most corrosive environments for Carbon steels in practical applications are sea water, hydrochloric acid, sulphuric acid and nitric acids.

Electrochemical techniques are the most widely used method to determine corrosion behavior of materials in laboratory. Linear Polarization Resistance (LPR) is the most common technique for Corrosion rate determination [3].

2 EXPERIMENTAL WORK

Material Selection

24 cylindrical samples (L=60 mm & Dia=7 mm) of AISI 1045 steel were prepared by machining. The chemical composition of the samples is, as shown in Table 1:

Table 1. Chemical compositions of AISI 1045 type steel (WT %), Iron as balance

Elements	C	S	Mn	Al	Si	Cu	Cr
Compos-ition	0.470	0.02	0.65	2.8	1.5	0.15	0.2

2.1 Heat Treatment

6 samples were then allocated for each Heat treatment, i.e Annealing, Normalizing, Water quenching and Oil quenching. After austenitizing and subsequent holding, all the samples were cooled according to the desired microstructure. Each sample was then ground to remove surface oxide layers.

2.2 Corrosion testing

Linear Polarization resistance test was used to check Corrosion rate on calibrated Gamry Potentiostat (Refrence 600) with Dr. Bob's cell.

Samples were used as working electrode while Ag/AgCl Standard Calomel Electrode (SCE) was used as refrence electrode. Pt electrode acted as

counter electrode. Following chemicals were used as electrolyte:
Seawater
1M Boric acid
33% HCl
65% HNO_3
LPR curves were obtained by scanning the samples in appropriate ranges. Samples tested in sea water were scanned from -1.2 mv to 0mv, while those tested in Boric acid were scanned from -1.2mv to 2mv. Samples in HCl and H_2SO_4 were scanned between -1.2 mv to 0 mv while samples in HNO_3 were scanned between 0mv to 2mv. Corrosion rate in mpy (mills per year) is calculated directly by the Gamry software.

2.3 Microstructural analysis

All samples were than ground and polished to mirror finish. These samples were than quenched in Nital and then analysed on Metallurgical microscope to develop the relation between phases and corrosion behavior.

3 RESULTS AND DISCUSSION

3.1 Linear Polarization Resistance test results in Seawater

Annealed, normalized, water quenched and oil quenched samples were tested in sea water. LPR curve shows that water quenched sample shows minimum corrosion current and corrosion rate (i.e 20.5mpy) among all sample tested in sea water Fig-1.

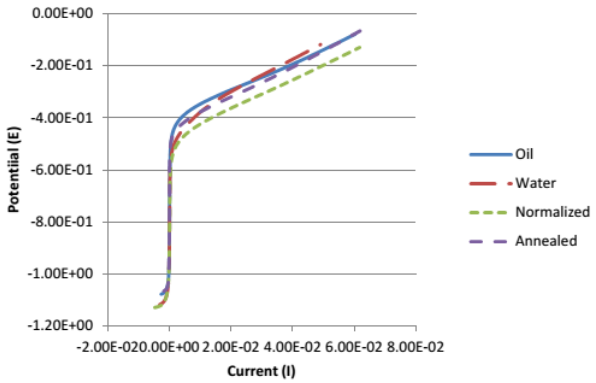

Figure 1. Comparison of all samples tested in sea-water.

The corrosion rate obtained for oil quenched sample is 25.74 mpy.
The corrosion rate obtained for water quenched sample is 20.51 mpy.
The corrosion rate obtained for normalized sample is 28.96 mpy.
The corrosion rate obtained for annealed sample is 27.67 mpy.
Water quenched sample shows the least corrosion in sea water because it has single phase on surface (i.e Martensite can also be observed in Figure 7). In other heat treated samples, multiple phases are present (i.e Pearlite: which is a combination of Ferrite and Cementite).

3.2 Linear Polarization Resistance test results in Boric acid

Boric acid which is a weak acid, corrodes steel in the similar manner as sea water does. Corrosion rate for Martensite (Water quenched) sample is least due to the presence of homogenous single phase.
Corrosion rate of Pearlitic microstructure is highest (In annealed and normalized samples) due to the formation of microcell between Ferrite and Cementite. Corrosion behavior of this steel in sea water and Boric acid is in accordance with the behavior reported by Sami I. al-rubaiye et al.[4],[5] Figures 1 & 2.

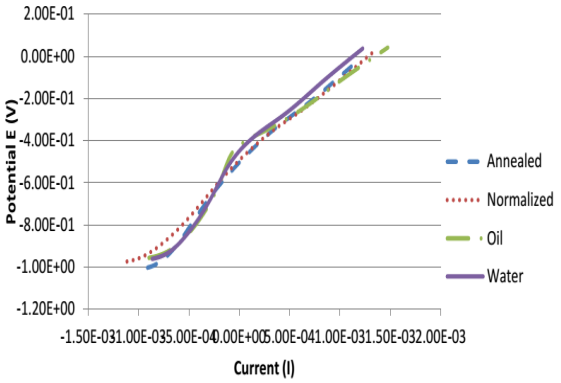

Figure 2. Comparison of all samples tested in Boric acid.

The corrosion rate obtained for annealed sample is 1.103 mpy.
The corrosion rate obtained for normalized sample is 1.247 mpy.
The corrosion rate obtained for oil quenched sample is 1.173 mpy.
The corrosion rate obtained for water quenched sample is 1.040 mpy.

3.3 Linear Polarization Resistance test results in Hydro chloric acid

Strong acids corrode metals very quickly particularly at higher concentration [6]. A reverse trend of corrosion has been observed in the case of these strong acids. Martensitic microstructure shows higher corrosion rate as compare to Pearlite. At higher concentaration of strong acids (such as HCl), not only general corrosion occurs but also Pitting participate in overall corrosion. In this case Martensite which has high overall energy (Non-equilibrium microstructure) corrodes at faster rate as compare to Pearlite, which is the most stable of all these. Corrosion behavior of this steel in HCl is in accordance with the behavior reported by David Abimbola Fadare et al.[6] can be seen in Figure-3.

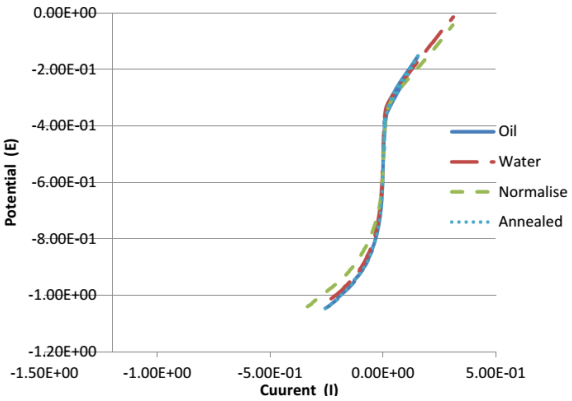

Figure 3. Comparison of all samples tested in Hydro chloric acid.

Corrosion behavior of Annealed sample is 152.1 mpy

Corrosion behavior of Normalized sample is 155.8 mpy

Corrosion behavior of Oil quenched sample is 199.6 mpy

Corrosion behavior of Water quenched sample is 164.3 mpy

3.4 Linear Polarization Resistance test results in Nitric acid

HNO_3 is a very stong oxidizing agent and hence most corrosive environment among all tested [7]. Corrosion trend is similar to the behavior exhibited in HCl (Both are strong acids). Martensite has been corroded at faster rate as compare to Annealed microstructure. Figure 4 shows comparisn of all samples tested in hydrochloric acid.

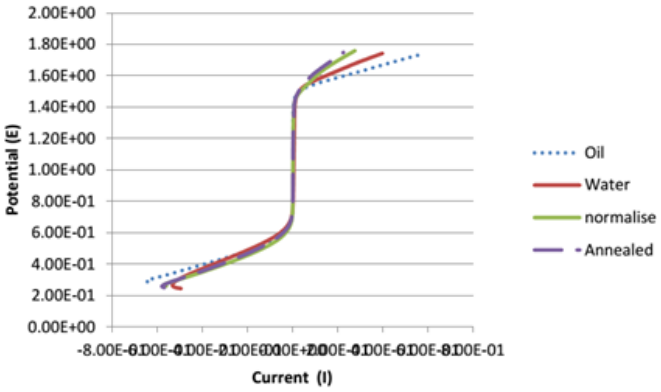

Figure 4. Comparison of all samples tested in Hydro chloric acid.

Corrosion behavior of Annealed sample is 158.9 mpy

Corrosion behavior of Normalized sample is 162.9 mpy

Corrosion behavior of Oil quenched sample is 245.2 mpy

Corrosion behavior of Water quenched sample is 185.6 mpy

3.5 Microstructural Analysis

Annealed Microstructure

The microstructure reveals coarse pearlite in black regions and ferrite as white regions after etching with 1% Nital, as shown in Figure 5.

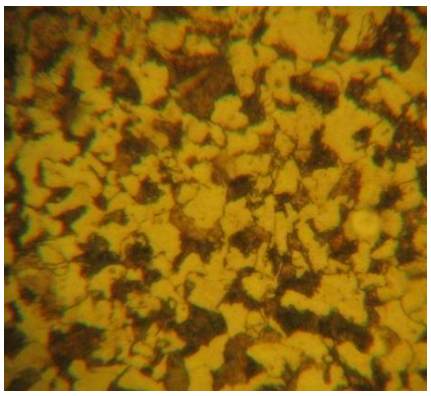

Figure 5. Microstructure of annealed sample at 400x.

Normalized Microstructure

The microstructure in Figure 6 reveals pearlite-ferrite regions in a much finer scale as compare to Annealed microstructure, as the cooling rate is high in normalizing.

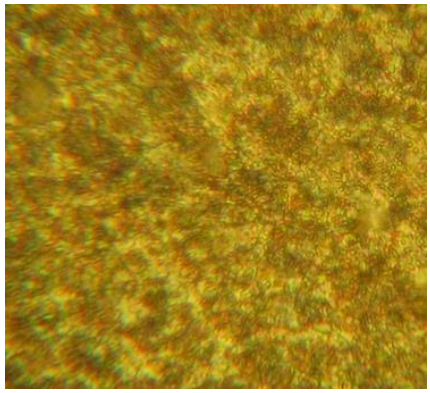

Figure 6. Microstructure of normalized sample at 400x.

Water Quenched Microstructure

In the Water quenched microstructure small needle like micro constituent phase, called Martensite is present within the matrix of Ferrite, as can be observed in Figure 7. Etching was done with with nital 1%.

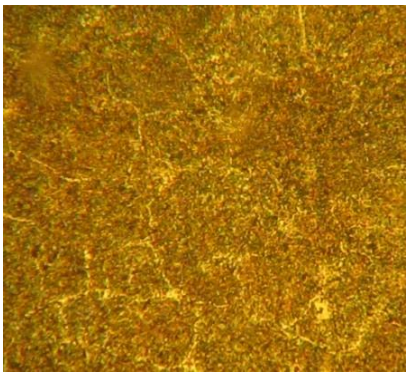

Figure 7. Microstructure of Water quenched sample at 400x.

Oil Quenched Microstructure

In oil quench microstructure Martensite is formed in small fraction due to the use of oil as quenching media, since oil has less quenching severity than water. This less severity causes yield of fresh Martensite to disrupt. It is important to note here that the presence of Bainite and tempered Martensite in the microstructure cannot be overruled Figure-8.

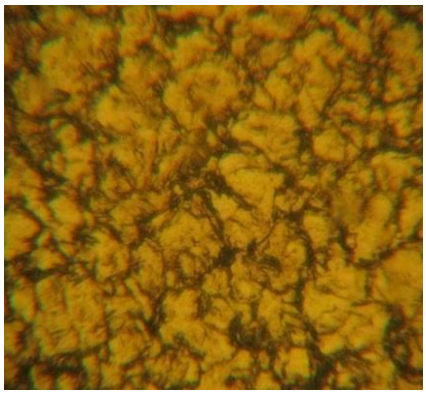

Figure 8. Microstructure of Oil quenched sample at 400x.

4 CONCLUSION

Conclusion of above work can be stated as follows:
Corrosion rate of Martensite is least in sea water and weak acids, as it is a single phase structure, fine pearlite which makes very strong microcells corrodes at highest rate in these environments.
In strong acids, corrosion rate of Martensite is highest due to being most unstable and non-equilibrium phase. With general corrosion these strong acids may cause Pitting, that accelerates the corrosion rate. In strong acidic environments Pearlite shows lesser corrosion rate.
HNO_3 is more corrosive to Carbon steels than HCl.

ACKNOWLEDGEMENTS

Authors would like to thank every individual who provided his assistance during any phase of this research and particularly to Mr. Zeeshan Hassan who as a Technician at Materials Deterioration lab, Department of Metallurgical Engineering, provided his assistance on numerous occasions.

REFERENCES

[1] Sami I. Al-rubaiey, Eman A. Anoon, Mahdi M. Hanoon, The Influence of Microstructure on the Corrosion Rate of Carbon Steels, Eng. &Tech. Journal, Vol. 31,Part (A), No.10, 2013

[2] Injeti Gurrappa, Guntupalli Malakondaiah, Effect of environment on corrosion characteristics of newly developed DMR-1700 structural steel *Iop publishing science and technology of advanced materials sci.* 9 (2008) 025005 (7pp) Published 12 June 2008.

[3] C. Andrade and C. Alonso, On-site measurements of corrosion rate of reinforcements *Construction and Building Materials*, Vol. 10, NO. 5, pp. 315-328, 1996 Copyright 8 1996 Elsevier Science Ltd.

[4] A. M. Ramirez-Arteaga, An Electrochemical Study of the Corrosion Behavior of a Dual Phase Steel in 0.5m H2SO4 *International Journal of Electrochemical science*, Int. J. Electrochem. Sci., 5 (2010) 1786 – 1798

[5] R. Whinston Revie, *Corrosion and corrosion control*, Wiley,2015 page-143

[6] David Abimbola Fadare, Corrosion Resistance of Heat-Treated NST 37-2 Steel in Hydrochloric Acid Solution Journal of Minerals and Materials Characterization and Engineering, 2013, 1, 1-7

[7] Osarolube, E., Owate, I. O. and Oforka, N. C. Corrosion behaviour of mild and high carbon steels in various acidic media, *Scientific Research and Essay* Vol.3 (6), pp. 224-228, June 2008 ISSN 1992-2248 © 2008.

COAL GASIFICATION AS A SOURCE OF SUSTAINABLE ENERGY – GEOMETRIC ANALYSIS USING ASPEN PLUS® MODEL

S. A. Taqvi[1,*], F. Uddin[2], Dr. I. Memon[2] and S. Nadeem[2]

[1]PhD Scholar, Chemical Engineering Department, University Technology Petronas Malaysia

[2]Chemical Engineering Department, NED University of Engineering & Technology, Karachi Pakistan,

[*]Corresponding author. Tel.: +60-017-3522501
E-mail address: s_taqvi@hotmail.com (S. A. Taqvi)

Abstract

The Energy Crisis at hand has been the focus of most of the research done recently across various disciplines. To come up with a sustainable yet inexpensive solution is a challenge for their work. Pakistan is a country blessed with many natural resources having vast potential to solve the issue both in short and long term basis, one of which is Coal. However, among other constraints, its environmental effects have been a topic of debate in engineering circles. This paper presents Coal gasification as a viable solution and proposes a model of indirect gasifier for this purpose. Results obtained from simulations on Aspen PLUS® show that cold gas efficiency and carbon conversion vary significantly as the diameter as well as height of the bayonets is altered, rising to about 50% and 90% respectively. Values of H_2/CO ratio obtained are approaching the conventionally desirable value of 3, but these parameters have relatively less impact on this ratio. The model also confirmed the reduced amount of SOx and NOx, without significantly affecting coal gas efficiency.

Keywords: Energy Crisis; Sustainability; Coal gasification; Aspen PLUS® Model

1 INTRODUCTION

Previous century was fuelled by the petroleum and natural gas. The pollutants unleashed by Petroleum are degrading the environment. In addition to their primary toxic nature, the sulfur and nitrogen compounds can also react further to produce other lethal chemicals. Furthermore, their depletion is at hand and it is high time to develop alternate fuels to go on with our lives as we do now. [**1**]

Coal is a reliable resource of energy due to its abundance in many countries of the world. However, it contains larger amounts of nitrogen and ash than those in other fuels, and its utilization has been questioned due to the environmental hazards it poses. The ash present in the coal causes metallurgical constraints for its processing. Burning coal produces massive amount of CO2, which is the main cause of global warming. There is a global requirement to develop technology so that the coal may be utilized in a highly proficient, environment friendly way. [**2**]

Gasification is a process in which combustible materials are partially oxidized. The product of gasification is a combustible synthesis gas, or Syngas. Because gasification involves the partial oxidization of the feed, gasification processes operate in an oxygen-lean environment. Gasification processes typically operate above their stoichiometric oxygen-to-fuel ratio to ensure near complete conversion to syngas. The amount of oxygen used in gasification, however, is always far less than that used in combustion and typically is less than half.

From a processing point of view the main operating difference is that gasification consumes heat evolved during combustion. Under the reducing environment of gasification the sulfur in the coal is released as hydrogen sulfide rather than sulfur dioxide and the coal's nitrogen is converted mostly to ammonia rather than nitrogen oxides. These reduced forms of sulfur and nitrogen are easily isolated, captured, and utilized, and thus gasification is a clean coal technology with better environmental performance than coal combustion.

2 SIMULATION MODEL

The development of the process for the reactions being carried out in gasifier is being carried out by using Aspen Plus® as the process simulator. The model comprises of three main processes i.e. coal drying, coal pyrolysis and char gasification carried out in the gasifier. The heat for these processes will be taken from the hot gaseous mixture passing through the section till the point that all the

materials in the top section are in thermal equilibrium.

2.1 Components:

The following components were selected from Aspen Plus® databank: O_2, CO_2, H_2, H_2O, CH_4, N_2, H_2S, C_6H_6, C, S and (Coal, Dry Coal, Char and Ash) were taken as Non-Conventional. The different components used in this study are described with their composition and property models are used for the approximation of their physical properties. For these components two models must be assigned: one for density (DCOALIGT) and the other for enthalpy (HCOALGEN), which requires knowledge of proximate analysis and ultimate analysis of the solids. These characteristics for coal are presented in paper, which is provided by Pakistan Council for Scientific and Industrial Research, PCSIR, Karachi Pakistan. These numbers represents, the PROXANAL and ULTANAL of air-dried sample of Thar Lignite Coal shown in Table 1.

1.3 Heat Integration:

Hot syngas stream available from the gasifier at high temperature is introduced in the cross-flow heat exchanger, where saturated steam is produced. The cold syngas stream is then fragmented in two parts. One is drawn as the product stream for further processing while the other goes for the combustion in the furnace combined with preheated air and then sent for combustion in the furnace where hot flue gases are generated. The saturated steam already produced is then used to generate superheated steam using the heat from the high temperature flue gases from the furnace. This steam is then sent to the gasifier to take part in the gasification reaction. Then the flue gases enter the bayonets to provide the heat required for gasification reaction. The flue gases from the gasifier bayonets are then used to preheat the air stream required for the combustion in furnace. The flow rate of the air stream is kept in excess to the stoichiometric air requirement for the combustion of syngas. Flue gases from the air preheat are then used to generate the corresponding saturated steam for the process and are exhausted to the atmosphere. The saturated steam produced here is mixed with the saturated steam produced from syngas cooling and sent for superheated steam generation. Hot ash from the gasifier is used for the preheating of water.

Table 1. Thar Coal Analysis

Proximate Analysis		**Ultimate Analysis**		**Sulphur Analysis**	
Element	Value (wt. %)	Element	Element	**Value (wt. %)**	**Element**
Moisture (wet basis)	8.5	C	54.57	Pyritic	1.46
		H	3.21		
Fixed carbon (dry basis)	25.83	N	1.07	Sulphate	1.47
		Cl	0		
Volatile Matter (dry basis)	53	S	4.39	Organic	1.46
		O	15.59		
Ash (dry basis)	21.17	Ash	21.17		

2.2 Process Description:

In this process, the coal is heated and a rapid process takes place with can be completed and certain temperature, the bounded moisture is removed from the coal by using steam that was injected from the bottom and coal from the top of the gasifier. The heated mixture contribute the breakdown of dried coal into char and other gases engendered form the conversion of volatile material into other products and tar. Heat required for the process can is supplied by the bayonets which are in vertical arrangement. The produced gases i.e. CO, CO_2, H_2, and CH_4 sent to the product stream with some other unreacted steam also escorts them. The ash discards off from the bottom. The product stream is alienated in to two parts, part of which is combusted in the furnace to derive gasifier bayonets and other as a sales product. Figure-1 shows the process of indirect gasification .

2.3 Chemical Kinetics:

In the process of char gasification, the following reactions are considered. [3][4]

$$\text{Coal} \rightarrow CO + H_2 + CO_2 + H_2O + H_2S + N_2 + CH_4 + C_6H_6 + \text{Char} \quad (1)$$

$$C + \frac{x+2y}{2x+2y} O_2 \rightarrow \frac{x}{x+y} CO + \frac{y}{x+y} CO_2 \quad (2)$$

$$C + H_2O \rightarrow CO + H_2 \quad (3)$$

$$C + CO_2 \rightarrow 2CO \quad (4)$$

$$C + 2H_2 \rightarrow CH_4 \quad (5)$$

$$CO + H_2O \rightarrow CO_2 + H_2 \quad (6)$$

$$H_2 + 0.5O_2 \rightarrow H_2O \quad (7)$$

Where, [**6**]

$$\frac{x}{y} = \frac{[CO]}{[CO_2]} = 2500e^{\frac{-6249}{T}} \quad (8)$$

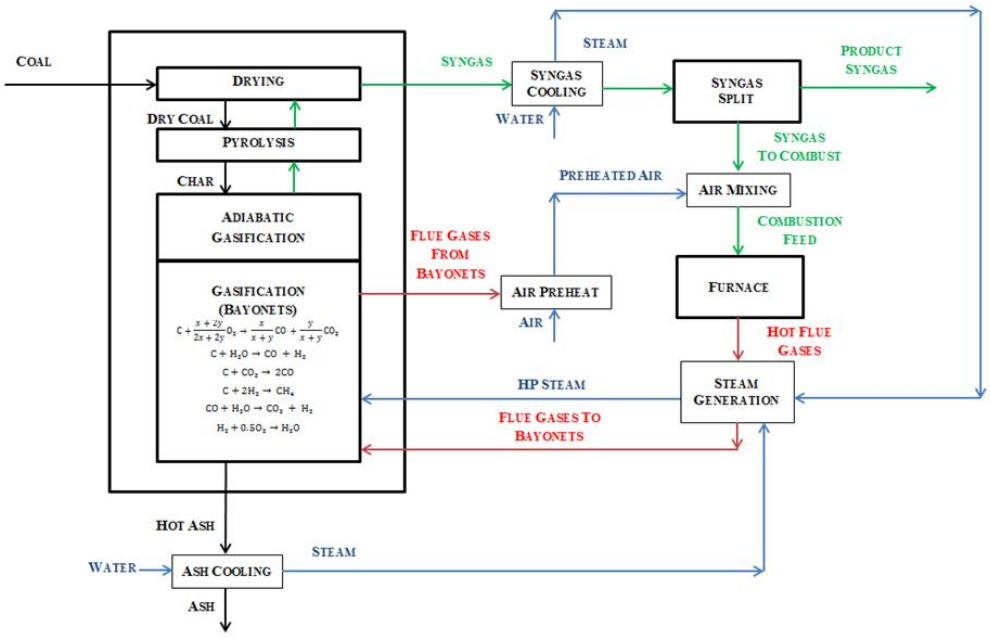

Figure 1: Process Scheme of indirect gasification using partial product syngas combustion with heat integration

3 RESULTS:

Results were generated by using different geometric variations in order to analyse their effect on the quality of the syngas produced. Feed conditions for both coal and steam were taken as same, with steam to coal ratio of 2.0. The effects of the following variables were analysed:

- Diameter of the gasifier;
- Height of Bayonets (making the non-adiabatic gasification section);

The performance indexes which were defined and estimated according to simulation results were following:

Cold Gas Efficiency

Cold Gas Efficiency of the process is calculated as:

$$\text{Cold Gas Efficiency} = \frac{Total\ Heating\ Value\ of\ Dry\ Syngas, kCal/hr}{LHV\ of\ Total\ wet\ Coal, kCal/hr}$$

Carbon Conversion

Conversion of coal in the reactor is based upon the conversion of carbon content in the char introduced to the gasification process:

$$X_c = \frac{m_{c_{in}} - m_{c_{out}}}{m_{c_{in}}}$$

H_2/CO molar ratio:

$$\frac{H_2}{CO} = \frac{\dot{n}_{H_2}}{\dot{n}_{CO}}$$

Simulation results for the Thar Lignite Gasification are presented in Figures 2, 3 and 4. These results are based on the analysis of dry syngas after condensate removal from the raw syngas product stream and were plotted by using MATLAB® 2013.

In Fig. 2, cold gas efficiency is reported as a function of diameter and bayonets' height. A trend similar to the elliptical valley was obtained. It is shown that cold gas efficiency varies significantly as the diameter as well as height of the bayonets are altered, rising in the middle to about 50%. The parameters, when altered, cause a change in superficial velocities within the gasifier and heat transfer between the flue gases and the gasifier environment. Hence the cold gas efficiency is drastically changed.

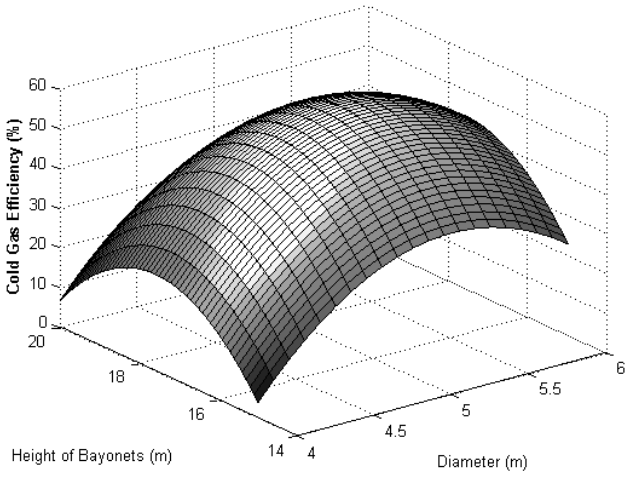

Figure 2: Cold Gas Efficiency v/s Height of Bayonets (m) and Diameter (m)

H_2/CO molar ratio is reported as a function of diameter and bayonets' height in Fig. 3. It can be seen that the values of H_2/CO ratio obtained are approaching the conventionally desirable value of 3. The sensitivity of the parameter is much increased at the higher values of diameter. H_2/CO molar ratio is showing increasing trend as with increase in diameter. However, it should be noted that the values of H_2/CO are all close to 2.7 and it can be concluded that these parameters have less impact on this ratio.

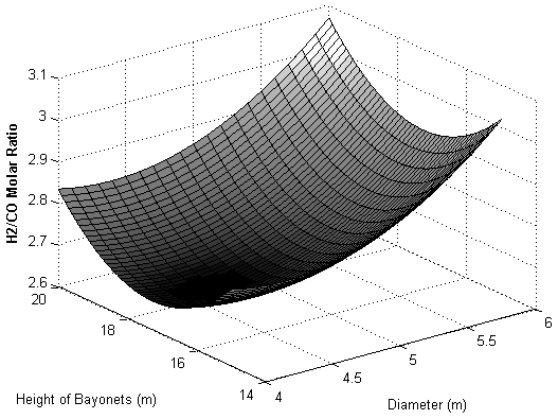

Figure 3: H_2/CO Molar Ratio v/s Height of Bayonets (m) and Diameter (m)

Carbon conversion in percentage is plotted as a function of diameter and bayonets' height in Fig. 4. The trend obtained was similar to that of cold gas efficiency. It was observed that the carbon conversion do not drop lower than 70% and can be as high as 90%. The Conversion of carbon in gasifier is showing optimum results by increase in the diameter of gasifier.

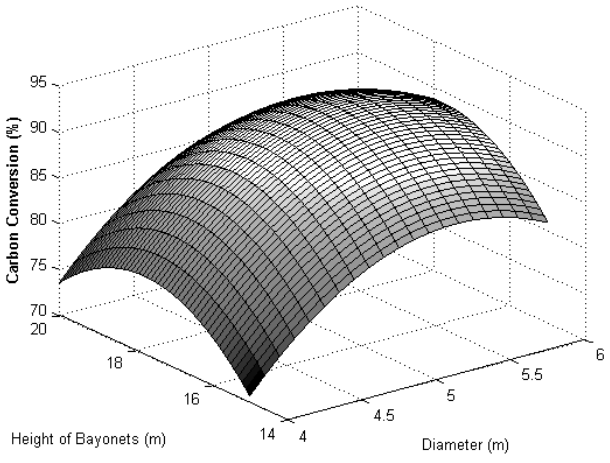

Figure 4: Carbon Conversion (%) v/s Height of Bayonets (m) and Diameter (m)

4 CONCLUSION:

The development of the gasifier environment is carried out by using Aspen Plus® process simulator. Coal, Dry Coal, Char and Ash are described using their proximate and ultimate analyses. In the gasifier, coal is de-moisturized, pyrolyzed and gasified to produce syngas. Part of the syngas stream is combusted in the furnace where hot flue gases are generated to provide the heat required for gasification reaction. Results were generated by using different geometric variations in diameter of the gasifier and height of bayonets. Cold gas efficiency, carbon conversion and H_2/CO molar ratio were considered as the performance indexes.

Results show that cold gas efficiency varies significantly as the diameter as well as height of the bayonets is altered, rising to about 50%. Values of H_2/CO ratio obtained are approaching the conventionally desirable value of 3, but are all close to 2.7 and it can be concluded that these parameters have relatively less impact on this ratio. Carbon conversion is affected considerably as the diameter and height of the bayonets is changed, attaining a maximum of about 90%. Production of SOxs and NOxs are also avoided due to the reductive environment of gasifier. Hence the scheme proposed is viable and can provide solution to the energy crisis as well as environmental pollution.

ACKNOWLEDGEMENTS

The authors are extremely thankful to Mr. Junaid Akhlas, (Enrolled Ph.D. student, Department of Chemical Sciences, University of Padova, Italy) who extended his helping hand in the ups and downs of this work. His experience and expertise in the software were cooperative in the generation of the results.

REFERENCES

[1] Maria Sudiro, Carlos Zanella, Alberto Bertucco, Luigi Bressan, Marco Fontana. Dual-Bed Gasification of Petcoke: Model Development and Validation. Energy Fuels, 24 (2010), 1213–1221.

[2] Maria Sudiro, Alberto Bertucco. Production of synthetic gasoline and diesel fuel by alternative processes using natural gas and coal: Process simulation and optimization. Energy, 34 (2009), 2206–2214.

[3] C.Y. Wen, H. Chen, M. Onozaki (1982). User's Manual for Computer Simulation and Design of the Moving Bed Coal Gasifier. Report submitted to Morgantown Energy Technology Center and U.S. Department of Energy, Contract No. DOE/MC/16474-1390.

[4] I.H. Rinard, B.W. Benjamin (1985). Great plains ASPEN model development: gasifier model. Literature Review and Model Specification. Presented to U.S. Department of Energy, Morgantown, WV, Final Topical Report DOE/MC/19163-1782..

[5] C.Y. Wen, T.Z. Chaung (1979). Entrainment coal gasification modelling. Ind. Eng. Chem. Process Des. Dev., 18, 684-695.